FINAL REPORT

THE OGO ATTITUDE CONTROL SUBSYSTEM REDESIGN AS A RESULT OF OGO III EXPERIENCE

67.7231.7-116

30 JUNE 1967

VOLUME I

SYSTEM ANALYSIS AND DESIGN STUDIES

Prepared by

K. J. McKenna

Approved by

M. S. Robinson
ACS Subproject
Manager

Approved by

M. J. Abzug
Assistant Manager
Controls Design
and Analysis Department

198 p

TABLE OF CONTENTS

TABLE OF CONTENTS (CONT'D.)

TABLE OF CONTENTS (CONT'D.)

TABLE OF CONTENTS (CONT'D.)

ILLUSTRATIONS

ILLUSTRATIONS (CONT'D.)

ILLUSTRATIONS (CONT'D.)

ILLUSTRATIONS (CONT'D.)

ILLUSTRATIONS (CONT'D.)

TABLES

1.0 SUMMARY

OGO-III experienced an oscillation in the roll control channel. The oscillation or limit cycle was the result of the EP-5 and EP-6 boom motion coupling into the control channel. The oscillation was sustained much of the time by the roll reaction wheel. This resulted in a high duty cycle of the roll wheel which eventually caused the motor driver magnetic amplifier to fail, shorting the inverter which supplies the Attitude Control Subsystem (ACS). This caused loss of earth stabilization capability.

The purpose of this report is to bring together under one cover major portions of the analysis effort precipitated by the OGO-III failure. This effort included; (1) an analysis of the OGO-III and OGO-II flight data to determine the nature and extent of the roll oscillation phenomena, (2) design analysis of the complete ACS to evolve changes which would prevent recurrences of the coupled ACS boom oscillation observed on OGO-III, (3) analog simulations to verify the performance of the design changes selected.

In this report selected portions of OGO-III and OGO-II flight data are illustrated and the major flexible body oscillations identified. A model of the major flexible appendage dynamics is developed and is shown analytically and through analog simulations to reproduce the OGO-III oscillation phenomena. One mode of oscillation which was observed in the flight data could not be verified by simulation.

The analysis and rationale behind the design changes evolved to prevent oscillations in future spacecraft is presented. Finally, the results of analog simulations made to verify the stability and determine the performance characteristics of the ACS with the design changes are presented.

The design changes which were found necessary were:

1. A reversal delay logic for the roll reaction wheels. This logic prevents the roll wheel from reversing its torque direction for 5 seconds. Thus, the wheel can not sustain a limit cycle of the type observed on OGO-III.

2. Widening of the solar array deadzone from 0.5 to 1.0 deg. Worst case studies showed the array might coast across the 0.5 deg deadzone and limit cycle on its own. The deadzone was widened to prevent this.

3. Modification of the OPEP control loop to include a filter and stabilizing feedback loops. The OPEP oscillated in sympathy with the roll oscillations, so the error signal was filtered to reduce OPEP sensitivity to spacecraft motion.

The design changes which were found desirable, i.e. provided increased margins considering the effects of flexible structure were:

1&2. A reversal delay logic for the yaw reaction wheel and increasing the yaw gas deadzone from 2.5 to 5.0 deg. Stability analysis showed that the yaw system could sustain a limit cycle in the same manner as the roll channel if the boom damping was very low. Thus these changes were made to improve the ACS flexible body stability margins.

3. Reversal delay logic for the array drive. The array was observed to oscillate in sympathy with the roll oscillations on OGO-III. Although the wider array deadzone should have prevented any future oscillation, the delay logic was added for insurance.

2.1 HISTORY

OGO III was launched 7 June 1966 from Cape Kennedy. The spacecraft was injected precisely into an EGO orbit with 146 nautical mile perigee, 66,200 nautical mile apogee and orbit period of 48 hours 37 minutes. The ACS proceeded smoothly through sun acquisition. The spacecraft was held in the sun pointing mode until horizon scanner and ACS operation could be assessed. When it was determined that operation was nominal, the ACS was released from its sun pointing mode and earth acquisition was accomplished easily. From this point through the approach to the first perigee (2 days later) ACS operation was normal and without incident. During approach to the first perigee at an altitude of approximately 2800 nautical miles, the roll reaction wheel began to exhibit a back-and-forth pulsing characteristic. This motion began to build slowly in amplitude until a definite limit cycle could be observed in the roll wheel tachometer with a period of approximately 2.5 seconds. Approximately 37 minutes later the oscillation amplitude had grown sufficiently so that the pneumatics also started limit cycling. A few minutes later the solar array drive also began to pulse back and forth in sympathy with the oscillation. The roll error signal amplitude reached a maximum amplitude of 0.6 degree peak-to-peak.

As soon as the gas activity was confirmed on the ground a command was sent to insert the gas delay logic. This prevented the pneumatics from participating in the oscillation. Through the reaction wheels continued to sustain the oscillation, the amplitude decreased sufficiently so that the array stopped oscillating. As the spacecraft approached apogee the roll reaction wheel activity ceased but reappeared again as the spacecraft again approached perigee. This behavior continued to repeat itself on succeeding orbits. The oscillation amplitude when driven by reaction wheels alone, was too small to be detected in the roll telemetry signal, thus the oscillation was not

affecting overall pointing accuracy of the ACS. A detailed description of the initial ACS operation is given in Reference 2-1.

Studies have confirmed that the ACS limit cycling was the result of the EP-5 and EP-6 experiment boom motion coupling into the ACS error signals. That is, bounded oscillations were created and sustained by the ACS at the flexible body frequency of the combined system of EP-5 and EP-6 booms and main box. These studies have also shown one of the major contributors to the initial excitation of boom motion was the solar array drive system.

On July 23, 1966, OGO III experienced a serious ACS failure which caused the loss of earth stabilization capability. An intensive effort was immediately undertaken to isolate the primary failure and to determine the potential impact on the OGO-D spacecraft.

It was concluded that the primary failure occurred in the roll wheel magnetic amplifier in the Attitude Control Assembly (ACA). The mag amps are employed in the ACA to supply drive to the reaction wheels. A short condition in the mag amp overloaded the ACS inverter and eventually caused that unit to fail. It was also concluded that the high duty cycle encountered in the roll channel due to the boom oscillation problem probably accelerated the failure of the mag amp although this in itself should not have caused a failure.

A detailed discussion of the magnetic amplifier failure analysis is given in References 2-2 and 2-3. It was found from these studies that the high duty cycle encountered in the roll channel due to the boom ACS oscillation overheated the magnetic amplifier and eventually caused its failure. Therefore, two courses of action evolved. One was the redesign of the magnetic amplifiers to insure that they would withstand a high duty cycle. The second was to determine ACS modifications which would eliminate the boom - ACS oscillation problem. This report is concerned exclusively with the latter problem.

2.2 OGO FLEXIBLE DYNAMICS

Figure 2-1 is a sketch of OGO with the major flexible appendages shown. The EP-5 and 6 booms have nearly equal cantilever natural frequencies of 0.24 cps. The boom torsional modes were adjudged to be an insignificant dynamic effect. The solar arrays have a cantilever bending natural frequency of 1.76 cps and a torsional frequency of 0.68 cps (Reference 2-4). The Haddock Antenna has a cantilever natural frequency of 0.023 cps.

An analysis of the EP-5 and EP-6 booms and the main box structure showed that there are two primary modes of oscillation about the roll axis at the frequencies of interest. The bending modes and frequencies are shown in Figure 2-2. The first bending mode yields a bending frequency near that of the cantilevered boom frequency (0.24 cps). It does not, however, result in rotation of the main box structure and thus cannot be sensed by the control system sensors. The second bending mode (0.42 cps) does result in box rotations and can be excited by torques on the main box such as those produced by the reaction wheels, gas jets and solar array drive. It was this second bending mode frequency (0.42 cps) that was observed during the OGO III flight.

A simplified block diagram for the roll axis ACS elements is shown in Figure 2-3. The significance of the various elements shown will be discussed in the succeeding sections. It is of importance to note that there are three possible sources of boom excitation: namely the wheels, gas jets and solar array drive.

2.3 CONTENTS OF REPORT

The sections which follow contain detailed discussions of virtually all of the analysis performed in support of the ACS redesign that was precipitated by the OGO-III failure. Not included in this report are the analysis and design details relating to the hardware component redesign. The hardware changes to the ACS included the redesign of the motor driver magnetic amplifiers, repackaging of the

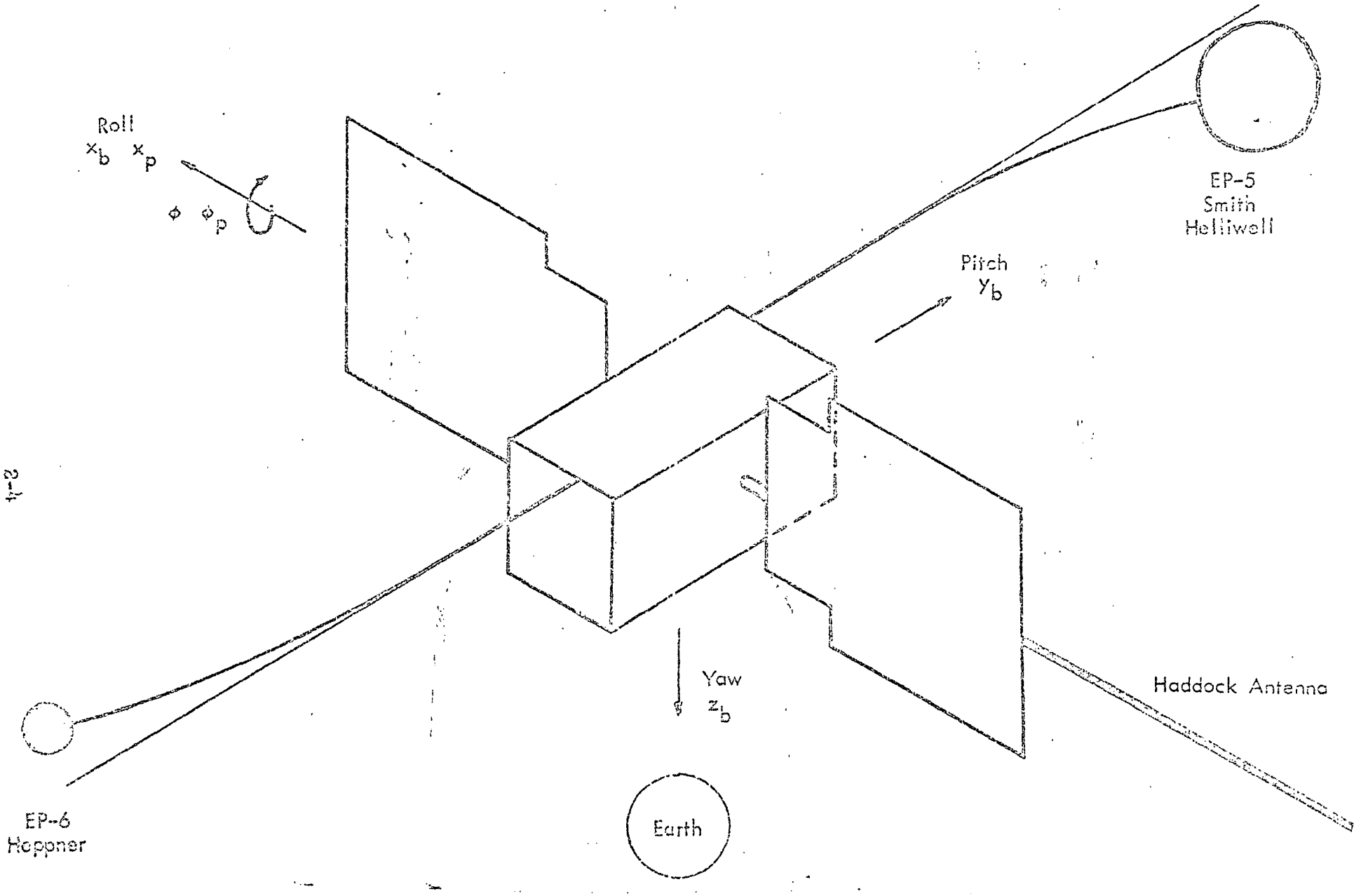

Figure 2-1; The CGO Spacecraft and Major Flexible Appendages

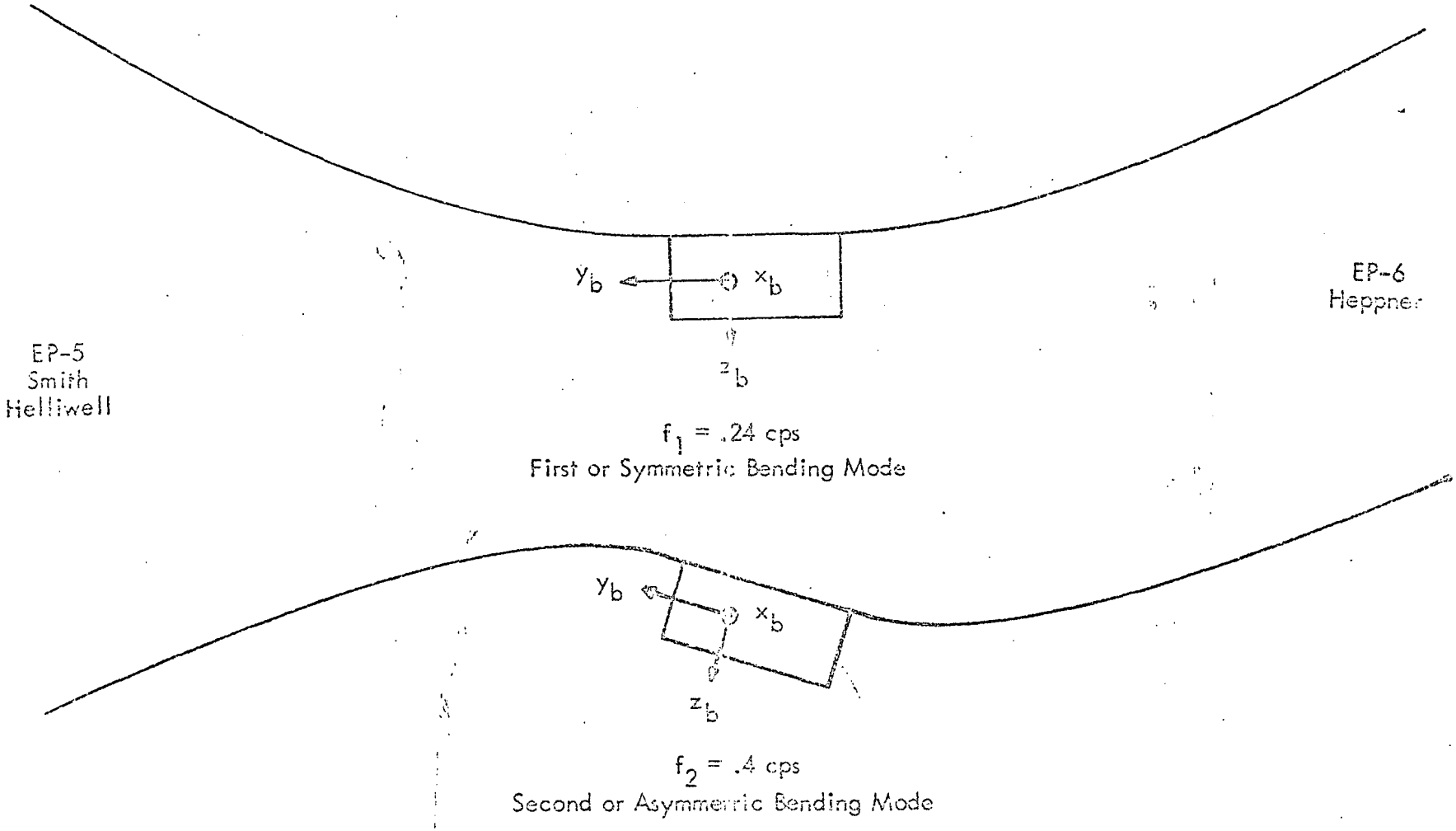

Figure 2-2, CCO Roll Axis Bending Mode Displacements

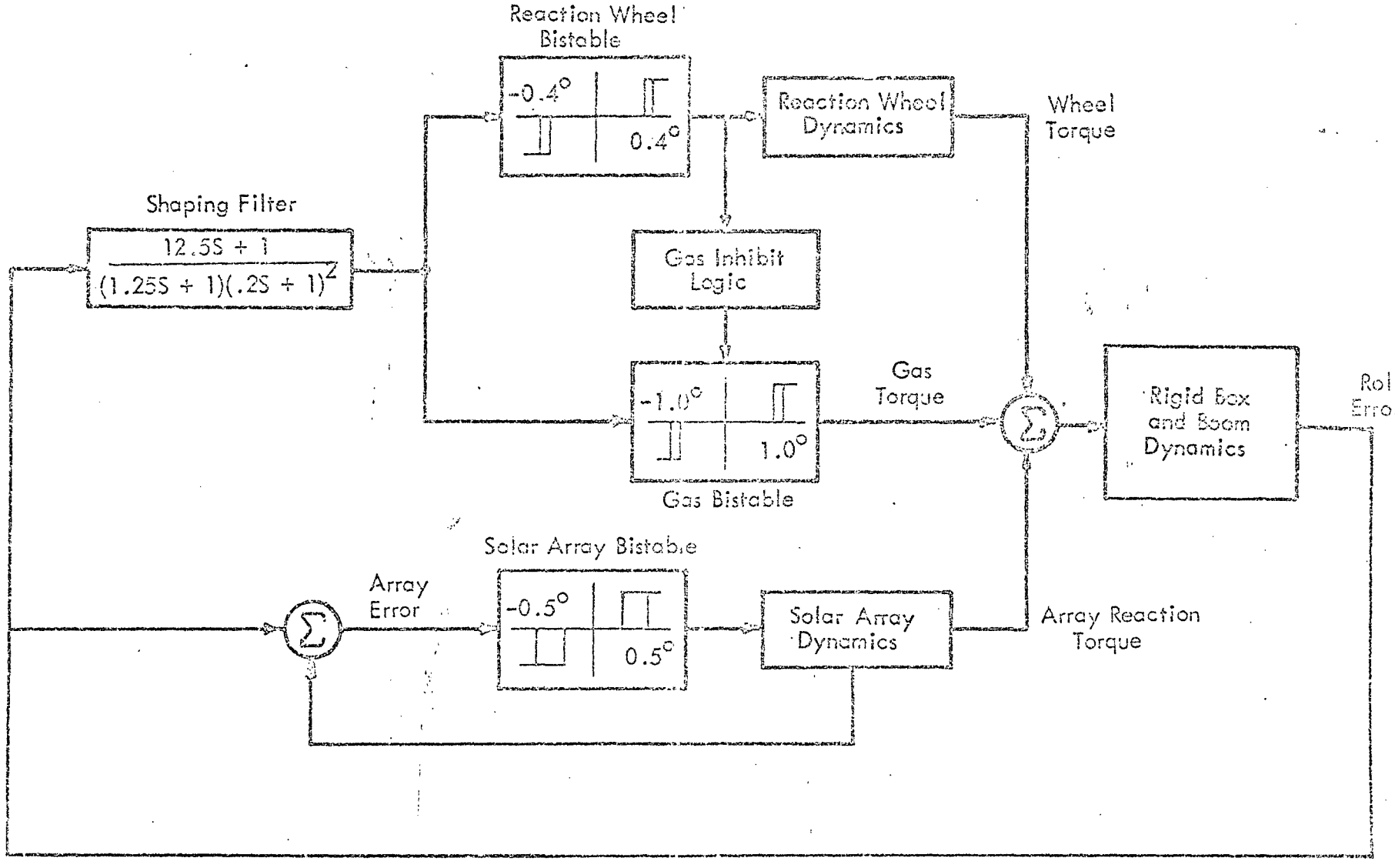

Figure 2-3, OGO Roll Axis Control Elements

bistable magnetic amplifiers and certain circuit design improvements.

Section 3.0 contains examples and analysis of flight data from OGO-III and OGO-II which relate to the boom oscillation problem. A model of the boom dynamics is developed in Section 4.0 and analyzed to show the causes of the roll oscillation observed on OGO-III. In turn the validity of the boom dynamics model is demonstrated by comparison of the model response characteristics to the OGO-III flight data. In Section 5.0 is a discussion of the design considerations and analysis which lead to the selection of the ACS modifications. The necessity for changes in the pitch and yaw control channels in addition to roll was explored. Section 6.0 contains results of analog simulation studies made to verify the performance and stability of each of the ACS channels (pitch roll and yaw) with the proposed changes.

3.0 PRESENTATION AND ANALYSIS OF FLIGHT DATA

3.1 SUMMARY OF FLIGHT DATA ANALYSIS

The OGO flight data was reviewed in an effort to identify all manifestations of oscillatory behavior and to understand the data in sufficient detail to effect corrective design modifications. To this end flight data from both OGO II and OGO III was examined. Various filters and scale expansion were applied to quantities of special interest. Particular attention was paid to the known areas of anomalous behavior, namely the oscillatory motions in the roll and solar array control systems.

3.2 TELEMETRY DATA REVIEWED

The OGO telemetry data available for analysis occurs in many forms, encompassing many conditions of orbit. For detailed review, however, only data taken during "interesting" periods and at high sample rates is useful. Signals indicating the significant flexible body oscillations must be sampled oftener than once each second to be useful and motor drive phasing information requires still more frequent sampling. In general the kinds of data reviewed were as follows:

- Real time maincom at 64 KBS (not too useful)
- Real time accelerated subcom 2 at 8 KBS or more
- Tape playback accelerated subcom 2 recorded at 1 KBS (not too useful)
- Tape playback flexible format 32 recorded at 1 KBS

The periods of interest on OGO III were those during which the roll oscillations occurred, when the OPEP was functioning, and just prior to the inverter failure. This restricts the significant information to periods when the spacecraft was sensibly close to perigee (good ground coverage at these times was frequently lacking). When data was obtained near perigee at adequate sample rates, detailed review was possible. Even then certain quantities could not always be studied due to adverse circumstances (the important array drive

motor and OPEP motor events telemetry is not available at useful sample rate in flexible format, for instance).

The most helpful data for study of the roll oscillation was obtained at rev 001 and rev 002 perigees and near the end of the minor axis of rev 021. The inverter failure data was, of course, taken from rev 023 from maincom at 64 KBS. OGO II telemetry was taken during periods of Mode 3 operation, and was especially useful during the 1st and 2nd earth acquisition transients. A tabulation of the telemetry data reviewed is given in Tables 3-1 and 3-2. Examples of the more significant portions of these data appear in later figures.

3.3. OGO III FLIGHT TELEMETRY

3.3.1 General Flight Experience

The first evidence on the ground of the OGO III oscillation was upon its first approach to perigee, when excessive use of control gas was noted by a remote tracking station. When this was confirmed at GSFC through the Rosman link, a command was sent to engage the ACS gas delay logic, terminating the excessive jet action at 04:51 GMT (shortly after rev 001 perigee). As has been stated earlier the problem was caused by a bounded oscillation in the ACS roll channel at the flexible body natural frequency. Analysis of the flight data showed as the first perigee was approached this oscillation progressed from very small amplitude through successive stages of increased amplitude, involving first the roll reaction wheel drive loop, then the roll gas loop and finally the solar array drive. When all three excitation sources were participating in the oscillation the roll amplitude reached a value of 0.6 degrees. When the gas delay command was exercised the gas jets ceased to participate, and almost immediately thereafter the array drive motor support ceased also. The roll reaction wheel continued to oscillate until the spacecraft reached the end of the minor axis, when it damped of its own accord.

Rev	Date(Z)	Approx. Time Period	Data Form	Basic Sample Frequency (samples/sec)	Data Processing	Indications
001	6-9-66	02:40Z to 04:40Z	RT ASC 8KBS	7	Filter and expanded scale on A5 and A11	Roll wheel and gas oscillation present. Start of array oscillation near perigee.
001	6-9-66	03:00Z to 05:00Z	DS FF32 1KBS	3.5	With and without filter and expanded scale on A5 and A11	Both start and termination of roll wheel, roll gas and array oscillations near perigee.
002	6-11-66	03:00Z to 05:00Z	DS FF32 1KBS	3.5	Filter and expanded scale on A5 and A11	Start of roll oscillation near perigee and two (only) occurrences of momentary array oscillation.
013/ 014	7-3-66	18:00Z	DS ASC 1KBS	0.9	None-tape not available	First eclipse and post eclipse turn. Apparent sporadic array oscillation occasionally.
017	7-9-66	21:22Z to 21:28Z	RT ASC 64KBS	56	Filter and expanded scale on A5 and A11	Roll oscillation after perigee.
018/ 019	7-13-66	1300Z	DS ASC ?	?	None - tape not available	Roll oscillation. Sporadic array oscillation.
019	7-13-66	20:36Z to 20:46Z	RT ASC 64KBS	56	Filter and expanded scale on A5 and A11	Slight ringing of booms is evidence. No oscillation. (Covers period about 6 hrs. after perigee.)
020	7-15-66	20:35Z to 20:45Z	RT ASC 64KBS	56	Filter and expanded scale on A5 and A11	" " " " " " "
021	7-17-66	20:20Z	RT ASC 64KBS	56	Filter and expanded scales on A5 and A11. Expanded scales on A4, A10, A12 and A17 also	Roll wheel and array oscillation. Shows termination of array oscillation.
023/ 024	7-23-66	16:00Z	RT MC 64KBS	0.44	None	Roll wheel and array oscillations just prior to and during ACS inverter failure. Shows sporadic load bus current and anomalous operation of roll wheel drive.

Legend:

RT = real time
DS = data storage(S/C tape recorder)
ASC = accelerated subcom
MC = maincom(normal subcom)

FF32 = flexible format No. 32
KBS = kilobits per second maincom rate
A5 = roll error signal
A11 = array error signal

Table 3-1, OGO III Telemetry Data Reviewed

Rev	Date	Approx. Time Period	Data Form			Basic Sample Frequency (samples/sec)	Data Processing	Indications
005	10-14-65	21:20Z to 22:00	RT	ASC	64 KBS	56	Filter and expanded scale on A5 and A11	Period including first earth acquisition. Ringing oscillation of booms indicated with initial, momentary support by roll wheel and array motor.
033	10-16-65	22:46Z	RT	ASC	64 KBS	56	Filter and expanded scale on A5 and A11	Period including second earth acquisition. Roll oscillation due to boom ringing indicated with initial, partial support from array motor and roll wheel during acquisition transient.
034	10-16-65	23:49Z to 24:00Z	RT	ASC	64 KBS	56	Filter and expanded scale on A5 and A11	Slight roll ringing with at least partial support of roll wheel. No consistent array motor participation. OFSP oscillation.

Legend:

RT = real time
ASC = accelerated subcom
KBS = kilobits per second maincom rate
A5 = roll error signal
A11 = array error signal

Table 3-2, OGO II Telemetry Data Reviewed

From that time onward the ACS gas delay logic remained in effect preventing further gas jet support of roll oscillations. On at least 70% of the subsequent orbits (until ACS failure on rev 024) roll oscillations began as the satellite approached perigee, involving the roll reaction wheel in an oscillation at the flexible body natural frequency at amplitudes of approximately 0.2°. On early orbits the solar array drive loop participated in the oscillation only rarely and sporadically (except on rev 001 when gas jet support was present). On later orbits, rev 021 being the best example, the array drive motor became heavily involved, continuing to support the roll oscillations until the satellite had receded toward apogee to an altitude of 20,000 to 30,000 n. miles. The array oscillation would then decay and cease spontaneously. The roll wheel would continue for some additional period, however, sometimes through apogee.

The roll channel oscillations did not appear to involve the pitch or yaw channels, although very small ringing motions in those axes could occasionally be discerned. The ACS appeared in general to perform as expected in the presence of such oscillations, i.e., no difficulty associated with ACS equipment could be detected (until rev 023).

At the perigee of revs 023/024 on 7-23-66 anomalous behavior of the ACS roll channel equipment was observed concurrently with indications of large, sporadic power loads. At that time the solar array and roll reaction wheel were both supporting a roll oscillation. As the large load current surges began to appear the roll reaction wheel responded peculiarly to the roll error signal, accelerating in the wrong direction at approximately 25% of its full capability. At that time and for the following two minutes the spacecraft bus current increased by some eight to ten amperes, finally increasing off scale. Approximately 40 seconds later the spacecraft undervoltage bus was automatically disconnected by the overload, interrupting the telemetry. Subsequent reset of the undervoltage bus restored telemetry but the ACS inverter never started again. It was therefore concluded that the ACS inverter had failed and had probably drawn the large bus currents observed. It could not be reasonably established that the inverter

was the primary fault. However, there is evidence that failure of the roll wheel drive magnetic amplifier provides more satisfactory explanations for the observed behavior (References 2-2 and 2-3).

3.3.2 Roll Channel Oscillations

The oscillations of the roll channel observed on OGO III were due basically to the effect of flexible body bending modes with very low inherent damping. The significant bending occurs in the long experiment booms, EP-5 and EP-6. A more complete flexible description of OGO would indicate a myriad of bending and torsional modes at a variety of frequencies. Many of these modes may couple. In addition to linear flexibility effects, many non-linear mechanisms can complicate the mechanical description by introducing step changes in parameter values, hysteresis, transport lags and variable friction, as well as by generation of harmonic responses. While much (perhaps most) of the phenomena observed during OGO III flight are explicable in terms of a simple, flexible structural model some of the more ragged waveforms and higher frequencies cannot be satisfactorily explained without introducing a more sophisticated structural description. Also much of the apparent oscillatory content of the telemetered ACS quantities appears to be due to beats between the legitimate signal frequencies, the telemetry sampling frequency and the dither oscillation present on the roll and pitch error channels as a result of the normal horizon scanner positor motion.

The roll oscillations observed on OGO III are of several kinds, differing in the type and degree of involvement of the several sources of roll torque. They are as follows:

A) Slight oscillatory motion in roll at the coupled, flexible natural frequency (second bending mode) with no participation of the reaction wheel, gas jets or solar array drive motor. This is sometimes referred to as "ringing" of the long booms and can be caused by any of a number of transient excitations.

B) Roll oscillation supported only by unidirectional reaction

wheel drive in synchronism. This probably results from occurrence of the ringing motion near the edge of the roll wheel deadzone, causing the wheel to actuate on peaks of the wave.

C) "Hard" roll oscillation supported by synchronous actuation of the roll reaction wheel alternately in both directions. In this case the oscillation amplitude is sufficient to exceed the roll wheel deadzone on each side resulting in full wheel participation at the flexible natural frequency (second bending mode).

D) Roll oscillation supported by synchronous actuation of the solar array drive in one direction only. This is similar to B) and is probably caused by existence of the ringing oscillation near the edge of the array error deadzone producing drive actuations on the peaks of the wave.

E) "Hard" roll and array oscillation with both the roll wheel and the array drive motor participating alternately in both directions. In this case the amplitude of the array error oscillation exceeds the array error deadzone on both sides although the roll error amplitude need not be large. This oscillation is usually observed at a frequency slightly different than the fixed array coupled natural frequency.

F) "Hard" roll oscillation supported by both the roll reaction wheel and roll gas jets. In this case the amplitude is sufficient to exceed the gas jet deadzone alternately on both sides.

G) "Hard" roll and array oscillation supported by synchronous, bilateral actuation of the roll reaction wheel, roll gas jets and the solar array drive.

3.3.3 Flight Data Description

Following are chronological descriptions of the observed roll oscillation behavior of OGO III during several portions of the first 23 orbits.

Upon approach to the first perigee after earth acquisition slight roll oscillations of type A (ringing) were observed. At approximately 03:50 Z on 9 June 1966 the roll reaction wheel began to participate in the oscillation first in a type B then in type C motion. This continued through perigee until approximately 04:33 Z when the roll gas jets began to support the oscillation in a hard limit cycle. The roll wheel and gas limit cycle (type F) frequency and amplitude were maintained at 0.40 cps and 0.3° respectively for several minutes (at least four) at which time the solar array drive began to contribute roll impulses (actually torque doublets) in synchronism. A hard oscillation was thus commenced with the roll wheel, roll gas jets, and array drive motor participating. This p rsisted at a frequency of 0.37 cps and a roll amplitude of 0.5° until 04:55 Z when a ground command engaged the ACS gas delay logic, terminating the gas participation.

The following three figures are reproductions of selected OGO III telemetry readouts of the rev 001 perigee period. Figure 3-1 shows the beginning of the gas oscillation in roll, the effects of which can be seen on the other channels. The data is shown in normal scale without filtering, and was taken from a playback of the spacecraft tape recorder in flexible format 32. Note that time increases to the left in the figure. Figure 3-2 is also tape recorder data in flex format 32 but its scales have been expanded and some filtering (not too effective) has been applied to the roll and array error channels. The assumption of gas jet participation and its effect on the roll error amplitude can be clearly seen. The sawtooth waves of approximately 30 second period seen on the array error channel are due to normal array drive sun pointing corrections at the high orbit rate near perigee. The frequency of these corrections (which introduce roll torques as great as 40 ft lb for very short times) increases gradually as perigee is approached until the period is as short as 10 seconds. This process may offer an explanation for the incidence of roll oscillations near perigee as the solar array corrective pulses can synchronously excite the long booms as the pulse application period sweeps over its wide range.

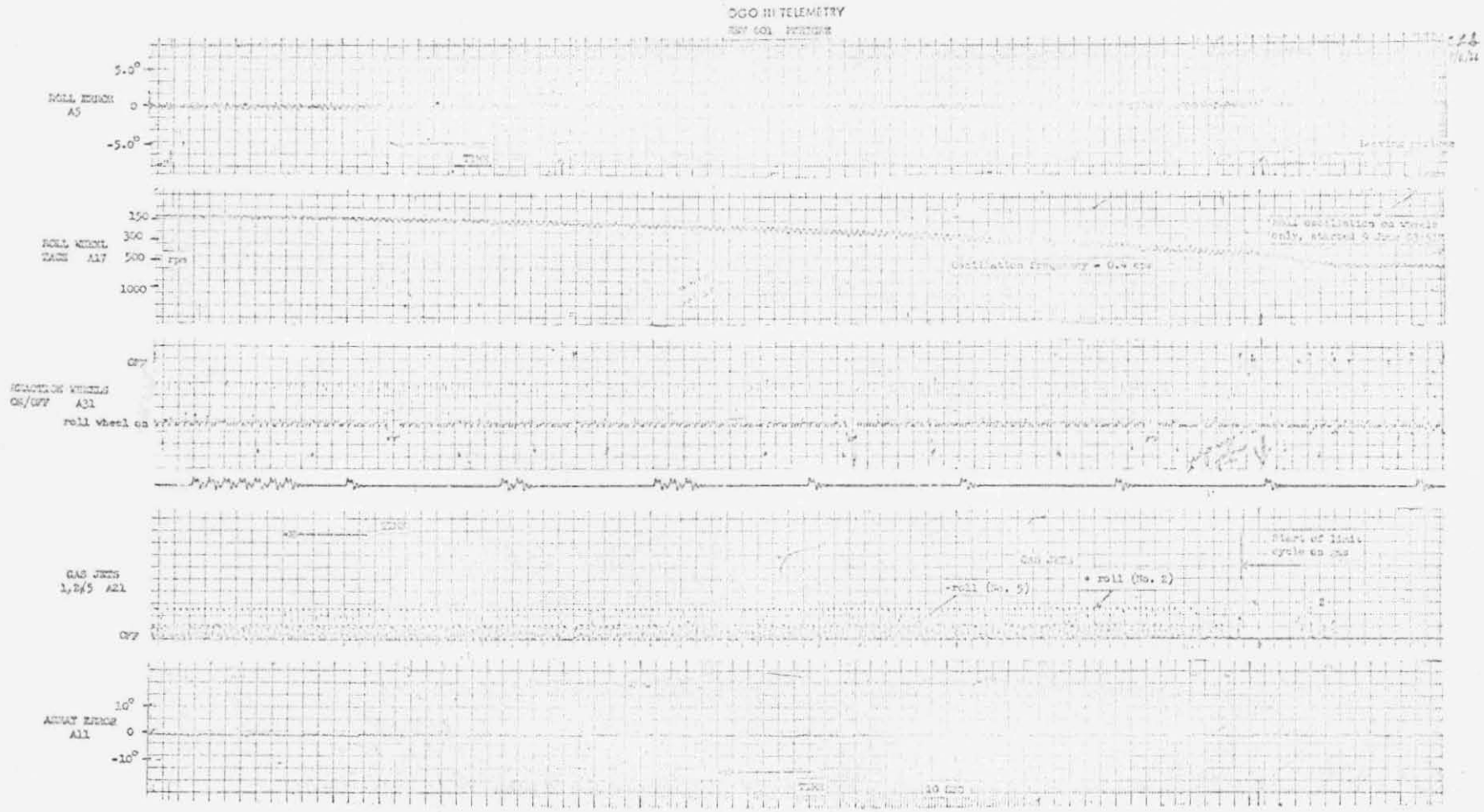

Figure 3-1

OGO III Telemetry Rev 001 Start of Gas Limit Cycle

FOLDOUT FRAME

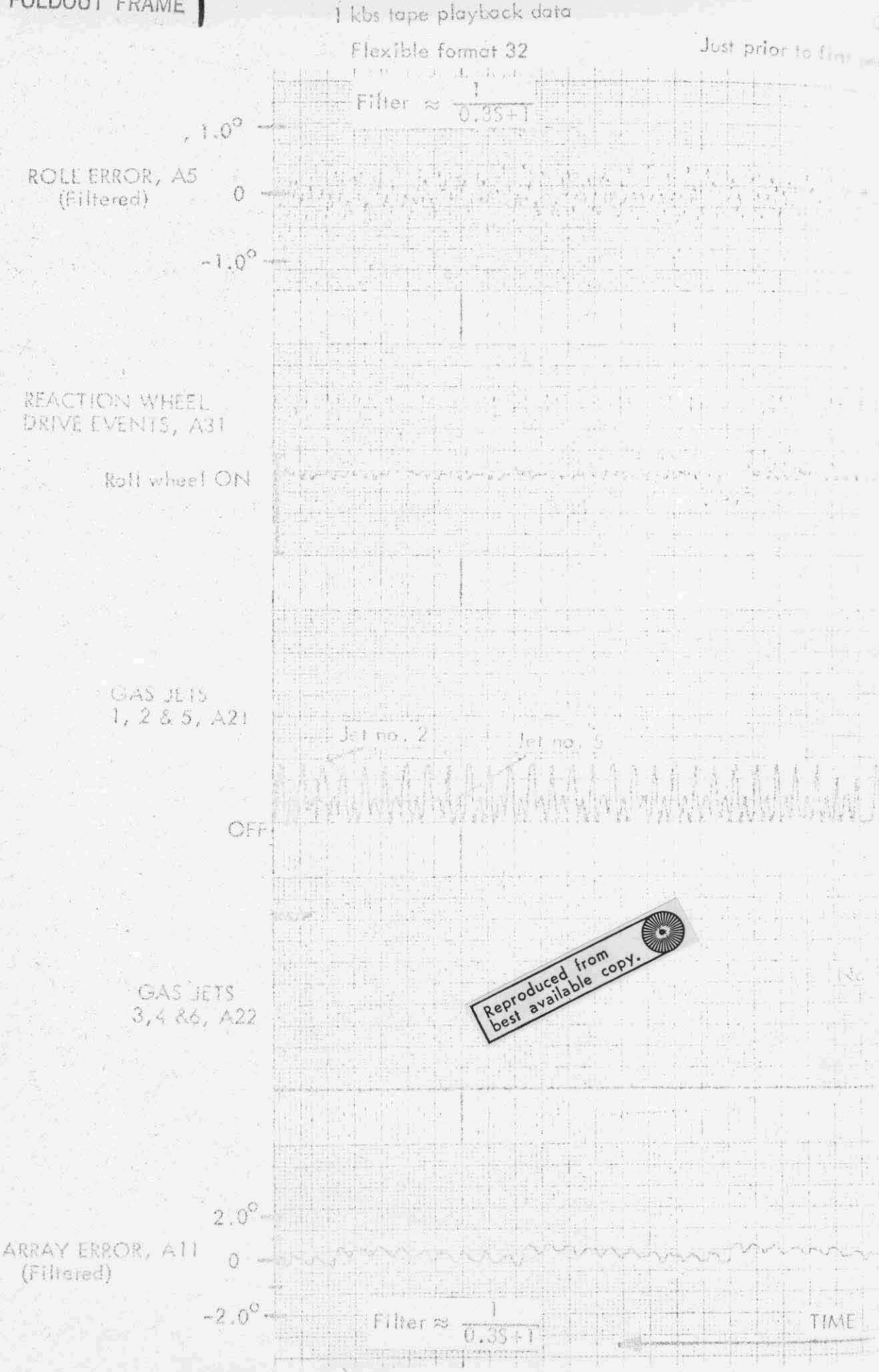

Figure 3-2 OGO III Telem

GO III TELEMETRY DATA

REV 001 9 June 1966

FOLDOUT FRAME 2

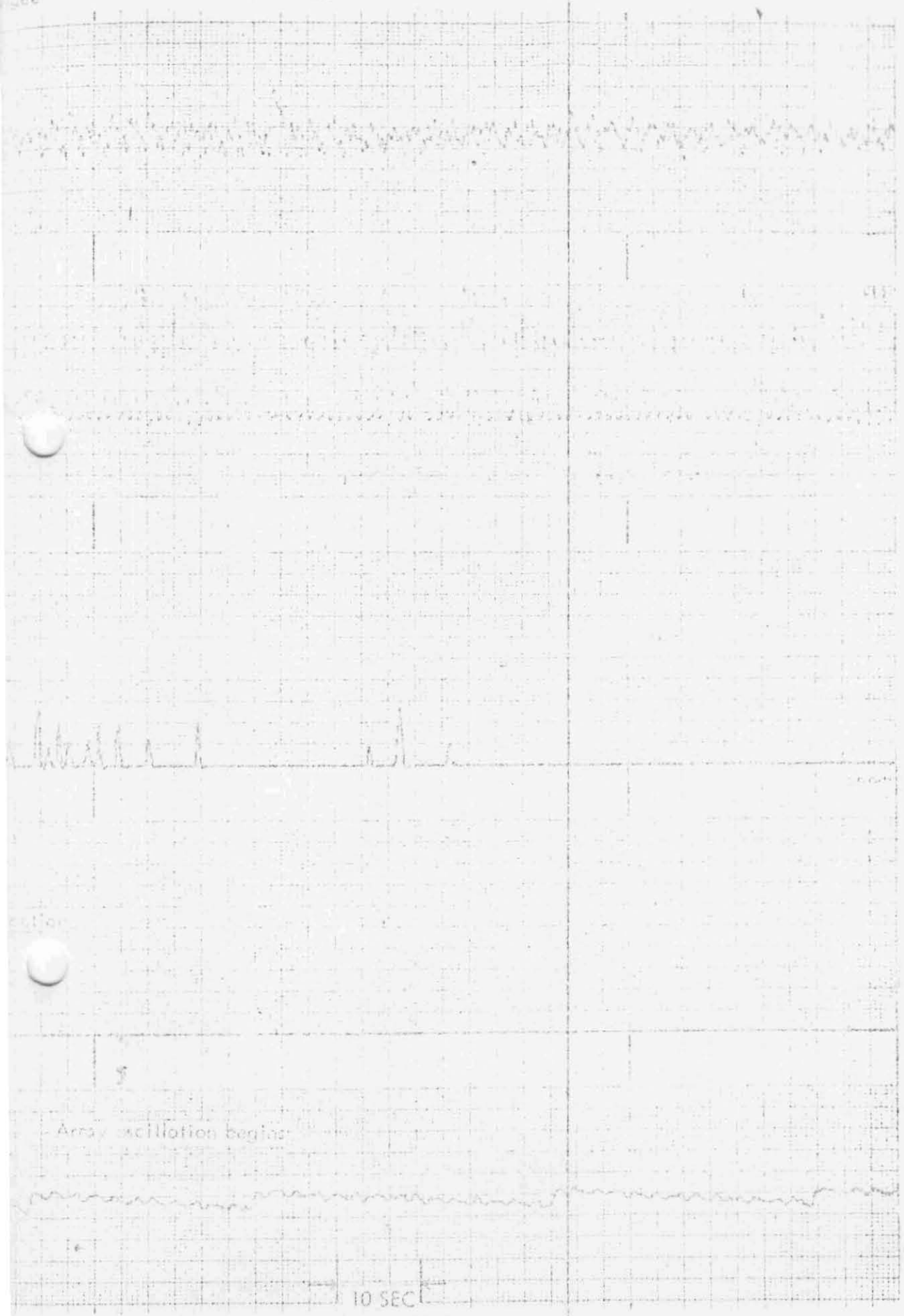

Telemetry Rev 001 Expanded Scale Start of Gas Limit Cycle

3-10 b

The presence of the 0.4 cps body natural frequency can be seen on the array error and gas jet actuation channels. It can also be seen that a 1.3 cps component is apparently present in the roll error signal in the second figure. At that time the telemetry sample rate (in flex format data storage mode) was 3.5 samples per second. The 1.3 cps component may be due to beats between the dither frequencies of the horizon scanner heads which form the error signal or between the dither and the telemetry sampling rate, or both. It is not thought to represent actual spacecraft roll motion.

Figure 3-3, obtained from 8 KBS real time accelerated subcom 2 data. The 1.3 cps frequency does not appear although the telemetry sampling rate on the roll error channel is 14 samples per second. A frequency component of 2.2 cps is present, however, with an amplitude that varies from maximum to minimum in approximately six seconds. This could result from beats between two scanner positor oscillations, the telemetry sampling rate and the scanner dither, or both. The six second envelope is suggestive of a beat situation. Note that six seconds is also the period of the first structural bending mode. A modulation envelope varying from maximum to minimum in 3 seconds is also present in the data.

The accelerated subcom data shown in Figure 3-3 is the best information obtained during rev 001 perigee. It shows the beginning of the array oscillation and the participation of the array motor (not available on flex format 32). The roll gas jets (not shown) are oscillating during the entire period. Note that the roll reaction wheel drives at approximately 90% duty cycle and that pitch and yaw actuations are infrequent. Note also the change in character of the array error waves as the array drive motor becomes involved. The average amplitude of the array error wave increases from 0.3° to nearly 0.9°. Moreover, the oscillation frequency decreases from 0.40 cps to 0.37 cps, and the relative phase of the roll and array error becomes less coherent.

Figure 3-4 is a tracing of several telemetry channels recorded just after rev 001 perigee. It encompasses the time the gas delay command

8 kbs accelerated subcom data

FOLDOUT FRAME 1

OGO III TELEMETRY

REV 001

9 June 1966 04:37Z

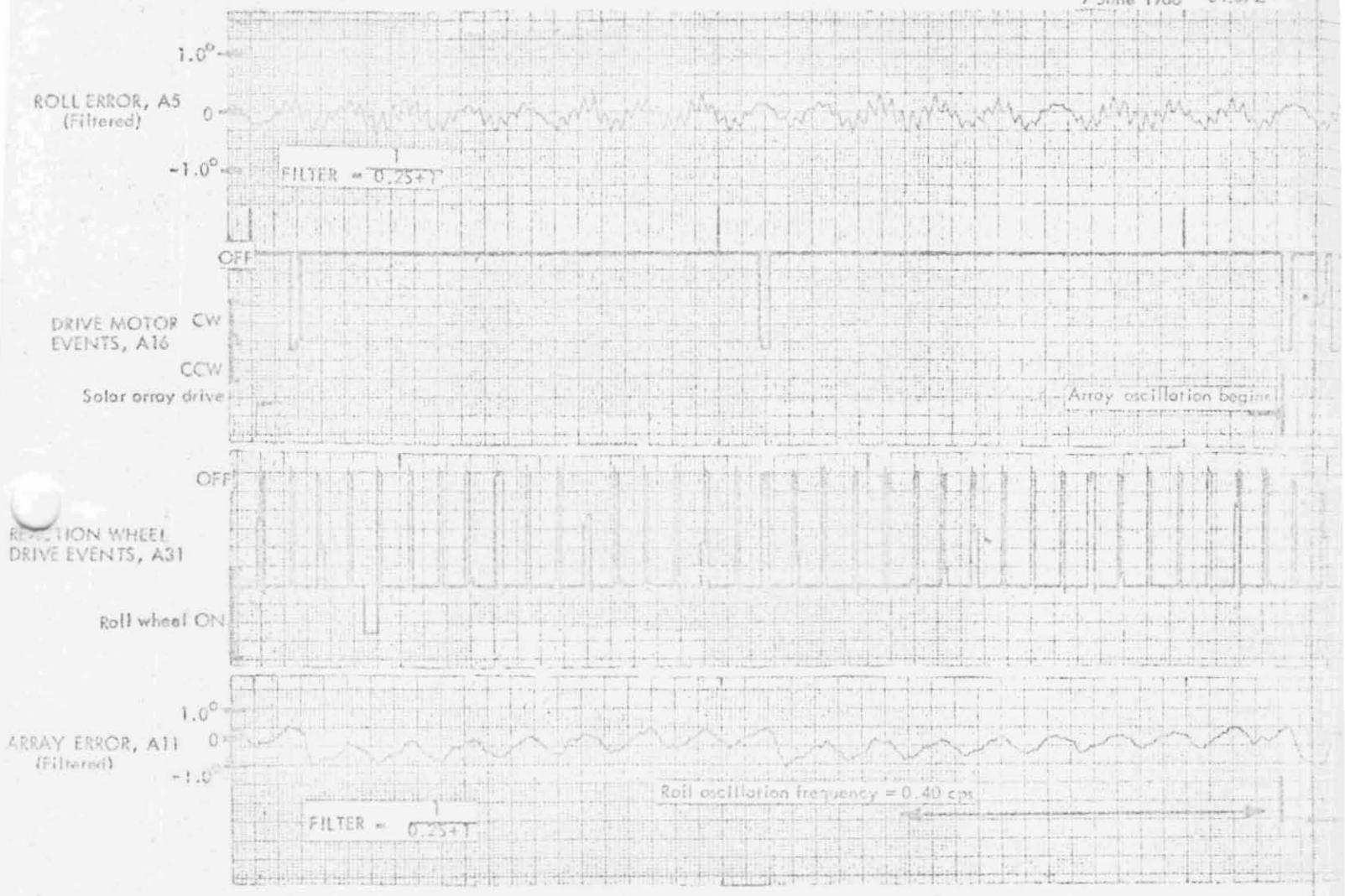

Expanded

3-12-a

FOLDOUT FRAME 2

DATA
Just prior to first perigee

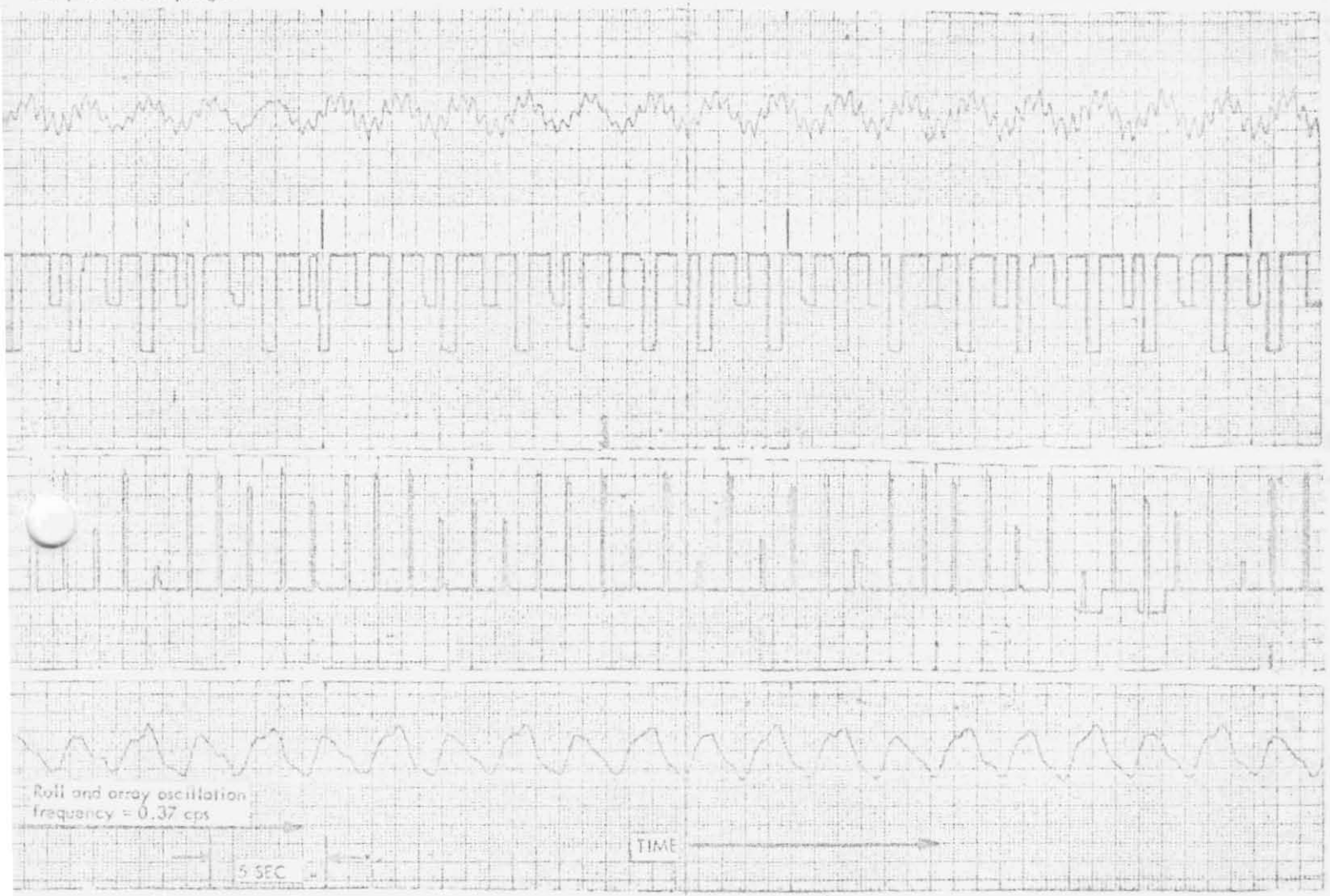

Figure 3-3

OGO III Telemetry Rev 001
d Scales Start of Array Limit Cycle

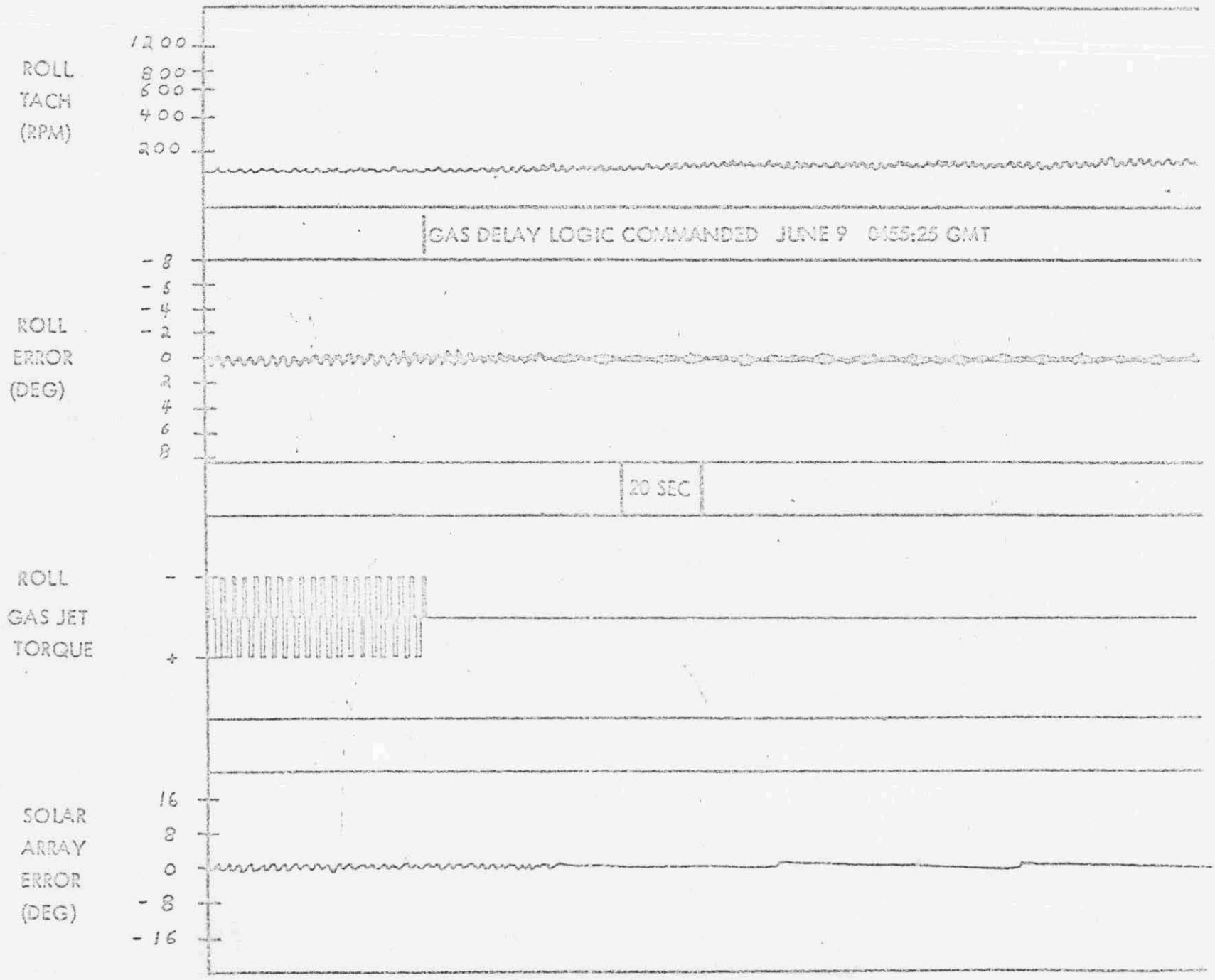

Figure 3-4 OGO III Telemetry Rev 001 Gas Delay Logic Command Event

was transmitted and shows the cessation of the gas oscillation (the gas jet torques are drawn rather than the actual telemetry indications). Within 40 seconds after the gas oscillation terminated the hard array oscillation ceased. The roll reaction wheel continued to support roll oscillations at low amplitude until orbital upsides, when it decayed spontaneously. During that period the array drive actuation frequency gradually decreased and the motor actuations could statistically have either added or removed energy from the flexible modes.

On the second approach to perigee on 11 June 1966 the gas jet inhibit logic was in effect preventing any roll jet participation. Figures 3-5 and 3-6 show the significant telemetry traces for rev 002. The roll wheel began to support the general ringing motion consistently at about 04:00 Z and the roll amplitude increased at that time to approximately 0.1° to 0.2° (difficult to assess due to higher frequency beat components). The typical sawtooth pattern of array error near perigee is seen with the roll oscillation superimposed. During the entire perigee pass the array broke into hard oscillation only twice, for some 15 seconds in each instance. This condition can be seen in Figure 3-6. Note that in spite of the gas delay logic one torque doublet was applied by the roll gas jets.

The reluctance of the array drive to oscillate without support from the gas jets was evident through rev 018. ACS behavior was examined at normal (compressed) telemetry scaling during the eclipse and post-eclipse turn of revs 013/014. Following the post eclipse turn the array oscillated briefly and the roll wheel oscillations continued for some time. Subsequent orbits exhibited roll oscillations continuing well after perigee in most cases. On rev 018/019 perigee just after eclipse the array oscillated sporadically as shown in Figure 3-7. It is seen that the oscillation spontaneously decayed and then restarted several minutes later. It is thought that the propensity for array oscillation increased as the mission advanced, perhaps due to wear of the array drive keyway and resultant increased backlash.

FOLDOUT FRAME

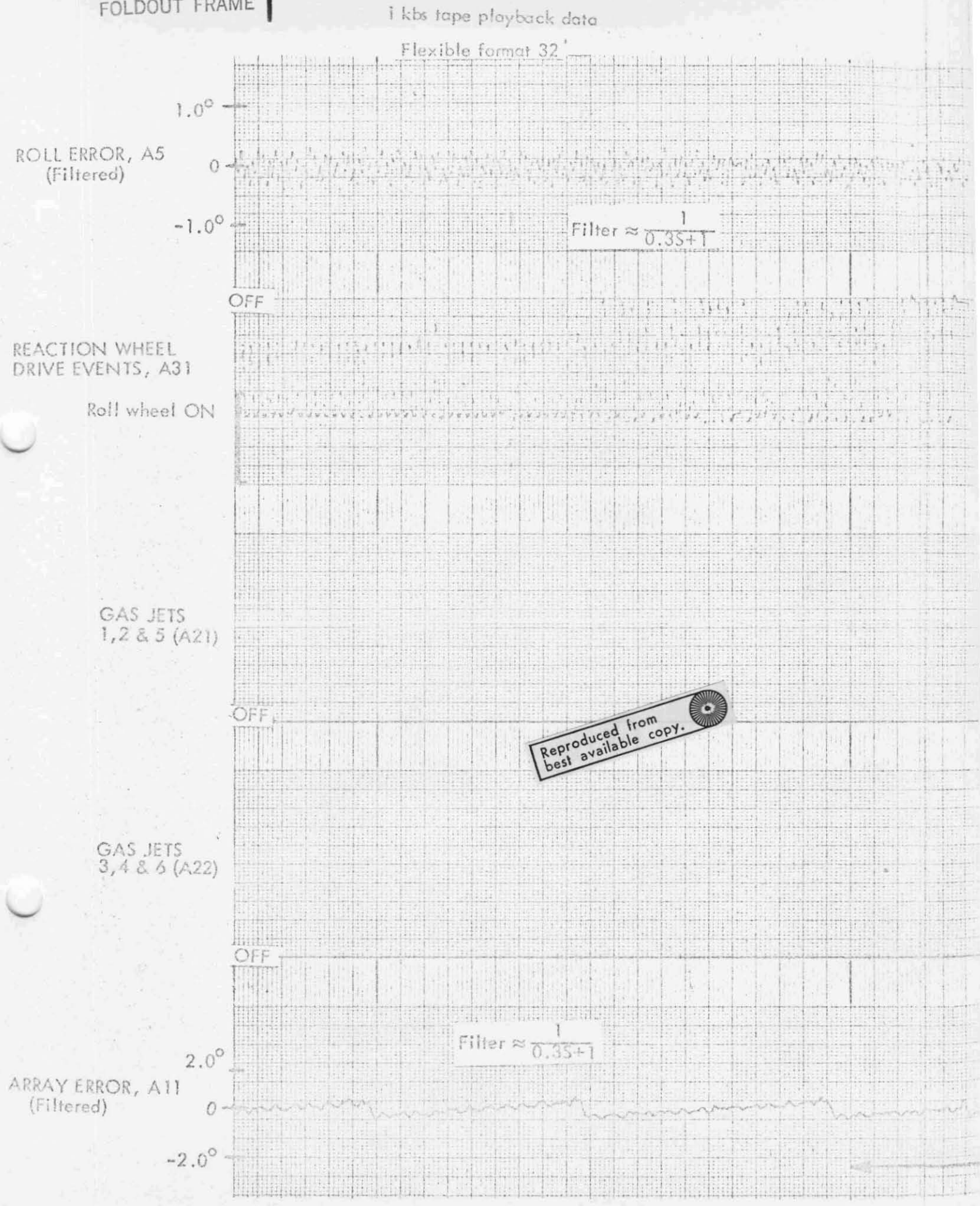

Figure 3-5 OGO III Telemetry Rev 002 Prior to Perig

11 June 1966 Approx. 04:00Z FOLDOUT FRAME 2

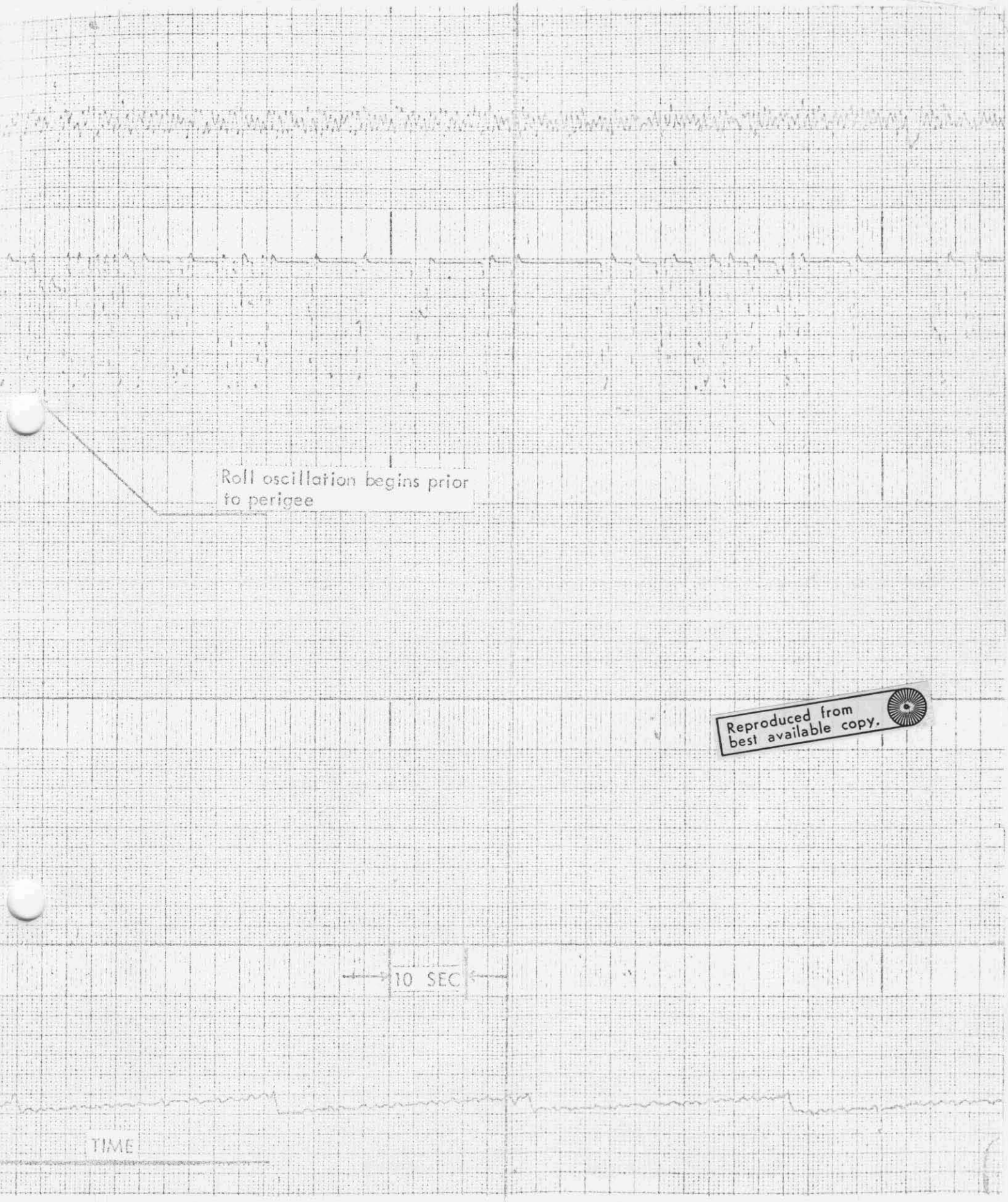

Perigee Roll Wheel Oscillation Begins

3-15-b

FOLDOUT FRAME 1

1 kbs tape playback data
Flexible format 32

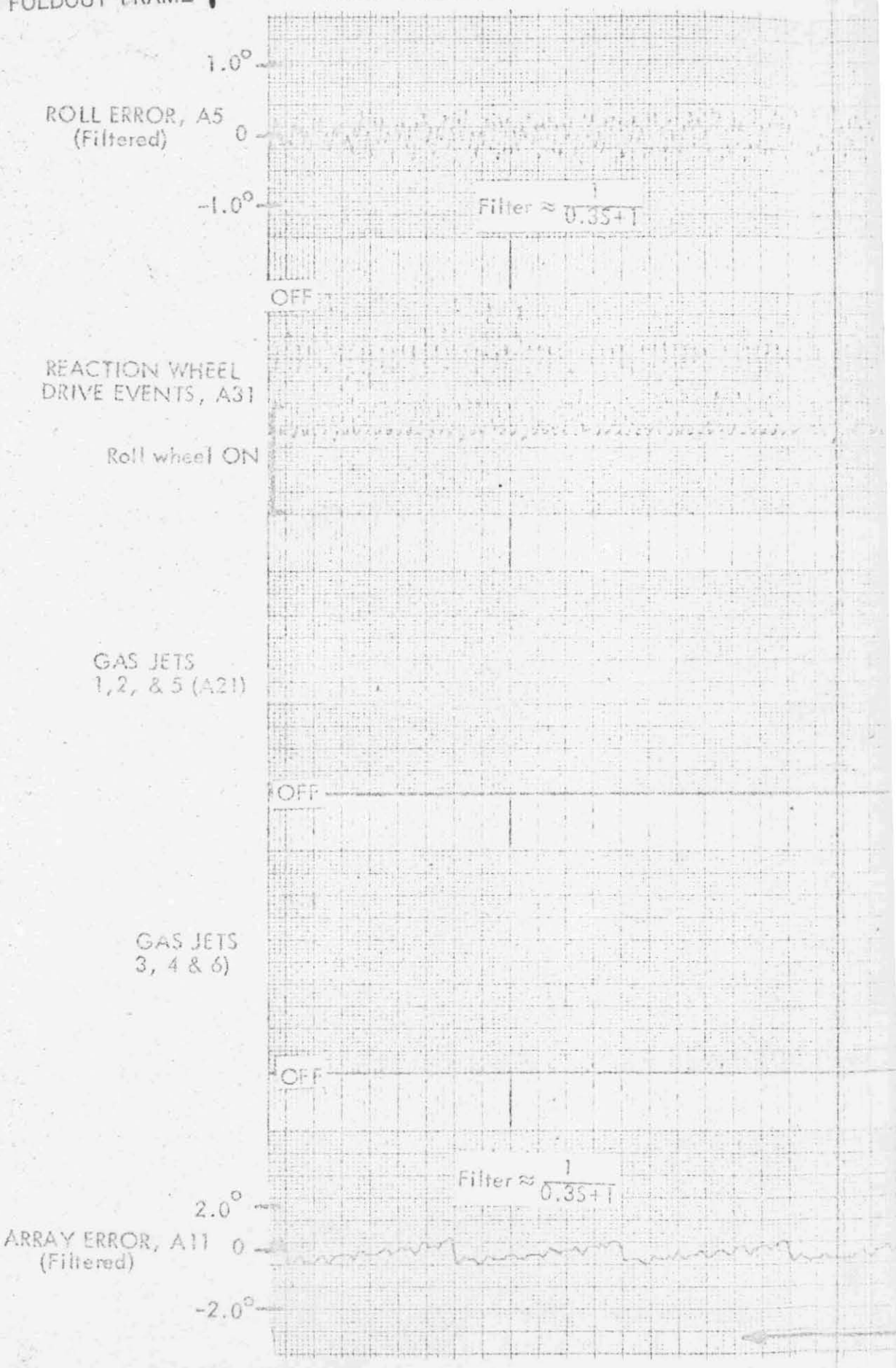

Figure 3-6 OGO III Telemetry Rev

11 June 1966 Approx. 04:00Z FOLDOUT FRAME 2

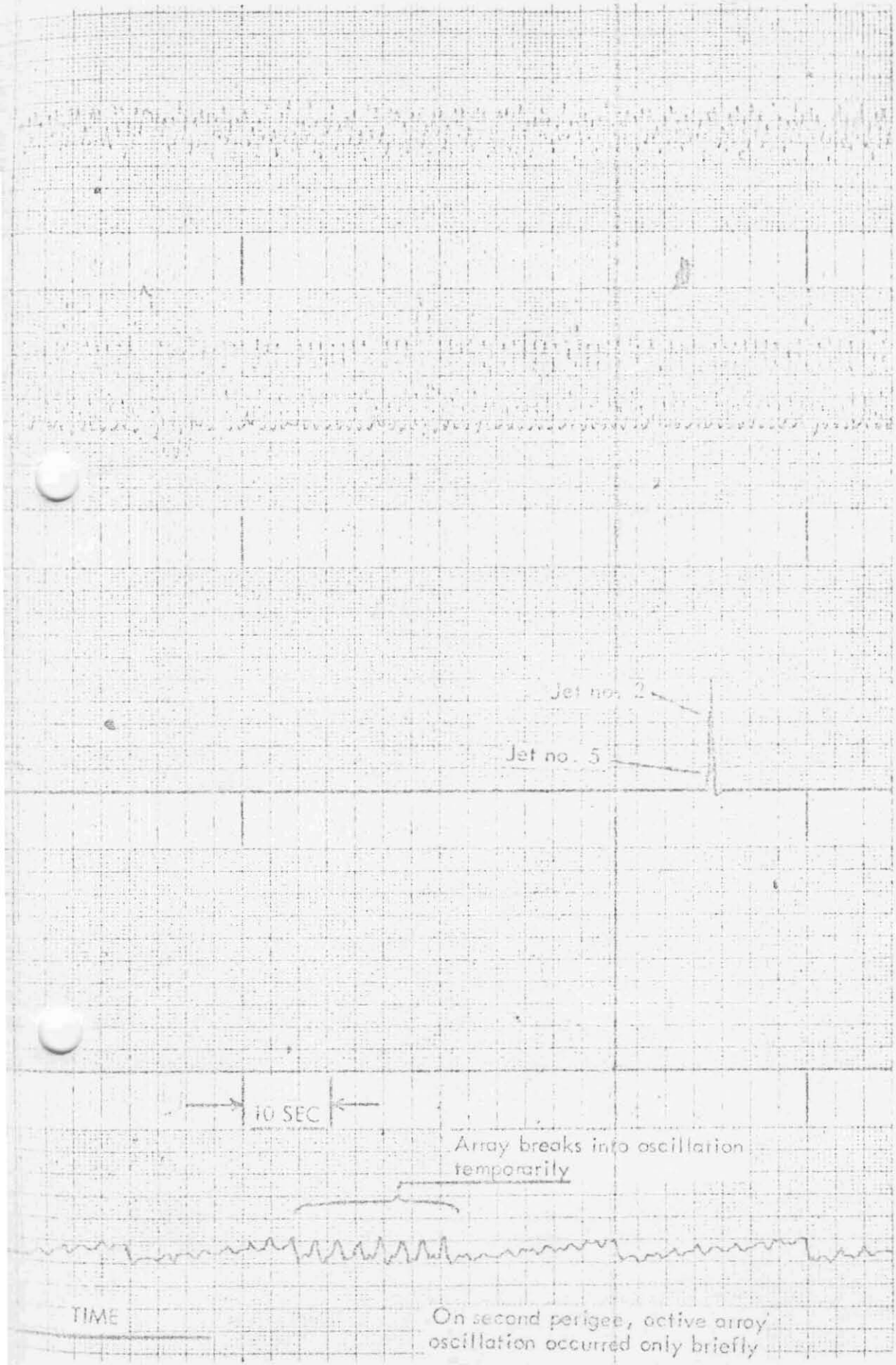

Rev 002 Prior to Perigee Array Limit Cycle Occurs

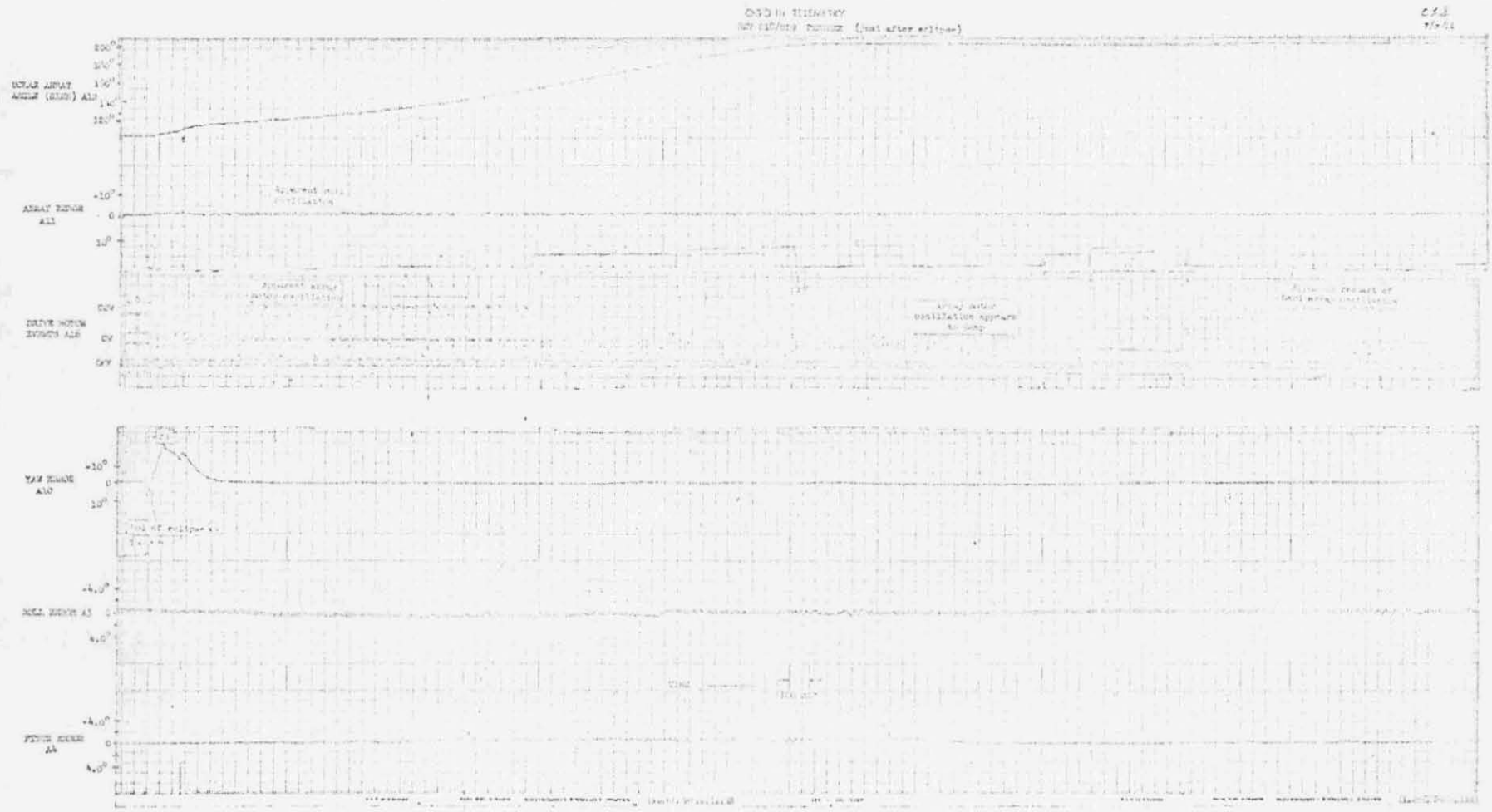

Figure 3-7

OGO III Telemetry Rev 018/019

Perigee Post Eclipse Turn and Array Limit Cycle

Examination of telemetry data for revs 019 and 020 revealed no active roll oscillation of any kind. Unfortunately the only clean data available covered periods approximately six hours after perigee by which times the oscillations may have decayed.

On rev 021 very clean, fine-grained data was obtained in accelerated subcom 2 at 64 KBS. For several minutes near 20:18 Z detailed roll wheel and array oscillations were observed. Figure 3-8 shows the significant telemetry channels on expanded scales with filtering applied. The period shown includes spontaneous cessation of array oscillation. The attendent decrease in roll error oscillation amplitude can be seer o be from approximately 0.18° to approximately 0.12°. The array drive train backlash is in evidence in the array angle (sine) channel which shows continued cyclic movement after the drive motor stopped. Note that in comparing the relative phase of the roll error on the second channel (with two lags) with the array error approximately 50° phase lag must be allowed. This is the first known instance of active array oscillation occurring so long after perigee. It is presumed to have continued since perigee. Note that the processed roll error shown on the first channel is filtered to represent the onboard ACS processing, and is the signal that is applied onboard to the reaction wheel and gas jet bistables. During the array oscillation the resultant error signal was of sufficient amplitude to actuate the gas jets had not the gas inhibit logic prevented the occurrence.

This detailed rev 021 data is the only flight information available adequate to permit a thorough investigation of the OGO III oscillations.

3.4 OGO II FLIGHT TELEMETRY

The pertinent OGO II flight telemetry has been reviewed for evidence of incipient roll oscillation in hope that information so gleaned will yield some understanding of the OGO III problem. Specifically, the intent was to assess the probable margin separating OGO II from active roll oscillation and to try to discern what the important differences were.

Figure 3-8 OGO III Telemetry Rev 021 Showing Cessation of Array Oscillation

3.4.1 General Flight Experience

The flexible body effects are readily apparent in the telemetry traces of OGO II when they are expanded and filtered to remove the horizon scanner dither components. The observed dynamic characteristics correlate well with calculated values, and the total roll behavior of OGO II was as expected for the observed values of flexible body damping. Active support of a roll oscillation at the flexible body natural frequency was uncommon, but did occur. Active "hard" oscillation of the solar array was never indicated on OGO II.

Second, there is little doubt that flexible body dynamics of OGO II contributed to the then recognized symptoms of copious gas firing in the roll channel. Roll gas pulses were often applied in doublets after small disturbances or even after gradual contact with the error deadzone edge. There appeared to be no tendency to assume a forced oscillation with gas jet participation, however.

3.4.2 Flight Data Description

The majority of interesting data from OGO II was obtained after the two earth acquisitions, as the transient motions at those time excited the flexible modes and caused the greatest participation of array and roll wheel drives. Figures 3-9 and 3-10 are accelerated subcom 2 traces taken just after the first earth acquisition on 14 October 1965 at 21:20 Z (rev 005). The roll and array error channels have been filtered and expanded to make the oscillatory motions more visible. The characteristic sawtooth pattern of array error is seen with small roll oscillations superimposed. Note that the oscillations appear much more damped than they do on OGO III, often decaying completely between excitation transients from the roll wheel. Note also the array drive motor action in correcting the array error. A trio of pulses is applied indicating that the first motor torque pulse excited a flexible mode which caused an opposite torque pulse to be applied one half cycle later. This is verified by the clearly discernable ringing motion on the array error trace and by comparison of the drive motor actuation

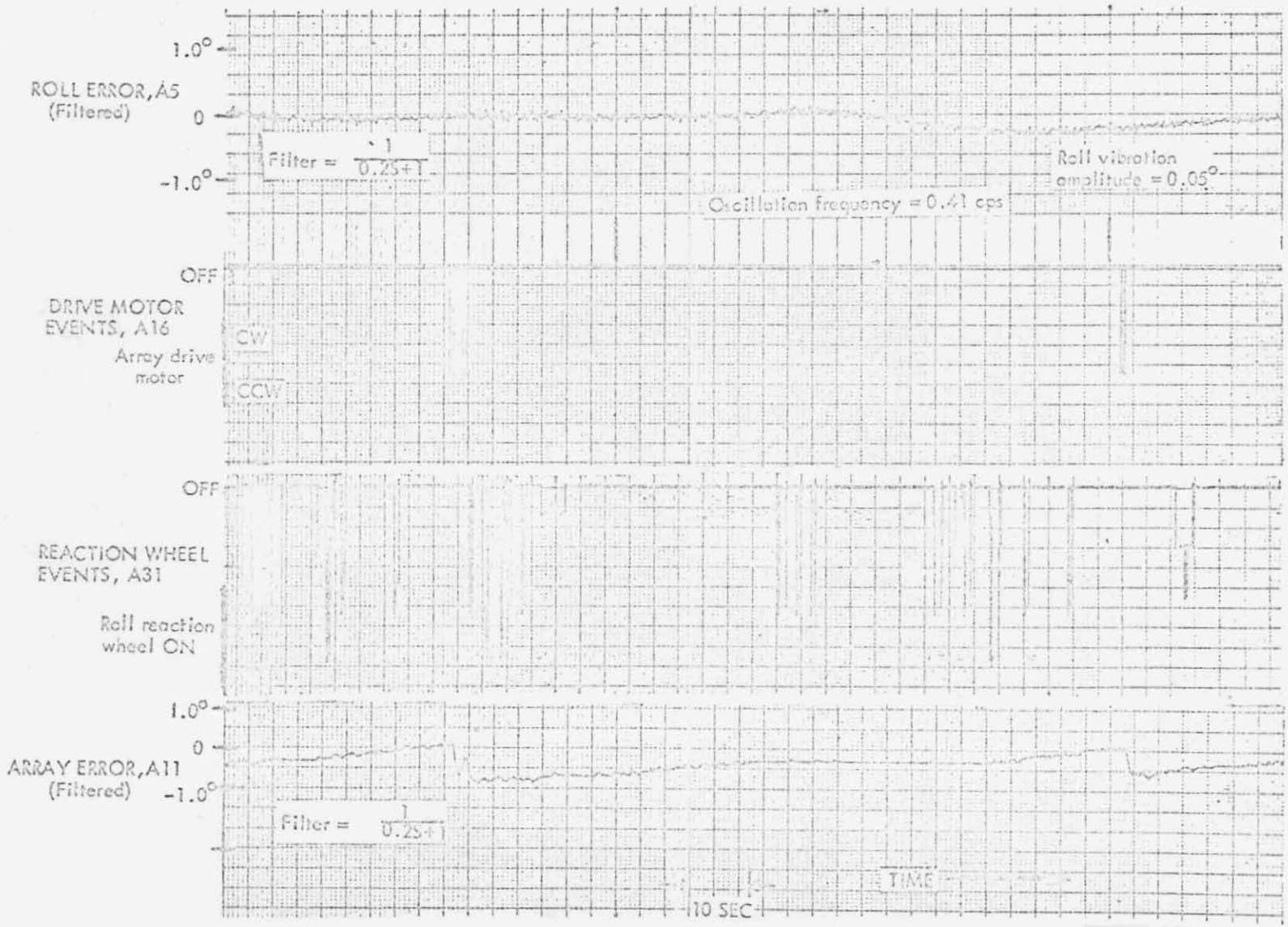

Figure 3-9 OGO II Telemetry Data Just After First Earth Acquisition

FOLDOUT FRAME

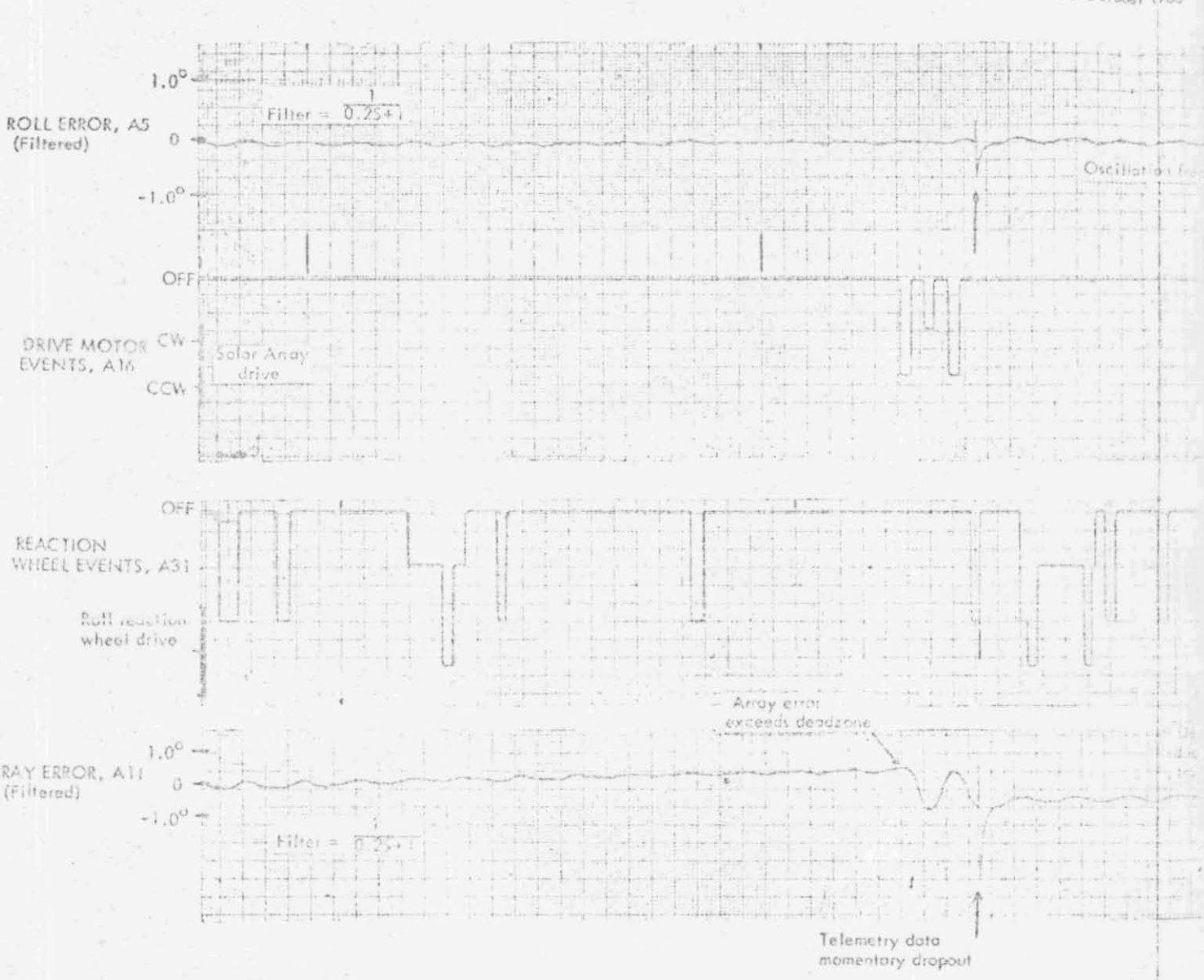

Figure 3-10 OGO II Telemetry Data Immedi

FOLDOUT FRAME 2

965 21:25 to 21:28Z

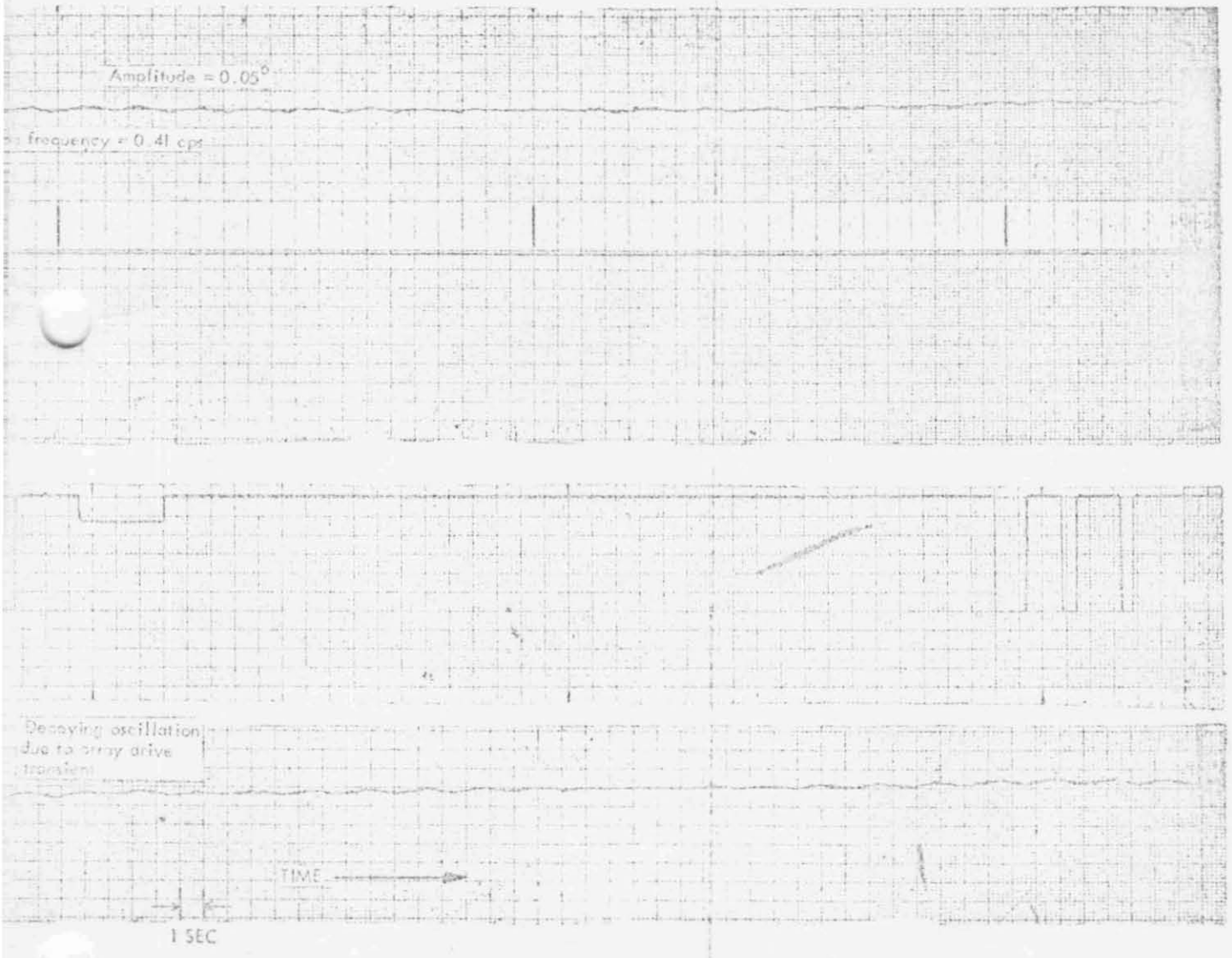

mediately After First Earth Acquisition

frequency with that of the second structural bending mode. Note the rapidity of damping in the second figure. Both figures show that, in spite of the frequent array corrections and the fact that the system is still recovering from its initial acquisition transient, there is little tendency to support the flexible body oscillations with either the reaction wheel or array drive motor. The system soon settled out and the roll oscillations all but ceased as time progressed.

The next period shown includes the second earth acquisition and the eight minutes immediately following. It is illustrated in the following two figures. Figure 3-11 shows the final earth acquisition transient in roll on expanded scale with filtering applied to the roll and array error channels. The solar array is driven in pulses at the flexible body natural frequency at first. Boom ringing excited by the initial large motions cause the array error to exceed its motor drive deadzone on peaks of the waves. This action ceases almost immediately and is not repeated. The roll reaction wheel is also actuated in pulses at the body natural frequency as the roll error becomes smaller, as it too is caused to drive only on peaks of the waves. Figure 3-12 shows the behavior eight minutes later and the reaction wheel is still pulsing at the body frequency although the roll error wave has decreased to less than 0.05° amplitude. This continues for several minutes, at times lapsing spontaneously and then resuming. Figure 3-13 is a condensed time scale view of the OGO II telemetry covering a three minute period near 23:56 Z on 16 October 1965, ten minutes after second earth acquisition. It shows the roll wheel activity in support of the oscillation, the spontaneous decay, and a period of new wheel activity. A few minutes later the oscillation ceased.

From the OGO II telemetry data it can be said that the roll channel oscillations due to body flexibility were not so severe as those of OGO III. They tended to damp more readily, never involved the solar array drive and rarely caused the gas jets to participate. The gas jet actuations which occurred in response to horizon scanner tracking transients were momentarily affected by the flexible dynamics. Even after one of the large error transients caused by the horizon anomalies

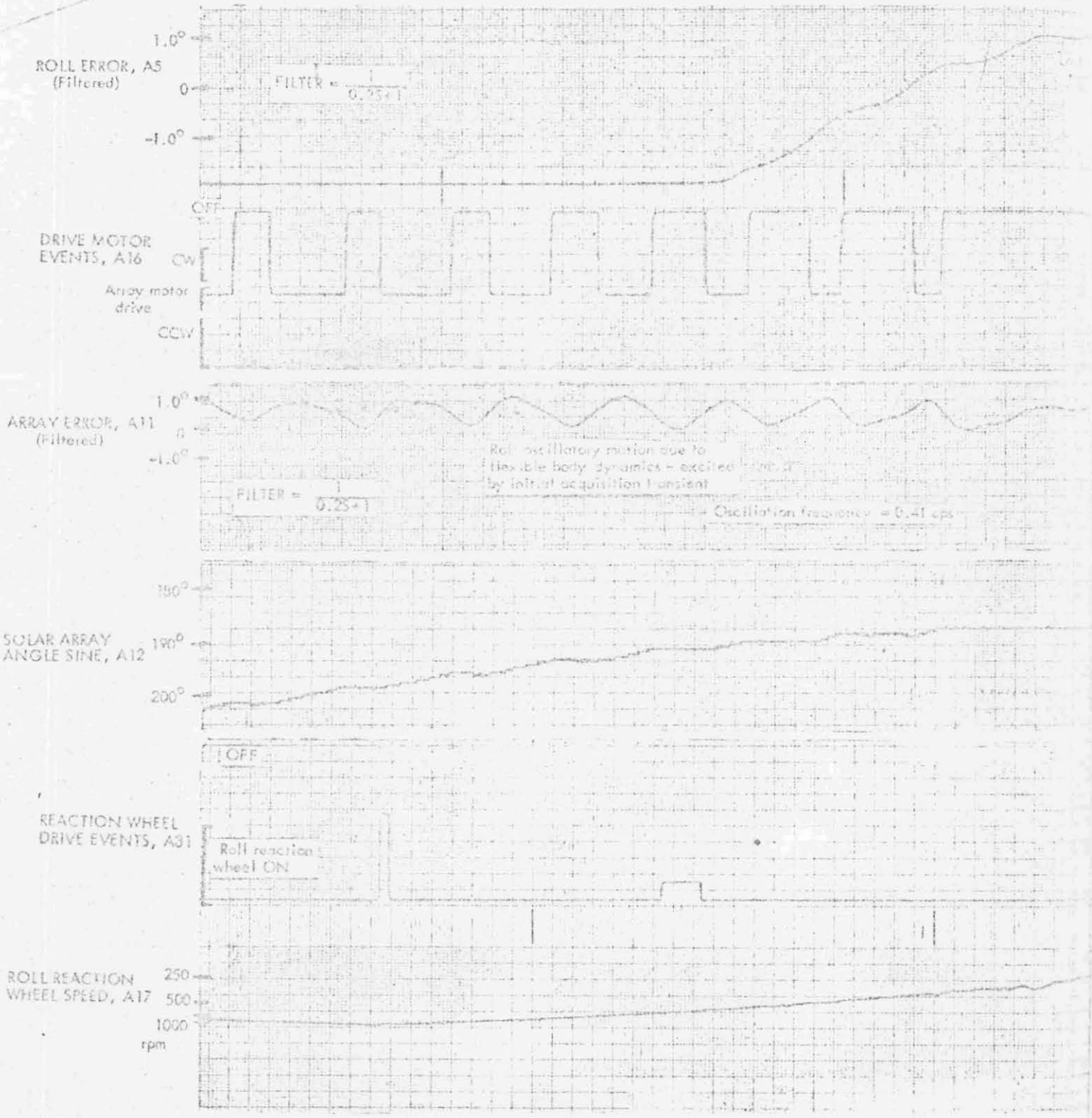

Figure 3-11 OGO II Telemetry Data Term

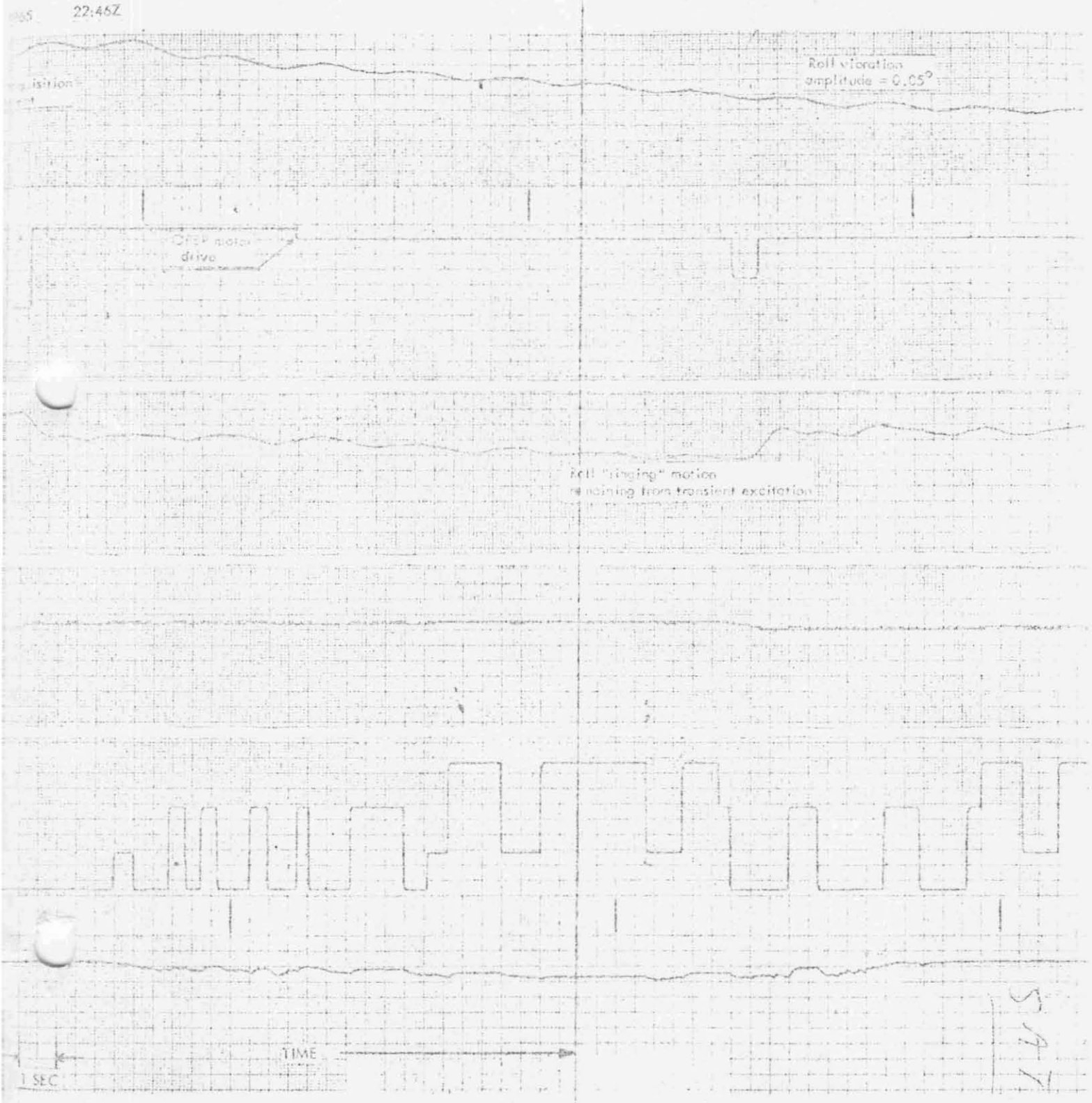

ul Transients of Second Earth Acquisition

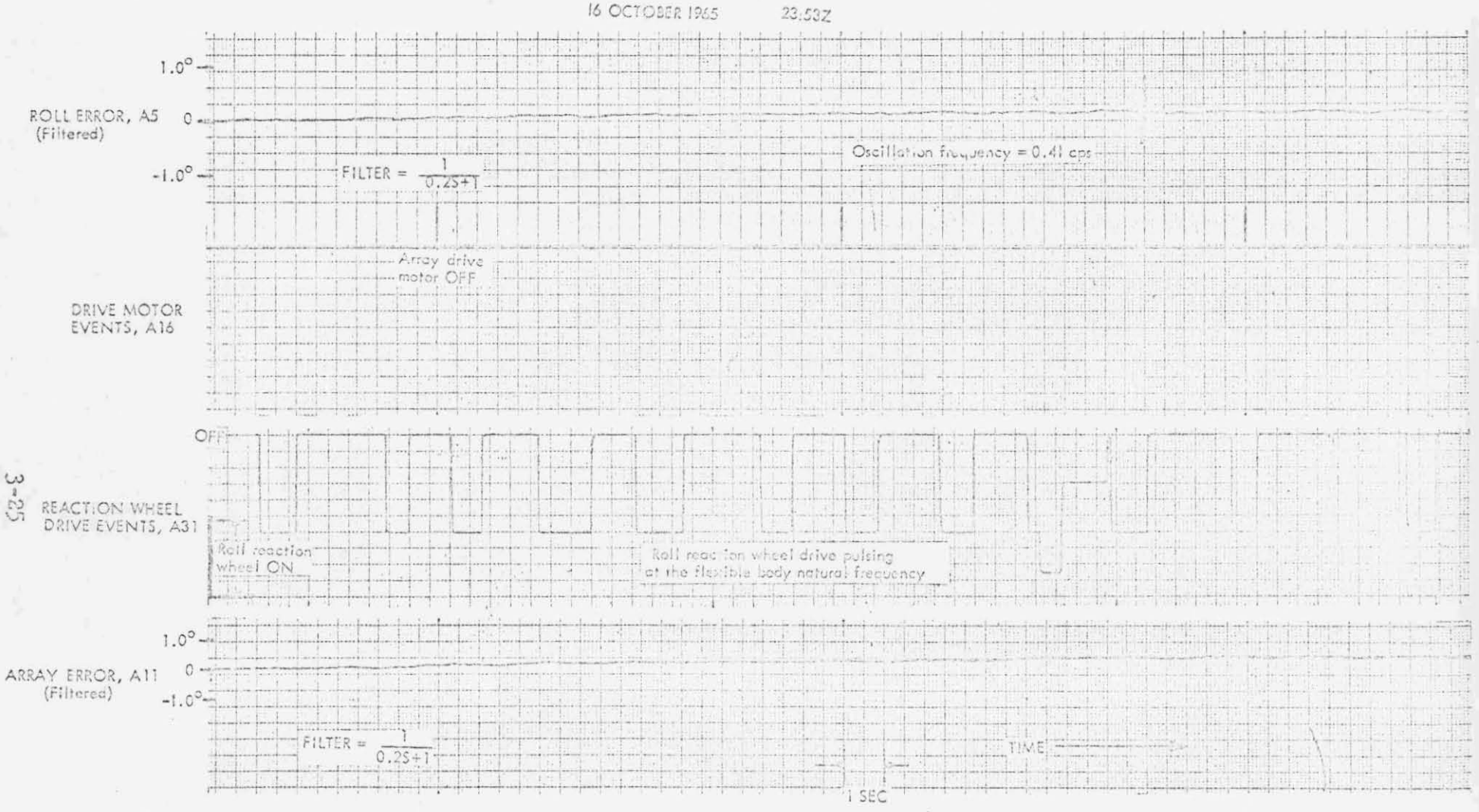

Figure 3-12

OGO II Telemetry Eight Minutes After Second Earth Acquisition

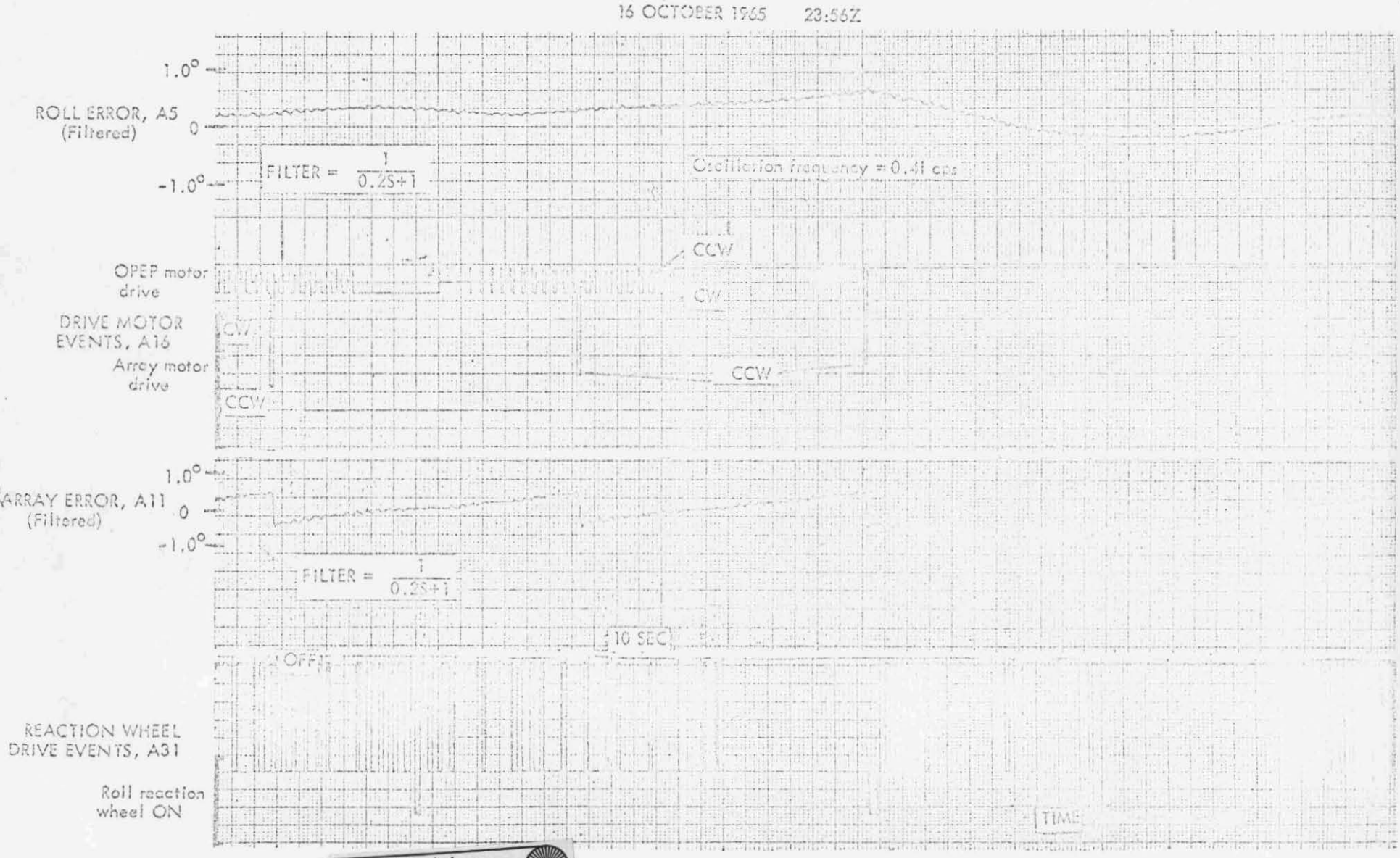

Figure 3-13 OGO II Telemetry Data Ten Minutes After Second Earth Acquisition

the gas jets did not actively assume and maintain the oscillations. Many explanations for these differences from OGO III are not directly supportable through flight data. They involve normal tolerance distributions of the significant parameters, such as array drive backlash, long boom damping, perhaps the different structural configuration, wheel and gas deadzones and hysteresis, motor torques, etc. The observed boom damping of OGO II was greater than OGO III. Also significant on OGO II is the absence of widely varying solar array actuation periods, the shortest period being three times as long as that of OGO III.

3 5 OGO III ACS EQUIPMENT FAILURE

Review of OGO III flight data yielded indication of incipient equipment failure only on rev 023/024, i.e., on 23 July 1966. Prior to that time all ACS equipment appeared to operate normally (excepting perhaps the excessive backlash in the array drive train). Just after rev 023 perigee, at the beginning of rev 024, anomalous behavior of the ACS roll channel was detected. Figure 3-14 taken from 64 KBS real time maincom data illustrates the sequence leading to the failure. The time scale of the Figure (not shown) is 2 seconds per large division.

During the period shown in the Figure 3-14 both the solar array drive and the roll reaction wheel were oscillating, the roll reaction wheel participating at approximately 90% duty cycle. Initially the spacecraft load current was reasonably steady at 10 to 11 amperes-not an abnormal value. Some 50 seconds after the start of the traces the roll reaction wheel accelerated at some fraction (approximately 30%) of its full capability toward positive momentum, i.e., it slowed its CW rotation, reversed, and gained speed in the CCW direction. This was accompanied by large, sudden increases in load current rising to peaks of 15, then 16.5 amps. At the time of this occurrence the roll error signal was oscillating about zero error and should have been actuating the roll wheel for approximately equal periods in both directions with no net change of wheel speed. In fact for 40 to 50 seconds after beginning of the traces such appeared to be the case. At the

FOLDOUT FRAME

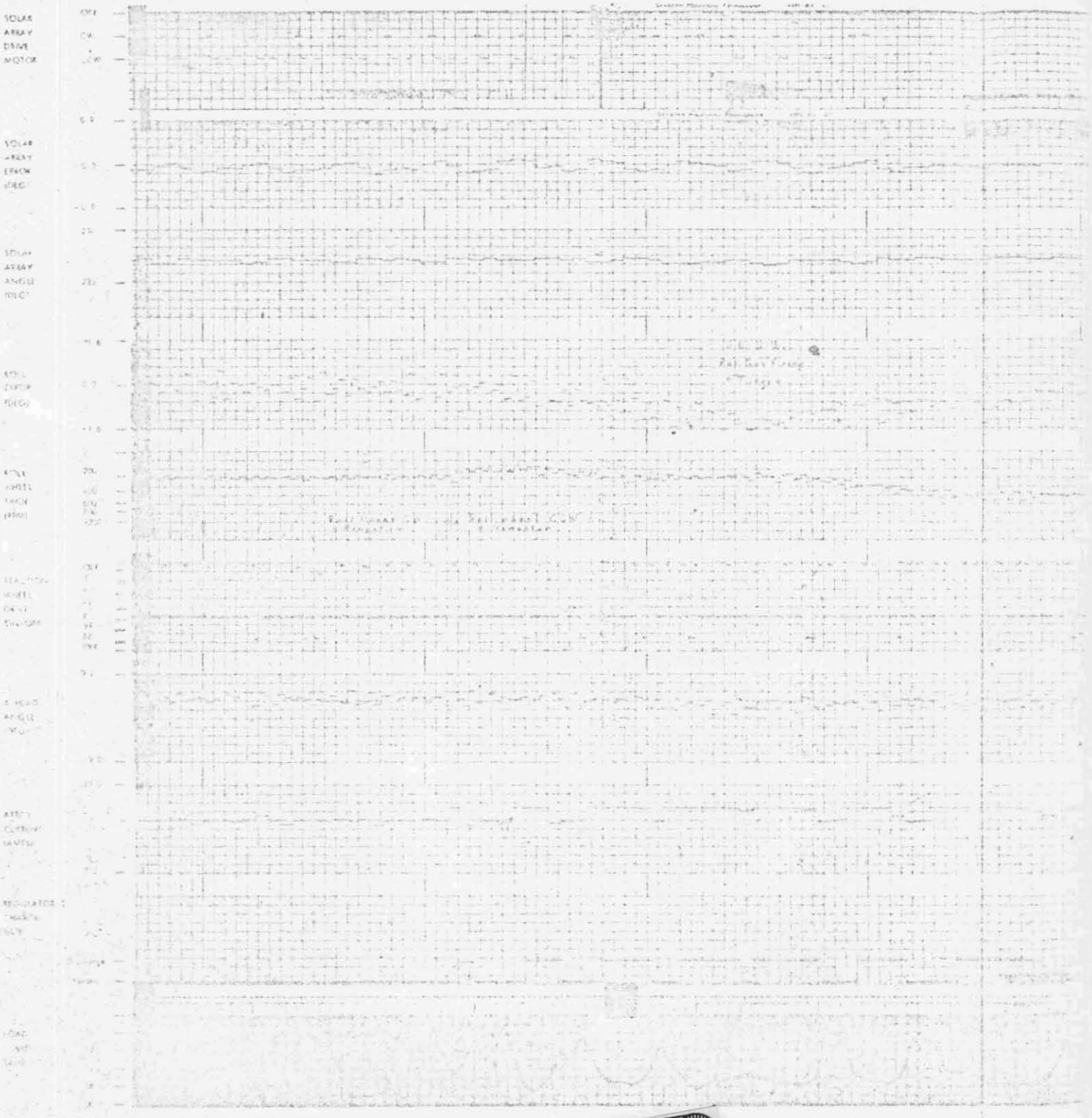

FOLDOUT FRAME 2

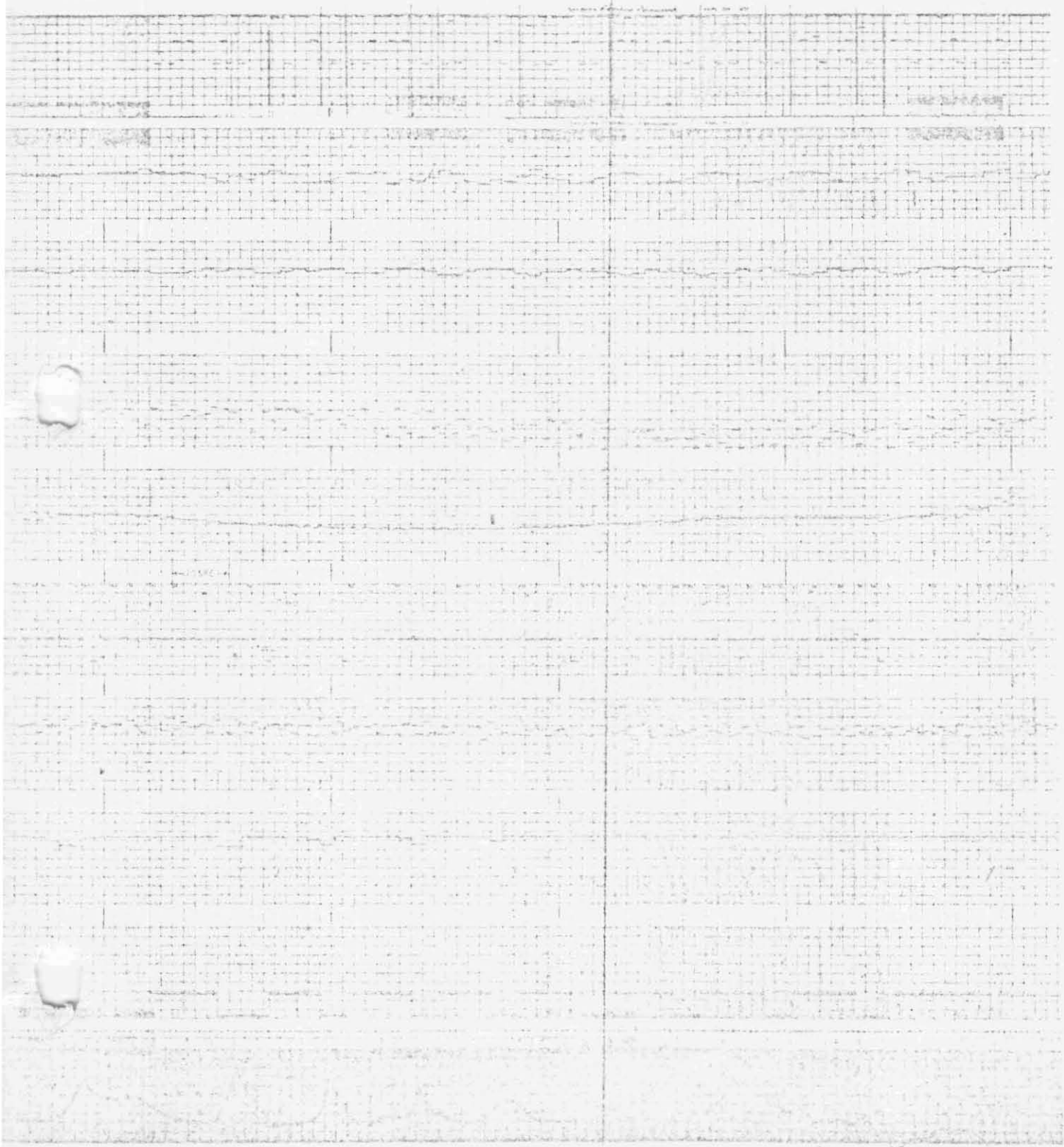

Figure 3-14 OGO III Telemetry Roll Wheel Mag Amp and Inverter Failure Sequence

time of load current increase, however, the wheel speed changed to add positive momentum and the average roll error moved away from zero toward negative error. Thus the roll wheel acceleration apparently caused the roll error - the reaction wheel did not accelerate in response to a roll error! This is evident from the relative directions as well as from the time order. The roll reaction wheel did not act to reduce the error - but instead aggravated it - for a period of three minutes. In the meantime the negative roll error reached such proportions (about 1.5°) that corrective gas jet torque was applied in spite of the gas inhibit (delay) logic. Four positive gas torque impulses were fired, reducing the roll error to -0.6° for a minute or so, after which it again moved toward -1.5°. During this period, when the direction of error drift actually reversed, the roll wheel continued to accelerate slowly in the wrong (not corrective) direction. Its average applied torque was +0.01 ft lb, accelerating at approximately 9.3 rpm per second. At approximately 4 minutes from the start of the traces the roll reaction wheel acceleration reversed for no apparent reason, thereafter applying corrective control torque at a 0.009 ft lb level (about 20% of its full capability). In response to this the roll error gradually reduced. After about 1 1/2 minutes the roll wheel suddenly applied full corrective torque, driving the roll error through zero and then positive. This soon resulted in applications of gas jet corrections. After that, in spite of indications of wheel actuation, the wheel speed no longer changed.

At the time of the reversal and thereafter the bus load current was heavy and became more uniformly heavier. As can be seen from the figure the load current appears in broad surges throughout the anomalous period. These surges seem to exhibit a periodicity of approximately 16 seconds for 2 or 3 minutes toward the end of the trace. One explanation for this is that the surges are not entirely real but represent beats of the telemetry sampling frequency with the roll oscillation, i.e., between 0.4 cps and 0.435 cps. During the laboratory simulation of magamp failure no such periodic load surges were noted. Toward the end of the traces the load current increases to 18 amperes

and then increases off scale. Approximately 1 1/2 minutes later the undervoltage bus automatically disconnects interrupting the telemetry. When the bus was reset later, restoring telemetry, the ACS inverter would not start and was presumed to have failed.

During the overload condition the inverter temperature increased and its regulated output (not the output used to drive the wheels) remained constant. It is speculated that the roll reaction wheel drive magamp overheated under the high duty cycle and developed a partial, internal short becoming worse with time. This is based upon the (now) known characteristics of the magamp and the evidence of anomalous wheel drive action at the time of failure. It further speculated that the resultant overload damaged the ACS inverter causing the overt inverter failure indication. After undervoltage reset, attempts made to start the inverter by alternately removing and re-applying bus voltage indicated that the inverter would no longer draw current. This symptom would occur with some types of inverter failure, but would also occur if its oscillator failed to start for any reason.

4.0 DEVELOPMENT AND VERIFICATION OF ROLL AXIS DYNAMIC MODEL

A simplified single axis representation of OGO's flexible appendages and their coupling to the ACS is developed in this section. The system dynamic equations are derived. A describing function representation for the reaction wheel and pneumatic nonlinearities is discussed. The validity of the above model and approximations is illustrated by the prediction of OGO-III reaction wheel limit cycle oscillation. Finally an analog computer simulation is used to provide a detailed comparison of the model response to the flight data.

4.1 ASSUMPTIONS

The assumptions used in all the flexible body analyses of this report are listed below:

1. Experiment booms EP-5 and EP-6 may be represented by a linear lumped mass-spring-dashpot model.
2. Dynamic cross-coupling between axes is negligible.
3. Small-angle approximations are valid.

4.2 SYSTEM DYNAMICS

A simplified single axis representation of the OGO main box, experiment booms and as it would appear for rotations about the roll axis is shown in Figure 4-1. The array flexible model, not shown here, is developed in Appendix B. Symbols are defined below.

$i = 1$ Experimental boom EP-5

$i = 2$ Experimental boom EP-6

I_B Moment of inertia of OGO main box (including solar arrays and attached DeHavilland booms) about OGO's roll axis (assumed to pass through the vehicle's center of mass). $(ft\text{-}lb\text{-}sec^2)$

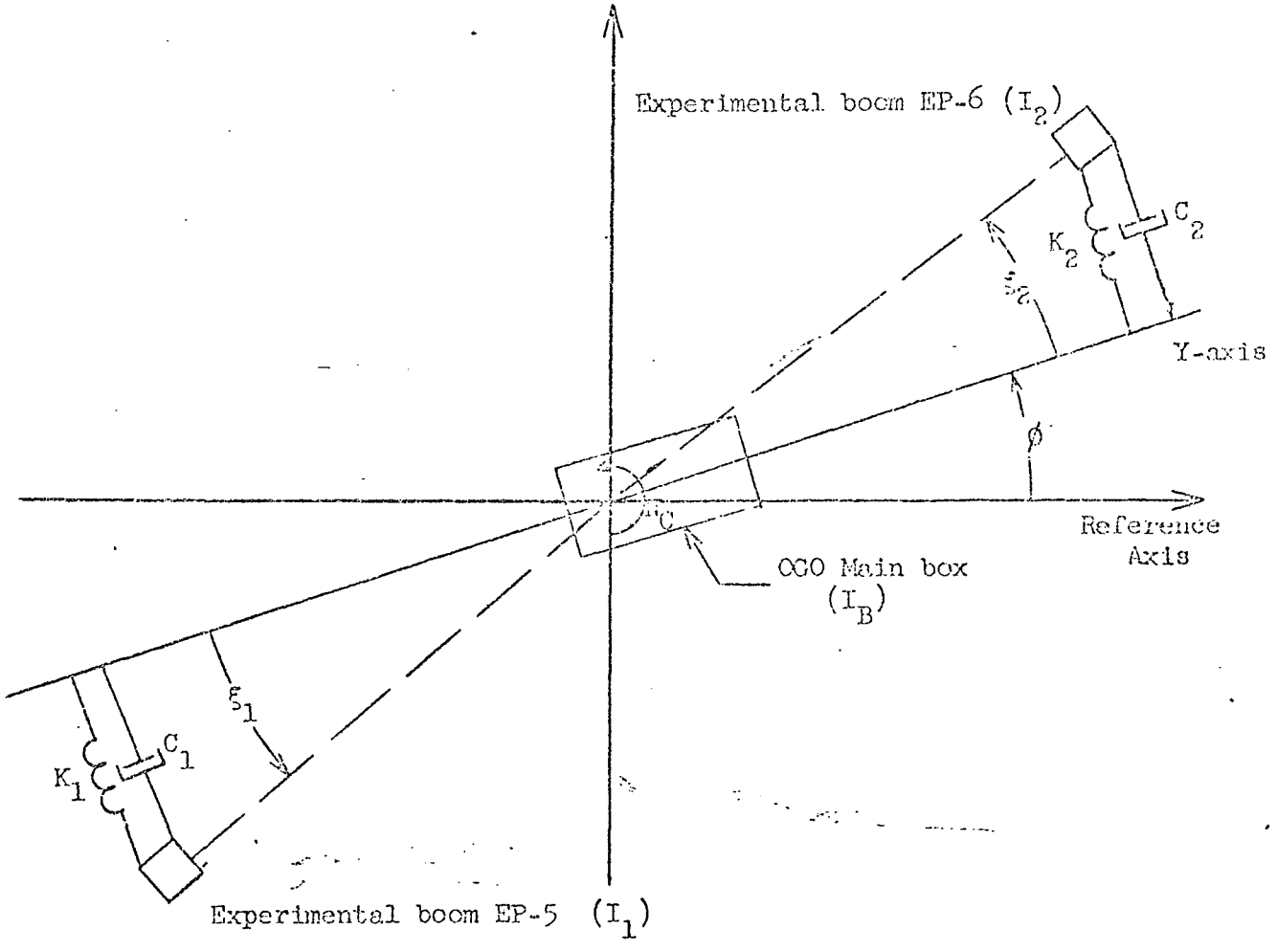

Figure 4-1

Simplified Single Axis (Roll) Model of OGO's Appendages

I_i Moment of inertia of i^{th} experimental boom (including experimental package) about the roll axis (ft-lb-sec^2)

K_i Spring constant of i^{th} boom (ft-lb/rad)

C_i Viscous damping constant of i^{th} boom (ft-lb-sec/rad)

ϕ Rotation of the OGO main box with respect to the reference axis (rad).

	Moment of Inertia I_i (slug-ft^2)	Resonant Frequency ω_i (rad/sec)	Damping* ζ_i (%)	Spring Constant K_i (ft-lb/rad)	Damping Constant C_i (ft-lb-sec/rad)
i = 0 (Main Body)	245				
i = 1 (EP-5)	216	1.51	0.3	493	1.95
i = 2 (EP-6)	209	1.66	0.3	576	2.08

Table 4-1, Parameter Values of Experimental Booms EP-5 and EP-6

*The amount of boom damping can not be predicted analytically but was chosen on the basis of comparison of model response to flight data as is discussed in Section 4.5.

The equations of motion for the mass-spring-dashpot system shown in Figure 4-1 are given below and are derived in Appendix A.

28

$$
\begin{aligned}
I_T \ddot{\phi} + I_1 \ddot{\xi}_1 + I_2 \ddot{\xi}_2 &= N_p + N_w + N_g = N_c \\
I_1 \ddot{\phi} + I_1 \ddot{\xi}_1 + C_1 \dot{\xi}_1 + K_1 \xi_1 &= 0 \\
I_2 \ddot{\phi} + I_2 \ddot{\xi}_2 + C_2 \dot{\xi}_2 + K_2 \xi_2 &= 0
\end{aligned}
\qquad (4\text{-}1)
$$

where

$I_T = I_B + I_1 + I_2$ = total roll inertia (slug-ft^2)

$N_c = N_p + N_w + N_g$ = total control torque (ft-lb)

N_g = gas jet torque (ft-lb)

N_w = reaction wheel torque (ft-lb)

N_p = array reaction torque (ft-lb)

The motion of OGO's main body about its roll axis and its interaction with the booms EP-5 and EP-6 as a function of an applied torque N_c may be investigated by the transfer function $\phi(s)/N_c(s)$ obtained from the Laplace transform of the equations of motion (Equation 4-1). Using the EP-5 and EP-6 parameter values defined in Table 4-1, the OGO roll axis dynamics are expressed by the following transfer function:

$$
\frac{\phi(s)}{N_c(s)} = \frac{0.234\,[s^2 + 0.09\,s + (1.51)^2]\,[s^2 + 0.1\,s + (1.66)^2]}{s^2\,[s^2 + 0.096s + (1.58)^2]\,[s^2 + 0.026s + (2.63)^2]} \ \text{deg/ft-lb} \qquad (4\text{-}2)
$$

The system's response is primarily determined by the lightly damped complex pole whose natural frequency is 2.63 rad/sec. Modal analysis (Section 2.0) indicates that this is the second bending mode frequency of the experimental booms EP-5 and EP-6. This asymmetric bending mode (ω_2 = 2.63 rad/sec or 0.42 cps) is excited by torques acting about the roll axis and is lightly damped ($\zeta \cong 0.5\%$). The booms' first bending

mode, represented by the other complex pole (ω_1 = 1.58 rad/sec or 0.24 cps), is more highly damped ($\zeta \cong 3\%$) and is partially cancelled by the nearby zeros. This is expected for the booms' symmetric first mode does not result in appreciable rotation of the main box and thus cannot be sensed by the control system sensors.

4.3 DESCRIBING FUNCTION ANALYSIS

In this section the dynamic model described above is used in conjunction with a describing function of the reaction wheel and gas jet bistable switches to prove the feasibility of a sustained limit cycle of the type observed on OGO-III. The effect of the array drive is ignored here. If the array is not being driven by the motor, it is locked by shaft friction to the main spacecraft body, hence can be considered rigid.

The simplified block diagram of the ACS roll channel (Figure 2-3) indicates that a "linear" analysis of the control loop requires a describing function representation of the nonlinear pneumatic and reaction wheel bistables. The effect of the nonlinearity upon the signal is represented by an equivalent gain and phase shift (as a function of input signal amplitude) denoted by the describing function G(x). Then the ACS reaction wheel or pneumatic control loop further reduces to Figure 4-2.

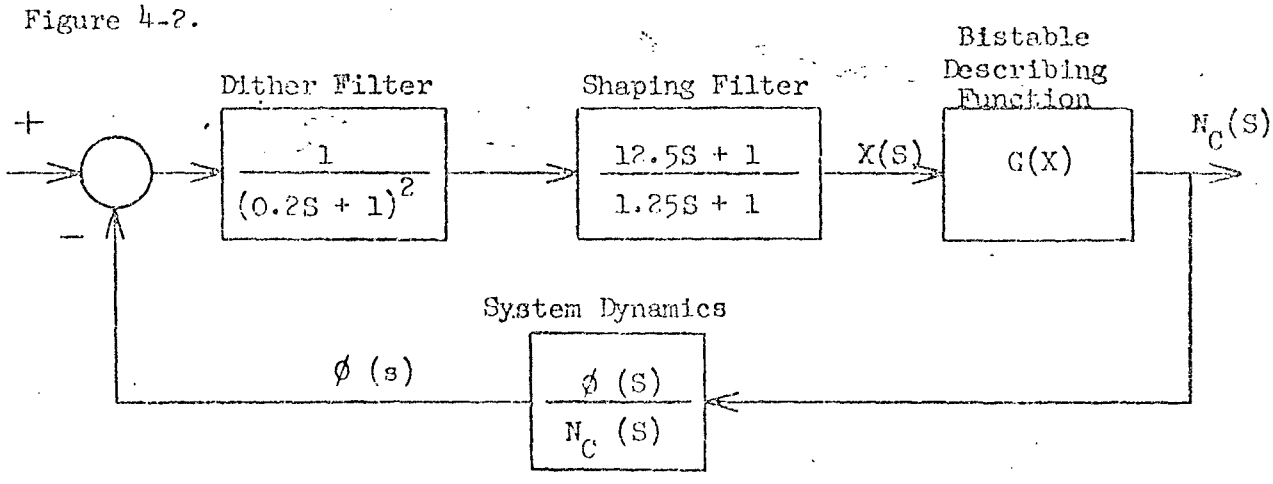

Figure 4-2, Simplified ACS Roll Axis Control Loop

The system's stability margins may be defined by the "closeness" of the system's open loop frequency response $T(s) = \frac{X(s)}{N(s)}$ to an intersection with the inverted describing function $1/G(x)$ (see Reference 4-1). An intersection of $T(s)$ and the $1/G(x)$ predicts a limit cycle oscillation. The system dynamics (Equation 4-1) effectively filter the bistable output so that the input to the bistables is a single frequency sinusoid thus satisfying the basic assumption of describing function analyses.

If the reaction wheel motor friction torque is neglected, both the reaction wheel and pneumatic nonlinearity may be modeled as shown in Figure 4-3.

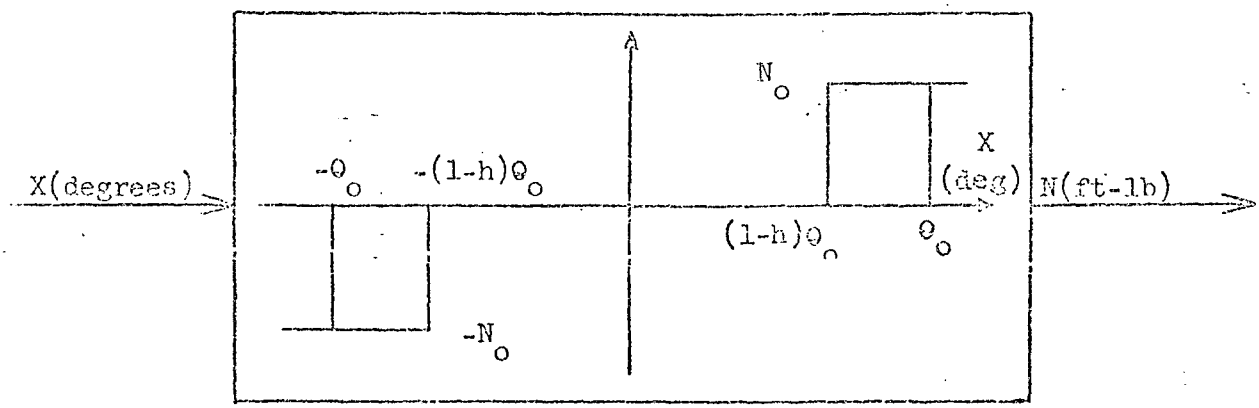

Figure 4-3, Reaction Wheel or Pneumatic Nonlinearity

The output torque level N_o, deadzone Θ_o, and hysteresis h are each important parameters affecting the describing function $G(x)$. These parameters are defined for both the ACS roll reaction wheel and pneumatic control loops during normal mode operation in Table D-2. Assuming $X \geq \Theta_o$, the resulting describing functions $G(x)$ are plotted both in phase and amplitude in Figure 4-4. A more detailed model of the reaction wheel nonlinearity was made assuming maximum friction torque of 0.006 ft-lb. No significant change in the describing function $G(x)$ was noted.

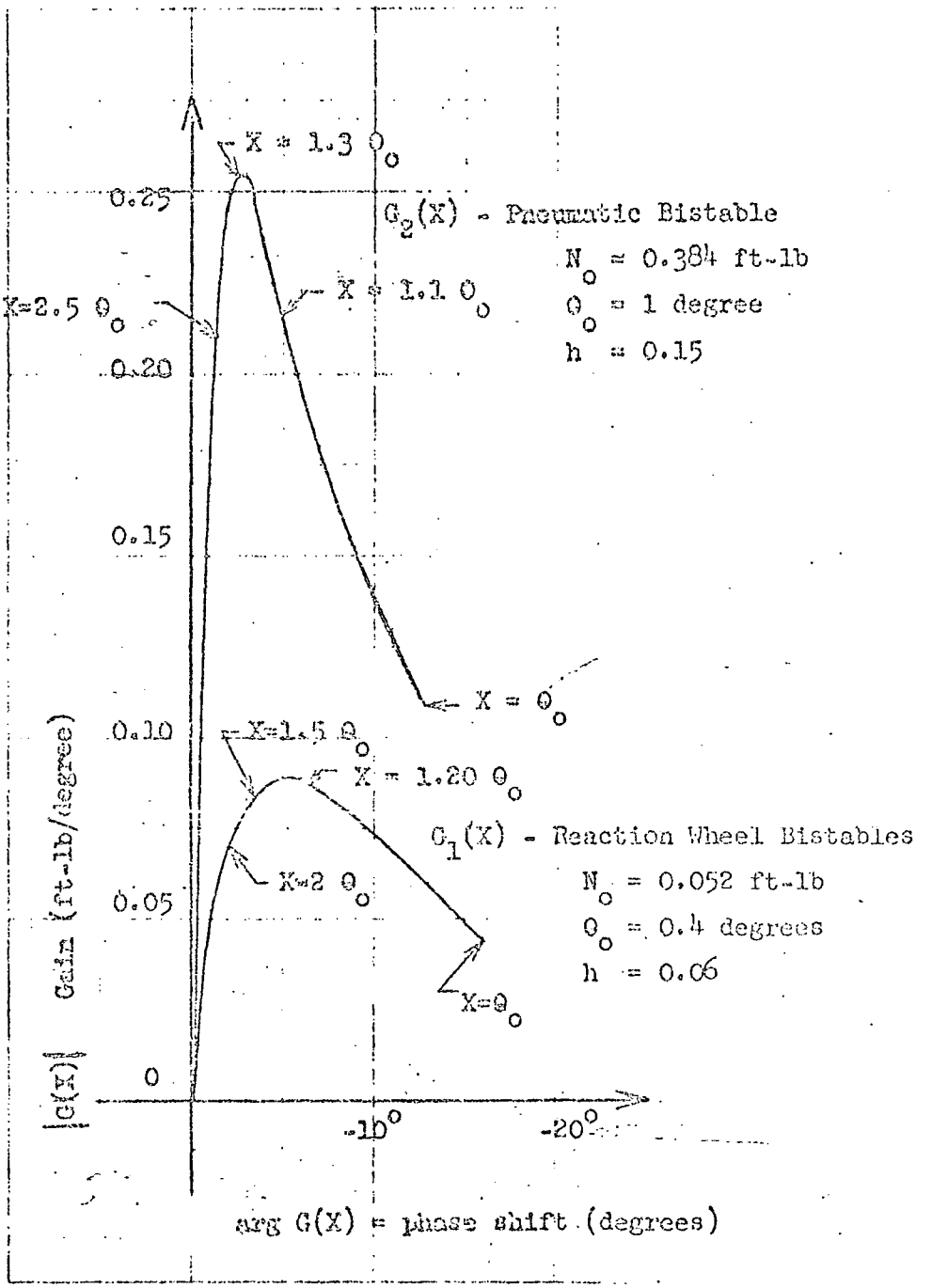

Figure 4-4

Describing Function for Pneumatic and Reaction Wheel Nonlinearities

4.4 ANALYTICAL MODEL VERIFICATION

The validity of the model developed above is supported by the prediction of roll reaction wheel oscillations during normal mode operation observed in OGO-III flight data. A Nichols plot of the roll channel's open loop frequency response T(s) during normal mode operation is shown in Figure 4-5 along with the reaction wheels' inverted describing function $1/G_1(x)$. Structural damping of 0.3% was used for booms EP-5 and EP-6. The intersection of T(s) and $1/G_1(x)$ indicates that the control loop will sustain a reaction wheel limit cycle at 2.64 rad/sec (0.42 Hz). The intersection of T(s) with the pneumatic describing function $G_2(x)$ also indicates that a gas limit cycle can be sustained. This did occur on OGO III, but when noticed was cut off by command activation of the gas inhibit logic. It should be understood that this type of analysis merely predicts that a limit cycle oscillation can exist and be sustained. For the limit cycle to occur, the booms must be excited initially at 2.64 rad/sec to a point where the reaction wheel bistable is turned on. The amplitude and frequency of OGO's roll error ϕ during reaction wheel limit cycle oscillations is calculated below to be 0.? degrees peak-to-peak at 2.64 rad/sec, an excellent agreement with OGO-III flight data.

From Figure 4-5 the transfer function T(s) magnitude is

$$\left|T(s)\right|_{s=j\,2.64} = \left|\frac{\phi(s)}{N_c(s)}\right| (67.3 \text{ deg/rad}) \left|\frac{(12.5\,s+1)}{(1.25\,s+1)(0.2\,s+1)^2}\right|_{s=j\,2.64}$$

$$= 11.2 \text{ deg/ft-lb}$$

or

$$\left|\frac{\phi(s)}{N_c(s)}\right|_{s=j\,2.64} = 1.5 \text{ deg/ft-lb} \qquad (7)$$

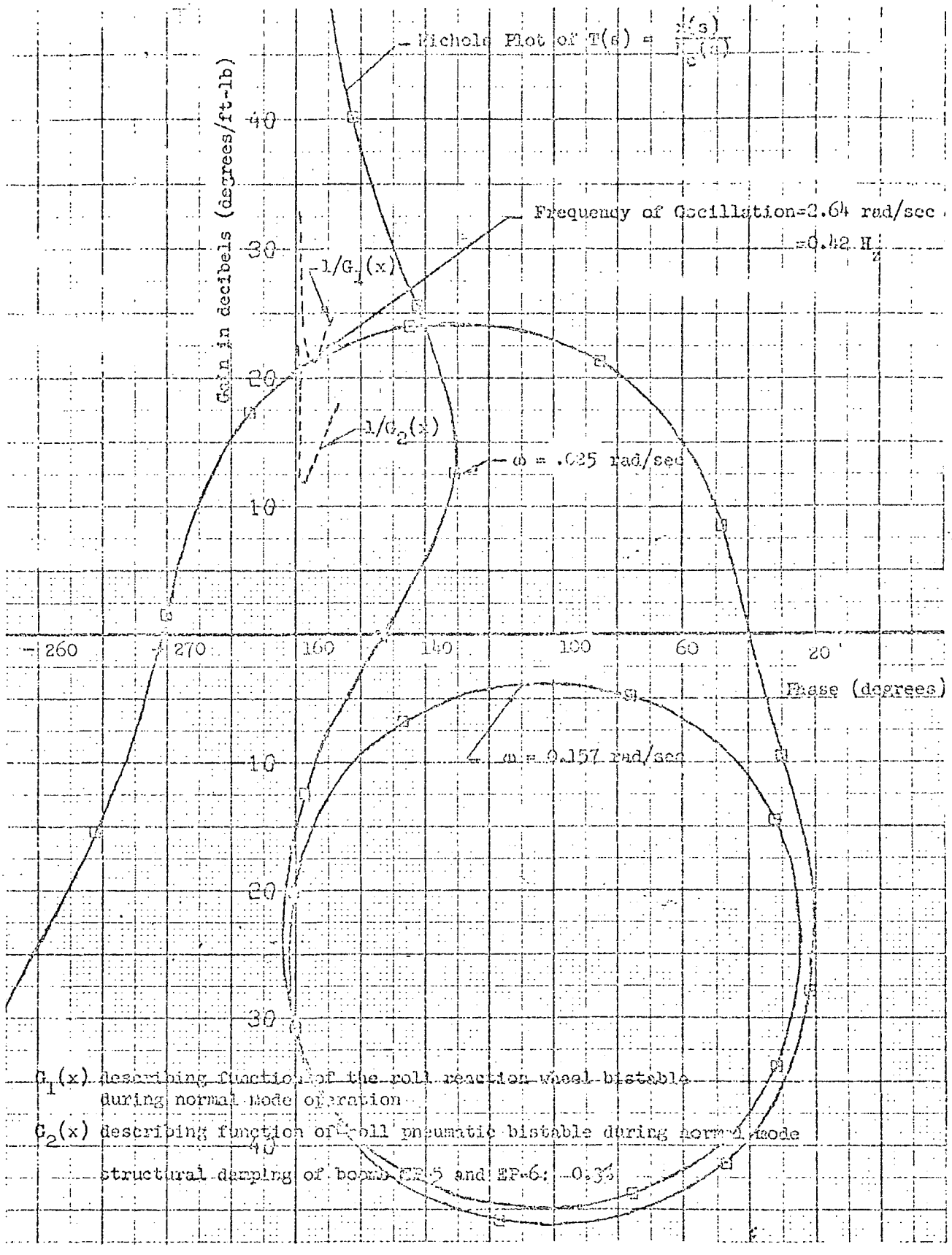

Figure 4-5 Open Loop Frequency Response Gain-Phase Plot of Roll ACS Channel - Normal Mode

Approximating the reaction wheel torque during limit cycle oscillations by a square wave (Figure 4-6), the Fourier series of the roll axis control torque applied to the OGO main body is

$$N_c(t) = N_w \sum_{n=1,3,5} \frac{4}{\pi n} \sin n\omega_c t$$

where

N_w = roll reaction wheel torque = 0.052 ft-lb

ω_c = frequency of oscillation = 2.64 rad/sec

= 0.42 Hz

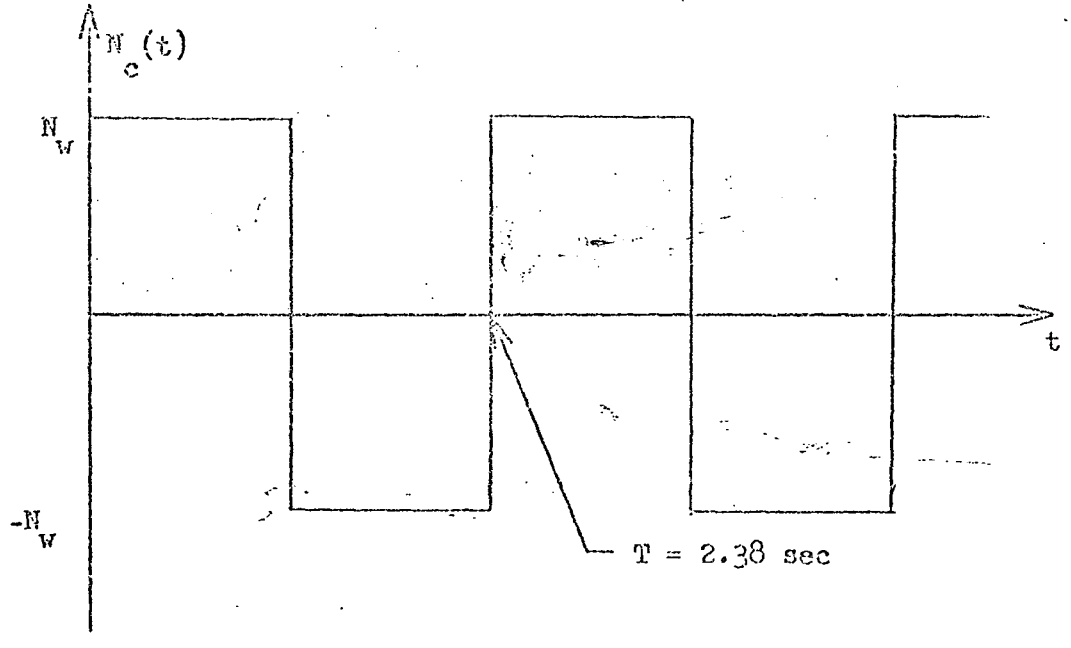

Figure 4-6, Approximate Control Torque During Roll Reaction Wheel Limit Cycle

Further approximating the control torque by its fundamental component only and using Equation (7), the angular displacement of the OGO main body about the roll axis during the reaction wheel limit cycle is

$$\phi(t) = \frac{4}{\pi} (0.052 \text{ ft-lb})(1.5 \text{ deg/ft-lb}) \sin \omega_c t$$

$$= 0.1 \sin \omega_c t \text{ (degrees)}$$

This is an excellent agreement with flight data which indicated a roll oscillation amplitude of $\pm$ 0.1 deg when only the roll wheel was oscillating.

The equations of motion (Equation 4-1) may also be solved for angular displacement from equilibrium of OGO booms EP-5 and EP-6. During roll reaction wheel limit cycle,

$$\xi_1(s) / N_c(s) \Big|_{s = j\,2.64} = 0.0398 \text{ rad/ft-lb}$$

$$\xi_2(s) / N_c(s) \Big|_{s = j\,2.64} = 0.0447 \text{ rad/ft-lb}$$

Again approximating the control torque by its fundamental component only, the linear displacement from equilibrium of the boom tips during roll reaction wheel limit cycle is

EP-5 = $\pm$ .73 inches

EP-6 = $\pm$ .83 inches

Unfortunately, no direct quantitative measurement of the boom motion was available from the flight data.

4.5 DIFFERENCES OF ANALYTICAL MODEL RESULTS

Several aspects of the analysis above deserve amplification.

No attempt was made a' priori to predict, either analytically or from test data, the damping forces in the booms because of the very small motion amplitude (less than ± 1 in. at the tip). Therefore, for this analysis the boom damping was considered a variable. By trial and error a boom damping of 0.3% was found to be the maximum which would allow the reaction wheels to sustain a limit cycle.

The amount of boom damping affects directly the magnitude of the open loop frequency response T(s) at the bending mode frequencies. As Figure 4-5 shows, a boom damping of 0.3% just produced an intersection of the describing function $1/G_1(x)$ and the open loop frequency response T(s). A lower damping raises the T(s) curve in the region of .42 cps for which the describing function analysis simply indicates a larger steady state oscillation amplitude (Reference 4-1). Increasing the damping lowers the T(s) curve, hence there would not be an intersection and no prediction of a reaction wheel limit cycle.

Data is presented in Reference 4-2 which indicates that the damping of the 0.42 cps bending mode is about 0.4%. This damping estimate was based upon a recent analysis of OGO-II flight data. To make a comparison of damping observed in flight with the above analysis one must examine the damping not in the booms alone but rather the damping in the asymmetric bending mode at 0.42 cps. It was shown in Equation 4-2 that with 0.3% boom damping, damping in the 0.42 cps bending mode was 0.5%. Thus, the flight data indicates the actual boom damping was below the maximum required to allow a reaction wheel limit cycle.

Previous analysis (References 4-3 and 4-4) of the EP-5 and EP-6 boom interaction with the roll ACS had indicated that little likelihood existed of a coupled ACS-boom oscillation. The major weakness of the previous work apparently was a discrepancy between the amount of structural damping assumed for the booms (1 to 2%) and the actual value which exists.

It is obvious from Figure 4-5 from the intersection of the T(s) with the pneumatic describing function, that 0.3% is far below the maximum damping required for prediction of a gas limit cycle. Here is the

place to emphasize the nature of the limit cycle predicted by the describing function analysis for this bang-bang control system.

The describing function analysis merely predicts the existence of the limit cycle. To start such a limit cycle the boom system must be initially excited to the point where error signal input to the gas (or reaction wheel) bistable is sufficient to alternately pulse the plus and minus torque command. Then the analysis predicts that the control system will pick up the oscillation and sustain a stable limit cycle. That is if the limit cycle amplitude is larger than the stable value the amplitude will decay and vice versa.

Another aspect of the describing function analyses results can be correlated to the flight data discussed in Section 3.2.3. The flight data indicated that on the approach to the first perigee the reaction wheel limit cycle was started by the array cogging exciting the booms.* However, the gas limit cycle did not begin until 37 minutes later. Analysis of other flight data and the analytical examination above show the stable or steady state reaction wheel limit cycle amplitude is $\pm$ 0.1 deg. This is well below that required to start a gas limit cycle. (Analysis indicates approximately a $\pm$ 0.15 deg. oscillation would produce a $\pm$ 1.0 deg. input to the gas bistables, enough to start a gas limit cycle.) This is further indication that the array cogging had to excite the boom oscillation to the point where the gas limit cycle could begin.

The third and final point that the analysis shows, is why no oscillations existed in roll during acquisition or in the yaw channel. The yaw channel is singled out here because the EP-5 and EP-6 booms have bending modes about the yaw axis similar to roll. Only the main box inertia is larger due to the large solar array inertia.

---

*This effect will be further proven in Section 4.6.

The roll shaping filter (see Figure 2-3) consists of a lead lag $\frac{12.5\ S+1}{1.25\ S+1}$ and a two first order lags $\frac{1}{(.2S+1)^2}$. The double order lags are necessary to filter out the dither which rides on the horizon scanner error signal. At the bending mode frequency (2.64 rad/sec) the over all phase shift of the total filter is a lag of approximately 40 deg. During the sun acquisition (Mode II) the double order lag is removed since the roll error signal comes from the array sun sensor. In this case the overall filter phase shift is a lead of 14 degrees. This shifts the trace of the open loop frequency response to the right as is shown in Figure 4-7. No intersection of the describing function occurs hence no sustained limit cycle is possible in roll during sun acquisition mode. The same is true of the yaw channel, for its filter has nearly zero phase shift at the bending mode frequency.

The point which the analysis demonstrates is that the phase lag introduced by the dither filter is one of the reasons that the roll channel during normal mode can sustain a boom oscillation.

4.6 COMPARISON OF ANALOG MODEL RESPONSE TO OGO-III FLIGHT DATA

As a further check on the model validity the complete roll control system, solar array drive system and boom dynamics (Equation 4-1) were programmed on the analog computer. The simulation block diagram and numerical data are given in Appendix C.

An attempt was made to reproduce the onset of oscillation observed on OGO-III. The initial conditions were selected to simulate the flight conditions.

Figure 4-8 shows the analog results. Examining the traces starting at the far left hand side, the run was started with zero initial body rate and attitude error but with an initial wheel momentum of 0.5 ft-lb-sec. A constant error rate of 0.03 deg/sec was applied to the solar array channel simulating the approximate orbital motion when the boom ACS oscillation started on OGO-III. The solar array

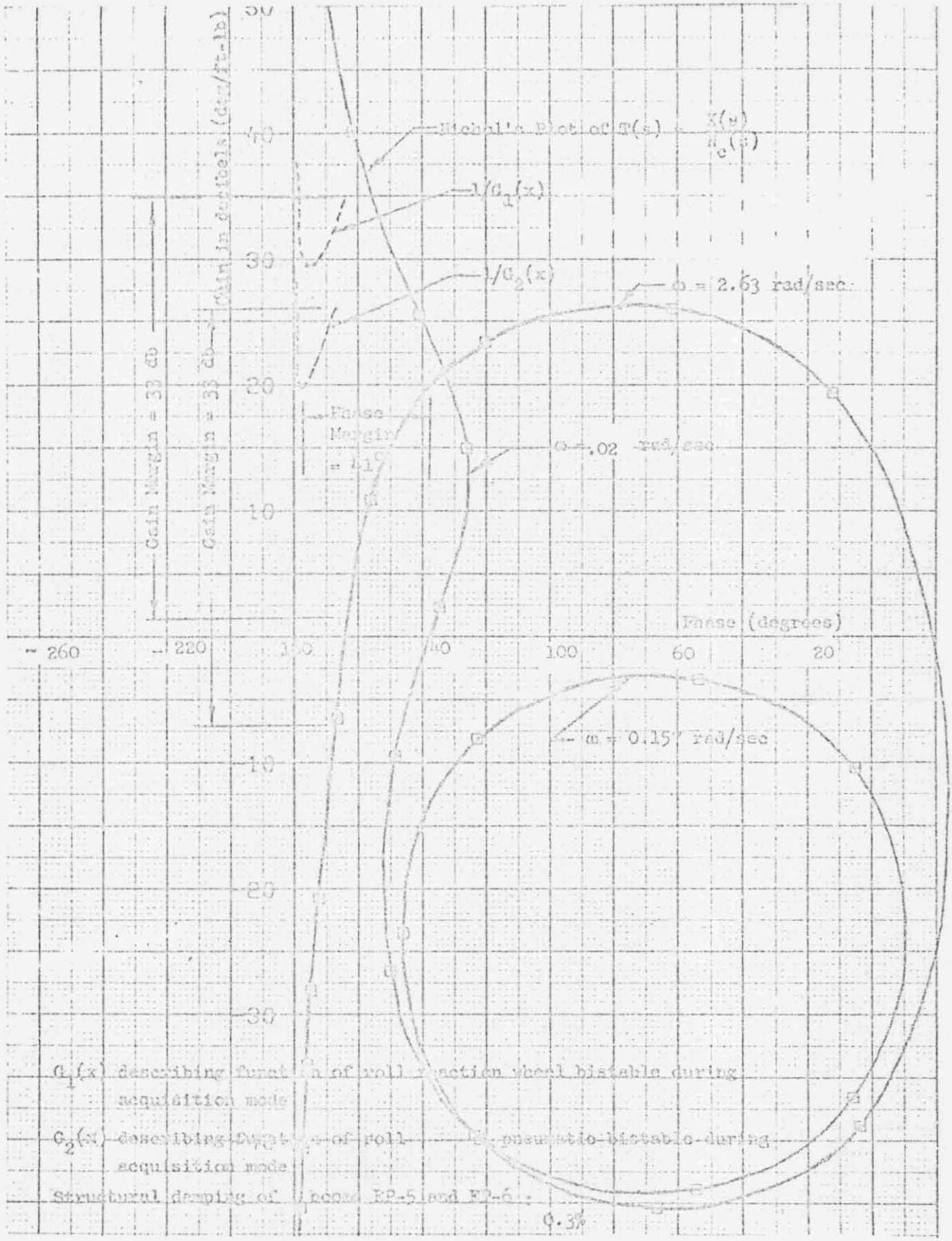

$G_1(x)$ describing function of roll reaction wheel bistable during acquisition mode

$G_2(x)$ describing function of roll pneumatic bistable during acquisition mode

Structural damping of modes EP-5 and EP-6 : 0.3%

Figure 4-7 Open Loop Frequency Response Gain-Phase Plot of ACS Roll Channel-Sun Acquisition

drive corrects for the orbital motion once every 25 sec, moving approximately 0.75 deg each time. With each succeeding cog of the array, the boom motion increases until finally the reaction wheels begin to limit cycle.

At this point the orbital rate was removed from the array and the oscillation sustained by the reaction wheel allowed to reach a steady state. The steady state oscillation is shown on an expanded scale in the middle of the figure.

Table 4-2 shows comparison made between the parameters observed in the OGO-III flight data and the analog results shown in Figure 4-8. For the available parameters an excellent correlation is obtained when only the reaction wheels are limit cycling.

No fine-grain data was available on the gas limit cycle observed on the first perigee pass so that no comparisons were made between the analog and flight results for that level of oscillation. Fine grain data was available on the combined array and reaction wheel limit cycle from Rev. 021 (see Figure 3-8). The analog model response with the array drive and reaction wheel limit cycling is shown in the right half of Figure 4-8. From the steady state reaction wheel limit cycle the orbit rate was again applied to the array so that it resumed excitation of the booms. The oscillation amplitude grew slowly in amplitude until the array drive started to limit cycle as can be observed from the traces in Figure 4-8. The steady state array and reaction wheel limit cycle is shown on the extreme right hand side of the Figure. A comparison of the analog and flight data parameters is shown in Table 4-2.

There is a glaring discrepancy between the amplitude of oscillation observed in flight ($\pm$ 0.2 deg) and the analog results ($\pm$ 1.8 deg). Despite some rather extensive investigation as to the fundamental cause of the discrepancy no fully satisfactory explanation has been found.

Several interesting aspects of the combined array reaction wheel oscillation have been discovered and analyzed, but to-date they remain simply facts without a theory. This data is discussed below in Section 4.8.

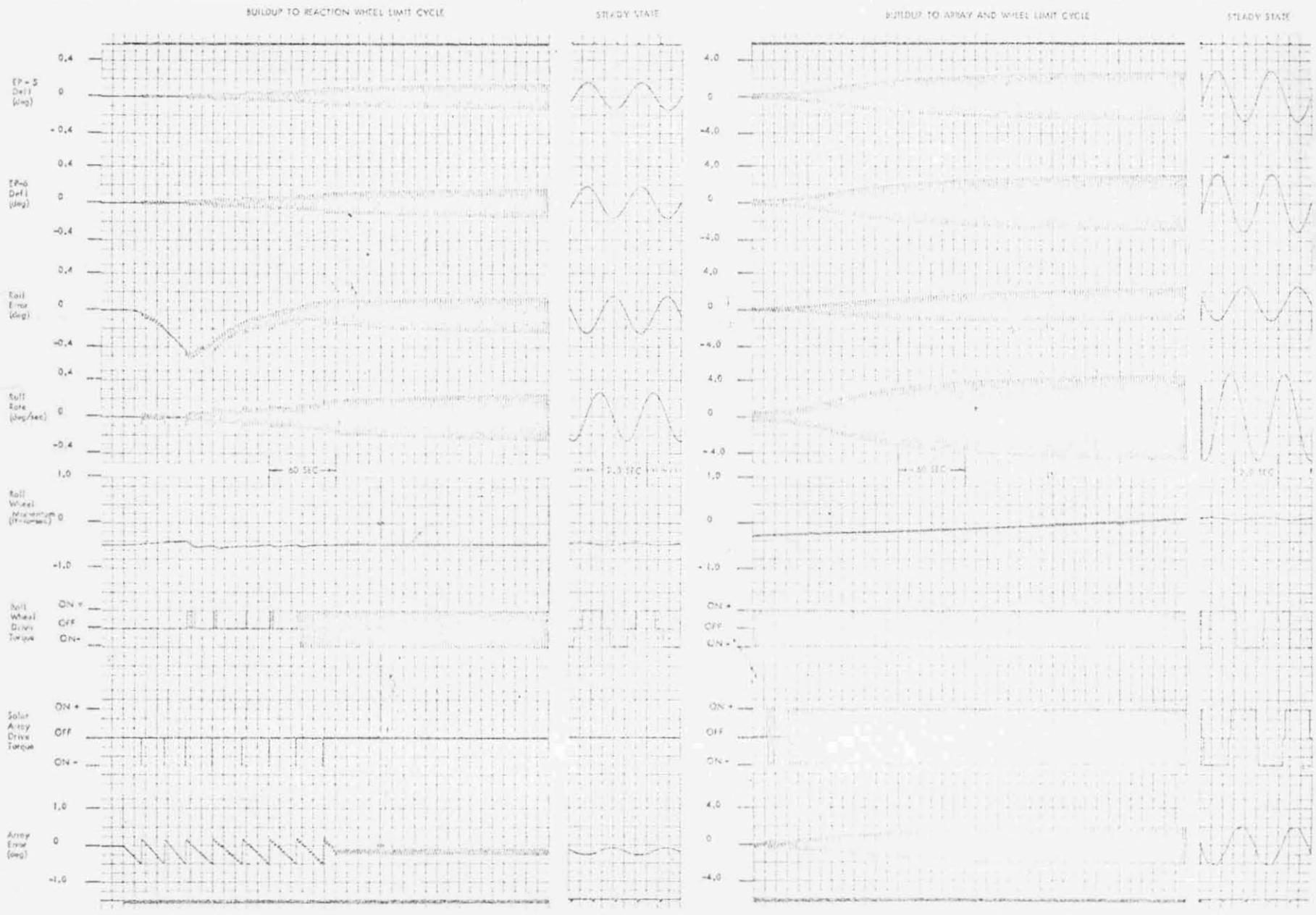

Figure 4-8 Roll Normal Mode Response to 0.03 deg/sec Array Drive Rate Gas Delay Enabled

Table 4-2

Comparisons of FTD and Analog Simulation
of OGO Roll Oscillation

a) No Solar Array Drive Oscillation Reaction Wheel Limit Cycle Only

Parameter	FTD*	Simulation
Frequency	0.42 H_z	0.42 H_z
Roll Error	0.2 deg p-p	0.2 deg p-p**
Reaction Wheel On Tim	0.8 sec	0.7 sec
Phase Lag Wheel On from Roll Error Zero Crossing	60 deg	58 deg

b) Solar Array Drive Oscillation and Reaction Wheel Limit Cycle

Parameter	FTD*	Simulation
Frequency	0.38 H_z	0.42 H_z
Roll Error	0.4 deg p-p	3.6 deg p-p
Reaction Wheel On Time	1.2 sec	1.1 sec
Solar Array On Time	0.5 sec	1.1 sec
Phase Lag Wheel On	42 deg	50 deg
Phase Lag Array On	0***	0 deg

*Rev 021

**Boom damping adjusted to give proper amplitude 0.3%

***Approximate value-resolution poor

The discrepancy in the model when the array limit cycles was annoying but was not considered serious enough to preclude evaluation of the changes to the ACS discussed in Section 5.0. In a sense the model may be considered conservative since the array boom oscillation is too large. Moreover, changes to the array drive control loop were considered only if they did not require an exact model of the array spacecraft coupling in order to evaluate their performance.

4.7 FLIGHT DATA ANALYSIS

OGO III telemetry was reviewed in Section 3.0 Regions of anomalous behavior, namely the oscillatory motions in the roll and solar array control systems, are discussed here again for comparison with the analog model dynamics. Oscillations of OGO III during revolution 21 was shown in Figure 3-8 both with and without solar array drive participation.

Many aspects of the analytical model are supported by the telemetry. For example, the solar array drive backlash is in evidence in the Array Angle (Sine) channel which shows continued cyclic movement during periods of solar array drive motor inactivity. The Array Sine, a measure of relative rotation between the OGO main body and solar array drive shaft, also indicates very little damping of these shaft oscillations.

The higher frequency components evident in both the Array Sine and Array Error signals during solar array drive activity have been analyzed. Figure 4-9 shows the power spectral density and Figure 4-10 shows the autocorrelation function of the Solar Array Error signal (Word A-11) and the Array Sine (Word A-12) from a period during revolution 021 when both the array and reaction wheel motors were limit cycling. The resonant frequency (0.38 Hz) of the EP-5 and EP-6 boom - main body dynamics is evident in both figures.* The power spectral density

*It is of interest to point out that the flight data indicated when the reaction wheels are limit cycling alone this frequency shifts to approximately 0.42 Hz. This effect was never reproduced on the computer. Regardless of which elements were active in a boom ACS limit cycle, the model frequency of oscillation remained near 0.42 Hz.

indicates the presence of two additional frequencies. A component at 1.0 Hz exists in both the Array Error and Array Sine and a component near 0.7 Hz is present in the Array Sine. Visual examination of the telemetry traces has verified these relationships.

The 0.7 Hz component in the Array Sine signal is near the computed fundamental resonant mode of the solar array (Reference 2-4). However, this mode of oscillation has little displacement at the Sine resolver pickoff point but a maximum at the Array Error signal pickoff point. On the other hand, the Array Error signal power spectral density shows no .7 cps signal. Thus, the flight data is the antithesis of the analytical model. Though additional analysis and modeling attempts were made, no analytical model was developed which would explain the frequency content of the observed Array Error and Array Sine signals. The flight data analysis was checked independently and adjudged to be valid. No testing has been done to validate the computed array dynamic model. It is felt the discrepancy must lie either in the array dynamic model or in the dynamic coupling (i.e., flexible structure effect) of the array motion through the array drive motor to the main body. Unfortunately, time did not permit the pursuance of a testing program which might develop sufficient structural data to refine the dynamic model.

Finally, there is the gross discrepancy compared to flight data in the model oscillation amplitudes when the array is limit cycling. The flight data indicated the oscillation amplitude changes from $\pm$ 0.1 deg to $\pm$ 0.2 deg when the array limit cycles. Analysis of the forcing function which would theoretically be induced by the array limit cycling supports the fact the oscillation amplitude should grow significantly more than the observed flight data values. The energy added by the array motion to the boom oscillation amplitude is theoretically an order of magnitude more than the energy added by the reaction wheel limit cycling. This discrepancy again points to the fact that model of the coupling array to the main spacecraft is apparently in error.

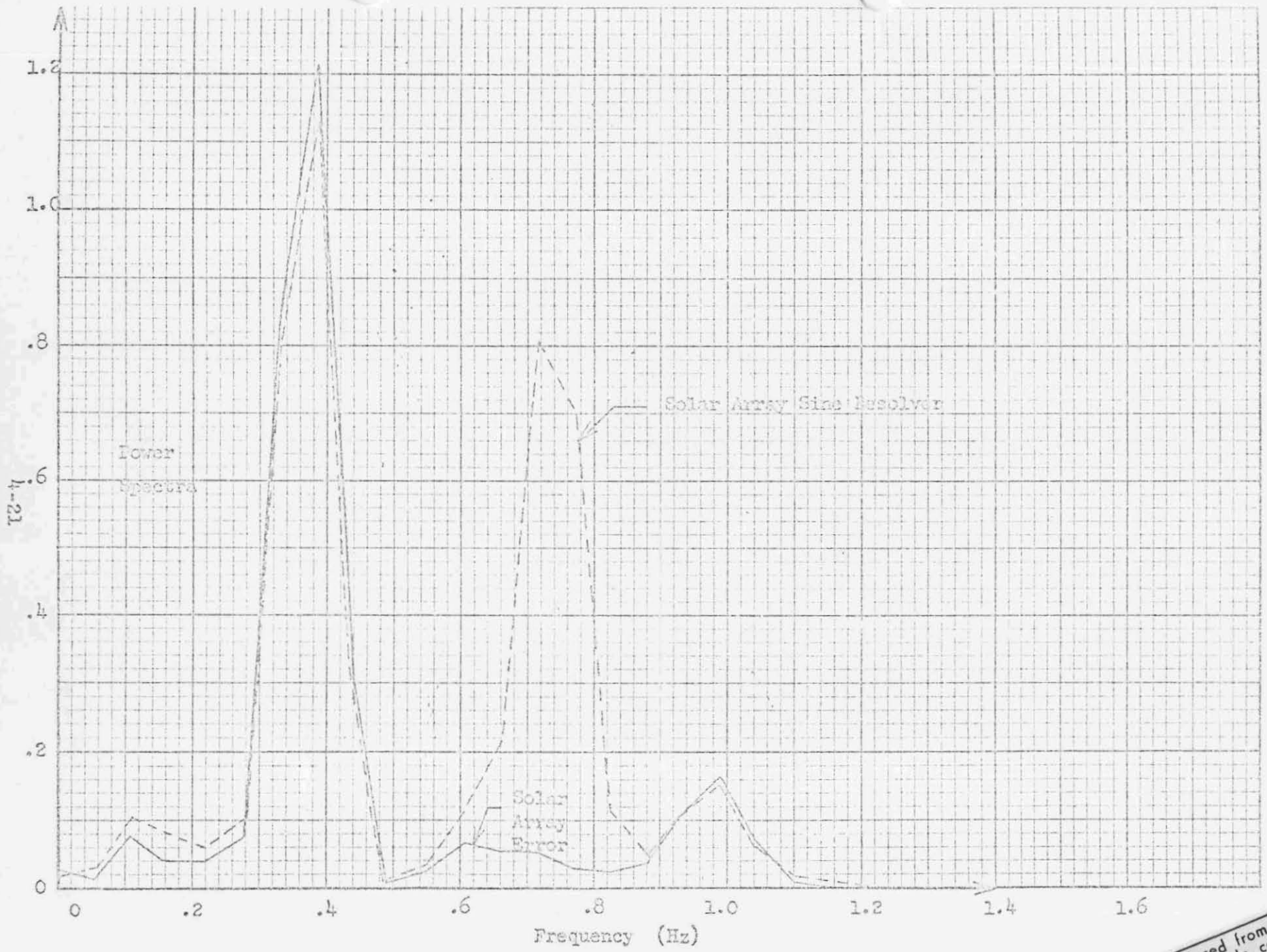

Figure 4-9 Power Spectral Density OGO III Flight Data Rev 021

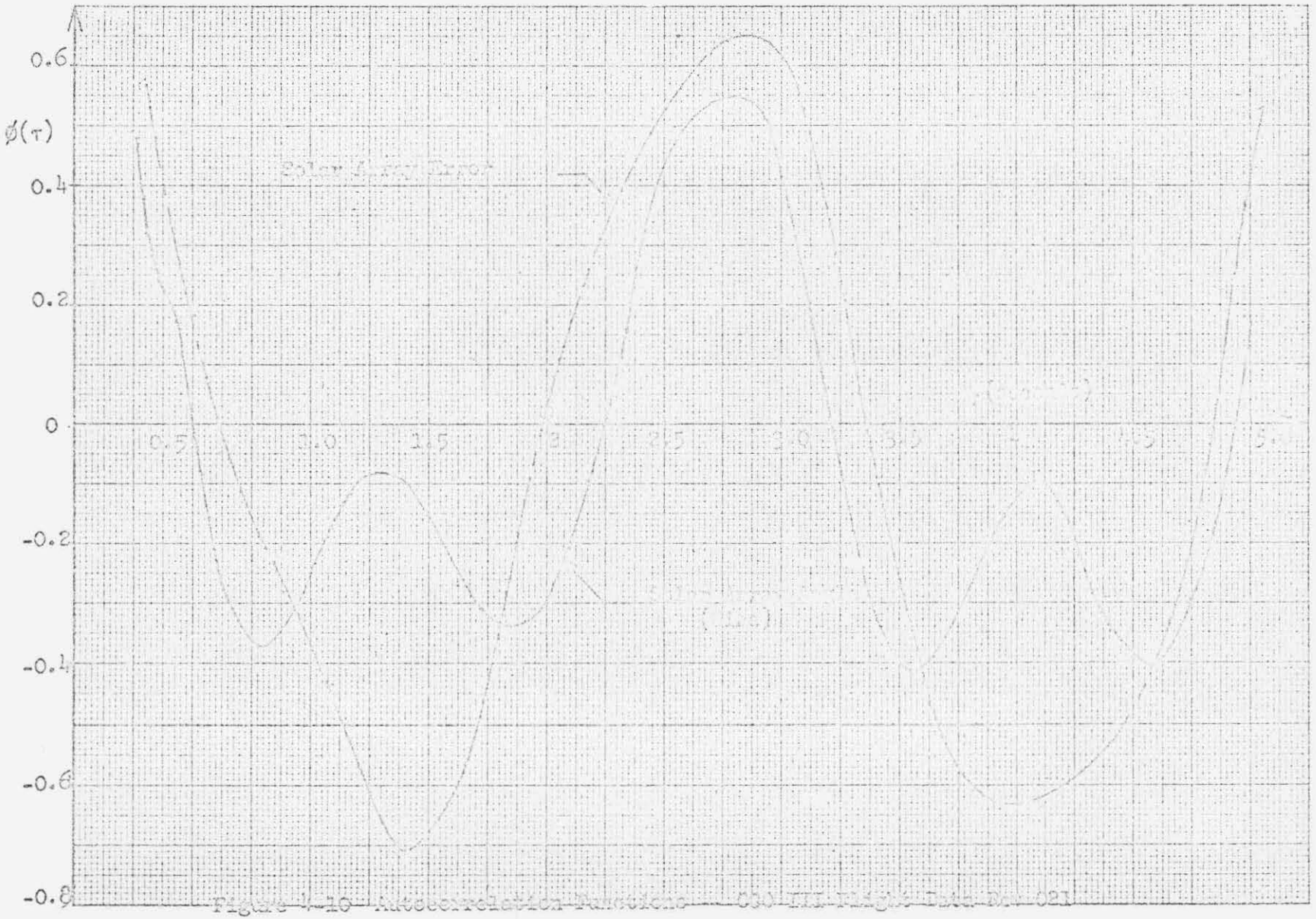

Figure 4-16 Autocorrelation Randomness (30) ITT Night Data Run 021

REFERENCES

4-1 "Automatic Feedback Control System Synthesis," Chapter 10, John G. Truxal. McGraw Hill, 1955.

4-2 66-3343.3-199, "Material Damping of the OGO EP-5 and EP-6 Booms," R. Gluck, 7 December 1966.

4-3 66-9352.1-102, "Roll Errors Induced in the OGO Attitude Control System by the Oscillation of the Helliwell and Heppner Instrument Booms", J. E. Dickinson, 10 January 1966.

4-4 9352.8-233, "Analysis of Effects of Appendage Oscillations on the OGO Attitude Control System Performance". H. L. Mork. 6 June 1963.

5.0 ACS REDESIGN ANALYSIS

The purpose of this section is to present the rationale and background studies which lead to the final selection of the ACS design changes. The previous section has discussed some of the known problems in the roll channel. In considering design changes, however, the whole ACS design was reviewed in the light of the new concern over flexible body dynamics.

Although the magnetic amplifiers were being redesigned to permit a 100% duty cycle it was considered imperative to prevent the reoccurance of a roll reaction wheel limit cycle such as observed on OGO-III. The gas delay logic was considered an adequate protection from a gas limit cycle based upon the OGO-III experience. Thus, the first design consideration was to eliminate the roll wheel limit cycle.

5.1 REVIEW OF PROPOSED FIXES FOR THE ROLL CHANNEL

One fix considered for the boom oscillation problem was that of adding dampers or vibration absorbers to the tip of each boom. This appeared attractive particularly since the problem was the result of low damping (0.3%) in the experiment booms. Moreover, no electronics changes to the ACS would be required. The design studies of the dampers are documented in References 5-1 and 5-2. They turned out to be relatively heavy devices, 7 to 11 lbs., however, which jeopardized the structural integrity and deployment of the booms. Thus, the boom dampers were discarded.

Since increasing the boom damping did not appear feasible, a design study was begun to conceive and evaluate electronic changes to the roll ACS channel. The roll channel was of prime concern since no oscillations were observed in pitch or yaw. Three possible changes were evaluated. One was simply to increase (say double) the roll reaction wheel and possibly the gas deadzone. Thus, the booms would have to be excited to a larger motion before the control system would pick up the oscillation. Increasing the deadzone also reduces the

"open loop" gain, which stability analyses showed would prevent the ACS from limit cycling. This technique is very easy to implement. However, studies showed widening the deadzones is easily negated should the boom damping be lower than expected and hence, it was discarded.

A second fix considered was that of altering the present compensation filter design to stabilize the control system at the bending frequency. The discussions in the Section 4.6 showed that the reaction wheel limit cycle was due in part to the phase lag of the horizon scanner dither filter. Filter designs which stabilized the roll channel at the bending frequencies were developed. However, the required filters were far more complex to implement than the present design. Thus, the filter change was discarded on the basis of implementation difficulties. Some alternate schemes were suggested in Reference 5-3. Again implementation difficulties appeared insurmountable.

The third change considered is similar in concept to the gas delay logic used on OGO-III. It was this so called "wheel delay logic" which was chosen to be implemented. A schematic of this scheme is shown in Figure 5-1.

The delay logic prevents alternating torques from being applied to the reaction wheel. For example assume an oscillatory error signal (i.e., one due to bending) is alternately switching the bistables on. When the (+) bistable is turned on it opens the ground path (via the transistor switch) for the (-) signal. The ground path is held open by the timing circuit for a period of 5 seconds after the (+) bistable turns off. Thus when the (-) bistable turns on, no torque is applied to the reaction wheel (current must flow in the motor driver magnetic amplifier control winding to turn on AC power to wheels). When the (-) bistable turns on it also opens the ground path for the (+) signal. If the oscillatory input signal is alternately switching the bistables more frequently than the delay period, torque is not applied to the wheel in either direction. Thus the delay logic very positively prevents the reaction wheels from participating in a bending oscillation such as that observed on OGO-III.

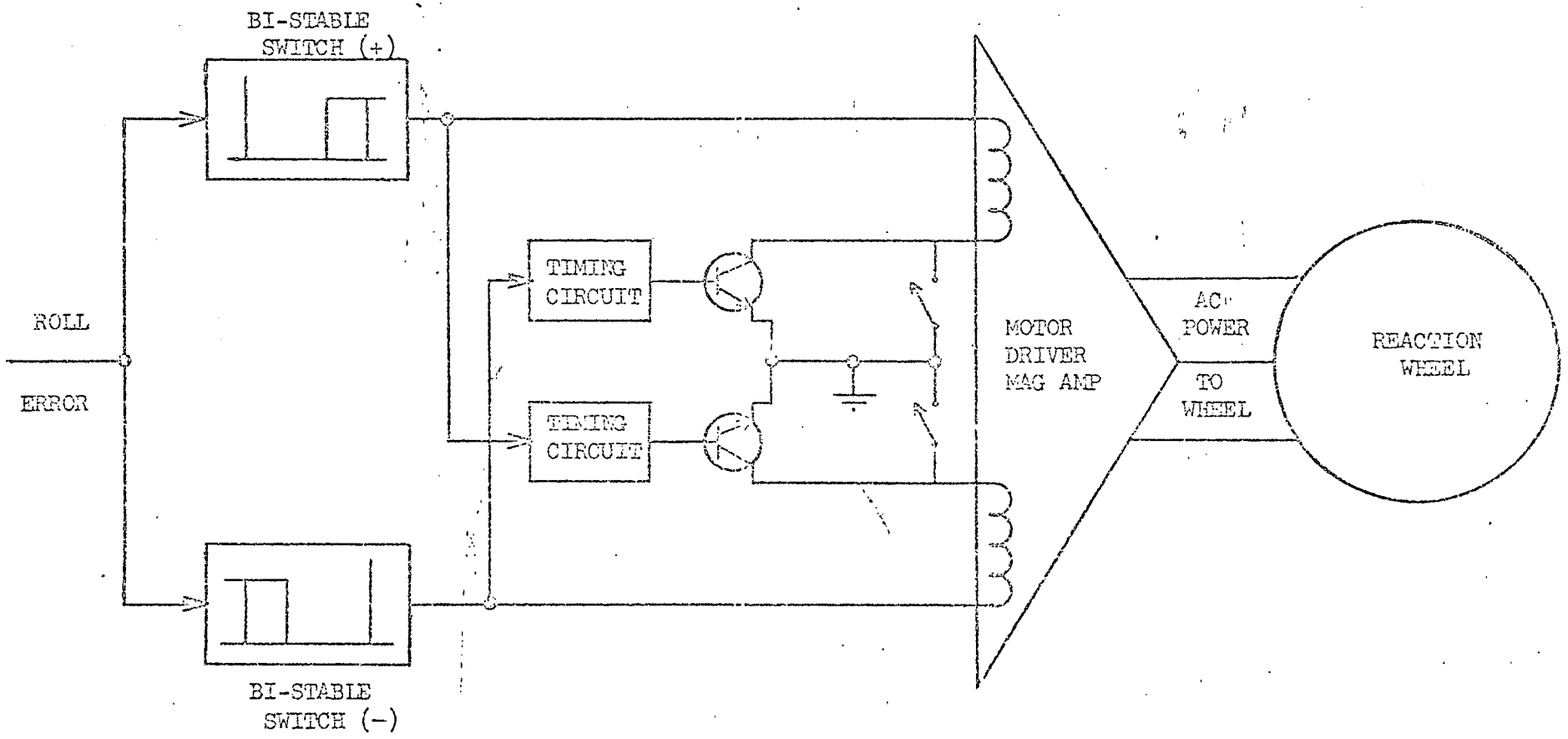

Figure 5-1

Reaction Wheel Delay Logic

Other operational aspects of the wheel delay logic are also attractive. Uni-directional inputs to the wheels are not affected by the wheel delay logic. The gas delay logic operation is also unaffected. The gas delay logic prevents the gas jet turned on by a positive error signal, for example, from firing until the corresponding wheel bistable (+) has been turned on continuously for a period of 15 sec. The gas delay logic prevents gas from firing due to a bending frequency (.4 cps) oscillatory input since the wheel bistable is only on for at most 1.25 sec. Since the wheel bistable operation is unchanged, the gas delay logic is similarly unchanged.

Both the wheel and gas delay logic must be turned on by command. The switching technique for the reaction wheel delay logic is also shown in Figure 5-1. Two latching relays are used to open the normal ground return of the motor driver magnetic amplifier input windings. The delay logic can only be activated by command when the ACS is in Mode III. It is automatically removed if the ACS is returned to Modes I or II. In fact the only method of removing the wheel and gas delay logic is to return to Mode I or II.

The implementation problems proved minimal with the delay logic scheme. Since the motor driver magnetic amplifiers were being redesigned, it was easy to bring out the control winding ground connections and provide the appropriate external switching. Moreover, with the shorting relay closed reaction wheel control is unaffected.

A delay period of 5 seconds was selected as the nominal design value. This allowed a considerable tolerance in the delay time; 1.25 seconds is sufficient to prevent a roll wheel limit cycle. Figure 5-2 shows the effect of the wheel and gas delay logic on the switching lines. Since during normal mode reaction wheel control maintains rates to less than 0.1 deg/sec, the delay logic should have little effect. A detailed evaluation of the roll control system performance via an anlaog simulation is discussed in Section 6.0.

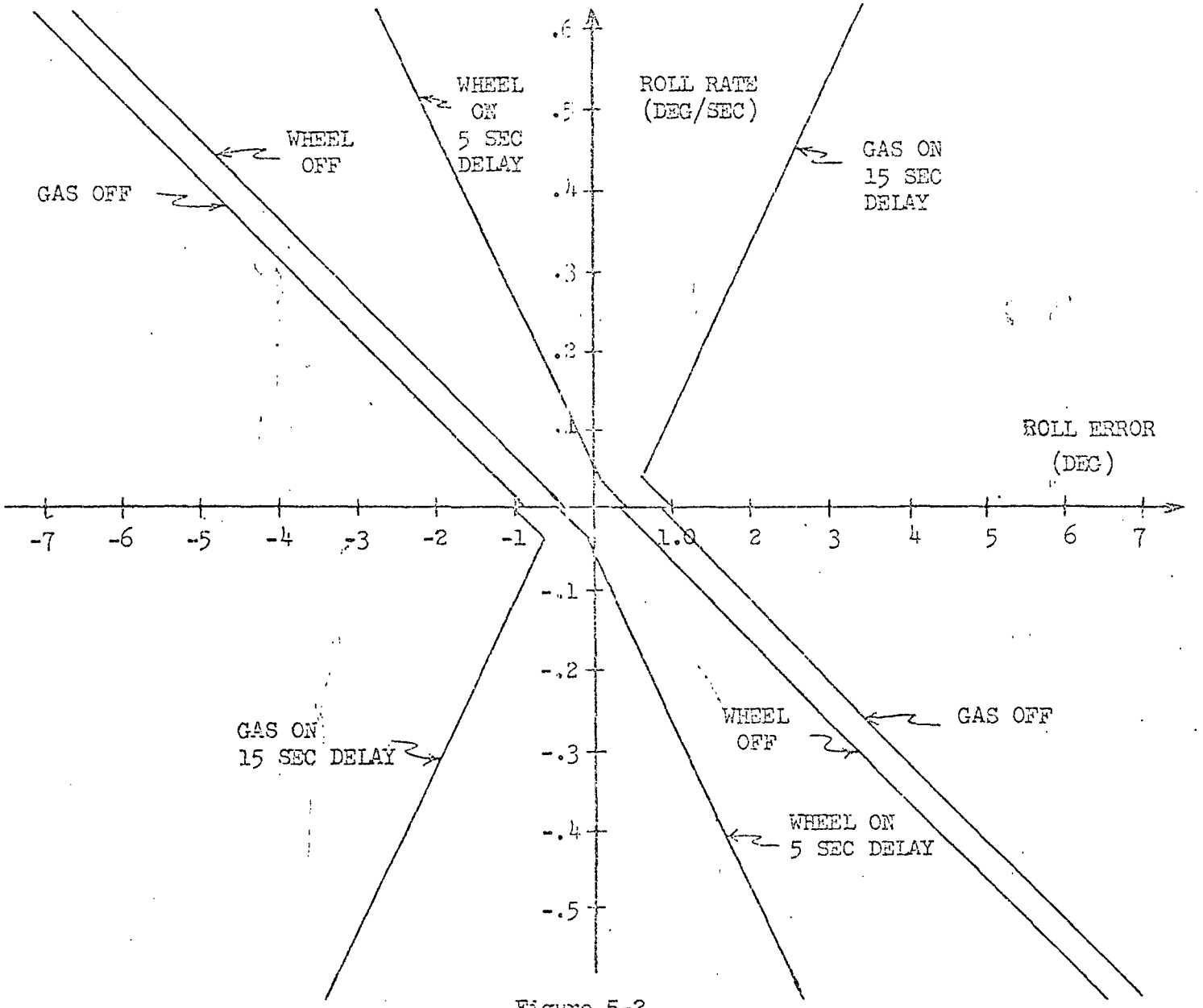

Figure 5-2
Roll ACS Mode III Switching Lines

5.2 ANALYSIS OF PITCH AND YAW STABILITY

Analyses were also made of the pitch and yaw control channels to determine if potential bending stability problems could exist in these channels. These analyses are documented in References 5-4 and 5-5. The results of these analyses are summarized in the following paragraphs.

5.2.1 Definition of Margins

The degree of stability is quantitatively measured by the control loop's margins. These margins are obtained by measuring the separation of the open loop frequency response T(s) from the describing function plot of $1/G(x)$ at the bending mode frequencies (for definitions see Section 4.4). An intersection of T(s) and $[1/G(x)]$ predicts limit cycle oscillations. The control loop's gain margin is defined as the increase in system's open loop gain required to achieve an intersection between T(s) and $1/G(x)$ at bending mode frequencies. Similarly, the control loop's phase margin is defined as the additional phase lag required to achieve an intersection between T(s) and $1/G(x)$ at bending mode frequencies.

5.2.2 System Dynamics

System dynamic equations for roll, yaw, and pitch are derived in Appendix A. Figure 2-1 showed the major flexible appendages which include the EP-5 and EP-6 booms, Haddock antennae and solar panels. The model assumes that each solar array has a De Havilland type boom attached (OGO E configuration) and that the "+x" and "-x" solar array boom combinations are identical. The OGO-D has a Haddock antenna only on the "-x" side but the assumed model is a worst case. Under this condition, the flexible dynamics of the solar array and Haddock booms may be modeled as one solar array-boom combination with a moment of inertia, spring and damping constant equal to twice that of a separate model for each side.

The dynamic model is modified depending upon the axis under consideration as defined below.

Roll - Torsional rotation of the solar array is neglected so the rigid body inertia I_B includes not only the OGO main box but the solar arrays and Haddock booms. Only experimental booms EP-5 and EP-6 are modeled as appendages in rotations about the roll axis.

Pitch - Neglecting cross-coupling, the booms EP-5 and EP-6 are considered as part of the rigid body interia I_B and only the solar array and Haddock booms are modeled as appendages.

Yaw - Experiment booms EP-5 and EP-6, solar array, and Haddock booms are modeled as appendages.

The parameter values are tabulated in Table A-1. The resonant frequencies, ω_1, ω_2 and ω_4 of EP-5, EP-6 and Haddock booms are accurately known from the boom's bending characterisitcs. The maximum structural damping of 0.3% used for EP-5 and EP-6 is that required to duplicate OGO-III flight data (see Section 4.6). The other values of resonant frequency and damping detailed in Table A-1 were preliminary estimates pending further bending model analysis.

The appropriate shaping filter and dither filter for each ACS channel during each mode is summarized in Appendix D. Nonidealities such as phase shifts at bending frequencies in the ACS amplifiers, bistables, and the like have not been considered in this analysis.

5.2.3 Stability Analysis Results

The ACS yaw channel open loop frequency response is the same for both acquisition and Mode III and is shown in Figure 5-3 for 0.3% damping of EP-5 and EP-6. The pneumatic control loop, operative only during acquisition, is seen to have 22° phase margin and 14 db gain margin. Again the stability is attributed primarily to the absence of the dither filter.

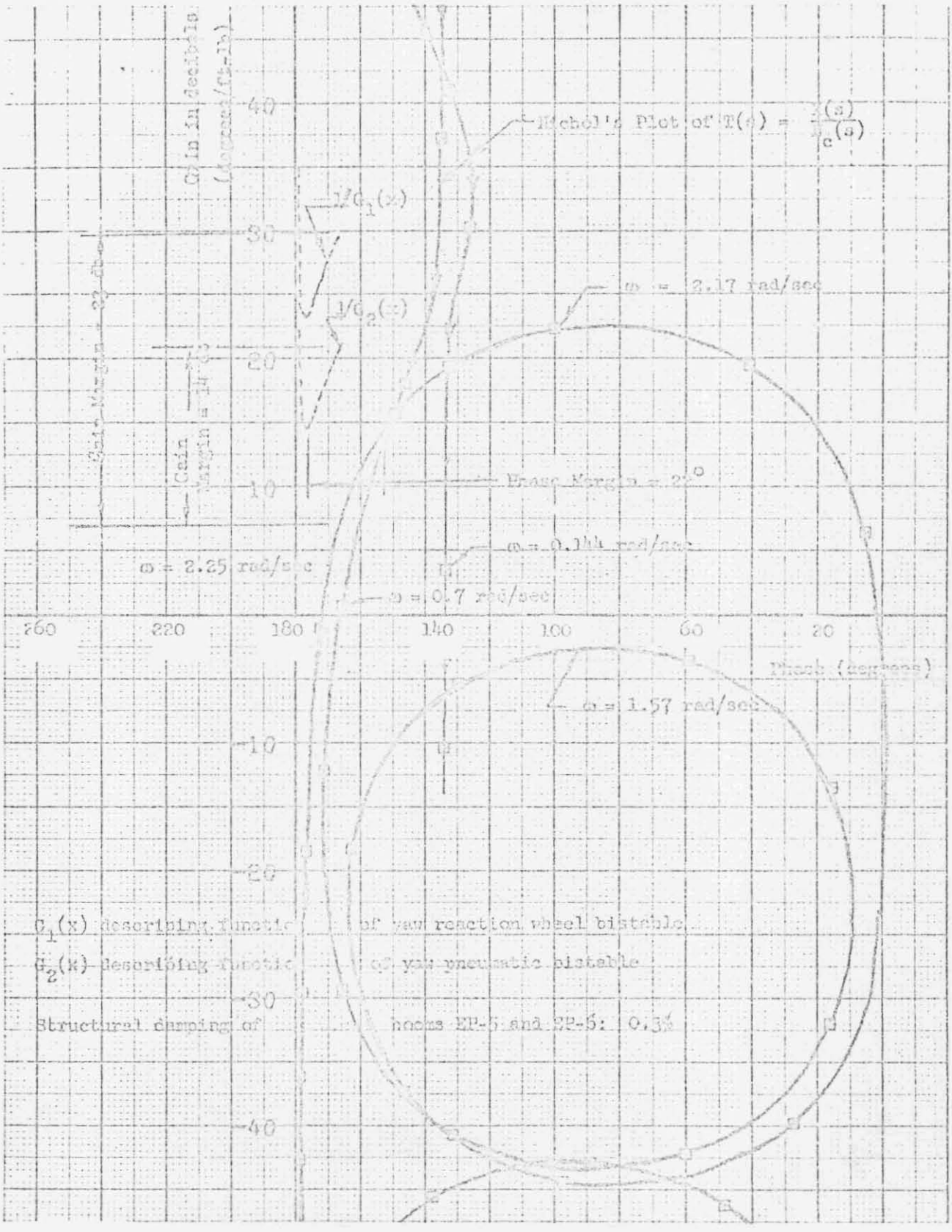

$G_1(x)$ describing function of yaw reaction wheel bistable

$G_2(x)$ describing function of yaw pneumatic bistable

Structural damping of hooks EP-5 and EP-6: 0.3%

Figure 5-3
Open Loop Frequency Response Gain-Phase Plot of Yaw ACS Channel

The pitch channel open loop frequency response is shown during normal mode in Figure 5-4. The experimental booms EP-5 and EP-6 are modeled as a part of the OGO main box, hence the only system resonance is at the natural frequency of the Haddock booms (0.023 Hz) and the solar arrays (5 Hz)*. It is seen that there is little likelihood of intersection of either of these bending modes with the describing function (1/G(x) for the assumed damping and resonant frequencies (see TableA-1). The phase margin is infinite and the gain margin, defined with respect to the solar array resonance, is 120 db.

The gain and phase margins as a function of structural damping of experimental booms EP-5 and EP-6 are summarized in Table 5-1 for the roll, yaw, and pitch ACS channels during acquisition and normal mode operation.

The results indicate that adequate margins exist in the pitch so that no changes are necessary.

The yaw axis wheel margins are adequate (30° phase margin and 8 db gain margin is good design practice) for EP-5 and EP 6 boom damping greater than 0.1%. Thus based upon this analysis a yaw wheel inhibit does not appear necessary. However, a decision was made at NASA's urging to include a yaw wheel inhibit to preclude any possibility of sustained oscillations.

On the other hand the yaw pneumatic system phase margin is small. It was, therefore, recommended that the pneumatic system deadzone be raised from 2.5 to 5.0 degrees. This increases the yaw gas phase margin to 52 degrees at 0.3% boom damping.

---

*The stability analyses were performed before completion of the array bending mode study (Reference 2-4). Later analog studies which considered the lower bending frequency (1.76 Hz) verified the conclusions of this section.

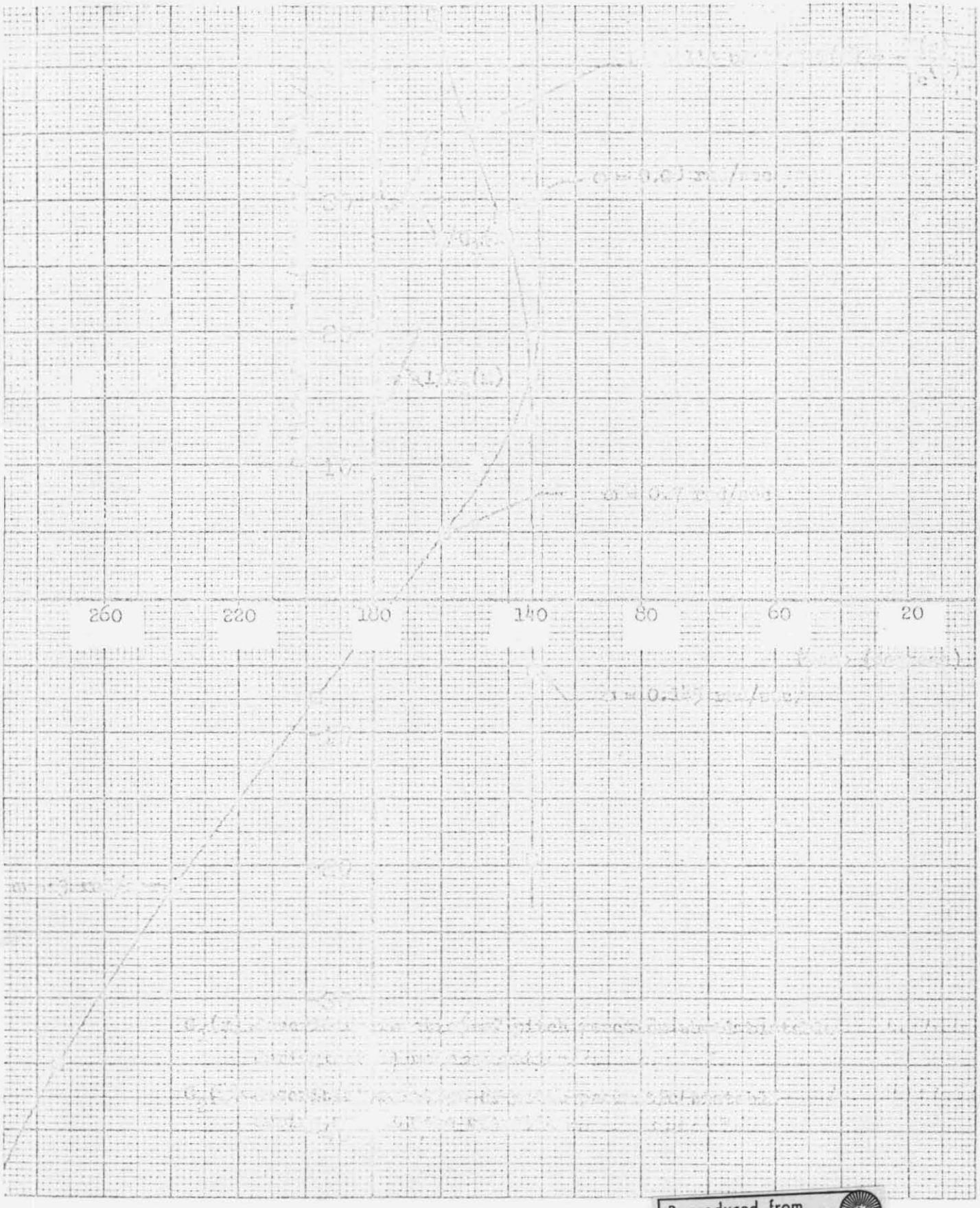

Figure 5-4
Open Loop Frequency Response Gain-Phase Plot of ACS Pitch Channel

Roll wheel and pneumatic inhibit logics have already been proposed to prevent roll oscillations during normal mode. Margins during acquisition are adequate.

5.3 SOLAR ARRAY DRIVE CHANGES

As stated earlier, it was believed the solar array drive initially excited the boom oscillation. Moreover, at times during the flight of OGO-III the solar array drive participated in the oscillation by limit cycling back and forth in sympathy with the boom oscillations.

The solar array drive system is an on-off control system so that in order for the solar array to remain pointed at the sun as the spacecraft rotates in orbit, error corrections are made in a step wise fashion. It is this "cogging" motion of the array which excites the booms. It would be difficult, without gross changes to the array drive, to eliminate this source of boom excitation.

A study was made of possible modifications to the solar array drive system, which would prevent its participation (i.e., the limit cycling) in the boom oscillation (Reference 5-6). In that study filtering of the error signal and the addition of stabilizing feedback loops were recommended. However, again due to a desire for reliable hardware design the delay scheme identical to the one used in roll wheel channel was finally selected. The delay will be commandable both on and off independent of the ACS Mode.

Another change made as a result of the analog study discussed in Section 6.1 was the increase of the solar array drive deadzone from 0.5 to 0.9 deg. The reasons for the change are discussed more fully in Section 6.1.3.1.1.

Finally, since there was evidence of backlash in the OGO-III drive and measurements indicated sizeable backlash in the OGO-E dirve assembly, mechanical changes were made to the drive to reduce the backlash. One change was to firmly attach the output drive gear to the

Table 5-1 - OGO ACS Bending Stability Margins

	Structural Damping of Experimental Booms EP-5 and EP-6							
	0.3%		0.2%		0.1%		0.05%	
	Phase Margin (degrees)	Gain Margin (db)	Phase Margin (degrees)	Gain Margin (db)	Phase Margin (degrees)	Gain Margin (db)	Phase Margin (degrees)	Gain Margin (db)
Roll - Acquisition								
Reaction Wheels		33	75	31	37	29	24	30
Pneumatics	41	33	30	33	21	32	17	31
Roll - Normal Mode								
Reaction Wheels	Limit Cycle Possible							
Pneumatics	Limit Cycle Possible							
Yaw - Acquisition								
Reaction Wheel		23	46	20	22	14	12	9
Pneumatics								
2.5 deg deadzone	22	14	16	11	8	10	Limit Cycle Possible	
5.0 deg deadzone	52	20	32	18	16	12	9	6
Yaw - Normal Mode								
Reaction Wheels		23	46	20	22	14	12	9
Pitch - Normal Mode	EP-5 and EP-6 Modeled as Rigid Body (see Section 3.3)							
Pneumatics	112 db							
Reaction Wheels	120 db							

shaft replacing a key which was subject to wear. The second was an alteration in the array hinge design to reduce its backlash. The overall array system backlash was predicted to be less than 0.4 deg as a result of these design changes.

5.4 OPEP DESIGN CHANGES

The OPEP was also observed to limit cycle in sympathy with boom oscillations because the OPEP gyrocompass sensed the roll motion. Since it was apparent that the boom motion could not be entirely eliminated, a filter was devised to smooth the bending signal from the OPEP error. The detailed analyses of the design change is presented in Reference 5-7. The paragraphs which follow briefly describe the design process. Figure 5-5 is a simplified block diagram of the OPEP control loop. A detailed discussion of the model appears in Appendix C.

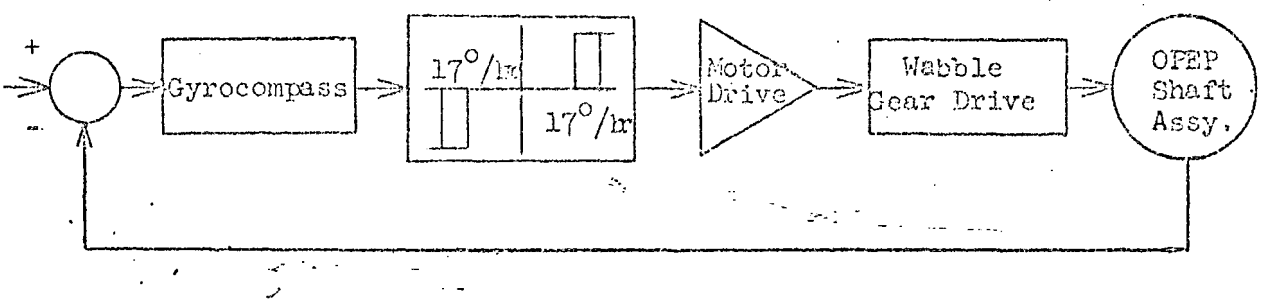

Figure 5-5, Simplified OPEP Block Diagram

With the inhibit logic in the roll reaction wheel, it was assumed that the largest magnitude of body roll rate would be one-half of the value observed for OGO-III when the reaction wheel was limit cycling (i.e. 1/2 of ± 0.1 deg). For the worst case where the OPEP gyro input axis is aligned with the spacecraft roll axis, the gyro would simply sense roll rate.

$\dot{\phi}$ = roll rate = .125 sin ωt deg/sec

and ω = oscillation frequency of the roll body motion,
2.5 rad/sec

The OPEP control problem can now be easily formulated. It was desired to redesign the system such that this disturbance would not result in a sustained OPEP oscillation. The simplest method is to low-pass filter the gyro output. However, because of the large phase lag introduced by simple lag filters, the stability of the control system becomes a major factor in the design.

5.4.1 OPEP Filter Design

Because of realizability and hardware limitations, the filter was selected to attenuate the roll rate to about one-half the deadzone at the frequency of interest. The chosen filter has a transfer function of

$$\frac{1}{1 + 20\ s}$$

To study the effect of adding the lag filter to the unmodified OPEP configuration, a closed loop stability analysis was made.

Figure 5-6 illustrates the control system which was analyzed and shows the describing function stability analysis. The stability analysis is represented on the gain (db) versus phase (deg) plot. Limit cycle operation will exist if

$$HG\ (j\omega) = -\frac{1}{K_D K_M}\quad \frac{1}{N(x)} \qquad (6)$$

However, with the filter inserted, stability margins are greatly reduced. In fact, for the orbital rate corresponding to the EGO Orbit, the OPEP control system could limit cycle. As indicated by Figure 5-6 no limit cycle exists for the unmodified OPEP configuration and there are ample gain and phase margins to insure stability with

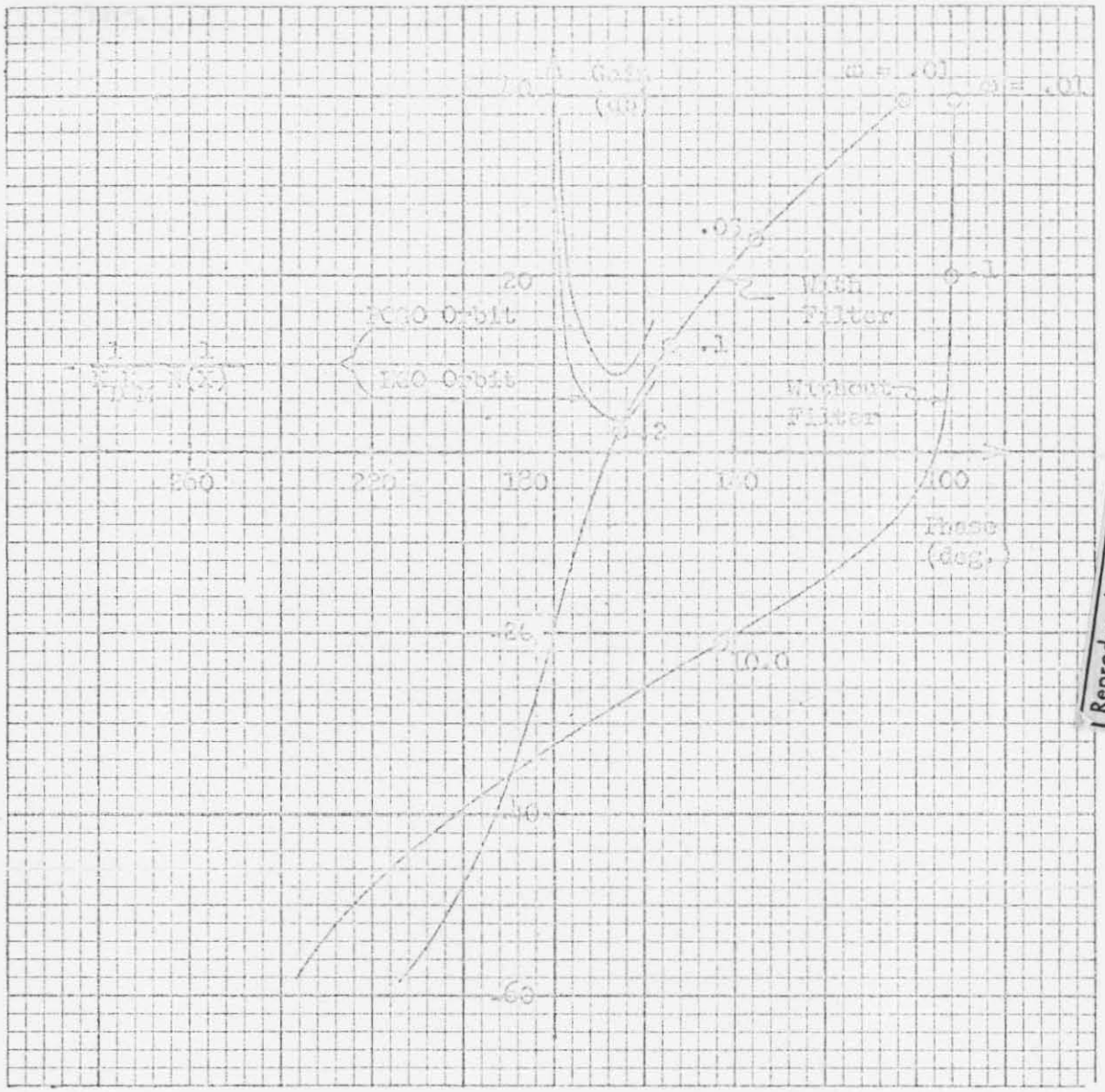

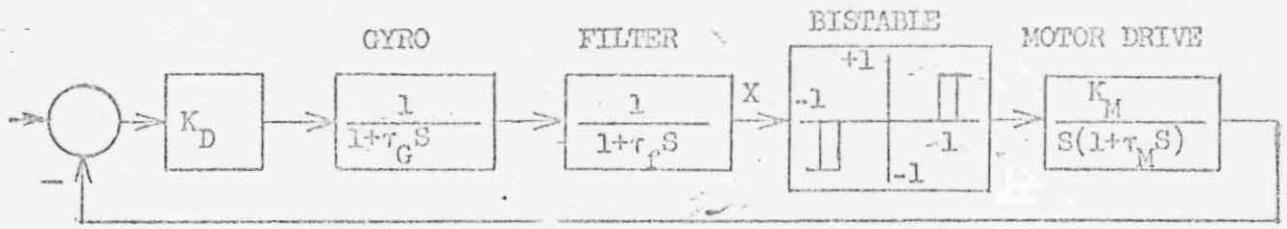

Control Loop Analyzed

No Filter - $HG(s) = \frac{1}{S(1+\tau_M S)(1+\tau_G S)}$

With Filter - $HG(s) = \frac{1}{S(1+\tau_M S)(1+\tau_G S)(1+\tau_f S)}$

Describing Function for Bistable = N (X)

Figure 5-6 OPEP Describing Function Stability Analysis

variations in the control system parameters.

To stabilize the OPEP control loop merely required the addition of a feedback path from the bistable switch output to the filter input. This control loop is shown in Figure 5-7. The feedback can be considered form of rate feedback. That is, when the drive motor is turned on the OPEP shaft drives at nearly constant rate. Therefore, the bistable output voltage is in a sense proportional to the OPEP rate. The analysis in Appendix C shows how the feedback provides stability, and the necessary parameter limits for stability.

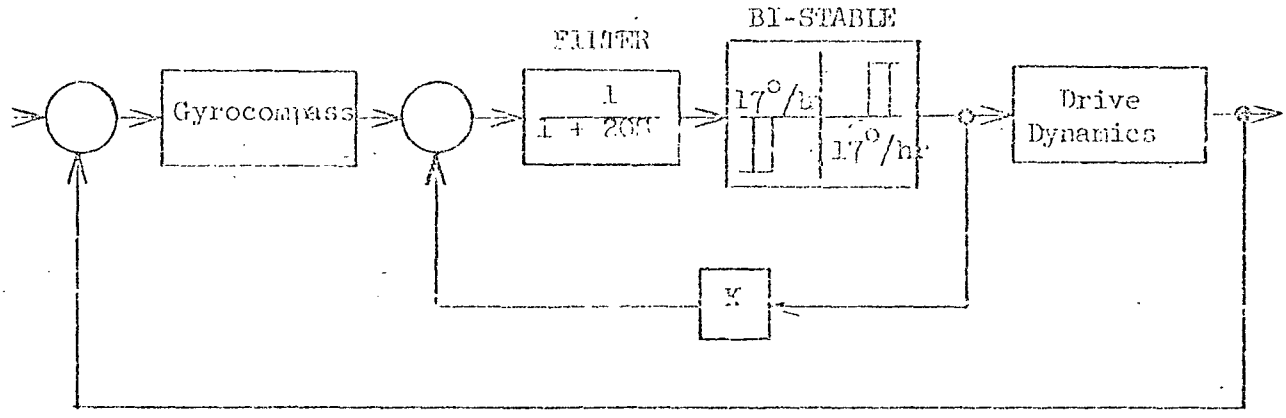

Figure 5-7, New OPEP Control Loop

Another method of looking at the loop stability is to note that the addition of the feedback-loop and lag filter forms a pulse modulator. If a constant error input is applied from the gyrocompass the drive motor is turned on in a pulsed fashion. This design is in fact the pulse ratio modulator discussed by Schaefer in Reference 5-8.

For stability the minimum on time of the modulator must be such that the motor does not drive the OPEP through the deadzone. Therefore, the feedback gain K was selected as a result of the following arguments. The OPEP drives at a nearly constant rate of 1.6 deg/sec when turned on. The minimum deadzone occurs for an EGO orbit and is

± 3.0 deg. Therefore, a gain K, which produced a minimum on time of 2 seconds, was selected. This results in a minimum OPEP motion of 3.2 deg.

The implementation of the modulator design proved relatively simple so that this modification was selected for the OPEP. The implementation aspects are discussed more fully in Reference 5-7.

5.5 INCREASE OF GAS DELAY TIME CONSTANT

In reference 6-4 an analysis was made of the gas consumption caused by the sun passing through the scanner field of view as the spacecraft completes a post eclipse turn. The problem arises because following eclipse the sun is near the horizon. As the spacecraft reorients to point the -y axis at the sun, the sun may pass through the field of view of the B or D scanner. This causes a jump in the scanner track point which can fire gas. It was found, however, that if the gas delay time constant was 15 instead of 12 seconds that virtually all gas consumption from this source was eliminated. Therefore on all future spacecraft the gas delay times constant was increased from a nominal value of 12 to 15 seconds. This change was incorporated in all the simulation studies reported in the section which follows.

REFERENCES:

5-1 66.7231.1-86, "OGO Boom Damper Design," t. R. Bierma, 30 November 1966.

5-2 66.3522.1-16, "OGO-Boom Damping Study," W. D. Brayton, D. B. Longcope, 1 September 1966.

5-3 7220.8-1 "OGO Roll Wheel Limits Cycle -- Results of Root Locus Analysis," M. J. Abzug, 11 November 1966.

5-4 66.7231.1-81, "Effect of OGO Appendage Oscillations Upon Attitude Control System Performance, " T. R. Bierma, 7 November 1966.

5-5 66.7231.1-82, "OGO Wheel Inhibit Requirements," K. J. McKenna, 18 November 1966.

5-6 66.7231.8-121, "Analysis and Test Results of the OGO Solar Array Drive Assembly Study," L. C. George, 10 November 1966.

5-7 67.7231.7-23, "Analysis and Test Results of the OGO OPEP Control System Study," L. C. George, M. Levenson, 26 January 1967.

5-8 "Pulse Ratio Modulation for Attitude Control," R. A. Schaefer, Space Aeronautics p 90-93, May 1963.

6.0 ACS PERFORMANCE VERIFICATION

Before the changes to the ACS discussed in the previous section were selected, analytical and analog computer simulation studies were made to establish feasibility. Due to the schedule pressure, however, a complete study of performance and stability was not possible. Therefore, extensive analog simulation studies were developed to thoroughly evaluate the design changes once they were chosen.

One simulation study examined the single axis small angle performance. Each control loop (i.e. pitch, roll and yaw) in both Mode II and Mode III configurations was examined. The significant flexible appendage dynamics affecting each axis were simulated. The simulation detail and results are discussed in Section 6.1. Simulation plans and other details are given in References 6-1 and 6-2.

The second simulation was a large angle rigid body study. Here the effects of the ACS changes on earth and sun acquisition were evaluated. These results are discussed in Section 6.2 and Reference 6-3.

6.1 SMALL ANGLE SIMULATION STUDY

6.1.1 Purpose

The purpose of the single axis analog simulations was to determine the ACS performance with the design changes and to verify the system stability. To review briefly the salient changes were the following:

1) Solar Array - The solar array deadzone was increased to 0.9^{o} nominal and a reversal delay logic circuit was added.

2) Roll Channel - A reaction wheel reversal delay logic was added and the gas delay logic time constant was increased from 12 to 15 seconds.

3) Yaw Axis - A reaction wheel reversal delay logic was added for the normal mode (Mode III), and the gas deadzone was increased from 2.5 to 5 degrees nominal for sun acquisition (Mode II b,c).

4) Pitch Axis - The gas delay logic time constant was increased from 12 to 15 seconds.

5) OPEP - Control logic was modified to a pulse ratio modulator.

The stability analysis discussed in Section 5.2 indicated that adequate margins existed in the flexible body stability margins. These analyses did not consider the effect of the inhibit logic nor variation in system parameters; the analog simulations, therefore, provided a more complete check of the stability of each control channel.

6.1.2 Description of Approach

6.1.2.1 Roll Axis Normal Mode (Mode III)

A majority of the simulation effort was directed to the roll channel during normal mode because most of the changes were made to the roll and array channels. The normal mode simulation was broken down into the subsections which follow.

6.1.2.1.1 Solar Array

To evaluate the effects of the changes on the solar array loop, the solar array loop was initially isolated from the rest of the roll control system. The solar array loop (see Appendix B) was comprised of the following: sun sensor, solar array bistable, inhibit, logic, motor drive and array dynamics. The response of the solar array to attitude errors with nominal and "worst-on-worst" cases parameters was determined. The component parameter values were selected for two "worst-on-worst" groupings to provide the most sluggish and most oscillatory responses. The most oscillatory grouping was defined as that which produced the maximum coasting of the solar array drive after the bistable was commanded "off". The most oscillatory grouping was comprised of the following:

a) Bistable - Minimum deadzone and maximum hysteresis.

b) Motor - Maximum inertia, stall torque and no load speed; Minimum coulomb friction and damping; maximum lag between time motor is commanded off and time motor turns off.

c) Solar Array - Maximum inertia and minimum coulomb friction.

d) Stiffness of Hinge between Paddle and Motor Output Shaft - Minimum

6.1.2.1.2 Nominal Roll System

Several checks were made on the nominal roll system design to verify stability and determine control system performance with the reaction wheel inhibit logic. To verify the wheels would capture with the inhibit logic, the nominal roll system was subjected to initial rates and attitude errors between -5° and $+5^{\circ}$ in 1° increments and rates between 0 and $.5^{\circ}$/sec in $.1^{\circ}$ sec increements. To evaluate the effect of solar array on boom motion and control system performance, the solar array was driven at orbit rates from $.025^{\circ}$/sec, and $.1^{\circ}$ sec (maximum EGO value). Boom damping was varied between 0.0625% and .25%.

In order to provide an indication of the margin of safety if a failure occurred, the nominal system was subjected to the following failures.

a) One side of reaction wheel bistable fails "open."

b) Gas inhibits and reaction wheel inhibits fail but can be bypassed.

In the latter case a gas limit cycle can occur depending on orbital rate and boom damping. That is the frequency of solar array cogging and the amount of boom damping will determine the induced boom oscillation amplitude. The boom damping was adjusted until a gas limit cycle was barely induced for orbital rates between 0.025°/sec and $.1^{\circ}$/sec. To determine the effect of the reaction wheel inhibit, the procedure was conducted with and without reaction wheel inhibit.

With the gas inhibit bypassed, regions of initial conditions which would start a gas limit cycle were determined. Here the combined excitation of gas firing, and solar array motion could be enough to excite the booms to the point of starting a gas limit cycle. The system was checked with and without a reaction wheel inhibit. The range of initial attitude errors and rates was from -5 to $+5^{\circ}$ and 0 to 0.5°/sec.

To provide an indication of the relative effects of parameter variations on the stability and response of the roll system yet avoid an exhaustive number of computer runs, the parameter variations were divided into the four groups of Table 6-1. The parameters changes in each group were selected to provide two "worst-on-worst" sets: the most destabilizing and the most sluggish. The direction of the parameter change for the most destabilizing condition is also indicated in Table 6-1. The tolerances considered for all the parameters are given in Appendix D.

With all parameters nominal except for one group, the response was evaluated to a given set of initial conditions. The procedure was repeated for all the groups. The groups were arranged in order of relative parameter sensitivity by using the time to termination of last gas pulse as a criterion.

To illustrate the overall system stability with worst-on-worst parameter stack-up, combinations of the groups were selected and subjected to the same initial conditions previously used.

Table 6-1

Parameter Variation Grouping

Group	Items in Group and Condition for Most Destabilizing Effect ( )
Gas	Gas Deadzone (minimum), Hysteresis (maximum), Gas Torque (maximum), Gas Inhibit Logic Time Constant (maximum)
Reaction Wheel	Wheel Deadzone (minimum), Hysteresis (maximum), Wheel Motor Torque (maximum) and Friction (minimum), Wheel Inhibit Logic Time Constant (maximum)
Control Law	Filter Time Constants (maximum), Lead-Lag Ratio (minimum), Total Inertia (minimum)
Boom	Boom Inertia (maximum), Frequency (minimum), Damping (minimum)

6.1.2.1.4 Gas Consumption During Post Eclipse Turn Sun Interference

The error signal shown in Figure 6-1 was used to: (1) reproduce the results of gas firing studies reported in Reference 6-4, and (2) determine the effects of the wheel inhibit logic on the results. Since in Reference 6-3, no solar array coupling onto the main body was simulated, the solar array coupling was omitted for consistency.

6.1.2.2 Roll Axis Sun Acquisition Mode (Mode II)

No changes were made to the roll system design for the Mode II configuration. However, a computer study was made to substantiate the stability analysis of Section 5.2.3, illustrate capture capability and provide an indication of stability with "worst-on-worst" parameter stack-up. Computer runs with nominal parameter and a most "destabilizing" stack-up were conducted.

6.1.2.3 Pitch Axis

No changes to the pitch control laws were made in either Mode II or Mode III except for the increase of the gas delay time constants from 12 to 15 seconds. Computer studies were therefore made of only the Mode III control loop. A parameter variation study similar to the roll (normal mode) was conducted. Runs consisted entirely of response to initial attitude and rate errors since no source of boom excitation exists in the pitch axis.

6.1.2.4 Yaw Sun Acquisition (Mode II)

The only change made to the yaw control system for Mode III was to increase the gas deadzone from 2.5 to 5.0 degrees. Thus, the questions of primary interest were the ability of the reaction wheels to capture and the stability of the flexible body modes. Again runs consisted exclusively of response to initial attitude and rate errors. Parameter variations were conducted in a manner similar to the previous channels.

FIGURE 6-1

Roll Error Signal Disturbance Due to B or D

- Scanner Head Sun Interference

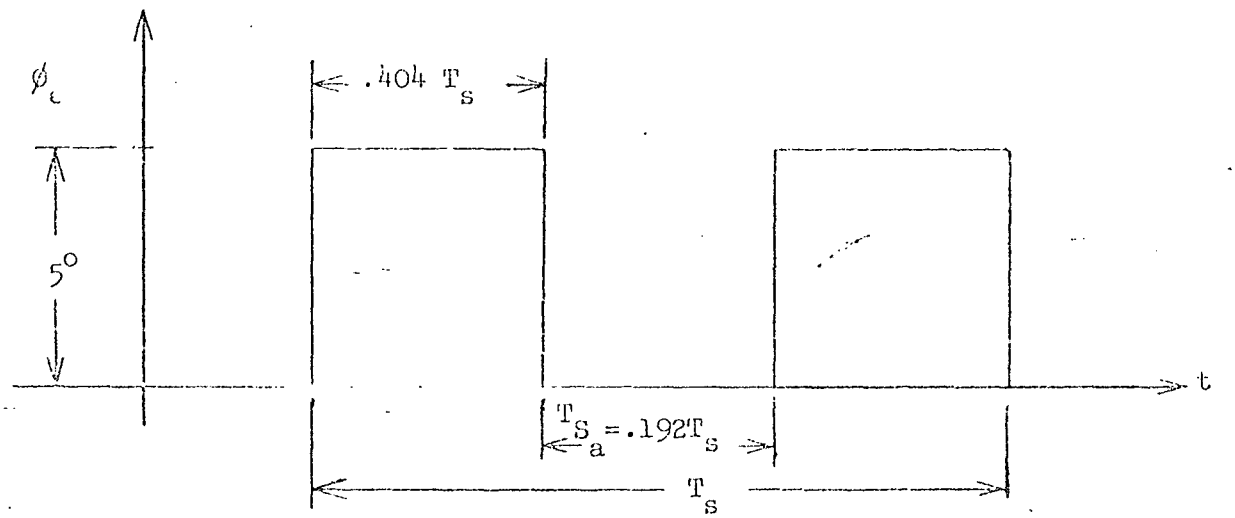

$10.9 \leq T_s \leq 21.4$ sec

6.1.2.5 Yaw Normal Mode (Mode III)

The wheel inhibit logic was the only change to the yaw normal mode control loop. The yaw loop performance was therefore, evaluated with and without the inhibit activated. Again since no source of boom excitation exists in the yaw channel runs consisted entirely of response to initial errors. The major difference was that the Haddock antennae comprise a new group and no gas grouping was used.

6.1.2.6 OPEP Simulations

The performance of the modified OPEP control system was also evaluated on the analog computer. The primary objective was to verify that the system will operate satisfactorily for worst case parameter variations, partial failure of the pulse ratio modulator and misalignment of the gyro input axis. The steady-state tracking errors of the OPEP control system for various CGO yaw axis turning rates were determined.

6.1.3 Simulation Results

The assumptions, computer models, definitions of nomenclature, and a delineation of parameter variations used in the simulations are provided in Appendix D.

6.1.3.1 Roll Axis - Normal Mode (Mode III)

The roll axis simulation included the effects of EP-5 and EP-6 boom dynamics, the Solar Array and Solar Array Drive Dynamics and all ACS functions including roll wheel, gas and solar array drive inhibits.

6.1.3.1.1 Solar Array Loop

The solar array loop was de-coupled from the rest of the roll system so that the effects of parameter variation upon its stability and response could be studied. The initial set of runs were made with the original 0.5 deg nominal deadzone. The solar array loop parameters

varied such as to produce the most de-stabilizing parameter stack-up presented in Table 6-2. The response of the array drive loop to an initial 0.5 degree error is shown in Figure 6-2. With the de-stabilizing parameters a limit cycle occurred in the solar array loop. To determine if the spring stiffness (K_s) or the backlash (ϕ_b) were the primary causes of the oscillation, a rigid body representation eliminating K_s and ϕ_b was constructed. The "rigid body" solar array was still unstable as illustrated in Figure 6-2B. The analysis in Appendix D demonstrates that with the "worst-on-worst" parameters the motor coasts across the 0.5 deg deadzone thus producing a limit cycle. Therefore, the solar array deadzone was increased to $0.9 \pm .1$ deg. With nominal parameters, the solar array loop response was satisfactory as shown in Figure 6-3A. The solar array loop parameters were changed to the values of Table 6-2 except the solar array bistable parameters were changed as follows:

$$\phi_{dp} = .3^{\circ}$$

$$h_{p1} = .28^{\circ}$$

$$h_{p2} = .15^{\circ}$$

$$h_{p1} + h_{p2} = .43^{\circ}$$

Under these worst-on-worst conditions, a solar array loop limit cycle resulted in Figure 6-3B. As shown in Figures 6-3C and 6-3D, by either setting the stiffness (K_s) to nominal or the paddle inertia (I_p) to nominal, a limit cycle was no longer produced in the solar array loop. Since the probability of all parameters values arranged to produce a worst-on-worst stack-up should be small, the performance of the solar array loop with a $0.9 \pm .1$ degree bistable deadzone was considered satisfactory. Also of interest is the extreme sensitivity of coast angle to parameter variations. The coast angle increased from 0.25° to 1.0° by changing the parameters from nominal.

TABLE 6-2

"Worst-on-Worst" Solar Array Loop Parameters*

Item	Parameter	Value
Solar Array Motor	I_m	66 slug ft^2
	T_s	46.5 ft-lb
	ω_s	1.92^o/sec
	T_{cm}	1.0 ft-lb
	C_m	55 (ft-lb)/(rad/sec)
Solar Array Paddle	$\lvert\phi_b\rvert$	$.2^o$
	K_s	960 ft-lb/rad
	I_p	15.6 slug ft^2
	T_{cp}	1.0 ft-lb
Solar Array	$\lvert\phi_{dp}\rvert$	$.4^o$
	h_{p1}	$.14^o$
	h_{p2}	$.15^o$
	$h_p = h_{p1} + h_{p2}$	$.29^o$

*where nominal deadzone is 0.5 degree

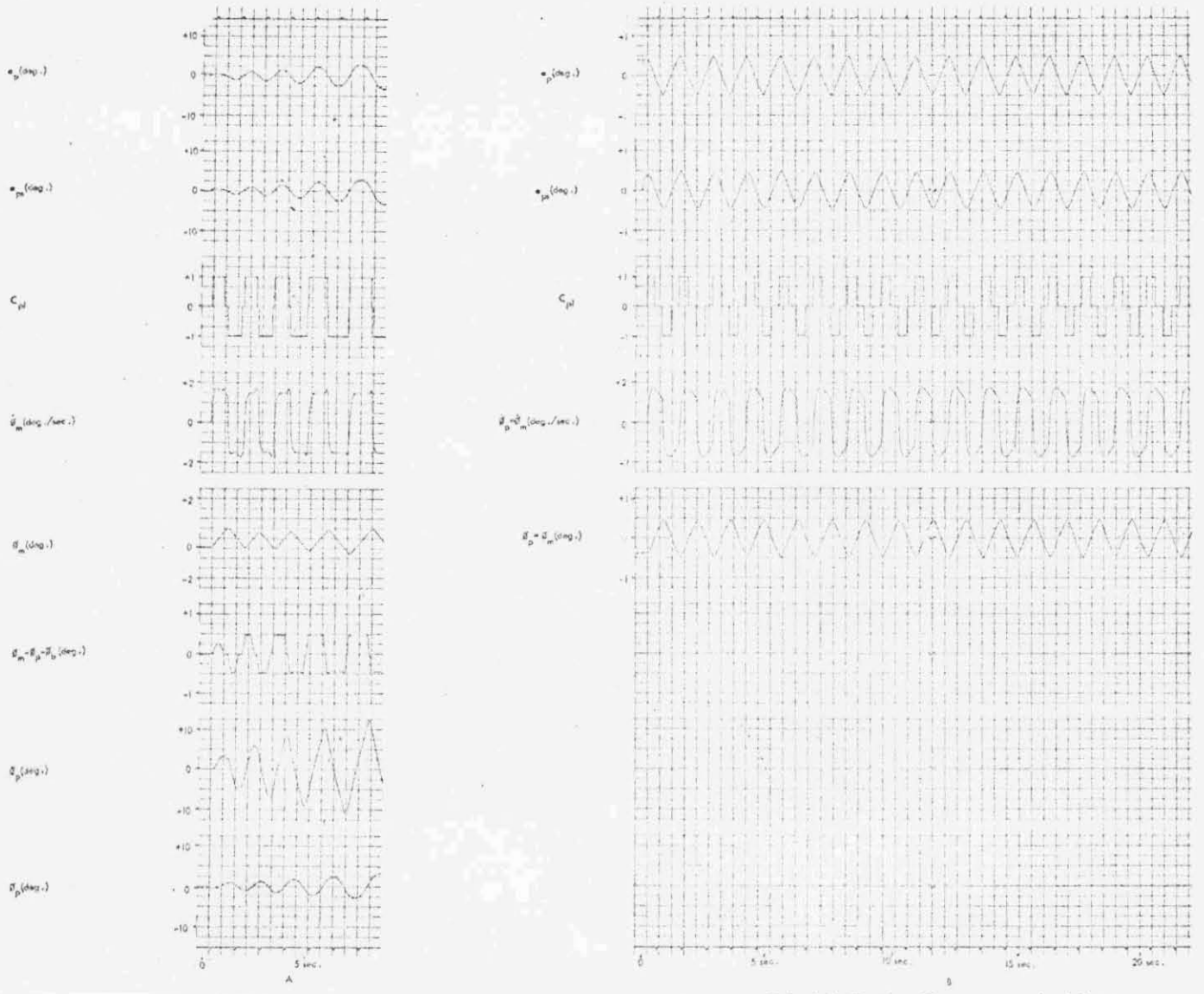

Flexible Array

Rigid Body Representation

Figure 6-2 Solar Array/Response with 0.5± .1 deg deadzone and most destabilizing parameters (Without solar array innibit)

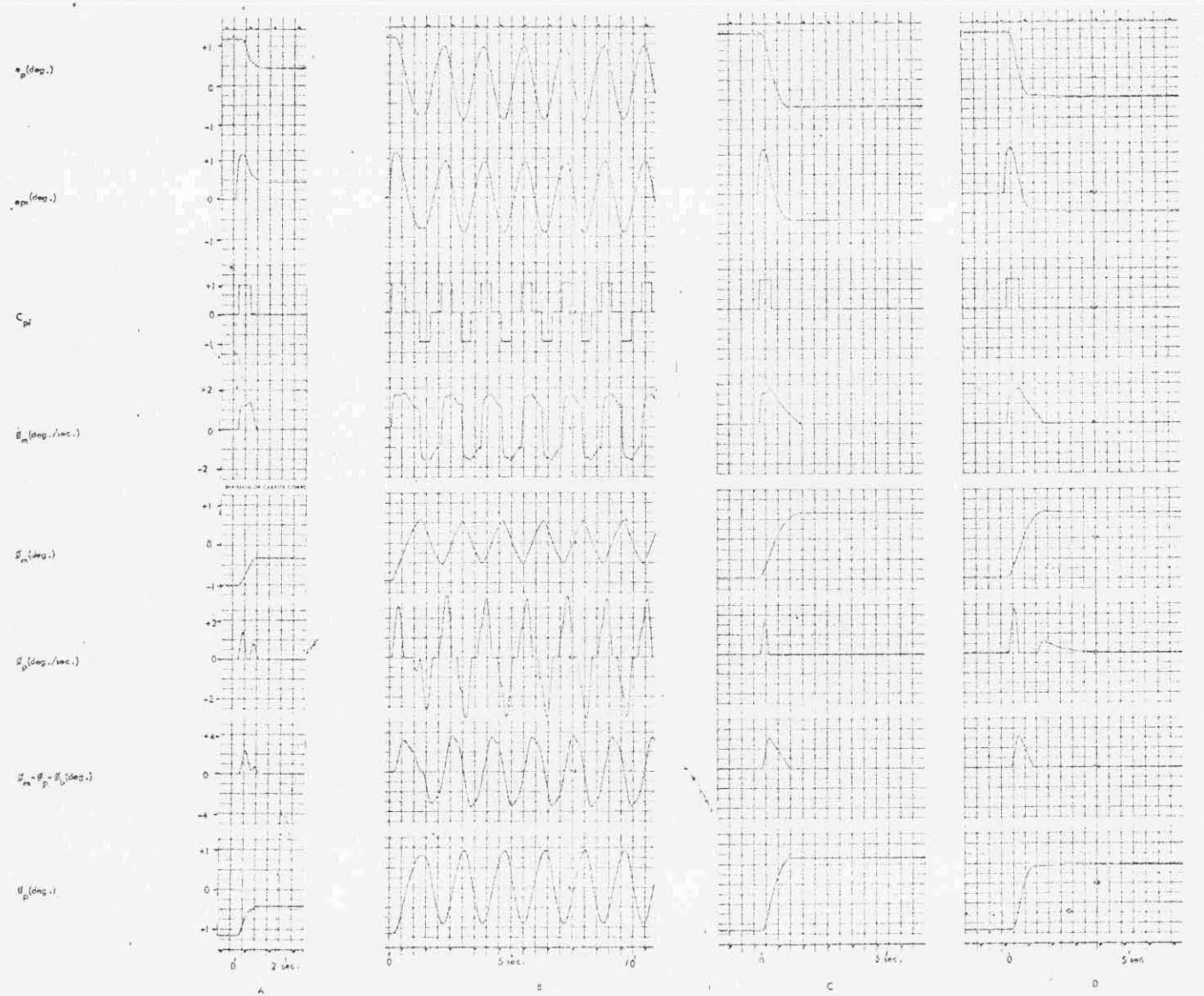

Nominal Parameters

Most Destabilizing Parameters without Solar Array Inhibit

Destabilizing Parameters Except K_s Nominal

Destabilizing Parameters Except I_p Nominal

Figure 6-3 Solar Array Response with 0.9 ± .1 Deg Deadzone

6.1.3.1.2 Nominal Roll System Performance

As outlined previously, the stability of the roll channel with the wheel reversal delay logic was checked by observing the response to initial rate and attitude errors. The initial body attitude, ϕ (0), and the initial body rate, $\dot{\phi}$ (0), were varied with all system parameters nominal. The roll angle was varied between -5° and $+5^{\circ}$ in 1° increments and the rate was varied between 0 and 0.5°/sec in 0.1°/sec increments. The system was stable, i.e. converged to normal reaction wheel control, irrespective of initial conditions within this range.

Figure 6-4 shows the roll response to he maximum attitude and rate error considered; ϕ (0) = 5.0 deg $\dot{\phi}$ (0) = 0.5 deg/sec. The effect of both the wheel and gas delay logic can be seen in the response pattern. The booms are excited by the combined torques produced by the wheel, gas and solar array motion.

The effect of the solar array cogging on boom motion and control system performance was evaluated for various values of boom damping and orbital turning rates. Typical responses are presented in Figures 6-5, 6, 7 and 8.

These runs illustrate a peculiar performance aspect of the wheel delay logic. The runs were purposely made with 1.0 ft-lb-sec initial momentum stored in the roll wheel. Because of windage and friction losses the wheel will tend to run down and impart a disturbance to the spacecraft which causes an attitude error. During normal operation the wheel controller would turn on briefly and bring the wheel back up to speed. The wheel delay logic affects this normal sequence, however. If the booms are excited to the point where the wheel bistables are alternately switched on and off, then the delay logic prevents the wheels from being switched on at all and the wheels continue to run down. The body attitude error will then continue to build up until the error is large enough so that only one bistable is turned on. The delay logic is then inactivated and the wheel will turn on. This effect can be clearly seen in Figure 6-5. In fact when the booms have

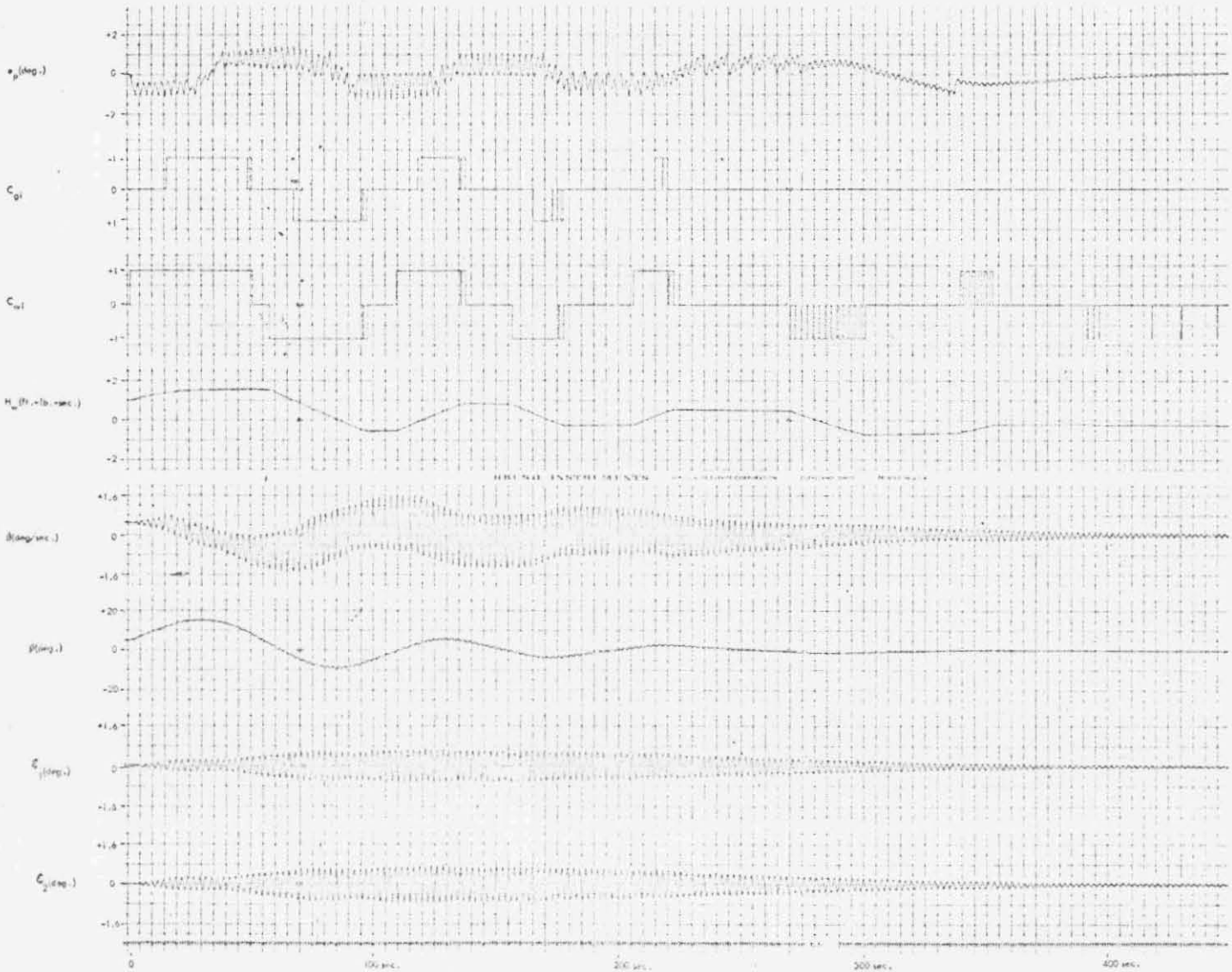

Figure 6-4 Nominal Roll Normal Mode System Response to Initial Body Rate and Attitude Errors

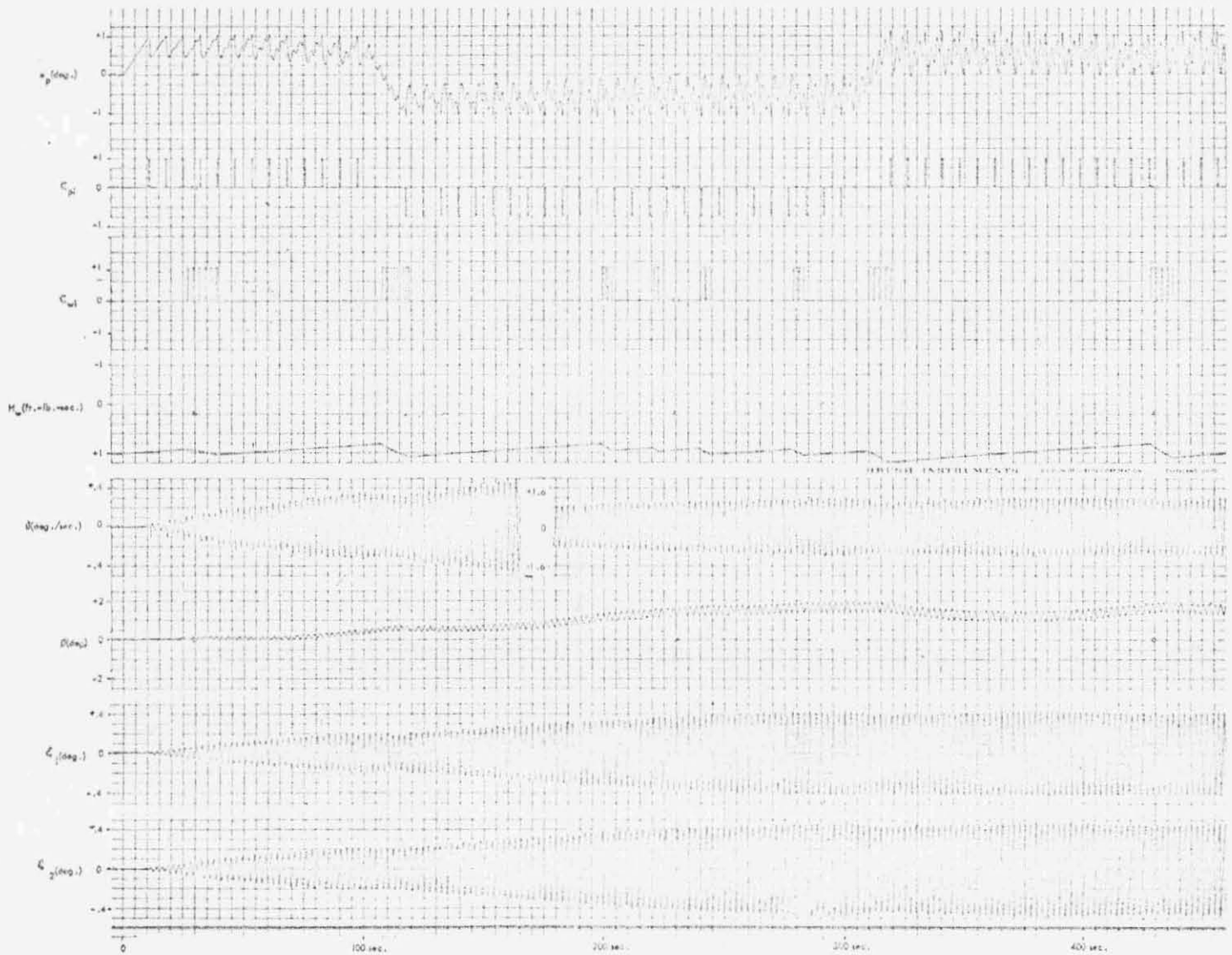

Figure 6-5 Nominal Roll Normal Mode System/Response Boom Damping ($\zeta_1 = \zeta_2$) = .125%; Orbit Rate (ω_o) = .1°/sec

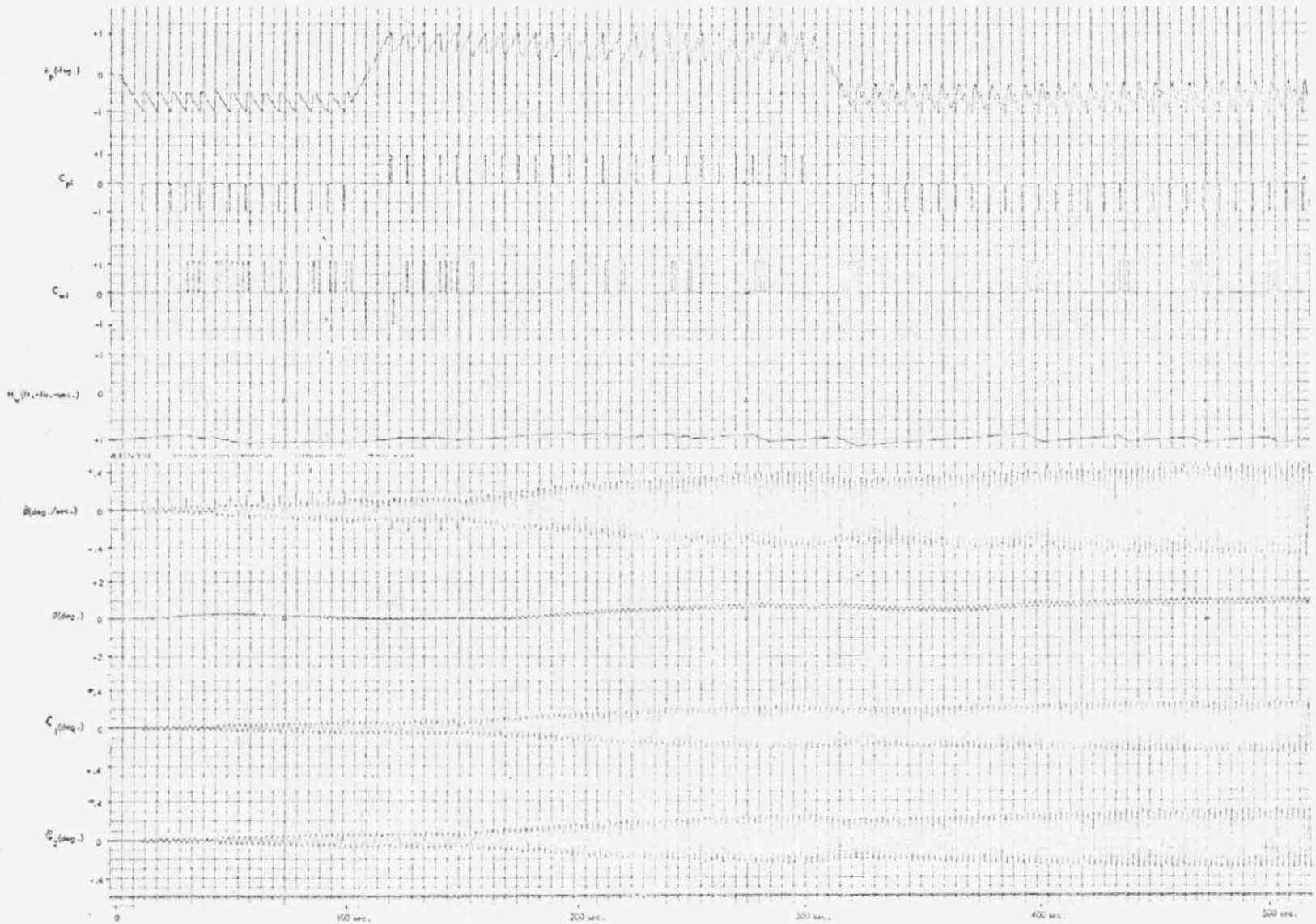

Figure 6-6 Nominal Roll Normal Mode System Response Boom Damping ($\zeta_1 = \zeta_2$) = .25%; Orbit Rate (ω_o) = .1°/sec

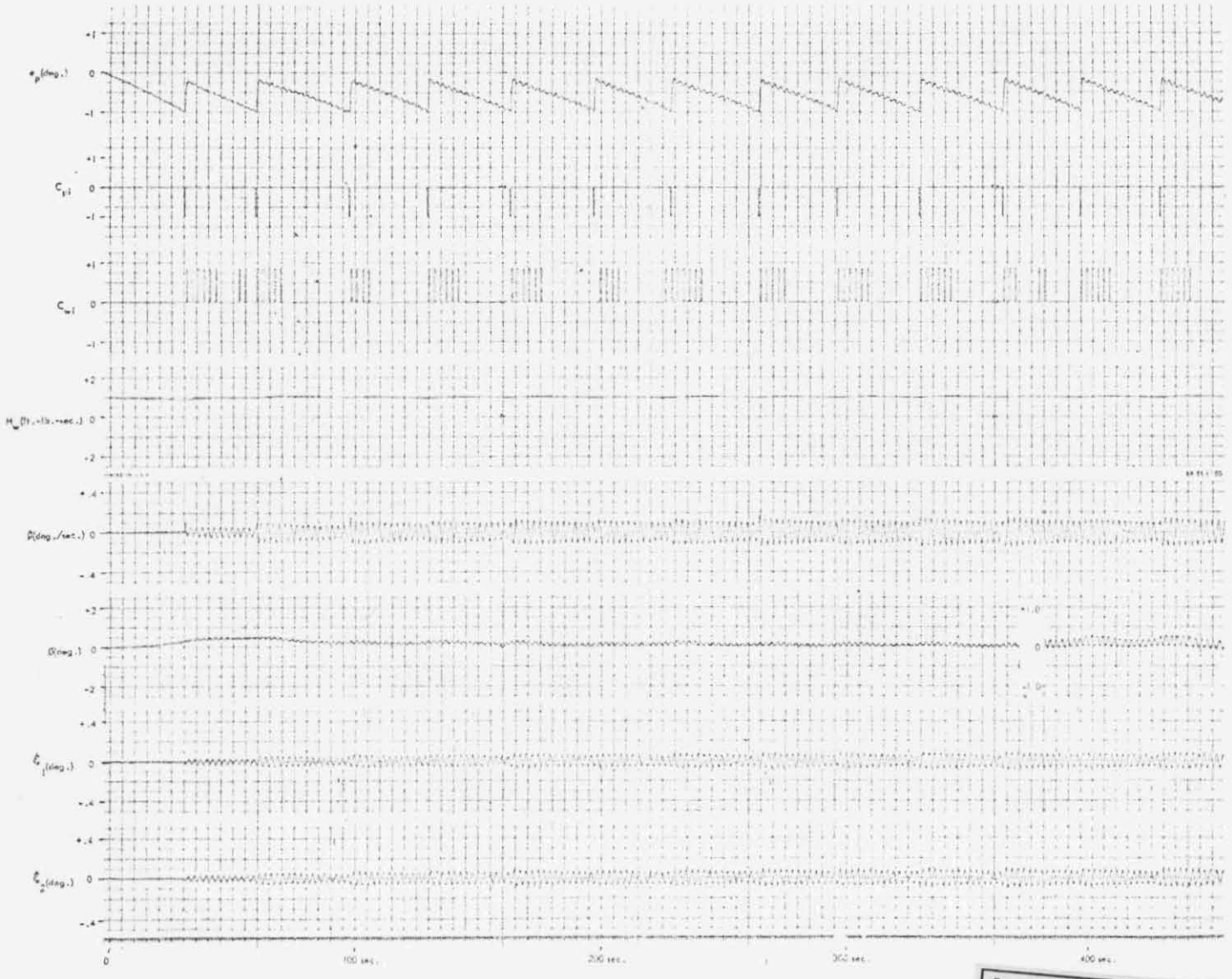

Figure 6-7 Nominal Roll Normal Mode System/Response Boom Damping ($\zeta_1 = \zeta_2$) = .25%; Orbit Rate = .025°/sec

FOLDOUT FRAME

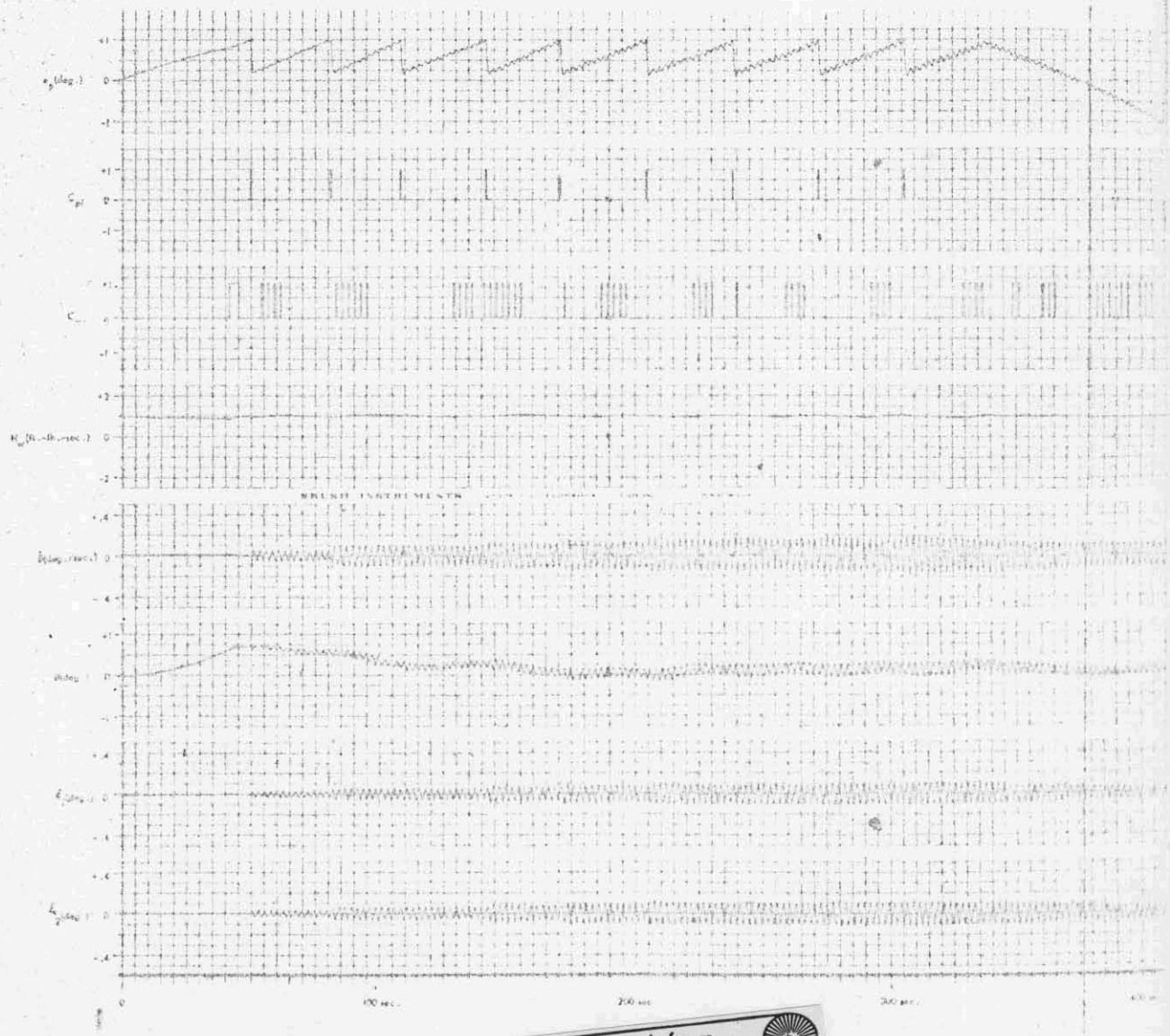

6-12a

FOLDOUT FRAME 2

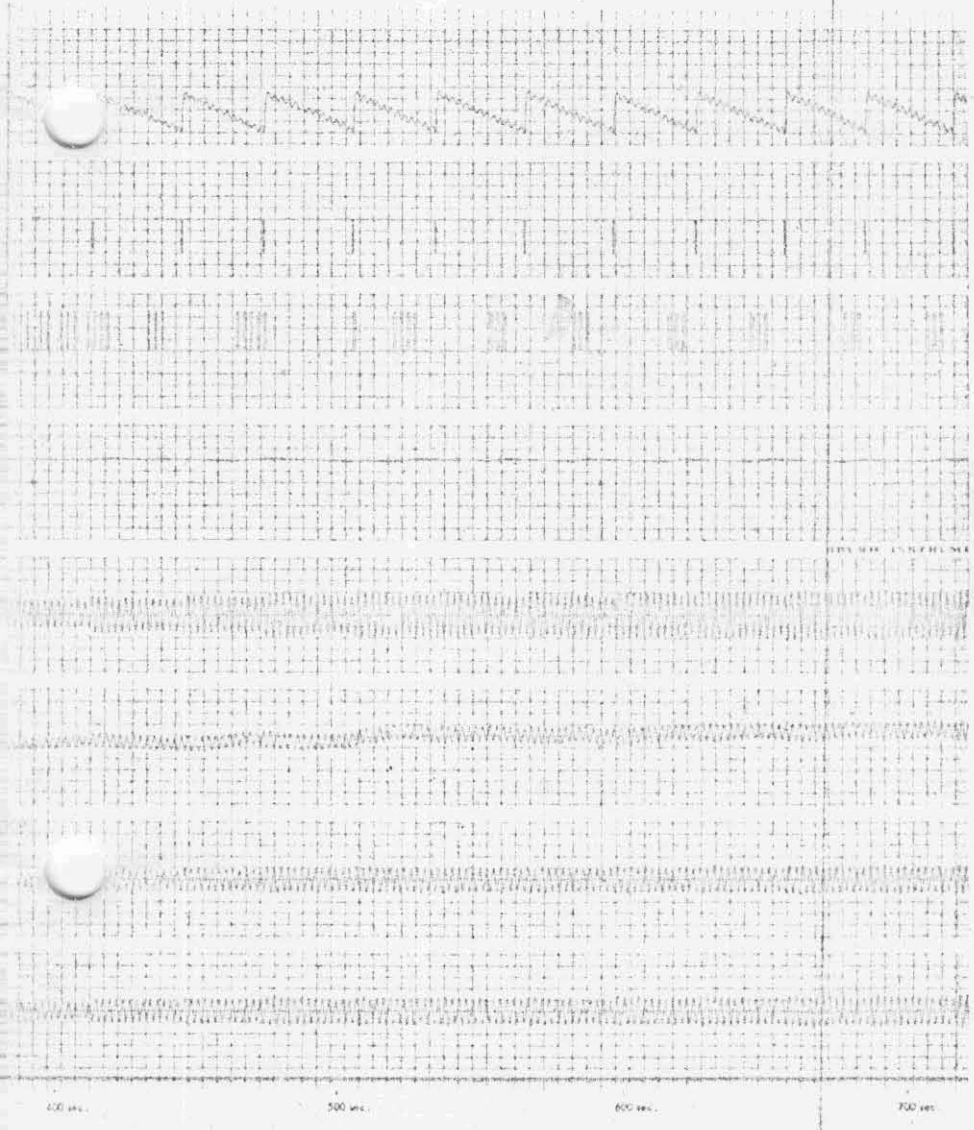

Figure 6-8 Nominal Roll Normal Mode System Response Boom Damping ($\zeta_1 = \zeta_2$) = .125%; Orbit Rate = .025°/sec

reached the steady state ringing amplitude (approximately ±0.25 deg) a body attitude error of 1.0 degree is necessary to allow proper wheel operation.

A word of warning is necessary here. It is felt that the boom motion, and attitude errors determined from the runs such as are shown in Figures 6-5 through 8 are extremely pessimistic. This feeling is further supported by the fact that the attempts to reproduce the array limit cycle on OGO-III with the analog model resulted in an order of magnitude larger limit cycle. With these words of caution the results of several runs made to evaluate the effect of array drive rate and boom damping are presented in Table 6-3. The data should be representative of relative performance but not necessarily the proper magnitude.

Another aspect of the runs shown in Figure 6-5 through 8 was that no gas was fired during these runs (not illustrated in the figures). This was due to the operation of the gas inhibit circuits. For example in Figure 6-6, the "steady state" attitude error, ϕ. is essentially comprised of a .4 cps sinusoid of .55 deg peak-to-peak and an "offset" of 2.0 deg. The filter output, ϕ_c, is also comprised of an offset plus a sinusoidal signal. However, since the filter gain at this frequency is

$$\frac{10\,\tau\,s + 1}{(\tau_\ell\,s + 1)^2\,(\tau\,s + 1)} \approx 7.5 \text{ at } .4 \text{ cps},$$

the amplitude of the sinusoidal output component of the filter is about 4.13 deg. peak-to-peak with an offset at 2.0 deg. To fire gas, the wheel bistable must be continuously on for a period in excess of 15 secs. Even though ϕ_c exceeds the gas deadzone (1°), the delay logic prevents it.

With gas inhibits inoperative, regions of boom damping and orbit rate (solar array drive rate) for which sufficient boom excitation exists to start a gas limit cycle were determined. Figure 6-9 shows the boundaries of boom damping vs solar array drive rate for which a gas limit cycle is started. As illustrated by Figure 6-9, lighter damping in the booms can be tolerated with a reaction wheel inhibit.

Orbit Rate (deg/sec)	Boom Damping (%)	Maximum Roll Attitude Error (deg)	$\Delta\phi$ Peak-to-Peak (deg)	$\dot{\phi}$ Peak-to-Peak (deg/sec)	ξ_1 Peak-to-Peak (deg)	ξ_2 Peak-to-Peak (deg)
0.1	0.25	1.1	0.32	1.0	0.5	0.6
0.1	0.125	2.0	0.55	1.5	0.8	0.9
0.1	0.0625	3.4	0.82	2.2	1.3	1.4
0.1	0.031	4.4	1.0	3.0	1.7	1.9
0.075	0.25	0.6	0.21	0.6	0.38	0.42
0.075	0.125	1.3	0.40	1.15	0.60	0.68
0.075	0.0625	2.0	0.60	1.50	0.95	1.00
0.050	0.25	0.3	0.15	0.42	0.24	0.24
0.050	0.125	0.6	0.23	0.64	0.35	0.38
0.050	0.0625	1.1	0.35	0.88	0.52	0.58
0.025	0.25	0.1	0.1	0.26	0.16	0.18
0.025	0.125	0.26	0.14	0.42	0.22	0.26
0.025	0.0625	0.50	0.18	0.48	0.28	0.34

$\Delta\phi$ = roll angle variation about a nominal roll error after "steady-state" has been attained

TABLE 6-3 Roll Error Dependence on Orbit Rate and Boom Damping

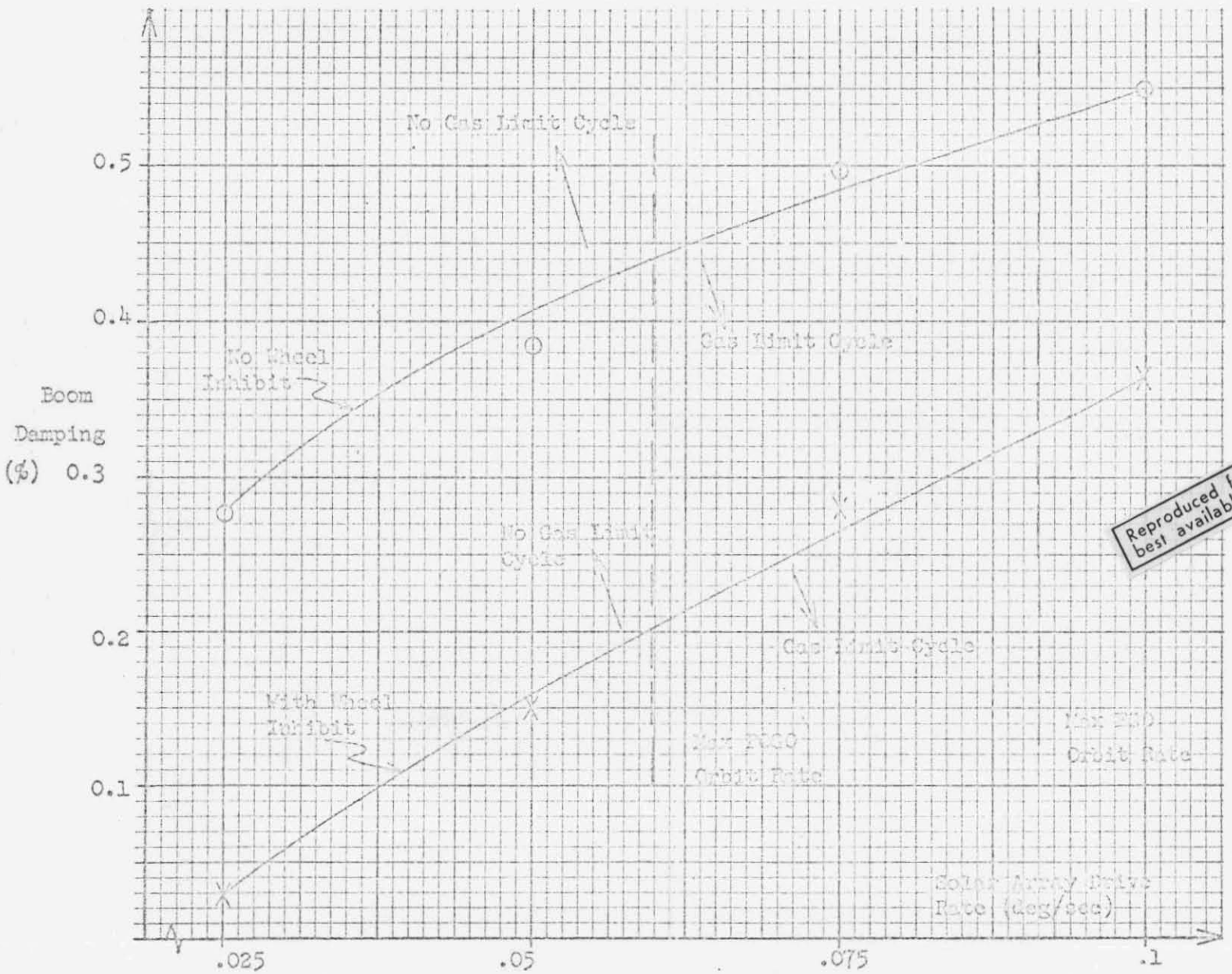

Figure 6-9 Boom Damping Boundaries vs. Solar Array Drive Rate for No Gas Limit Cycles

Also with gas inhibits inoperative, regions of initial body attitude error and body rate errors which resulted in gas limit cycles were determined. The boundaries are shown in Figure 6-10. As illustrated in Figure 6-10, the development of a gas limit cycle depends very little on the reaction wheel inhibit. It must be remembered that these results summarized in Figures 6-9 and 6-10 expected to be pessimistic for the reasons discussed above.

The effect of one side of the reaction wheel delay logic failing open was simulated. This merely means that the reaction wheel cannot be commanded "on" in the failed direction. The other side of the bistable is assumed to be unaffected. The results are discussed in the following paragraph. The analog run was too lengthy to reproduce for this report.

The reaction wheel was initialized to spin in the direction which required periodic torquing on the failed side to replace windage and friction losses. Then lack of torque allowed the reaction wheel to run down. This caused the spacecraft to drift over to the gas deadzone just as in the case of normal wheel unloading. Several gas firings occurred until the wheel was completely unloaded and the wheel speed direction reversed. The spacecraft then drifted to the other side of the reaction wheel deadzone and returned to normal reaction wheel control. A disturbance was applied to reverse wheel speed to the direction of the failed bistable. This caused the spacecraft to again drift over to the gas deadzone and a pulse of gas returned the spacecraft to the reaction wheel control on the good side.

6.1.3.1.3 Effects of Parameter Variations

The effects of parameter variations were evaluated by observing the roll system response to initial attitude and rate errors of 5.0 deg and 0.5 deg/sec respectively. The nominal system response to these initial conditions was shown in Figure 6-4. In that run the time from initiation of the run to termination of the last gas pulse was 219 seconds.

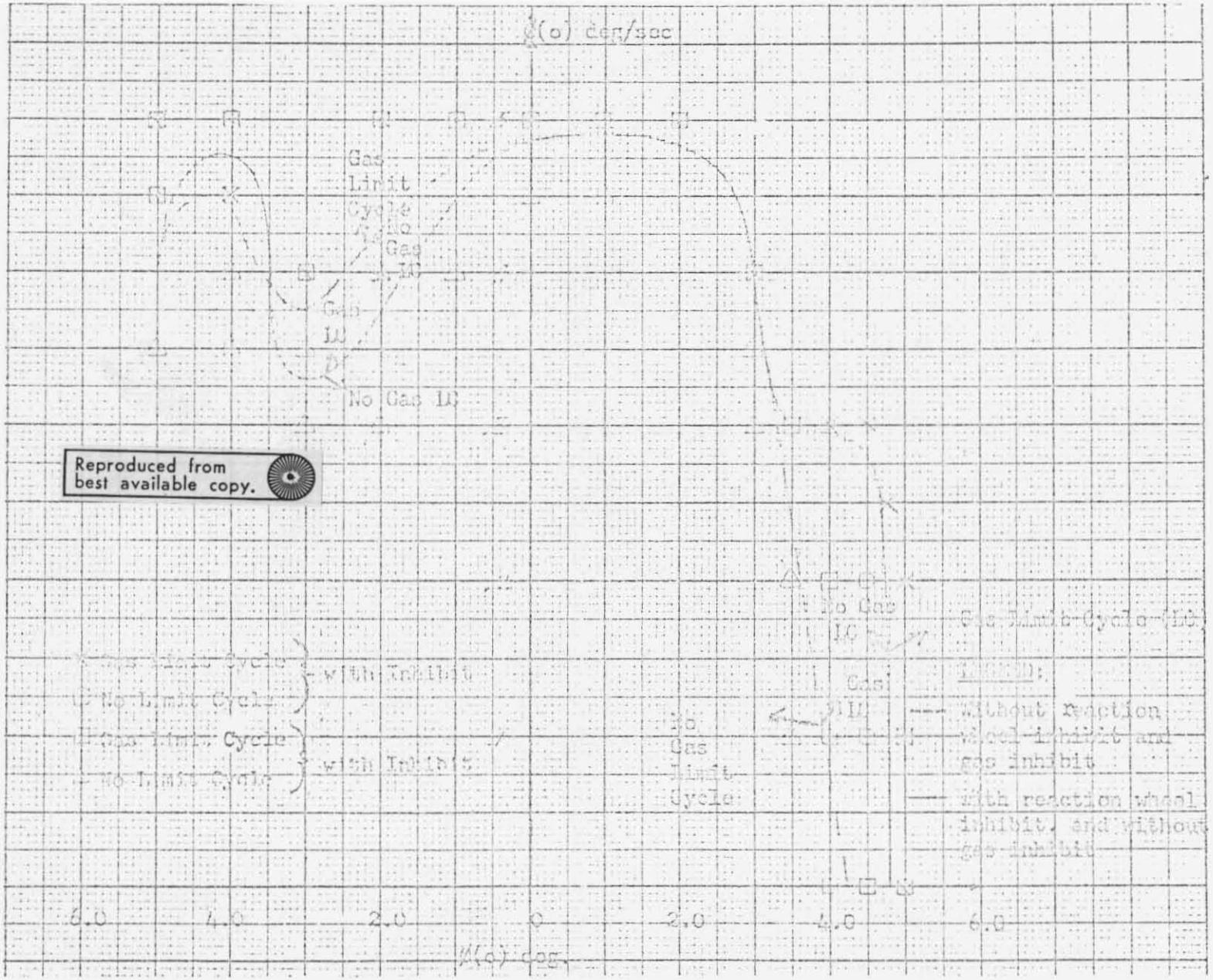

Figure 6-10 Roll System Gas Limit Cycle Dependency Upon Initial Conditions

With all other parameters nominal, the "de-stabilizing" and "sluggish" sets of each groups in Table 6-1 were selected and the roll system subjected to the same initial conditions. The results are summarized in Table 6 which illustrates that the system was most sensitive to gas parameter variations. The system response with "worst-on-worst" gas parameter stack-ups is shown in Figure 6-11.

Group	Range of Times to Termination of Last Gas Pulse (sec)
Gas	175 to 373
Reaction Wheel	267 to 347
Control Laws	238 to 342
Booms	190 to 256

Sensitivity to Parameter Groups (Roll Axis)

TABLE 6-4

The groupings were assembled to provide worst-on-worst overall de-stabilizing parameter sets. The response of a worst-on-worst group stack-up is shown in Figure 6-12. In this case it took nearly 765 seconds to the time of the last gas firing.

6.1.3.1.4 Gas Consumption During Post Eclipse Turn Sun Interference

Sun Disturbance - As previously mentioned, the control system was subjected to the sun disturbance of Figure 6-1. The results of Reference 6-3 without the reaction wheel inhibit were not reproduced exactly; but the same general trend was obtained as shown in Figure 6-13. The major item of interest is that less gas is used with the reaction wheel inhibit. A typical response is presented in Figure 6-14.

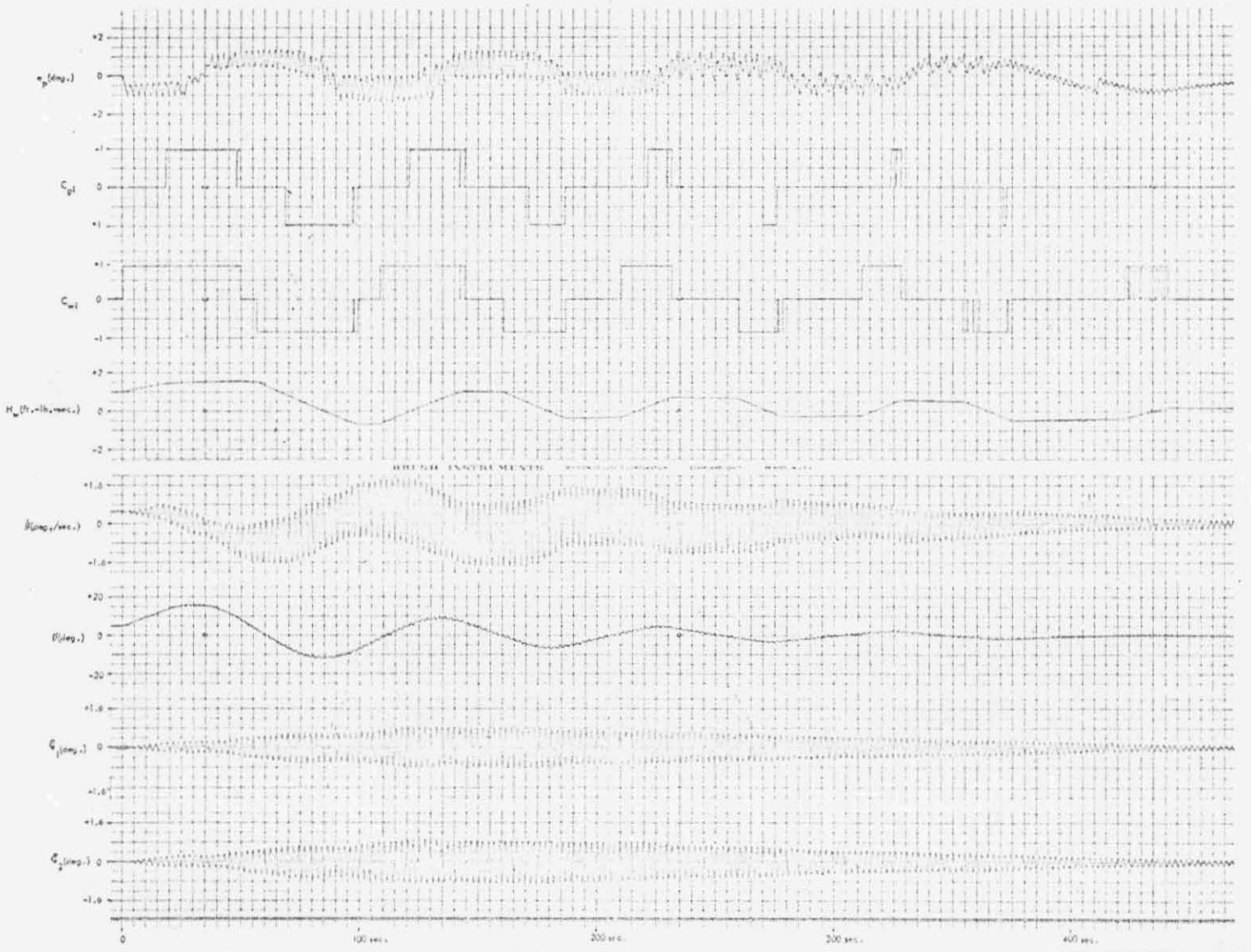

Figure 6-11 Nominal Roll Normal Mode System Response Destabilizing Gas Parameters

FOLDOUT FRAME 1

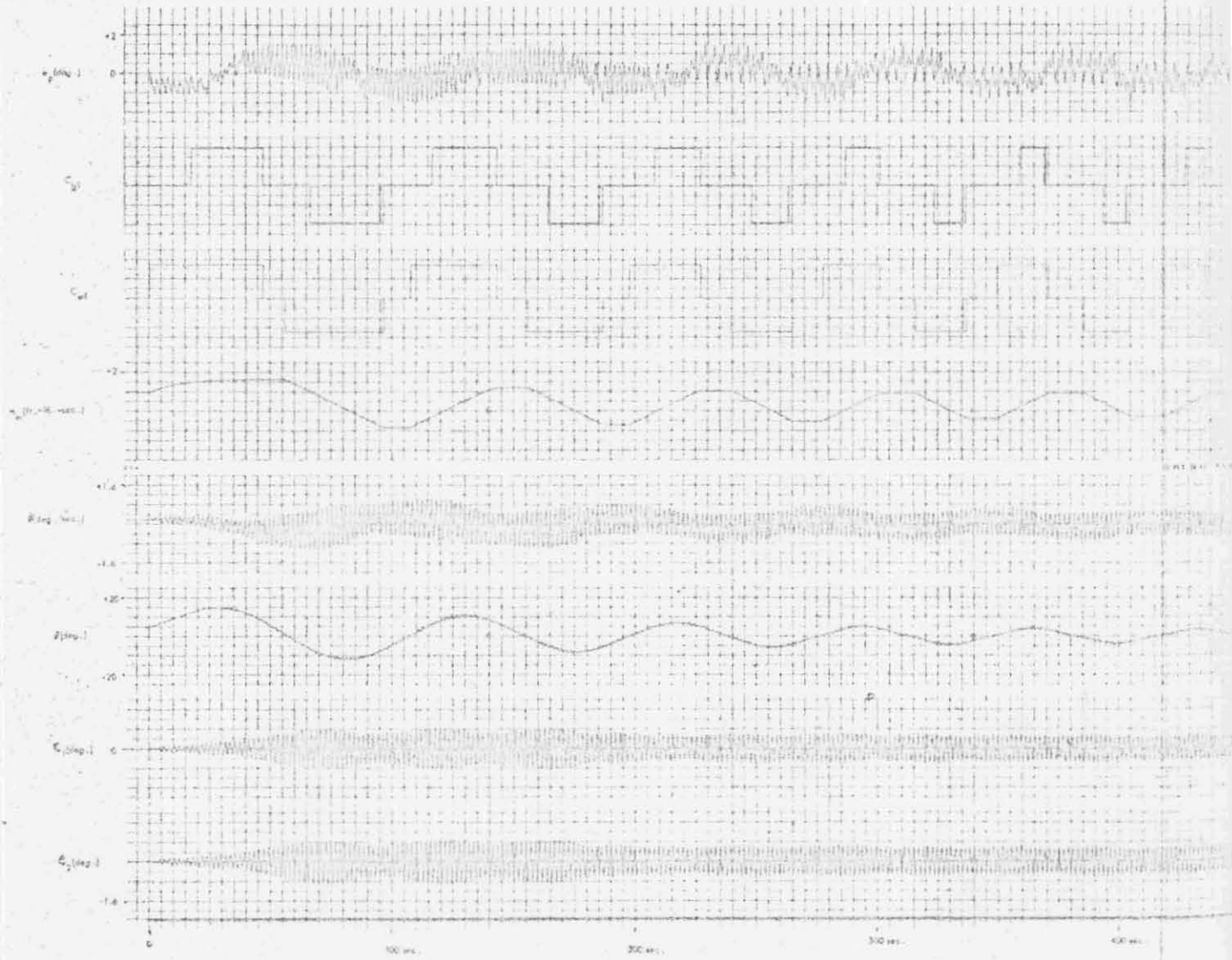

6-25-a

FOLDOUT FRAME 2

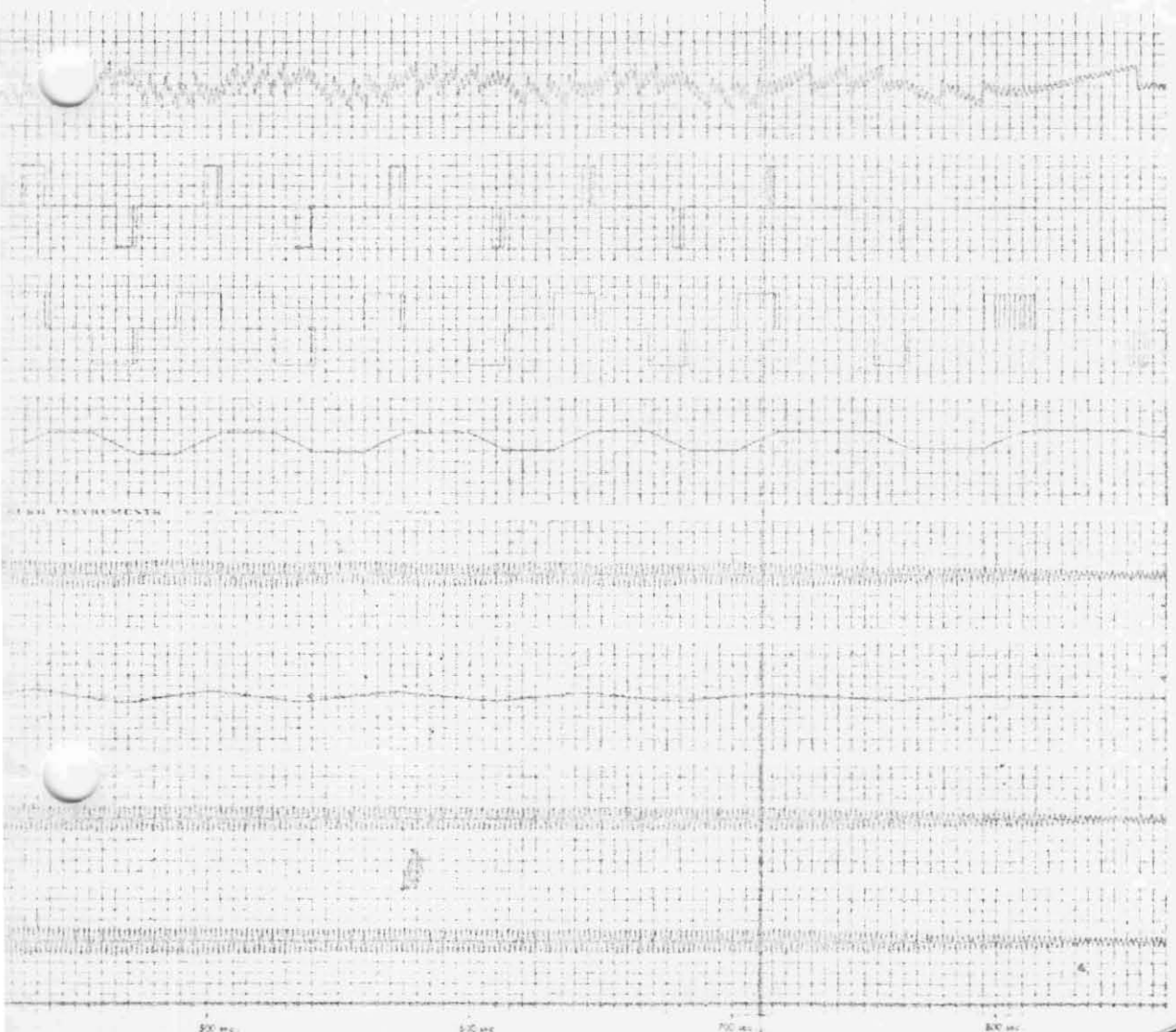

Figure 6-12

Roll Normal Mode System Response with Most Destabilizing Parameters

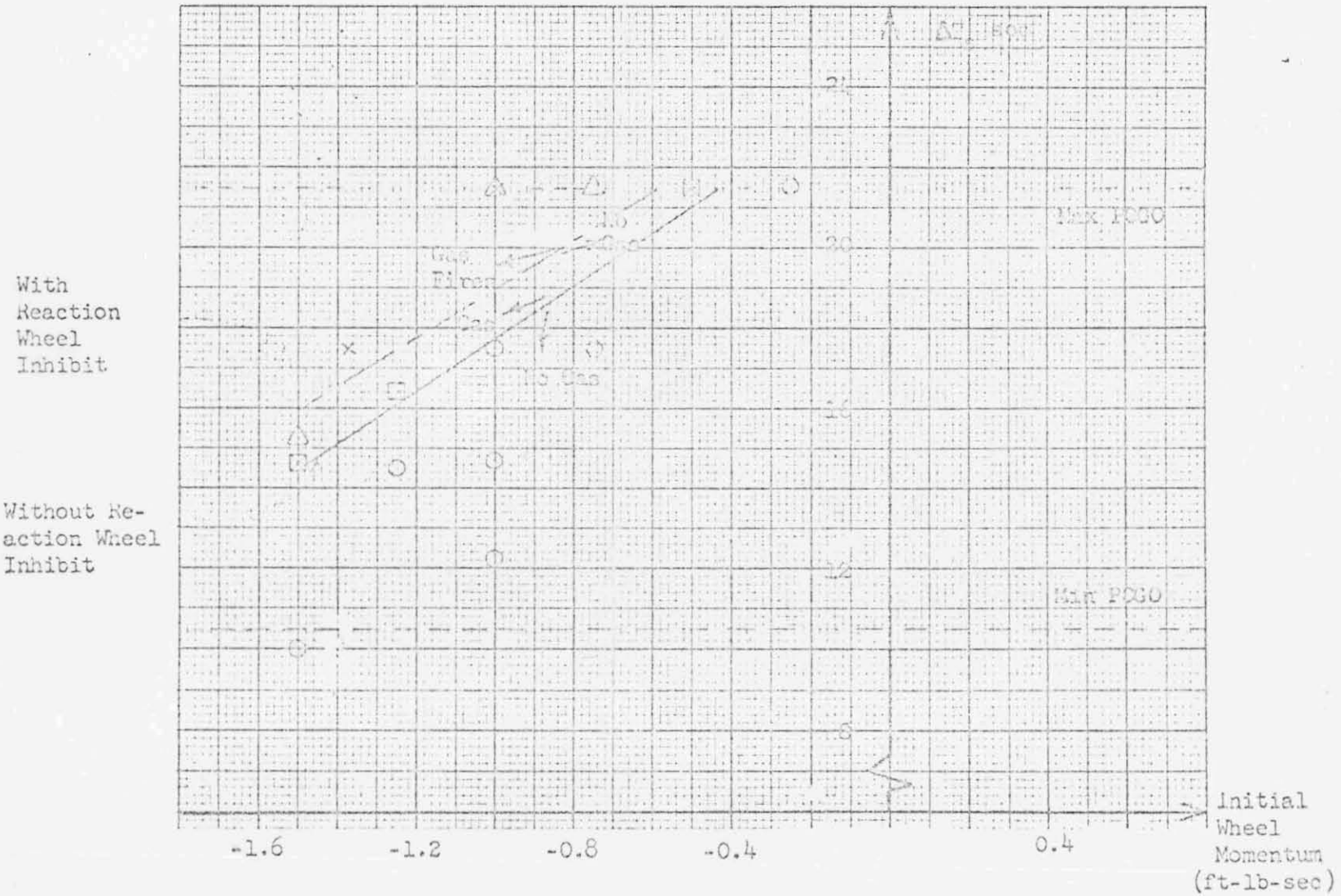

Figure 6-13 Sun Interference Gas Firing Boundaries for Roll System With and Without Wheel Inhibit Logic

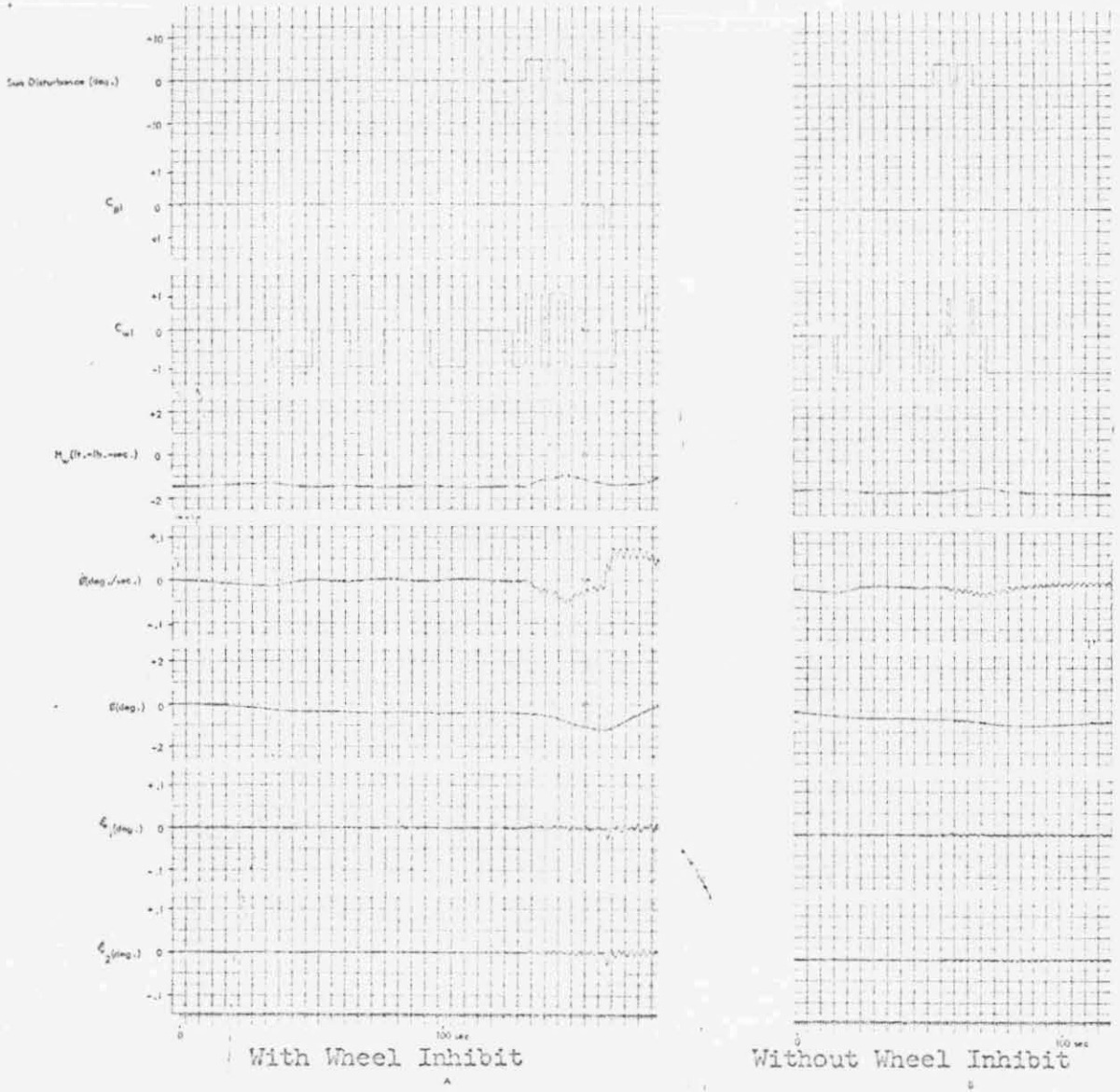

Figure 6-14 Roll System Normal Mode Response to Post Eclipse Sun Disturbance of 14.7 sec Duration (ΔT_s) with Initial Angular Momentum $(H_w)_s$ = 1.5 ft-lb-sec

6.1.3.2 Roll Axis Sun Acquisition Mode (Mode II)

The roll sun acquisition simulation also included the effects of EP-5 and EP-6 boom dynamics and all ACS functions. No wheel or gas inhibits are activated during Mode II, however. As previously mentioned, the computer model and parameter values used in the simulation are provided in Appendix D. With nominal parameter values, the response of Figure 6-15A was obtained. Even with a worst-on-worst destabilizing parameter stack-up, the system responded well as shown in Figure 6-15B.

6.1.3.3 Pitch Axis

The pitch simulation included the effects of flexible solar paddles and Haddock antennae dynamics and all ACS functions including gas inhibits.

The response of the nominal pitch system (Mode III) subjected to initial attitude and rate errors of 1.0 deg and 0.5 deg/sec is shown in Figure 6-16A. The time from initiation of the run to termination of the last gas pulse was 139 seconds.

The system response was also evaluated with the de-stabilizing and sluggish parameter set of each group in Table 6-1. The Haddock antennae parameters were varied in the manner the EP-5 and EP-6 parameters were changed for the roll axis. The results are presented in Table 6-5 which illustrates that the system was most sensitive to variations in the gas parameters. The time to termination of the gas pulse varied from 65 seconds to 211 seconds amongst the groupings.

Group	Range of Time to Termination of Last Gas Pulse (Sec)
Gas	118 to 197
Reaction Wheel	195 to 158
Control Law	137 to 160
Haddock Antennae	64 to 95

Parameter Sensitivities (Pitch Axis)

TABLE 6-5

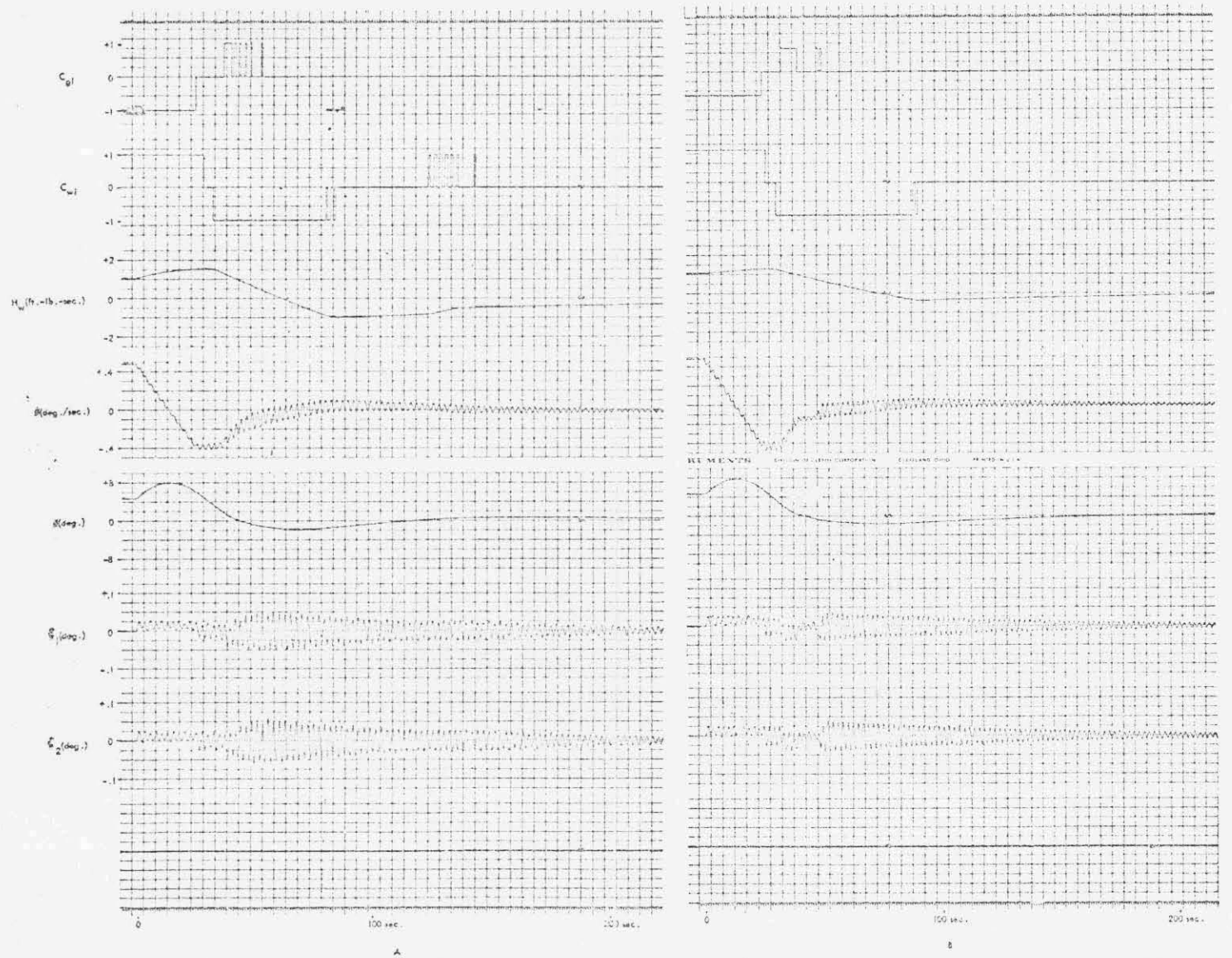

Nominal Parameters

Destabilizing Parameters

Figure 6-15 Roll Response for Sun Acquisition Mode

FOLDOUT FRAME

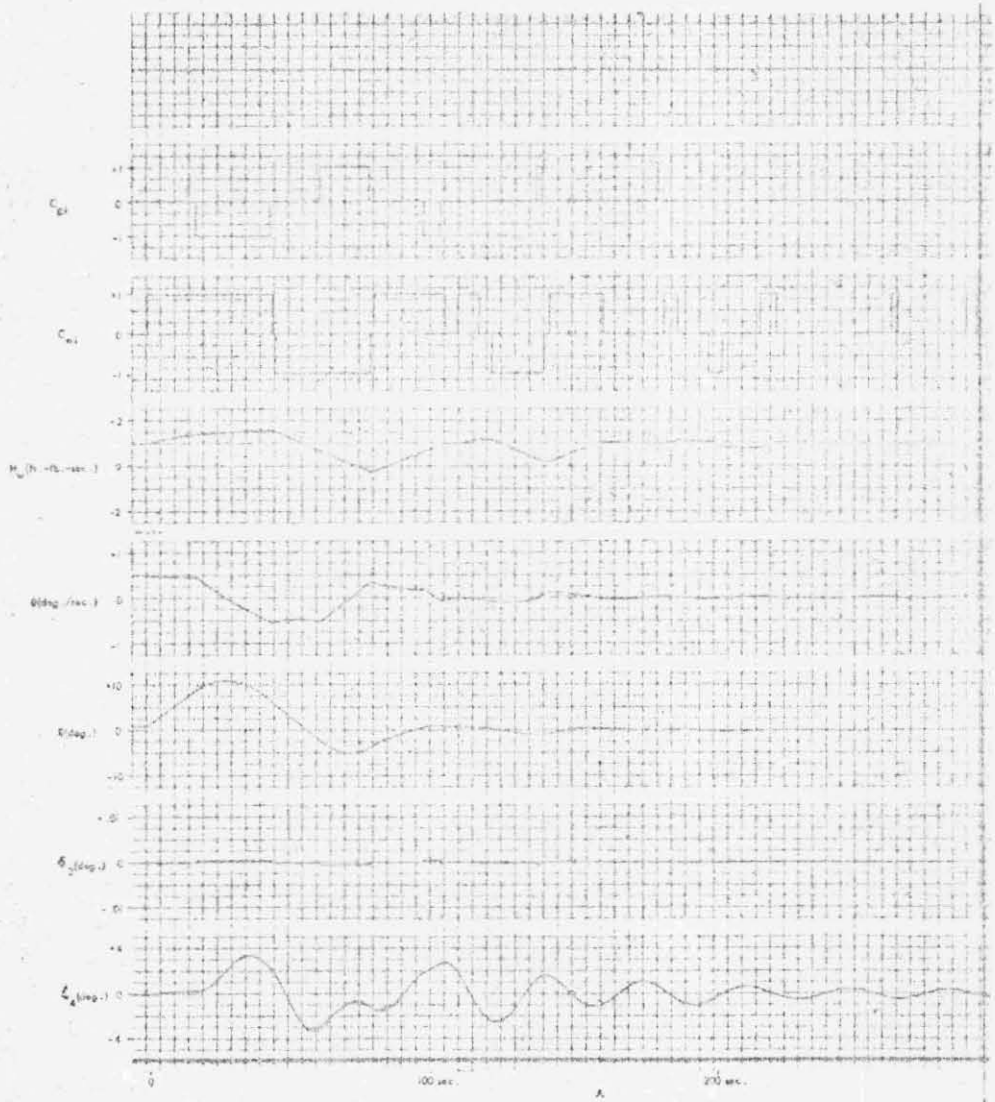

Nominal Parameters

FOLDOUT FRAME 2

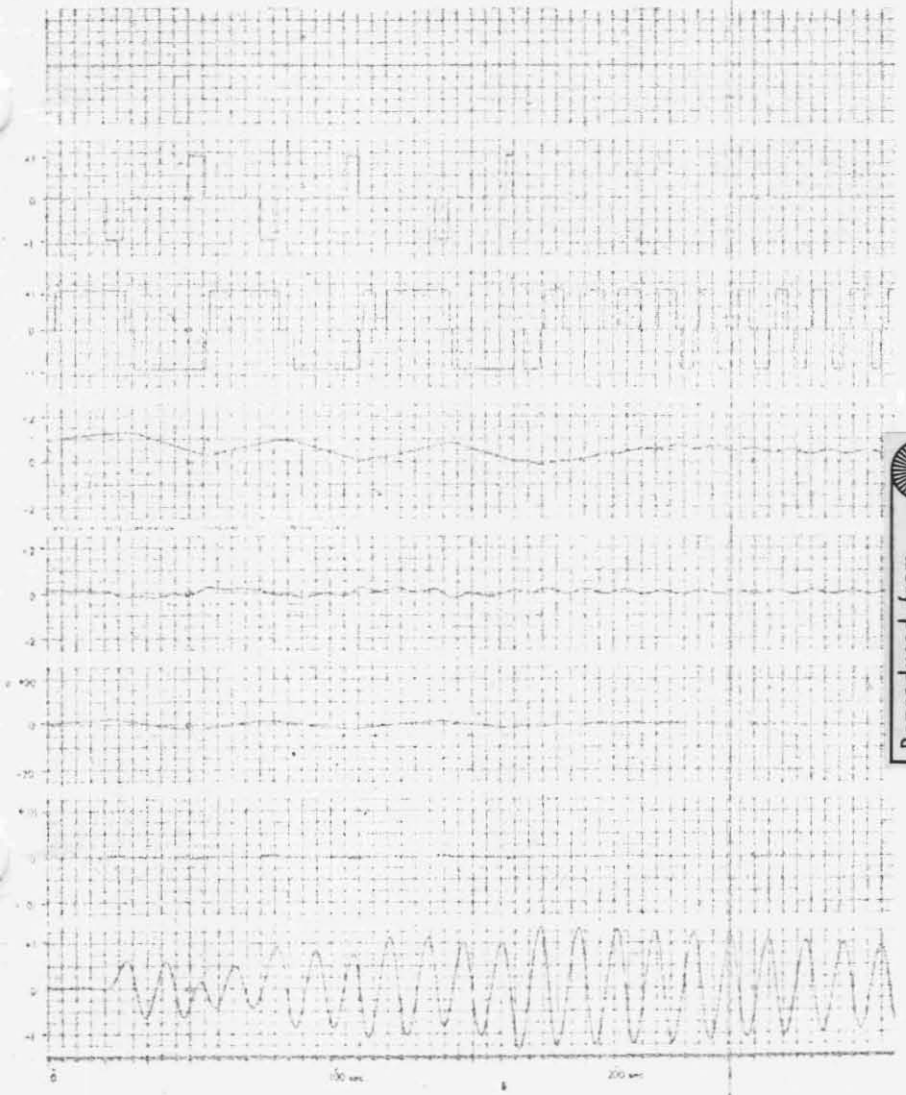

Destabilizing Parameters

Figure 6-16 Pitch Normal Mode System Response

The groupings were assembled to provide worst-on-worst overall de-stabilizing parameters. The response of a worst-on-worst group stack-up is shown in Figure 6-16B.

Initially the worst case reaction wheel torque was reduced to 50% of the nominal value. Under these conditions the wheels did not capture and a gas limit cycle occurred. However, further checking showed the reaction wheel torque is never less than 65% of nominal. The run in Figure 6-16B with this minimum wheel torque was stable.

6.1.3.4 Yaw Sun Acquisition (Mode II)

The yaw simulation included the effects of EP-5 and EP-6 boom dynamics, flexible solar paddles, Haddock antennae dynamics, all ACS functions including the gas deadzone increase from 2.5 to 5.0 deg.

The response during sun acquisition with nominal parameters is shown in Figure 6-17A. Initial conditions were a 1.0 deg attitude error and 0.5 deg/sec rate error. Similar to the pitch and roll studies, the parameters were broken down into groups and the system response evaluated for the same initial conditions as the nominal system. No significant differences could be discerned between the response of the group by using time from termination of the last gas pulse as the criteria for determining relative stability. Even with worst-on-worst parameter stack-ups, the yaw axis responded satisfactorily during sun acquisition as illustrated by Figure 6-17B.

6.1.3.5 Yaw Axis Normal Mode (Mode III)

The yaw response for normal mode operation with the reaction wheel inhibit is illustrated in Figure 6-18. With worst-on-worst parameter stack-ups, the yaw system also responded satisfactorily as illustrated in Figure 6-19.

Nominal Parameters Destabilizing Parameters

Figure 6-17 Yaw Sun Acquisition System Response

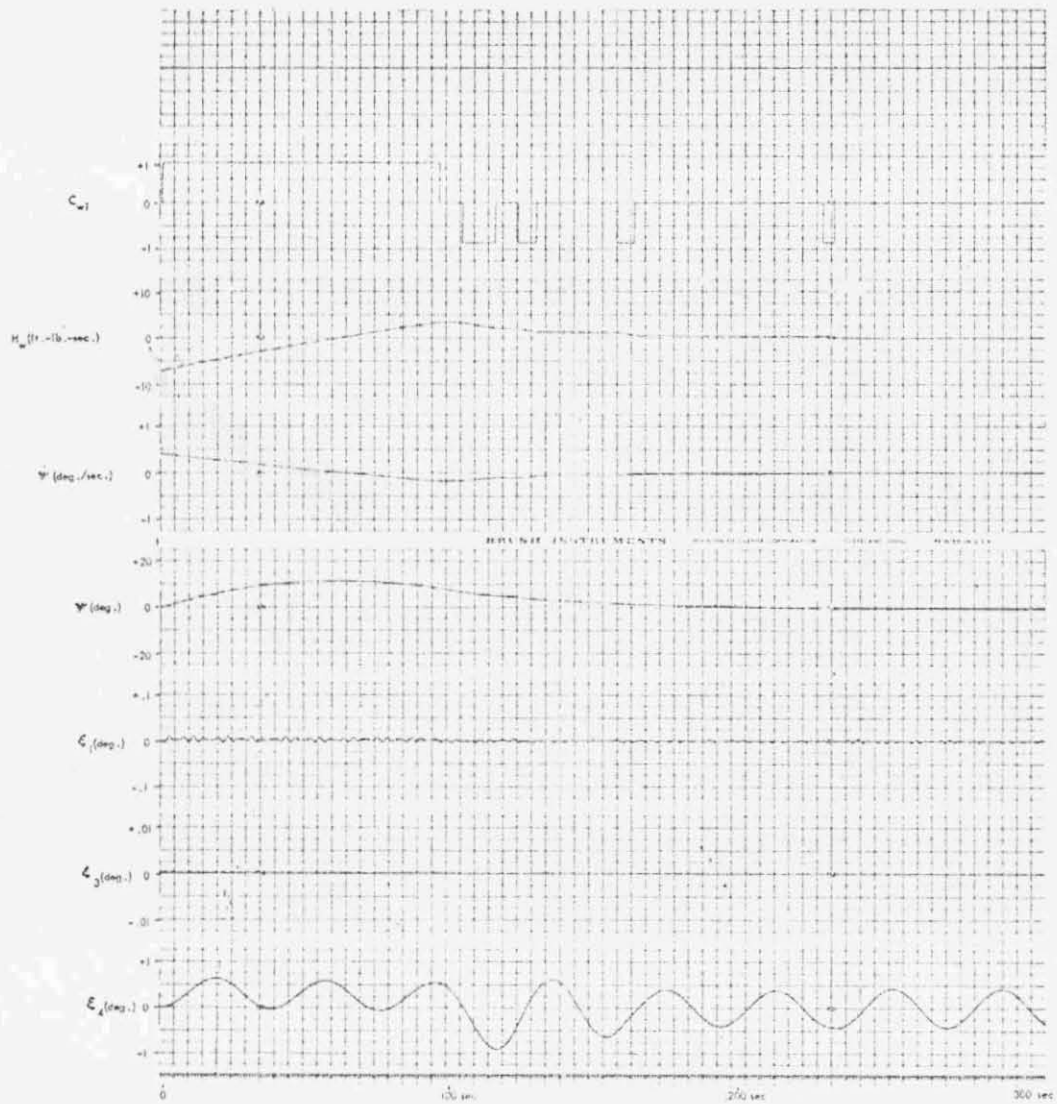

Figure 6-19 Yaw Normal Mode System Response with Nominal Parameters

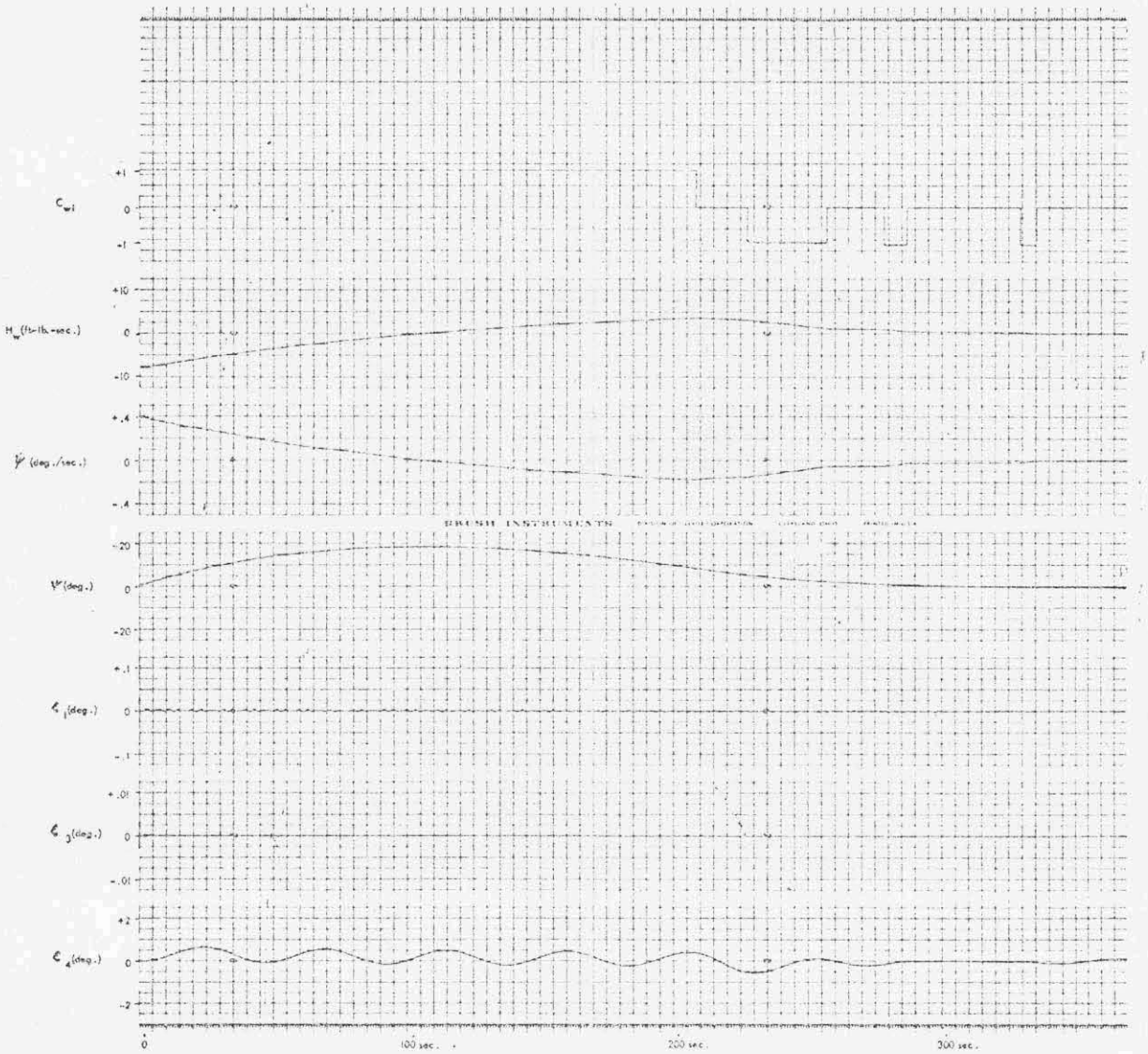

Figure 6-19 Yaw Normal Mode System Response with Destabilizing Parameters

6.1.3.6 OPEP

The OPEP model is presented in Appendix C and the analog schematic is shown in Figure D-5 of Appendix D. The nomenclature and parameters used are given in Appendix C.

Figure 6-20 shows the response of the nominal OPEP system for an initial OPEP attitude error, $\psi_e(o)$ = 10 degrees and no yaw body attitude command. The cases with K_D = .226 and .34 correspond to the POGO and EGO orbits, respectively. As K_D is increased, both the system response time and stability margin are decreased. Limit cycle operation occurs between K_D = 0.8 and 0.9, which is more than double the nominal system gain. Increases in K_D could result from either or all of the following:

a. Decrease of the deadzone
b. Increase in orbital rate
c. Increase in motor rate

It is not likely that the uncertainties or variations due to age will cause the combined effect of over a 100% change in gain.

Figure 6-21 shows the OPEP performance for the following assumed worst case parameter variations:

a. Filter time constant is increased by 50%, τ_f = 30 sec
b. Coulomb friction is decreased by 50%, T_c = 1 ft-lb
c. Motor viscous friction is reduced by 50%, which increases the motor time constant.
d. Modulator feedback gain decreased by 20%, K_1 = 1.47.

For these variations, the system performance is seen to be acceptable for both the POGO and EGO orbits. However, limit cycle operation will now occur for K_D between 0.50 and 0.54. Therefore, the gain margin has been decreased from the nominal case.

Figures 6-22 and 6-23 show the OPEP performance for an initial attitude of ψ_e = 10 degrees, under the assumptions that the gyro input axis is misaligned by plus or minus 0.2 degree. Figure 6-22 corresponds to negative rate feedback, while Figure 6-23 corresponds to positive rate feedback. For negative rate feedback, the response is more sluggish

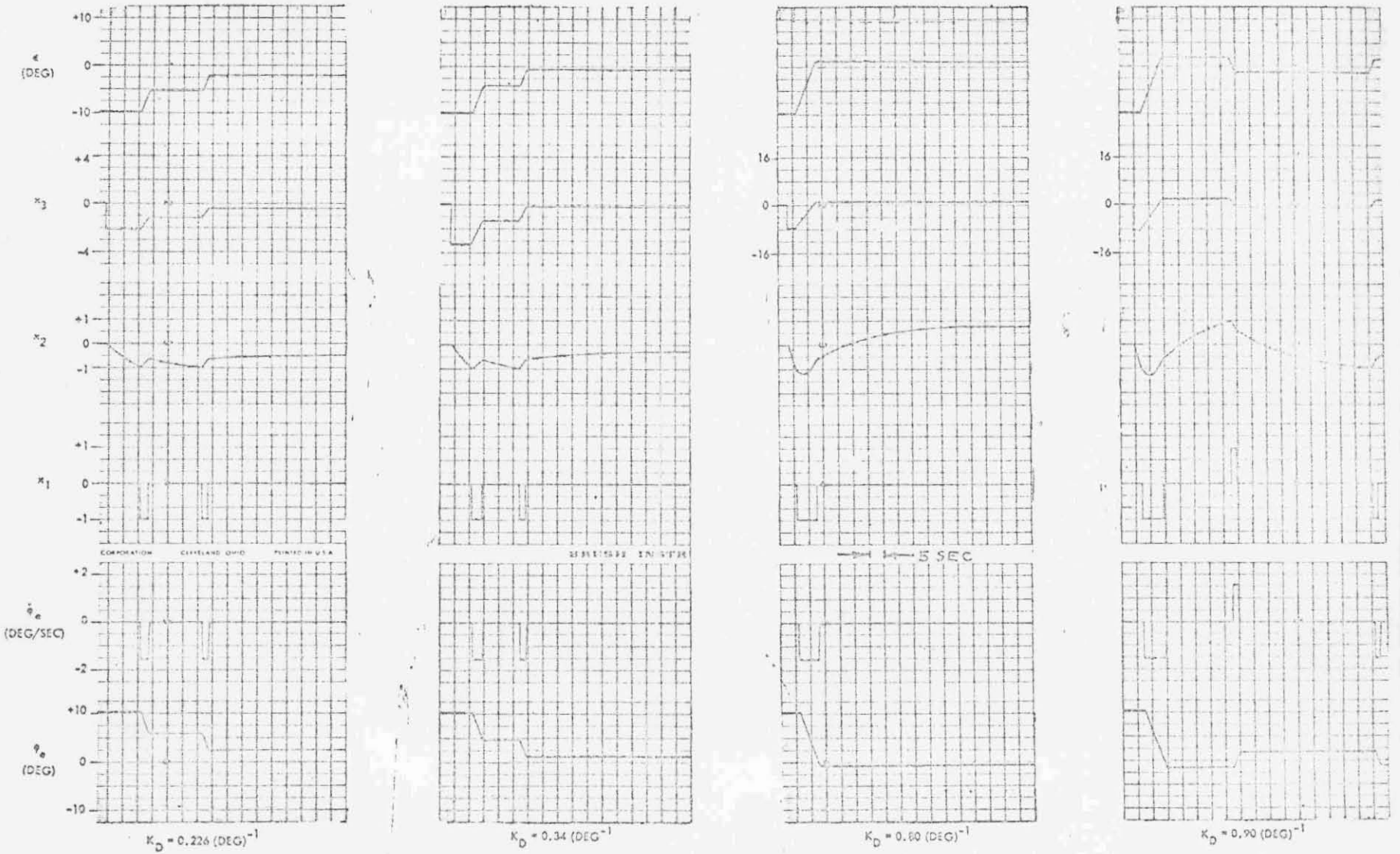

Figure 6-20 Modified OPEP Control System Performance Nominal Parameters, $\psi_e(o)$ = 10 DEG

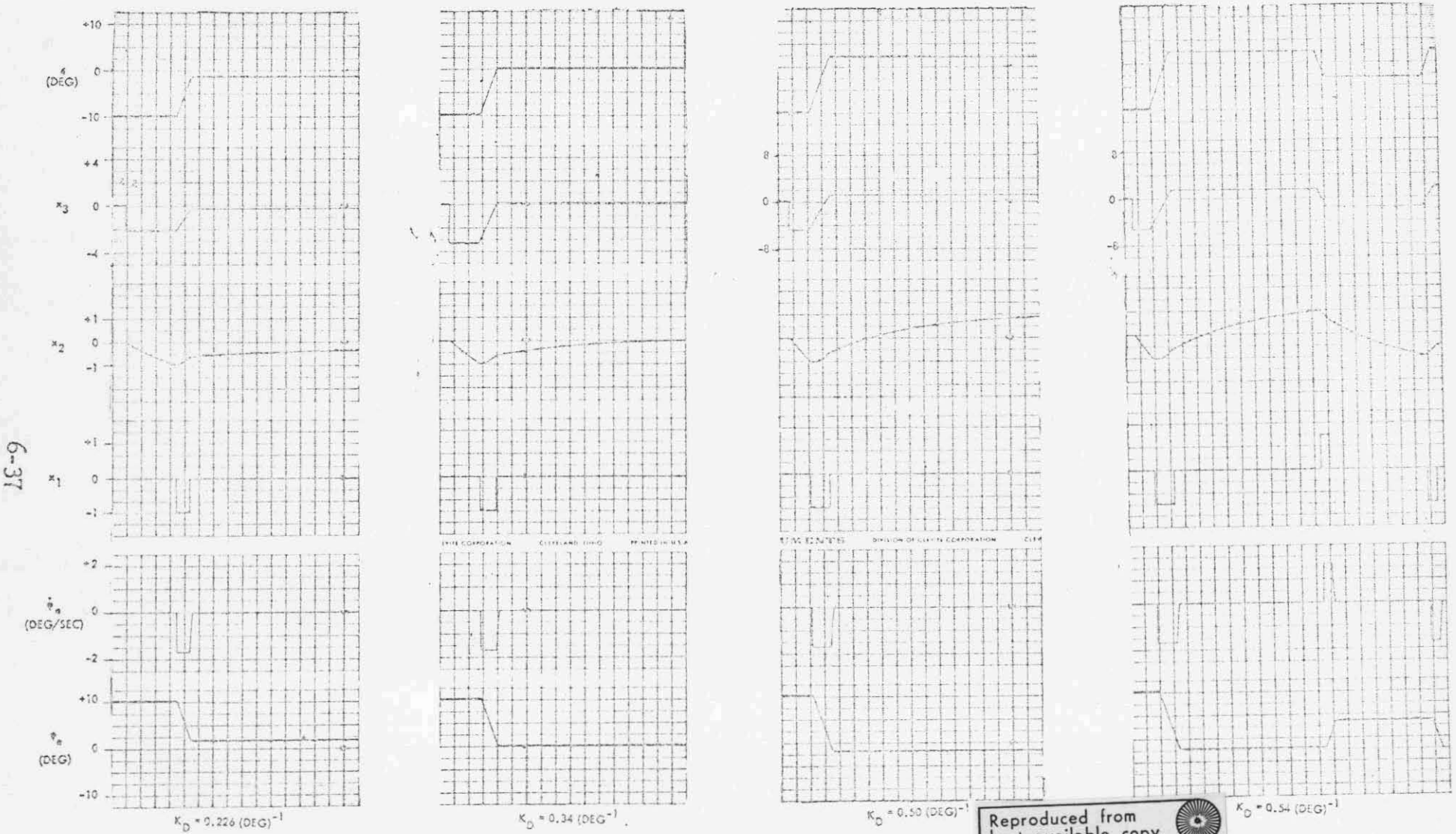

Figure 6-21 Modified OPEP Control System Performance Worst Case Parameter Variations, $\psi_e(0) = 10$ DEG

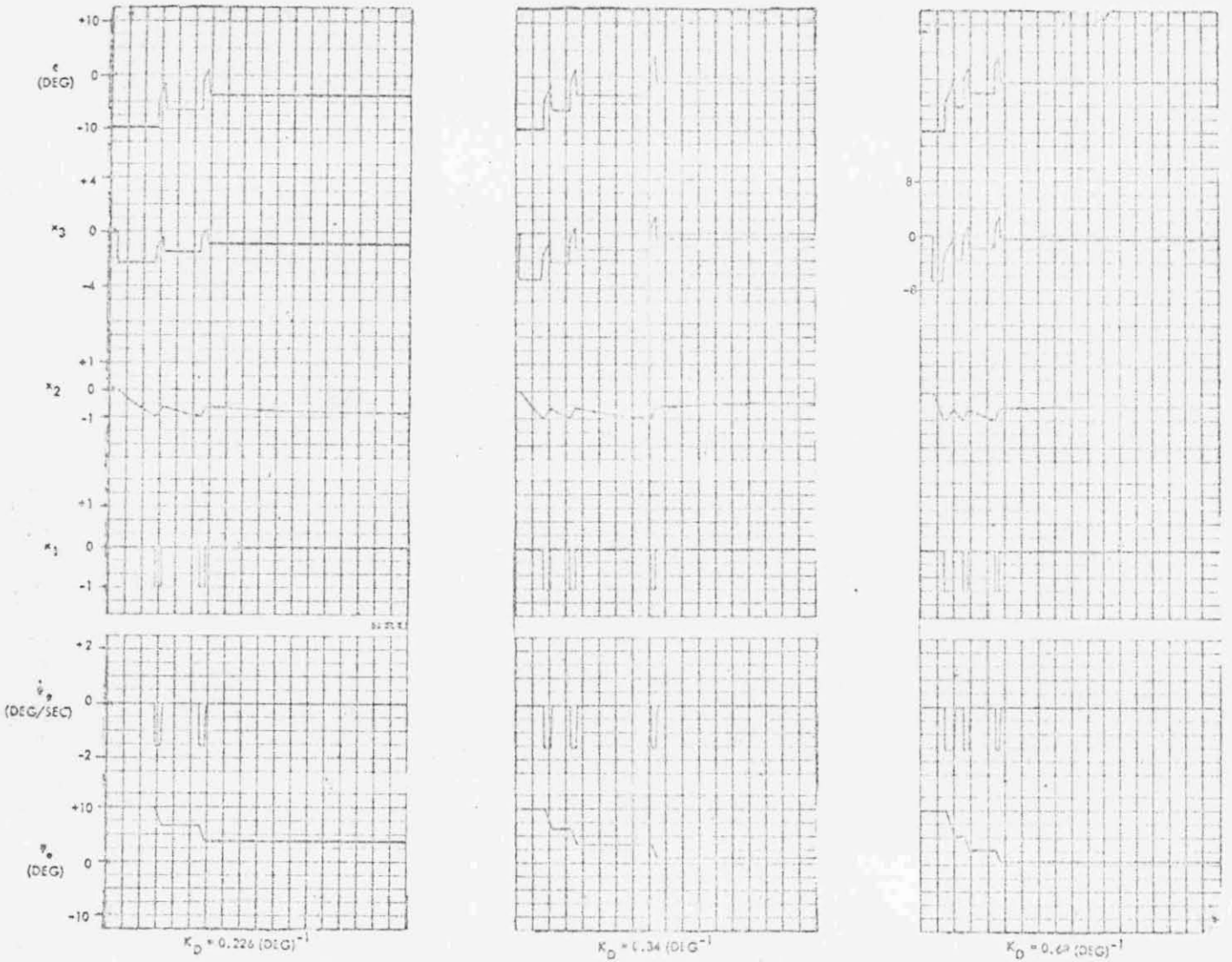

Figure 6-22 Modified OPEP Control System Performance with Gyro Input Axis Misaligned in Direction to Yield Negative Rate Feedback, Misalignment Magnitude = 0.2 DEG., Nominal Parameters, $\psi_e(o)$ = 10 DEG.

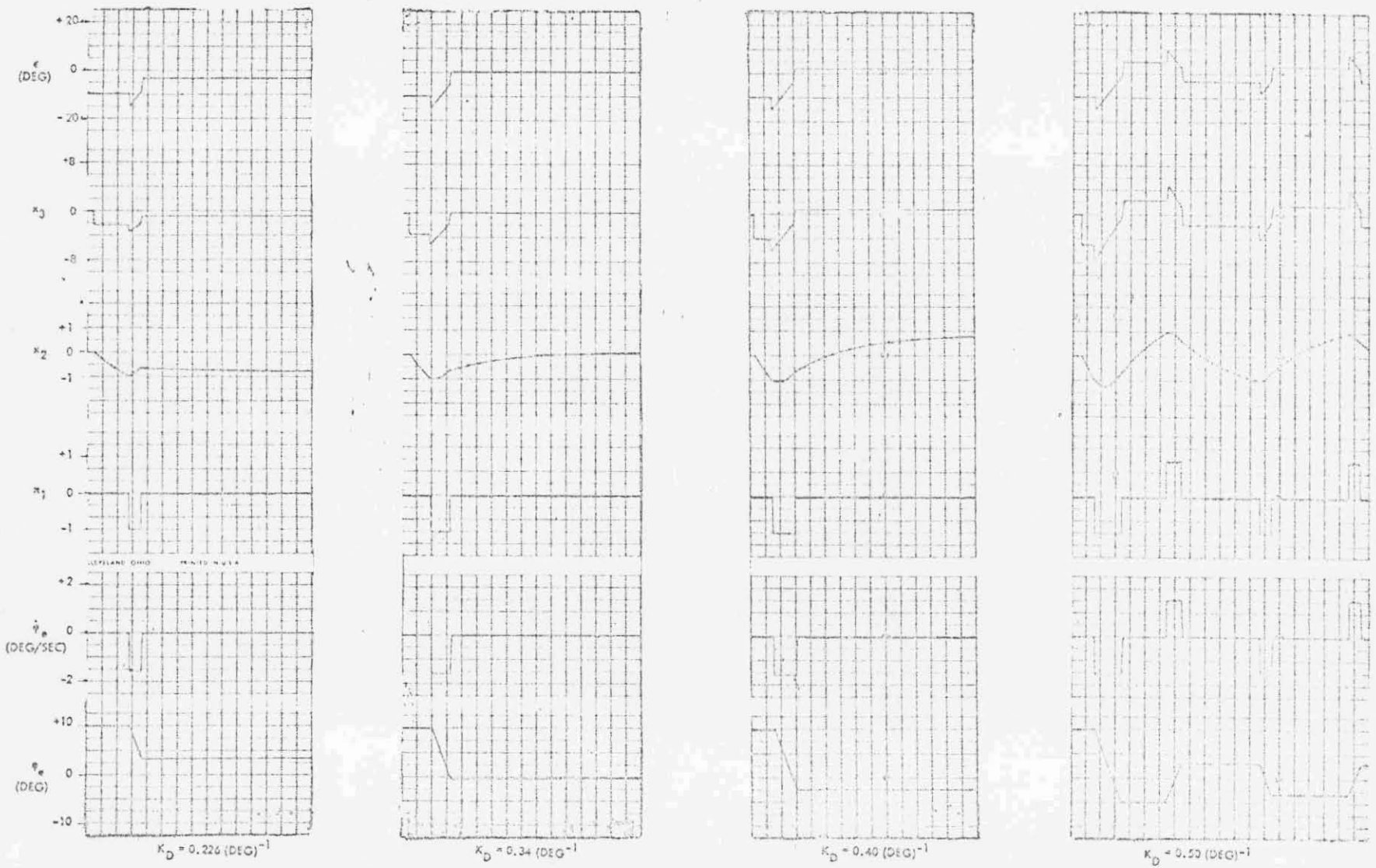

Figure 6-23 Modified OPEP Control System Performance with Gyro Input Axis Misaligned in Direction to Yield Positive Rate Feedback, Misalignment Magnitude = 0.2 DEG, Nominal Parameters, $\psi_e(o)$ = 10 DEG.

than the nominal system but the OPEP will not limit cycle for a 100% variation in K_D. For positive rate feedback, the response is faster but limit cycle operation will occur for K_D between 0.4 and 0.5. Therefore, as expected, positive rate feedback decreases the gain stability margin.

Figure 6-24 shows a failure mode OPEP response where one of the pulse ratio modulator feedback loops is disabled. Although it can be seen that the OPEP will converge satisfactorily, it takes much longer to reach steady-state. The system did not limit cycle for a 350% change in K_D.

Figure 6-25 illustrates the tracking capability of the nominal system. Three cases are shown for yaw body axis rates of 0.1°/sec, 0.25°/sec and 0.5°/sec. The maximum OPEP pointing error is tabulated below.

TABLE 6-6

OPEP Following Error

Yaw Rate (deg/sec)	Max OPEP Error (deg)
0.1	11
0.25	14
0.5	18

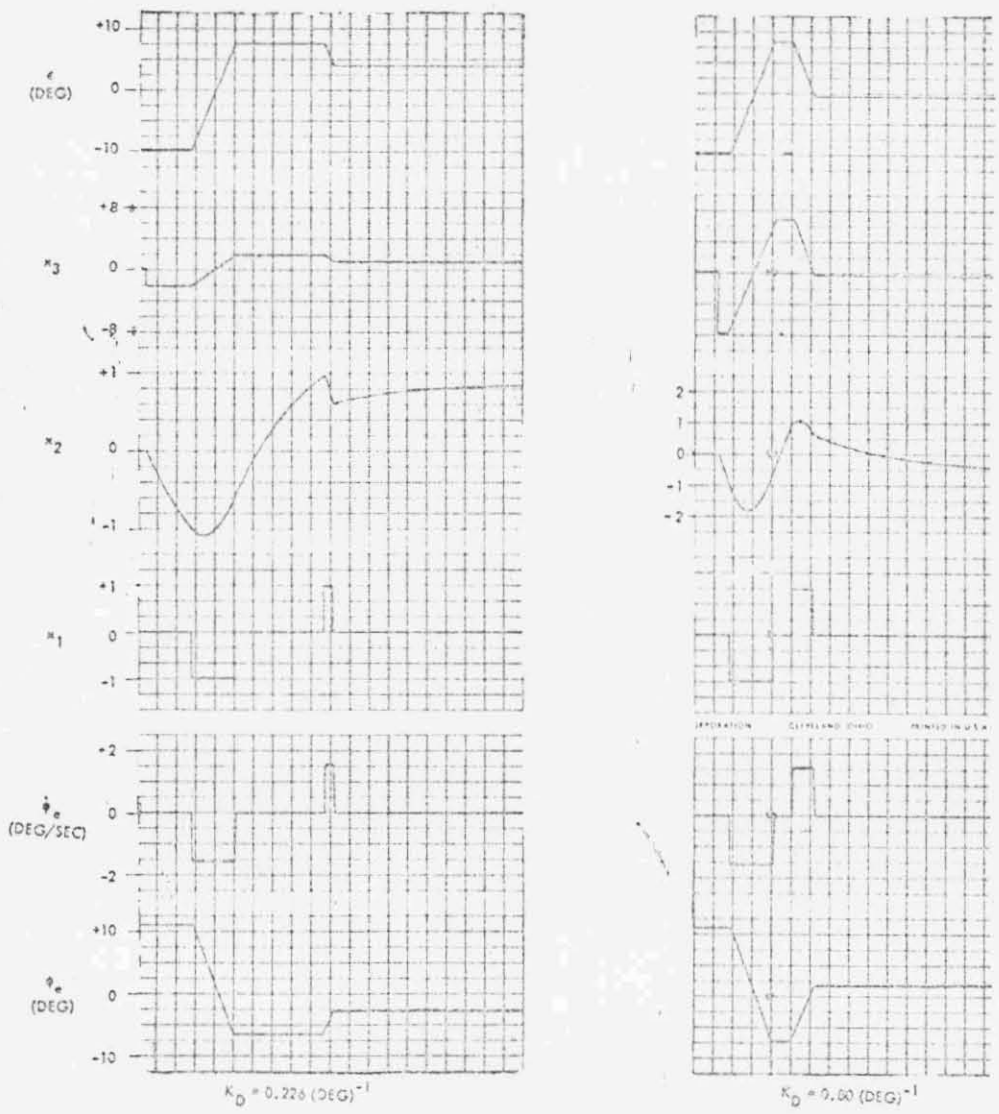

Figure 6-24 Modified OPEP Control System Performance Where One Side of Pulse Ratio Modulator Feedback Loops is Disabled. Nominal Parameters, $\psi_c(o)$ = 10 DEG

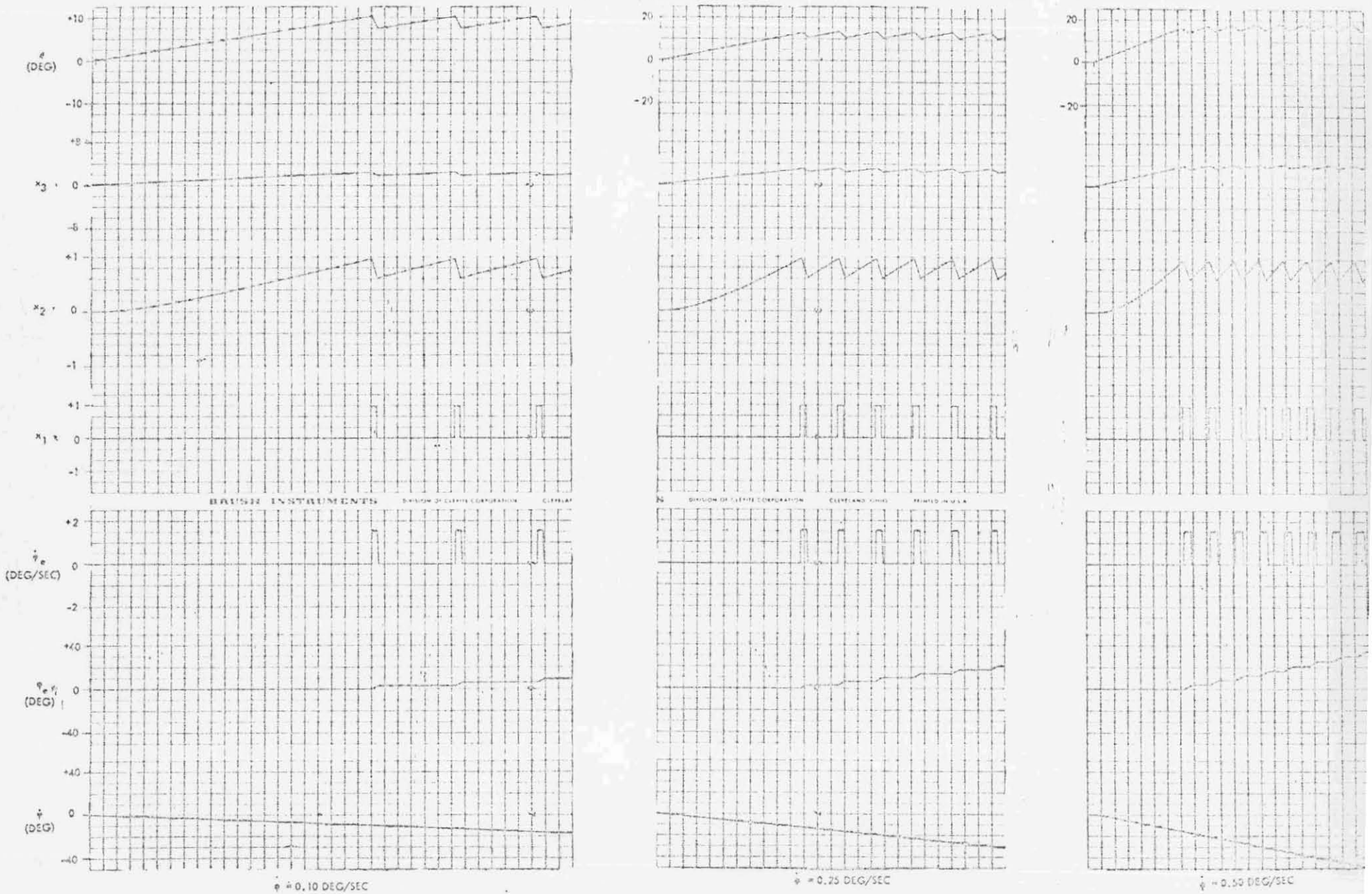

Figure 6-25 Modified OPEP Control System Performance for Constant Yaw Turning Rates. Nominal Parameters, $K_D = 0.226\ (DEG)^{-1}$, POGO Orbit

6.2 LARGE ANGLE SIMULATION STUDY

6.2.1 Purpose

Though most of the ACS changes would have no direct effect on acquisition it was necessary to eliminate any doubt about the potential effect of the changes. The only change which could directly affect acquisition was the widening of the yaw gas deadzone from 2.5 to 5.0 degrees. Normally the reaction wheel and gas delay logic would be disabled during acquisition but it was deemed necessary to verify the ability of the ACS to acquire even though the delay logic was active.

6.2.2 Description of Studies

Variations in Attitude Control System configuration evaluated for sun acquisition were:

(1) The nominal OGO-D System.

(2) The nominal OGO III System which differed from the OGO-D system in the size of the yaw pneumatic deadzone employed (2.5 degrees compared to the OGO-D value of 5.0 degrees).

(3) A failure mode where the pneumatic and reaction wheel inhibits are activated.

(4) A failure mode where pitch control is not provided due to a failed rate gyro.

(5) The nominal configuration with worst case parameter tolerances.

A nominal ACS configuration was employed in earth acquisition studies. However for reacquisition studies, a departure from the nominal system was made by activating the pneumatic and reaction wheel inhibits; this constituted a failure mode arising from either an actual logic failure or inadvertent activation of the inhibits by ground command. The impulse requirements were thus somewhat larger than would be expected. A worst case combination of parameters was also evaluated.

6.2.3 Simulation Model

The analog computer simulation of the OGO ACS and vehicle dynamics allowed the evaluation of rigid body response during sun and earth acquisition for unrestricted initial conditions on body attitude and rate. Six direction cosines were needed to provide attitude references with respect to the sun and earth. Drift correction for the direction cosines and orbital dynamics were not required as acquisition time was relatively short.

Figure 6-26 is a block diagram illustrating the model used in the analog simulation. The equations employed in the mechanization are given in Reference 6-3. The sun sensor and horizon scanner angles, and scan head tracking logic are derived using direction cosines. A simplification of the sun-earth referenced coordinate system was possible for acquisition studies - which did not restrict vehicle freedom-by selecting the sun-earth line normal to the orbit plane.

All pertinent limits have been mechanized: sun sensor and horizon scanner ranges, electronic limits, electronic dynamic ranges and reaction wheel saturation. The bistables are electronic switches with positive feedback to produce a hysteresis characteristic. The reaction wheels have square torque-angular momentum characteristics: the torque is constant from zero to maximum velocity. Reaction wheel and pneumatic inhibits have been breadboarded using OGO circuits. In the 5 second inhibits, OGO transistors have been used as the transistor current gain influences the inhibit time. The 5 second inhibits, employed in roll and yaw, prevent reaction wheel reversal for 5 seconds. The 15 second inhibits, employed in roll and pitch, prevent operation of the pneumatic controls until 15 seconds after initiation of reaction wheel control. The pitch and yaw pneumatic torques are reduced by one-half when they exist simultaneously since pitch and yaw controls employ the same jets and always have one pair of jets operating in opposition.

Mode switches establish either sun acquisition (Mode II) or normal mode (Mode III). In Mode II roll and yaw control signals are obtained from the sun sensor and pitch control feedback is provided by a rate gyro. Roll bistable deadzones are 2.5 times higher than in Mode III.

FOLDOUT FRAME 1

BLOCK DIAGRAM OF OGO LARGE ANGLE S

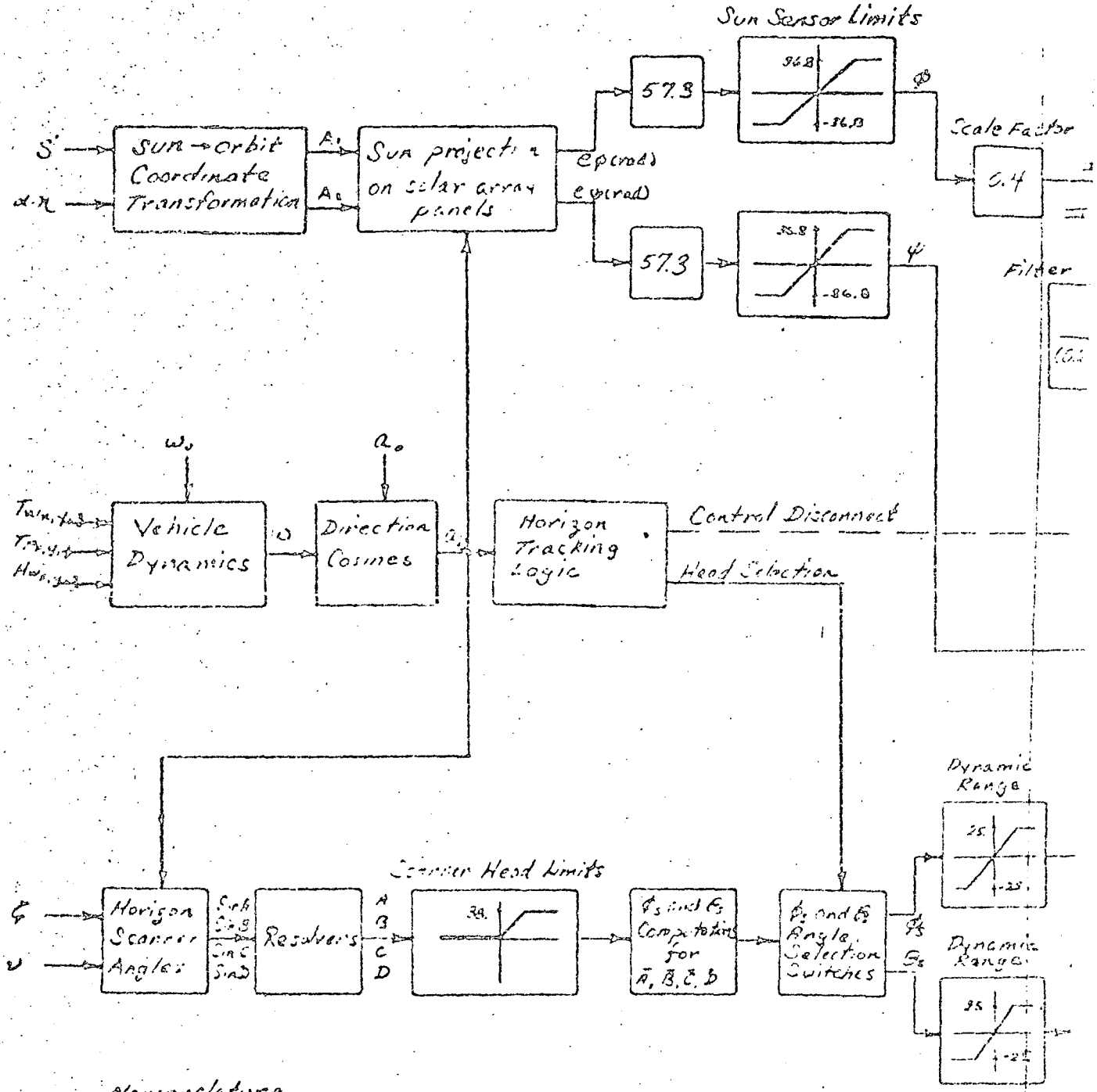

Nomenclature

S' = angle between earth/sun line and line normal to orbit plane
$\alpha \cdot \mathcal{R}$ = angle between earth/sun line projection in orbit plane and earth/vehicle line
A = sun/orbit plane direction cosines
a = vehicle/earth/sun direction cosines
ζ = Horizon cone half angle
ω = Attitude error plane misalignment
T = Torque
H = Angular momentum
w = Body angular velocity

6-45-a

FOLDOUT FRAME 2

E SIMULATION

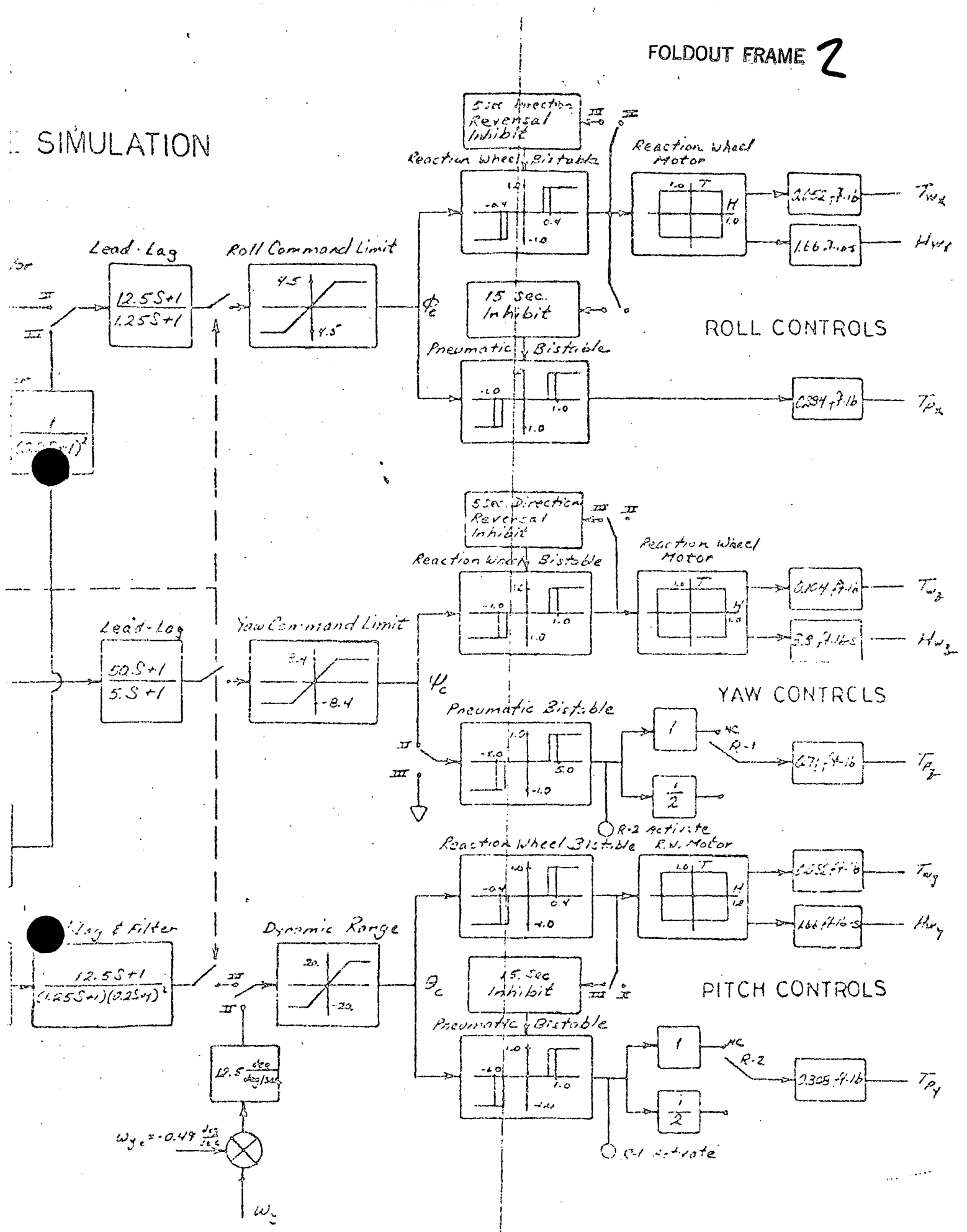

Figure 6-26

In Mode III, roll and pitch control signals are obtained from the horizon scanners and the yaw control signal is obtained from the sun sensors as in Mode II. Yaw pneumatic control is inhibited in Mode III.

The direction cosines are used to determine which heads are non-tracking. This information is used to set logic switches to provide the proper computation of roll and pitch angles from the head angles. If two or more heads are not tracking, control about all three axes is inhibited. If control is not resumed within seven minutes, control will revert to the sun acquisition mode.

6.2.4 Simulation Results

6.2.4.1 Sun Acquisition (Mode II)

In Mode II the ACS attempts to point the body negative y-axis ($-y_b$) at the sun by controlling roll and yaw body motions. The body pitch rate is commanded to -0.49 deg/sec.

Sun acquisition was initiated from 25 positions over the vehicle sun unit sphere (vehicle at center of sphere and unit vector directed towards the sun). Each position was evaluated for 17 sets of initial body rates (combinations of ± 1, ± 0.5 and 0 deg/sec). Initial conditions evaluated are shown in Table 6-7.

The sun acquisition performance of the ACS with the increased yaw pneumatic deadzone was evaluated using the initial condition set described above. The impulse, in units of lb-sec needed to acquire the sun from each set of initial direction cosines - for the worst case combination of body rates - are indicated in Figure 6-29. The large circles represent planes of constant a_{22} intersecting the unit sphere. Data points for the appropriate initial values of a_{12} are indicated by small circles.

The maximum impulse required for Mode II was 70 lb-sec for initial conditions of $a_{12} = 0$, $a_{22} = a_{32} = -0.707$, $\omega_x = \omega_y = 0.5$, and $\omega_z = -0.5$ deg/sec. Acquisition time was 9.2 min. In general 5-15 lb-sec impulse and 100-150 sec were required to complete sun acquisi-

TABLE 6-7

Sun Acquisition Initial Conditions

Case No.	a_{12}	a_{22}	a_{32}
1	0	-1	0
2	.707	-.707	0
3	-.707	-.707	0
4	0	-.707	.707
5	0	-.707	-.707
6	0	.707	-.707
7	0	.707	.707
8	.707	.707	0
9	-.707	.707	0
10	-.707	0	.707
11	-.707	0	-.707
12	.707	0	-.707
13	.707	0	.707
14	.577	-.577	-.577
15	-.577	-.577	-.577
16	-.577	-.577	.577
17	.577	-.577	.577
18	.577	.577	.577
19	-.577	.577	.577
20	-.577	.577	-.577
21	.577	.577	-.577
22	0	0	1
23	0	0	-1
24	-1	0	0
25	1	0	0

Rates $\omega_x = \omega_y = \omega_z$ = 1.0, 0.5, and 0 deg/sec

Sub Case	ω_x	ω_y	ω_z
a	+	+	+
b	+	+	-
c	+	-	-
d	+	-	+
e	-	-	+
f	-	+	+
g	-	+	-
h	-	-	-
i	0	0	0

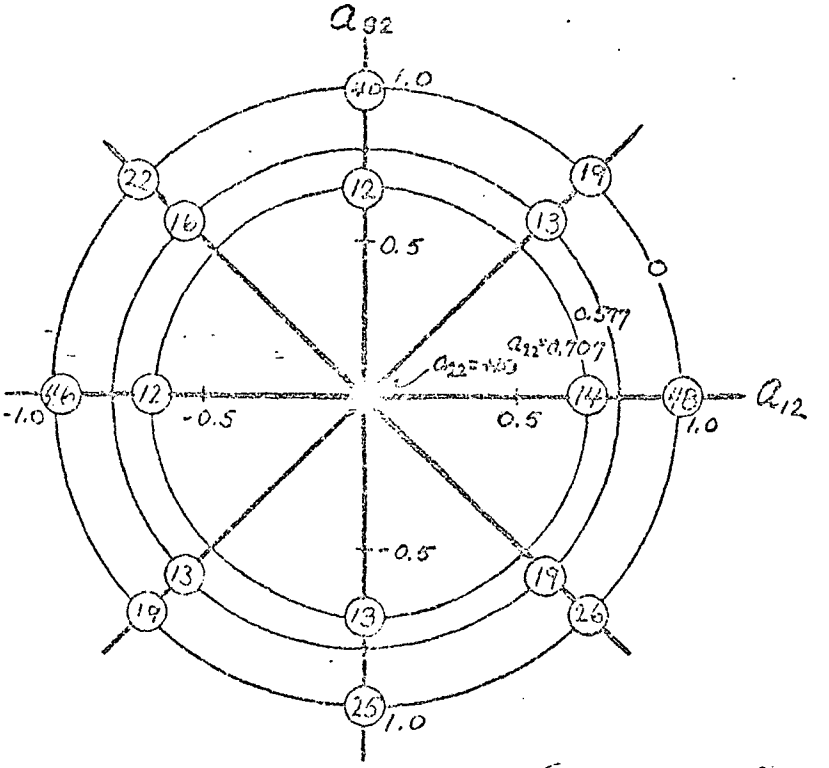

(a) a_{22} greater than 1.0

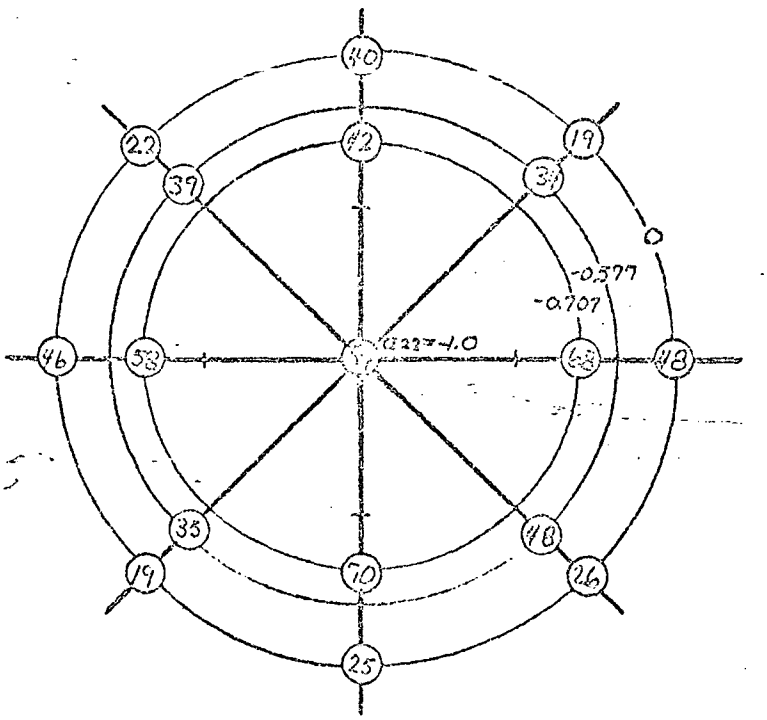

(b) a_{22} less than 1.0

Figure 6-27 Worst Case Impulse for Sun Acquisition vs. Initial Orientation for Worst Case Initial Rate Combination

* (70) indicates 70 lb-sec of impulse was consumed to acquire sun from a_{12} (0) = 0 $a_{32} = a_{22} = -.707$ for worst case set of initial rate combination which in this case was $\omega_x = \omega_y = 0.5$ and $\omega_z = -0.5$ deg/sec.

tion for $a_{22} < 0$ and 20-50 lb-sec impulse and 100-300 sec for $a_{22} < 0$.

Sun acquisition was evaluated for several configurations other than nominal to determine if the sun could be acquired in the presence of noncatastrophic failures or for worst case system parameter tolerances. Configurations evaluated were:

(a) The new nominal system (CGO-D).

(b) Pneumatic and reaction wheel inhibits active. This could only occur for a logic failure since the inhibits are normally deactivated during Mode II.

(c) No pitch control. Loss of pitch control could result from failure of the rate gyro.

(d) Former nominal system (CGO-III). The significant difference between the former and new nominal ACS insofar as Mode II performance is concerned has been the widening of the yaw pneumatic deadzone from 2.5 to 5.0 degrees.

(e) Worst case tolerances for vehicle mass properties and ACS parameters. Worst case tolerance polarities chosen were obtained from single axis studies.

Configurations other than nominal were evaluated only for $a_{22} < 0$. Figure 6-28A and 6-28B are brush recordings of vehicle response for the nominal system and the four variations from nominal for initial conditions of $a_{22} = -1$ and body rate = 1 deg/sec (except for case c). The sun was acquired in all cases. Nominal system response is shown in Case a of Figure 6-28A and 6-28B.

The effect of activating the pneumatic and reaction wheel inhibits was to reduce system damping (see Figure 6-30 and 6-31) and thus increase impulse requirements and acquisition time. The sun was acquired generally within 400-900 seconds with 30-70 lb-sec impulse; this compares with 100-300 seconds and 20-50 lb-sec impulse for the nominal system.

All 25 combinations of direction cosines were evaluated for Case (c) above. Zero initial body rates were employed to accentuate the effects of not controlling pitch. In general the impulse and acquisition times

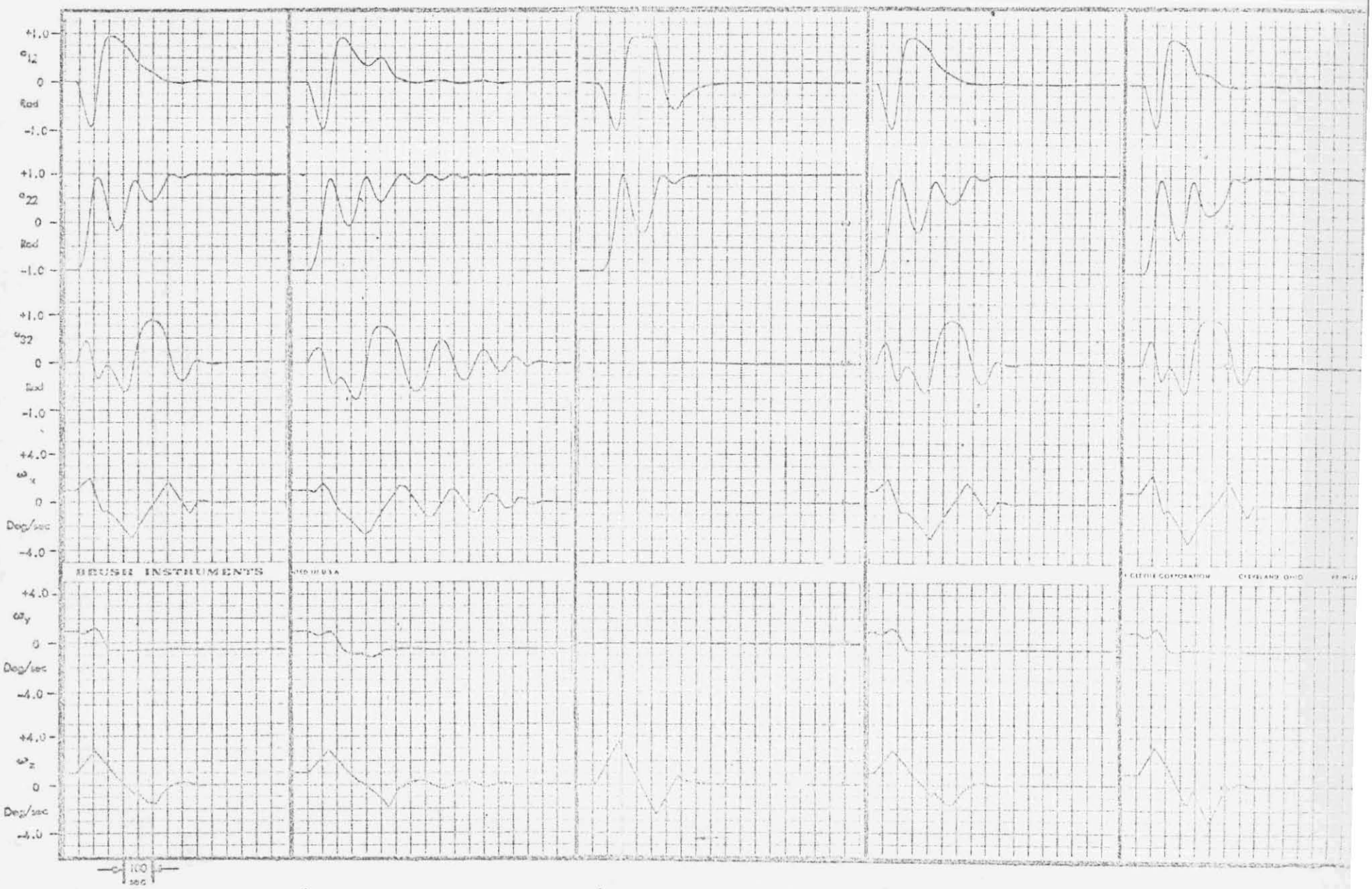

a) Nominal b) Inhibits Active c) No Pitch Control d) Old Nominal e) Worst Parameters

Figure 6-28A Typical Sun Acquisition Response for Various ACS Configurations

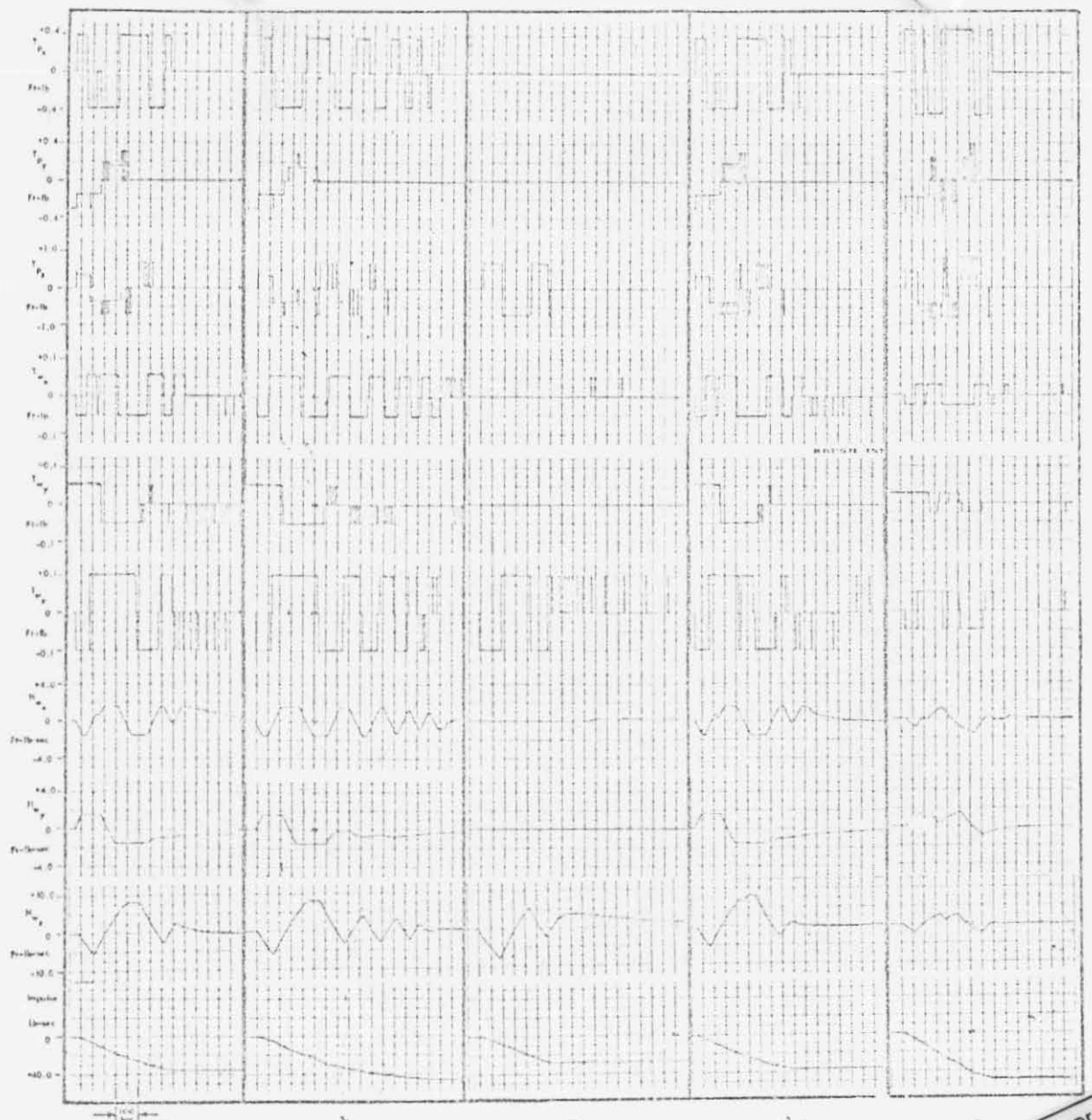

a	b	c	d	e
Nominal	Inhibits Active	No Pitch Control	Old Nominal	Worst Parameters

Figure 6-28B Typical Sun Acquisition Response for Various ACS Configurations

TABLE 6-8

Initial Direction Cosines Evaluated in Mode III Studies

				$a_{12} = 0$		$a_{22} = 0$	
Case No.	a_{13}	a_{23}	a_{33}	a_{22}	a_{32}	a_{12}	a_{32}
1	0.2	0.2	0.9592	0.9790	-0.2041	0.9790	-0.2041
2	0.2	-0.2	"	"	+	"	-
3	-0.2	-0.2	"	"	+	"	+
4	-0.2	0.2	"	"	-	"	+
5	0.4	0.2	0.8944	0.9759	-0.2182	0.9128	-0.4082
6	-0.4	0.2	"	"	-	"	+
7	-0.4	-0.2	"	"	+	"	+
8	0.4	-0.2	"	"	+	"	-
9	0.4	0	0.9165	1.0	0	0.9165	-0.4
10	-0.4	0	"	"	0	"	0.4
11	0.2	0.4	0.8944	0.9128	-0.4082	0.9759	-0.2182
12	0.2	-0.4	"	"	+	"	-
13	-0.2	-0.4	"	"	+	"	+
14	-0.2	0.4	"	"	-	"	+
15	0	0.4	0.9165	0.9165	-0.4	1.0	0
16	0	-0.4	"	"	0.4	1.0	0
17	0.3	0.5	0.8124	0.8517	-0.5241	0.9381	-0.3464
18	0.3	-0.5	"	"	+	"	-
19	-0.3	-0.5	"	"	+	"	+
20	-0.3	0.5	"	"	-	"	+
21	0.5	0.3	"	0.9381	-0.3464	0.8517	-0.5242
22	0.5	-0.3	"	"	+	"	-
23	-0.5	-0.3	"	"	+	"	+
24	-0.5	0.3	"	"	-	"	+
25	0.6	0	0.8	1.0	0	0.8	-0.6
26	-0.6	0	0.8	1.0	0	0.8	-0.6
27	0	0.6	"	0.8	-0.6	1.0	0
28	0	-0.6	"	0.8	0.6	1.0	0

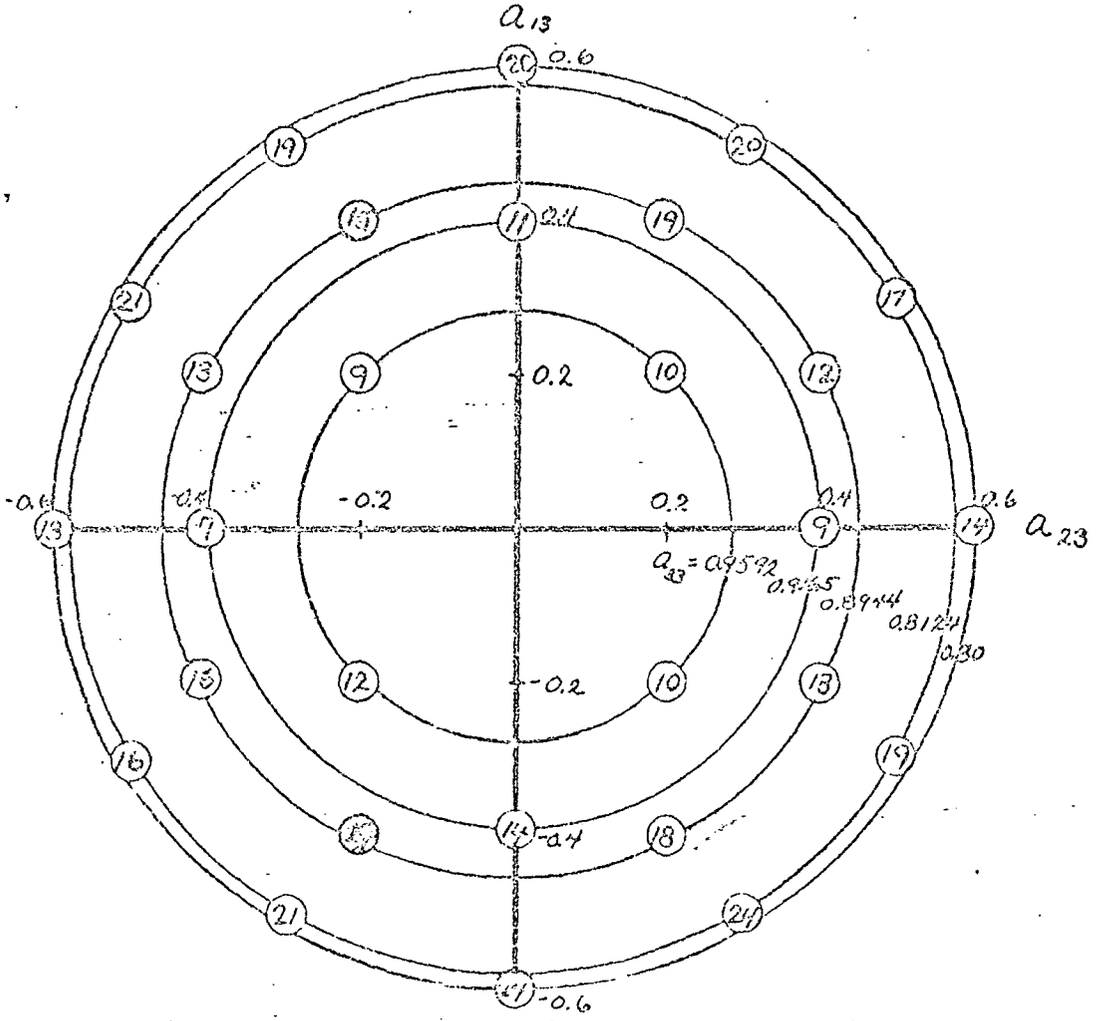

a) Earth Reacquisition (Zero Initial Rates)

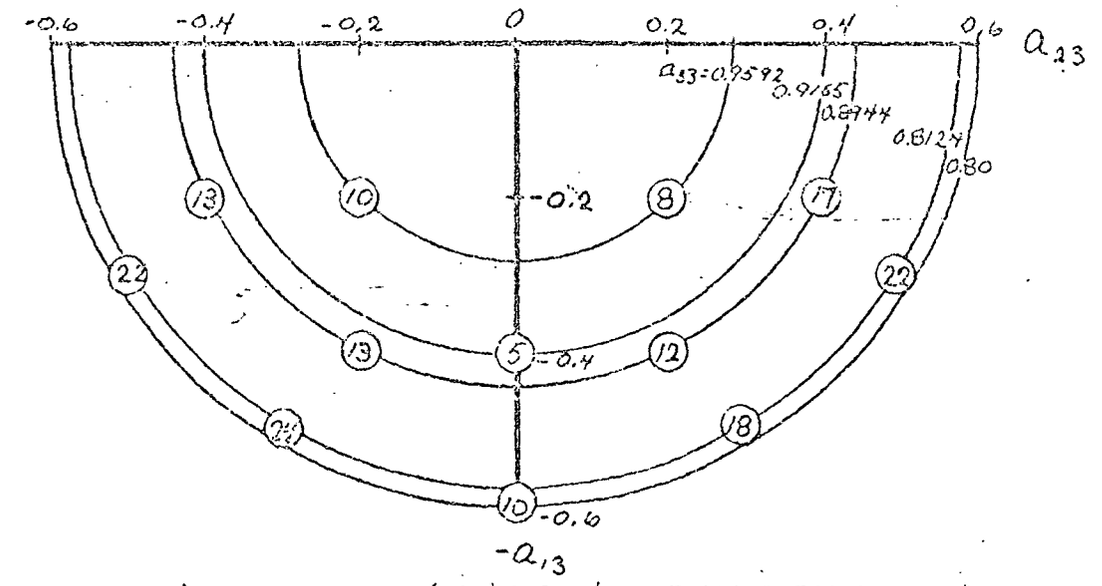

b) Acquisition (-0.49 deg/sec Initial Pitch Rate)

Figure 6-29 Earth Acquisition Impulse with Inhibits vs Initial Attitude

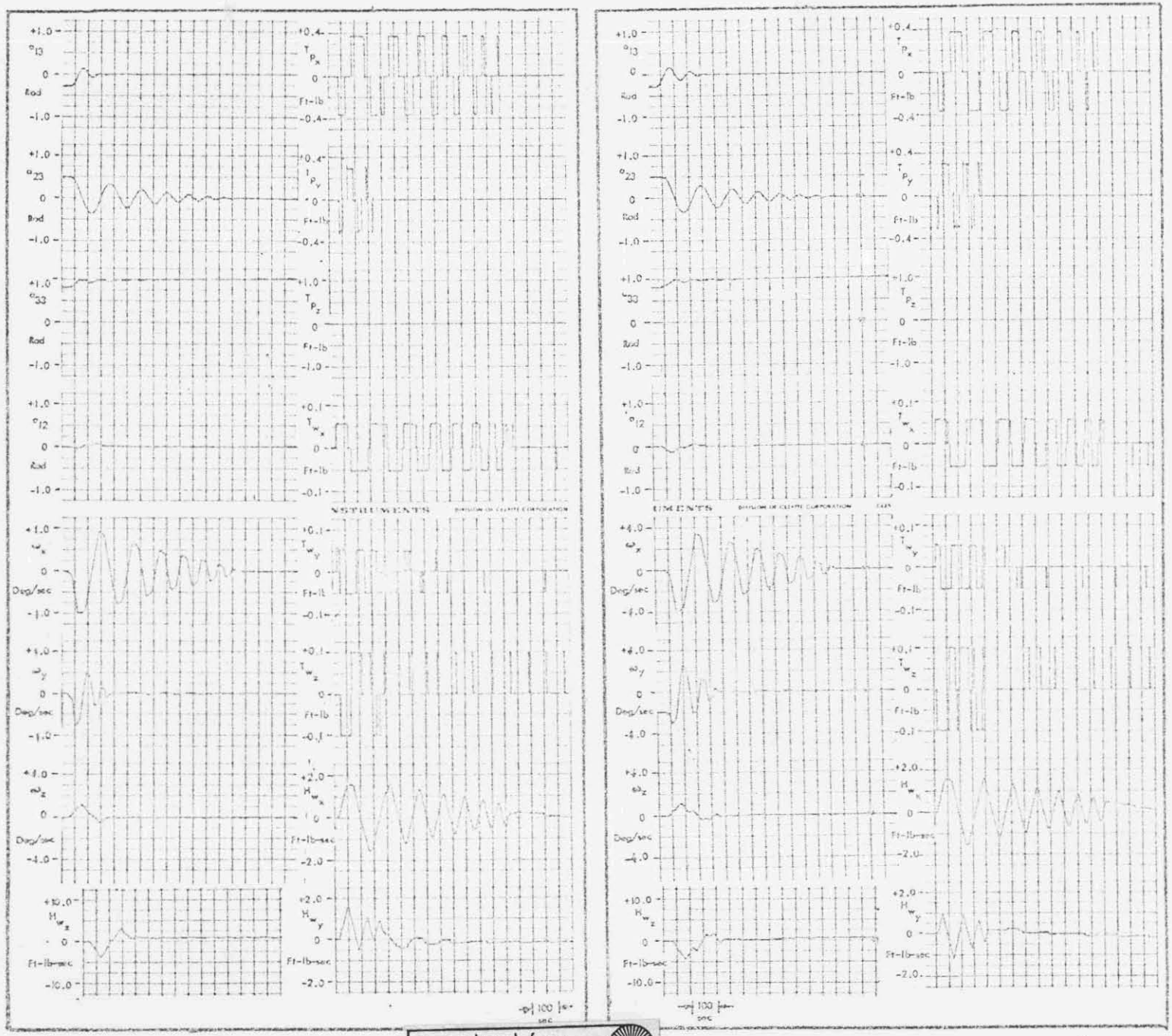

a) Reacquisition $\omega_i(o) = 0$

b) Acquisition $\omega_y(o) = -0.49$ ~~deg/sec~~

Figure 6-30 Typical Earth Acquisition Response Inhibits Active

List of References

6-1 67-7231.7-8, "Simulation Plan for CGO Roll Axis Design Verification", R. W. Hoffman, 18 January 1967

6-2 67-7231.7-18, "Simulation Plan for CGO Pitch and Yaw Axis Design Verification," R. W. Hoffman, 19 January 1967.

6-3 67-7231.1-59, " CGO Acquisition Simulation," G. Hobbs, 6 April 1967.

6-4 66-7231.1-50, "Evaluation of PCGO ACS Performance Following Sun Disturbances Generated by the Horizon Scanners During Post Eclipse Maneuvers," J. E. Dickinson, 22 July 1966.

APPENDIX A

SYSTEM DYNAMIC EQUATIONS

Figure A-1 defines a simplified single axis representation of the OGO as it would appear for rotations about the yaw axis. In addition to the assumptions detailed in Section 4.1, the model further assumes that each solar array has a De Havilland type boom attached (OGO E configuration) and that the "+x" and "-x" solar array boom combinations are identical. Under this condition, the flexible dynamics of the solar array and Haddock booms may be modeled as one solar array-boom combination with a moment of inertia, spring and damping constant equal to twice that of a separate model for each side.

The model shown in the figure is modified depending upon the axis under consideration as defined below.

Roll - Torsional rotation of the solar array is neglected so the rigid body inertia I_E includes not only the OGO main box but the solar arrays and Haddock booms. Only experimental booms EP-5 and EP-6 are modeled as appendages in rotations about the roll axis.

Pitch- Neglecting cross-coupling, the booms EP-5 and EP-6 are considered as part of the rigid body inertia I_B and only the solar array and Haddock booms are modeled as appendages.

Yaw - Experimental booms EP-5 and EP-6, solar array, and Haddock booms are modeled as appendages (Figure A-1).

Symbols are defined below:

M_D equivalent mass of two Haddock booms (slugs)

L_D length of Haddock boom (ft)

L_A length from center of mass of OGO main box to point of attachment of Haddock boom on solar array (ft)

ω_i fundamental resonant frequency of i^{th} appendage (rad/sec)

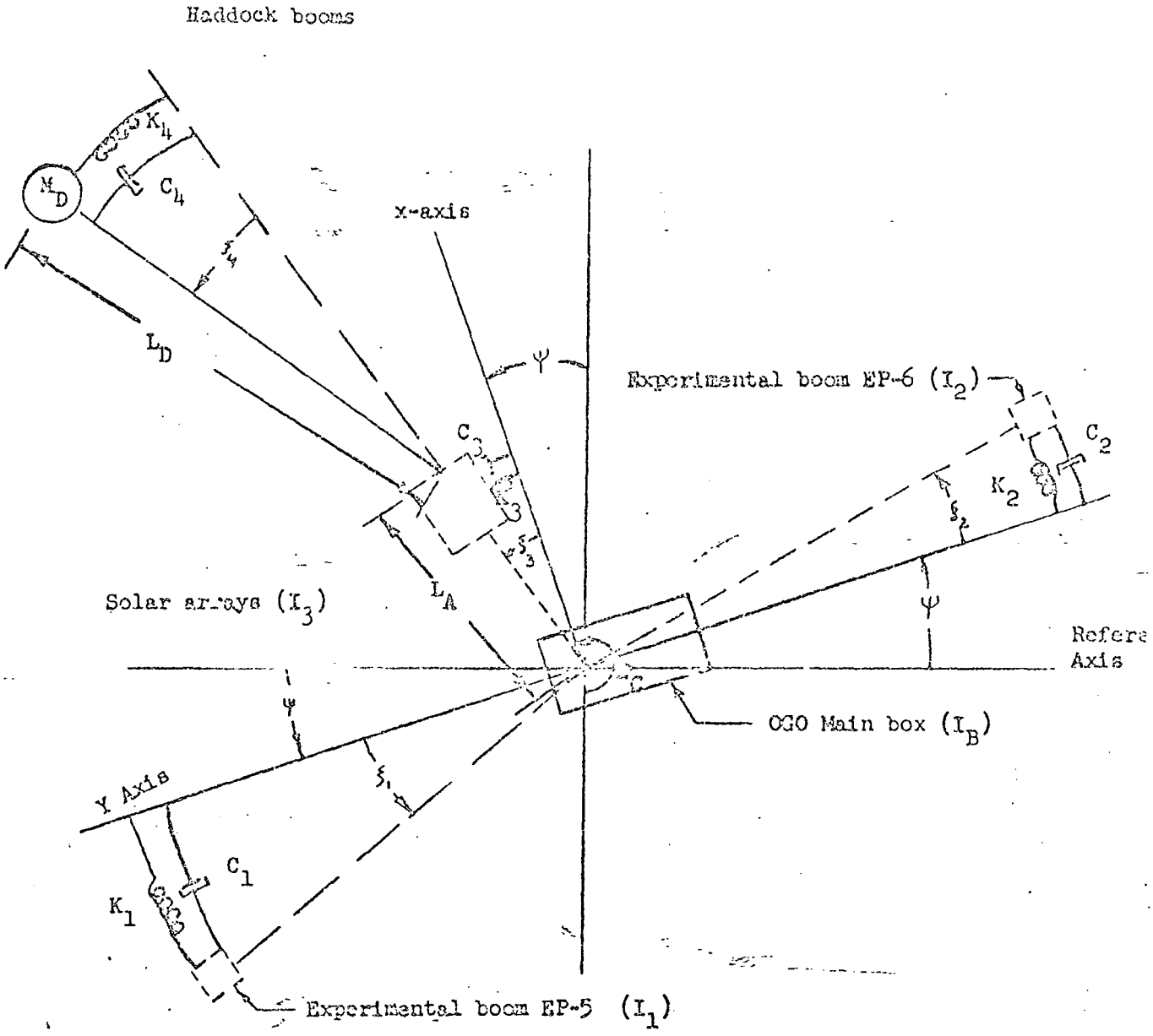

Figure A-1. Simplified Single Axis (Yaw) Model of OGO's Appendages

I_B moment of inertia of OGO main box about its center of mass (slug-ft^2)

I_i moment of inertia of i^{th} appendage about OGO's center of mass (slug-ft^2)

K_i spring constant of i^{th} appendage (ft-lb/rad)

C_i damping constant of i^{th} appendage (ft-lb-sec/rad)

ξ_i rotation of i^{th} appendage with respect to its equilibrium position (rad)

ϕ, ψ, θ rotations of OGO's main box with respect to inertial space about the roll, yaw, and pitch axes respectively (rad)

Lagrange's equation may be utilized to establish the equations of motion:

$$\frac{d}{dt}\left[\frac{\partial f}{\partial \dot{q}_i}\right] - \frac{\partial (T-U)}{\partial q_i} + \frac{\partial F}{\partial \dot{q}_i} = N_c \qquad \text{A-1}$$

where

T is the system kinetic energy in terms of the generalized coordinates $\dot{q}_i$

U is the system potential energy in terms of the generalized coordinate q_i

F is the Rayleigh dissipation function

N_c is the applied control torque

In terms of the generalized coordinates $q_i = \psi, \xi_1, \xi_2, \xi_3$, and ξ_4,

$$T = \frac{1}{2} I_B \dot{\psi}^2 + \frac{1}{2} I_1 (\dot{\psi} + \dot{\xi}_1)^2 + \frac{1}{2} I_2 (\dot{\psi} + \dot{\xi}_2)^2 + \frac{1}{2} I_3 (\dot{\psi} + \dot{\xi}_3)^2$$

$$+ \frac{1}{2} M_D \left[(L_D + L_A)(\dot{\psi} + \dot{\xi}_3) + L_D \dot{\xi}_4\right]^2 \qquad \text{A-2}$$

$$U = \frac{1}{2} \sum_{i=1}^{4} K_i \xi_i^2 \qquad \text{A-3}$$

$$F = \frac{1}{2} \sum_{i=1}^{4} C_i \dot{\xi}_i^2 \qquad \text{A-4}$$

Substituting equations (A-2, 3, 4) into (A-1) the equations of motion are:

$$\begin{aligned}
&\left[I_B + I_1 + I_2 + I_3 + M_D (L_D + L_A)^2 \right] \ddot{\psi} + I_1 \ddot{\xi}_1 + I_2 \ddot{\xi}_2 \\
&\qquad + \left[I_3 + M_D (L_D + L_A)^2 \right] \ddot{\xi}_3 + M_D L_D (L_D + L_A) \ddot{\xi}_4 = N_c \\
&I_1 \ddot{\psi} + I_1 \ddot{\xi}_1 + C_1 \dot{\xi}_1 + K_1 \xi_1 = 0 \\
&I_2 \ddot{\psi} + I_2 \ddot{\xi}_2 + C_2 \dot{\xi}_2 + K_2 \xi_2 = 0 \\
&\left[I_3 + M_D (L_D + L_A)^2 \right] (\ddot{\psi} + \ddot{\xi}_3) + C_3 \dot{\xi}_3 + K_3 \xi_3 + M_D L_D (L_D + L_A) \ddot{\xi}_4 = 0 \\
&M_D L_D (L_D + L_A) (\ddot{\psi} + \ddot{\xi}_3) + M_D L_D^2 \ddot{\xi}_4 + C_4 \dot{\xi}_4 + K_4 \xi_4 = 0
\end{aligned} \qquad \text{A-5}$$

where $N_c = N_w + N_g + N_p$ the wheel and gas control torques and solar array drive reaction torques respectively.

The rotation of OGO's main body about the yaw axis and its interaction with the flexible dynamics as a function of applied torque N_c may be investigated from the transfer function $\frac{\psi(s)}{N_c(s)}$ obtained from the La Place transform of the equations of motion (Equation A-5). Rotation about pitch and roll is also defined from Equation A-5 by deleting the appropriate appendage equation and incorporating the appendage into the body inertia.

The numerical values used in the analyses are summarized in Table A-1. The spring constant K_i and damping constant C_i are chosen to yield the same resonant frequency and damping as that of the appendage when cantilevered, i.e.,

$$K_i = I_i \omega_i^2$$

and

$$C_i = 2I_i \omega_i \zeta_i$$

where

ζ_i is the estimated appendage damping

ω_i is the fundamental resonant frequency of the i^{th} appendage determined from a bending mode analysis.

	Moment of Inertia I_i (slug-ft^2)	Resonant Frequency ω_i (rad/sec)	Damping ζ_i (%)	Spring Constant K_i (ft-lb/rad)	Damping Constant C_i (ft-lb-sec/rad)
YAW					
i = 0(Main Body)	213				
i = 1(EP-5)	216	1.51	0.3-0.05	493	1.95-0.32
i = 2(EP-6)	209	1.66	0.3-0.05	576	2.08-0.35
i = 3(2 solar array)	295	31.7	3	2.91×10^5	556
i = 4(Haddock booms)	52	0.145	0.05	1.1	7.6×10^{-3}
ROLL					
i = 0(Main Body)	245				
i = 1(EP-5)	216	same as	YAW	493	1.95-0.32
i = 2(EP-6)	209	same as	YAW	576	2.08-0.35
i = 3(2 solar array)	0	modeled as	rigid body	0	0
i = 4(Haddock booms)	0	modeled as	rigid body	0	0
PITCH					
i = 0(Main Body)	57				
i = 1(EP-5)	00	modeled as	rigid body	0	0
i = 2(EP-6)	0	modeled as	rigid body	0	0
i = 3(2 solar arrays)	305	31.4	3	2.91×10^5	556
i = 4(Haddock booms)	52	0.145	0.05	1.1	7.6×10^{-3}
L_D = 60 ft L_A = 8.7 ft $I_4 = M_D L_D^2$					

Table A-1 Parameter Values

APPENDIX B

SOLAR ARRAY DRIVE ASSEMBLY MODEL

B.1 Assumptions

A simplified schematic of the motor drive assembly is shown in Figure B-1. The computer model schematic is included as a part of Figure C-2.

The following assumptions were made in developing the model. For a more complete discussion of the model development see Reference B-1.

1. Sun Sensor - The sun sensor can be simulated by a first order lag with a 50 millisecond time constant.
2. Bistables and Magnetic Amplifier - The bistable are assumed to be a purely on-off element except for a turn-off time delay of the bi-stable and motor amplifier which can be represented by an equivalent increase in hysteresis.
3. Drive Motor -
   a) Motor torque/speed curve is linear (i.e., the torque decreases linearly with speed).
   b) Motor is rigidly coupled to main body.
   c) Compliance of coupling between motor rotor and wobble gear output is negligible.
   d) Static friction at motor output shaft is negligible.
   e) Coulomb friction and viscous friction in motor drive are considered lumped parameters and are referenced to motor shaft (wabble gear) output.
4. Paddles -
   a) Paddles are rigid. Only significant compliance of paddle section is torsional compliance of shaft.
   b) Paddles are identical, thus may be considered a single composite element.
   c) Wrap-up Coulomb friction forces act directly on paddles. This is not strictly true but a great simplification of the analog simulation results as compared to the case

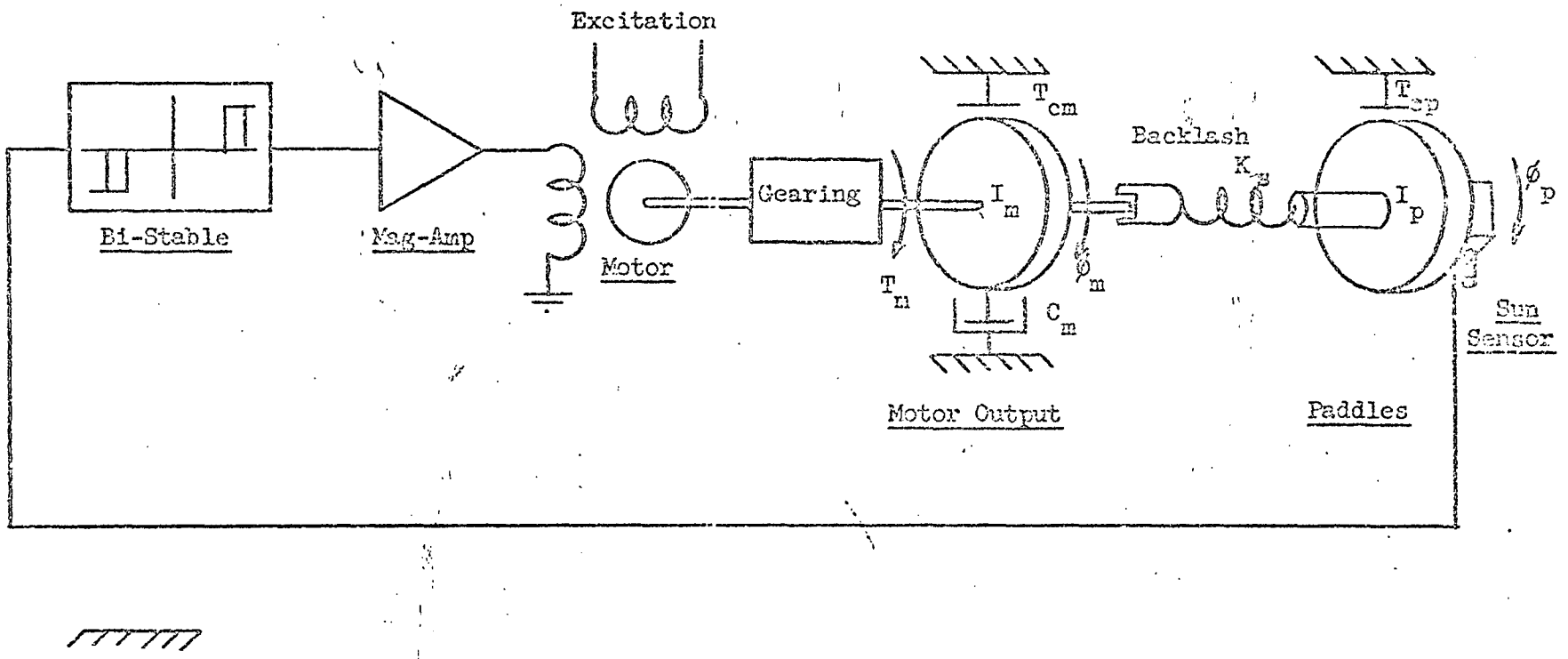

Figure B-1

Solar Array Drive Assembly Model Schematic

where the coulomb friction acts entirely on the shaft.

d) Structural damping of shaft is negligible relative to wrap-up Coulomb friction.

5. Coupling between Motor Output Shaft and Paddle Shaft - The effective backlash can be lumped between the motor output shaft (wabble gear) and paddle shaft.

B.2 Equations

The equations used for representation of the solar array drive motions were the following:

$$I_m \ddot{\phi}_m = T_m - C_m \dot{\phi}_m - T_{cm}(\text{sign } \dot{\phi}) - A$$

$$I_p \ddot{\phi}_p = -I_p \ddot{\phi} - T_{cp}(\text{sign } \dot{\phi}_p) + A$$

$$N_p = T_{cp}(\text{sign } \dot{\phi}_p) - A = -I_p(\ddot{\phi}_p + \ddot{\phi})$$

where

$$A = \begin{cases} K_s\,(\phi_m - \phi_p - \phi_b) & \text{for } (\phi_m - \phi_p) \geq \phi_b \\ 0 & \text{for } |\phi_m - \phi_b| < \phi_b \\ K_s\,(\phi_m - \phi_p + \phi_b) & \text{for } (\phi_p - \phi_m) \geq \phi_b \end{cases}$$

N_p = Torque of solar array on the main spacecraft.

B.3 Parameter Values

The parameter values presented in Table B-2 used for the model are taken from Reference B-1 and further testing of the solar array models.

References

B-1. 66.7231.8-121, "Analysis and Test Results of the OGO Solar Array Drive Assembly Study," L. C. George, 10 November 1966.

Symbol	Definition
ϕ_m	- Solar array drive motor angle
ϕ_p	- Paddle angle relative to body
ϕ_{pi}	- Paddle angle relative to inertial space
ω_o	- Orbit rate
e_p	- Solar array drive error (see Figure C-2)
e_{ps}	- Sun Sensor Output (see Figure C-2)
I_p	- Paddle Inertia
τ_s	- Sun sensor time constant
ϕ_{dp}	- Solar Array bi-stable deadzone
h_{p1}	- Hysteresis of solar array bi-stable
h_{p2}	- Hysteresis equivalent to solar array motor turn off delay time
h_p	- $h_{p1} + h_{p2}$
T_p	- Solar array inhibit logic time delay
I_m	- Motor inertia reflected to output shaft (wobble gear output)
T_{ms}	- Motor stall torque reflected to output shaft
ω_s	- Motor no load speed reflected to output shaft
T_{cm}	- Motor Coulomb friction at output shaft
C_m	- Motor Viscous friction at output shaft
ϕ_b	- Backlash between output shaft and solar array paddle
K_s	- Stiffness of interposing surfaces of output shaft and solar array paddle
T_{cp}	- Coulomb friction at solar array paddle
N_p	- Torque imparted to main body by solar array

Table B-1 Solar Array Drive Nomenclature

Item	Parameter	Nominal Value	Max. Variation About Nominal
Sun Sensor	τ_s	.05 sec	0%
S.A. Bi-Stable	$\lvert\phi_{dp}\rvert$	0.9^o	± 20%
	h_{p1}	$.21^o$	± 33%
	h_{p2}	$.1^o$	± 50%
Solar Array Inhibit Logic	T_p	5.0 sec	± 50%
S.A. Motor	I_m	55.0 slug ft^2	± 20%
	T_s	35.0 ft lb	± 30%
	ω_s	1.6^o/sec	± 20%
	T_{cm}	2.0 ft lb	± 100%
	C_m	110 (ft-lb)/(rad/sec)	+ 100%; - 50%
S.A. Paddle	$\lvert\phi_b\rvert$	$.1^o$	+ 100%; - 50%
	K_s	1920 (ft-lb)/rad	± 100%
	I_p	10.4 slug ft^2	± 50%
	T_{cp}	2 ft lb	± 100%

Table B-2 Solar Array Drive Parameter Values

APPENDIX C

OPEP MODEL

A complete description of the OPEP control system can be found in References C-1 and C-2. For purposes of this study, the block diagram of Figure C-1 was used for both the analysis and the analog computer simulation and is valid for small OPEP error angles. The various parameters shown in the diagrams are defined in Table C-1.

C.1 Assumptions

The assumptions made in deriving the OPEP motor drive model were essentially the same as the solar array drive (see Appendix B), with the following additions:

1. The effect of drive backlash was neglected.
2. The experiment package inertia was neglected.
3. Turn off time delay of the bistables was neglected.
4. The gyro could be represented by a first order lag with a 50 millisecond time constant.

C.2 Block Diagram Reduction

The purpose of the following analysis is to demonstrate that the pulse ratio modulator does provide an effective rate feedback in addition to the large lag time constant of the filter. A block diagram of the OPEP control system which was used for the analysis is shown below in Figure C-2. This block diagram was derived from Figure C-1 by neglecting the motor Coulomb friction and normalizing the bistable where

$$K_D = \omega_o O_d$$

$$K_1 = KO_d$$

$$K_m = T_{ms}/C_m$$

$$\tau_m = I_m/C_m$$

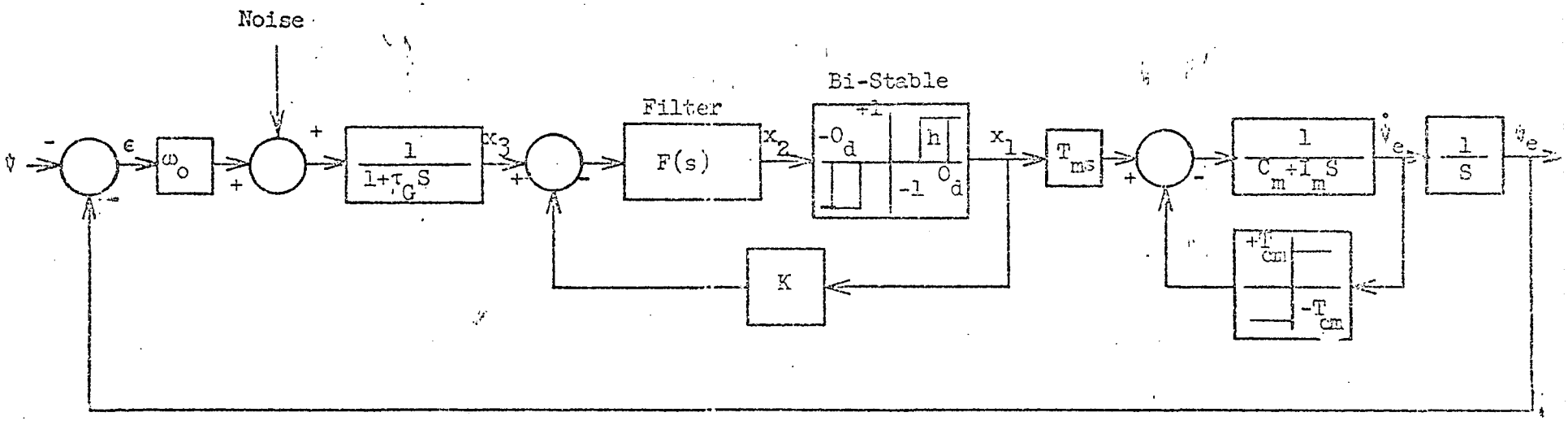

Figure C-1. OPEP Control System Block Diagram

Symbol	Definition	Value
ϕ_e	- OPEP angle with respect to body	
ϵ	- OPEP error	
X_1	- Bi-Stable output	
X_2	- Filter output	
X_3	- Gyro output	
ω_o	- Orbit rate	Max POGO - .06? deg/sec Max EGO - .09? deg/sec
τ_G	- Gyro time constant	.050 sec
τ_f	- Filter time constant	?0.0 sec
O_d	- OPEP bi-stable deadzone	17.?5 deg/sec
h_o	- OPEP bi-stable hysteresis	3.4 deg/hr
I_m, C_m, T_{cm}, ω_s, T_{ms}	See Appendix B	

Table C-1 OPEP Nomenclature

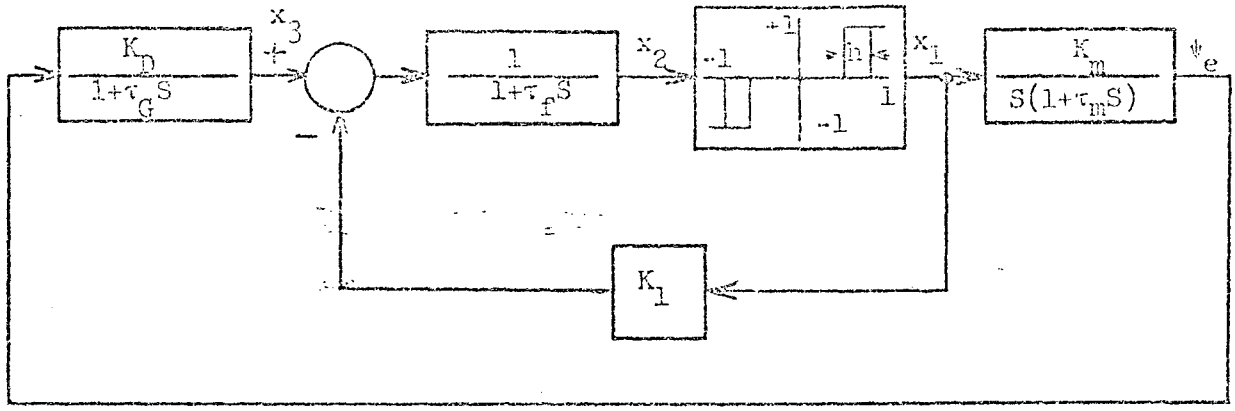

Figure C-2 - OPEP Control System Block Diagram

Since τ_G and τ_m are much small than τ_f, the time constants of the gyro and motor are neglected and the resulting block diagram is shown below in Figure C-3.

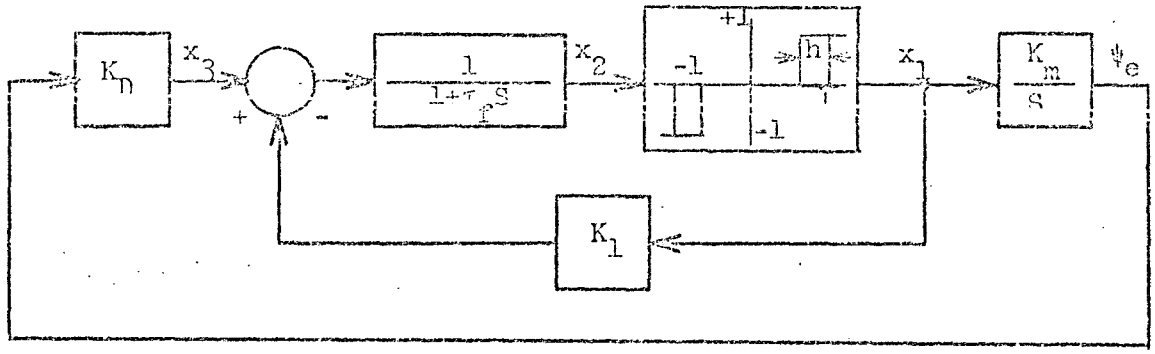

Figure C-3 - OPEP Control System for $\tau_F >> \tau_G, \tau_m$

By block diagram manipulation, without changing the input and output of the nonlinearity, the above diagram was redrawn to the following.

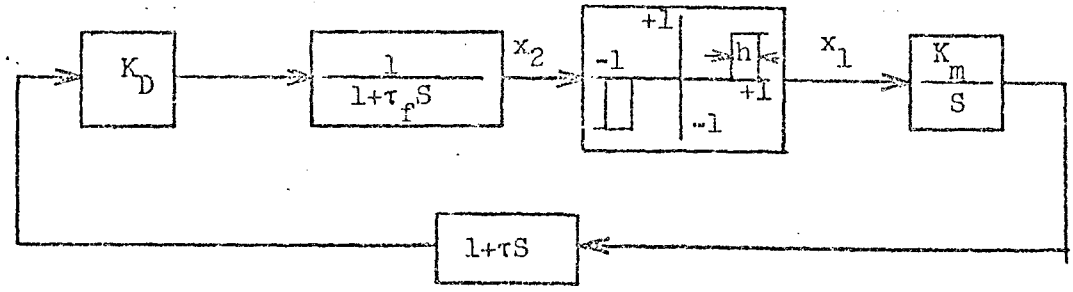

Figure C-4 - Simplified OPEP Control System Block Diagram

where,

$$\tau = \frac{K_1}{K_D K_M}$$

It can now be clearly seen that the pulse ratio modulator introduces lead into the OPEP control loop which reduces the destabilizing effect of the filter phase lag. For the selected pulse ratio modulator configuration, τ = 10.1 sec for the POGO orbit.

C.3 Stability Analysis

It was demonstrated above that the pulse ratio modulator introduces phase lead in addition to the filter phase lag. In this section, a relationship between the system parameters is derived to insure that limit cycle operation will not occur.

The block diagram of the OPEP control system is shown in Figure C-4, where the time constants for the motor and gyro were neglected and $\dot{\psi}$ = 0. Representation of the system in terms of the state variables (y_2, y_1) makes it convenient for phase plane analysis and the application of point transformation to determine limit cycle operation.

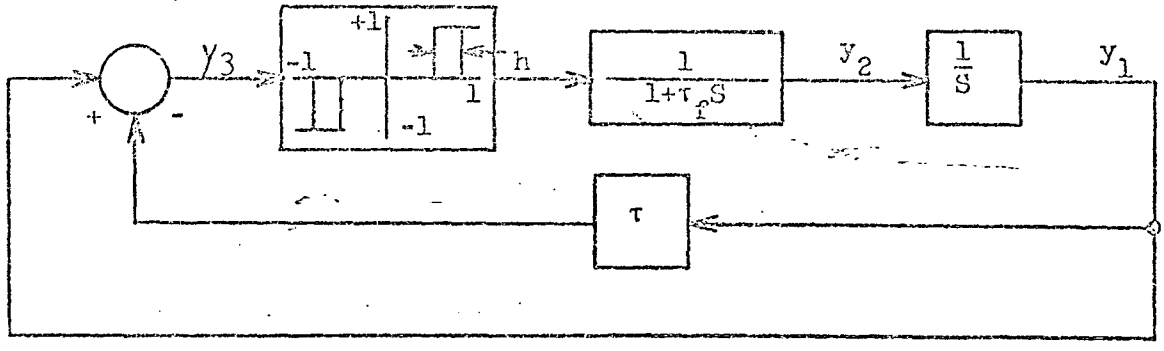

Figure C-5

The parameters in Figure C-5 are related to those used in Figure C-2 by the following:

$$d = \frac{1}{K_M K_D}$$

$$\tau = \frac{K_1}{K_M K_D}$$

The OPEP angle (ψ_e) is related to the state variables by the following transformation.

$$\psi_e = K_m y_1 (1+\tau_f S)$$

To investigate the existence of limit cycle operation, it is sufficient to analyze the system in the phase plane. In terms of the state variables, the dynamic system can be represented by the following equations.

$$\dot{y}_1 = y_2 \qquad \text{(C-1)}$$

$$\dot{y}_2 = -\omega_f \left[y_2 - n(y_3) \right] ; \quad \omega_f = \frac{1}{\tau_f} \qquad \text{(C-2)}$$

$$y_3 = -(y_1 + \tau y_2) \qquad \text{(C-3)}$$

$$n(y_3) = \begin{cases} 0, & \text{in Region I} \\ -1, & \text{in Region II} \\ +1, & \text{in Region III} \end{cases} \qquad \text{(C-4)}$$

Equation (3) together with the bi-stable nonlinearity define the switching lines between the regions of the phase plane. Figure C-6 illustrates the phase plane with the switching lines between the regions of operation. Also, a typical phase plane trajectory is shown for the existence of a limit cycle.

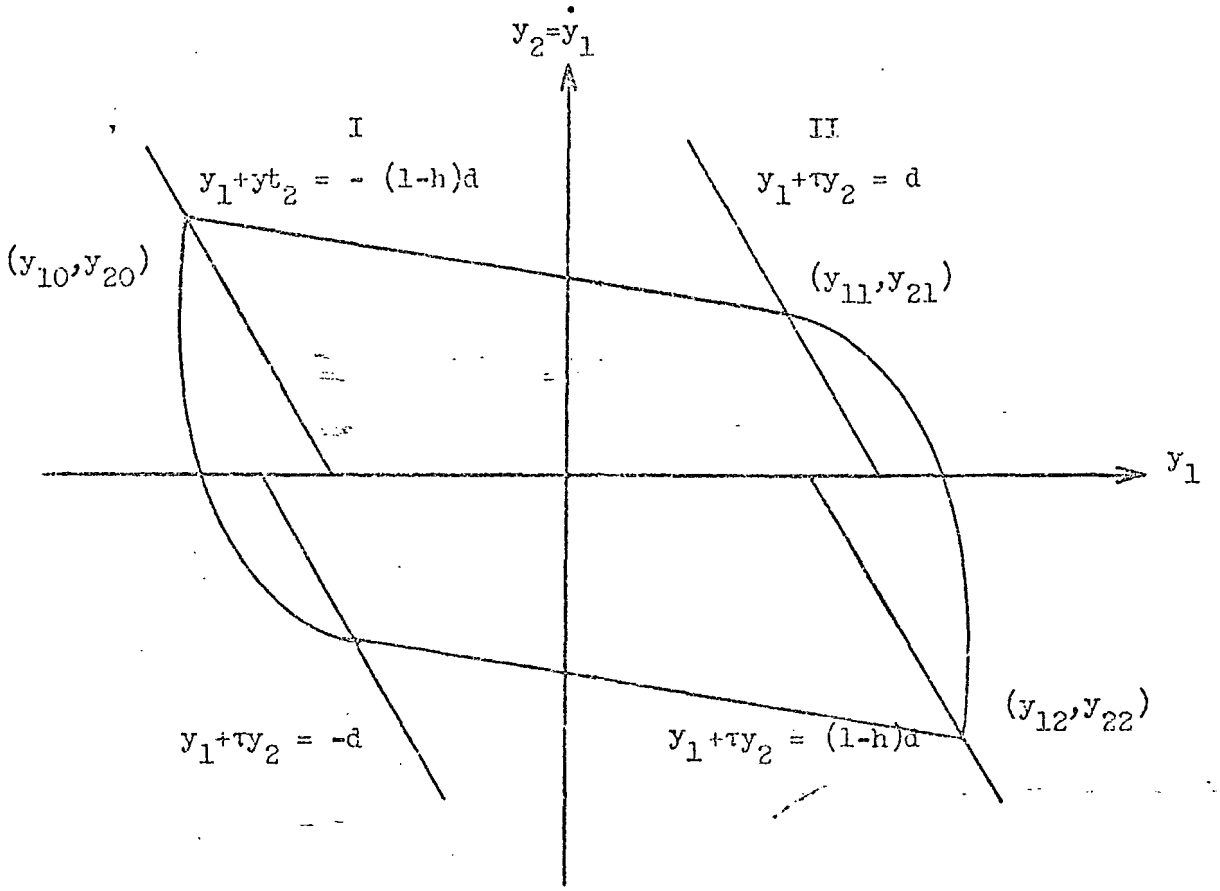

Figure C-6 Phase Plane

The trajectories in the three regions of the phase plane can be found from

$$\frac{dy_2}{dy_1} = \frac{-\omega_f [y_2 - n(y_3)]}{y_2} \qquad (C\text{-}5)$$

and are

$$\text{Region I} : \quad y_2 + \omega_f y_1 = c_1$$

$$\text{Region II} : \quad y_2 + \omega_f y_1 = \ln(y_2 + 1) + c_2 \qquad (C\text{-}6)$$

$$\text{Region III} : \quad y_2 + \omega_f y_1 = -\ln(y_2 - 1) + c_3$$

Using Equations (5) and (6), and the appropriate switching lines as indicated on Figure C-5, a relationship which maps state y_{20} into y_{22} on the phase plane was determined. This mapping is given by Equation (7).

$$\left[1 + y_{20} - \frac{\omega_f d\ (2-h)}{1-\omega_f \tau}\right] \exp\left[-(1-\omega_f \tau)\ y_{20} + 2\omega_f(1-h)d\right] =$$

$$(1 + y_{22}) \exp\left[-(1-\omega_f \tau)\ y_{22}\right] \qquad \text{(C-7)}$$

Because the nonlinearity is symmetric, the limit cycle must also be symmetric. Therefore, for a limit cycle to exist the following equations must be satisfied.

$$y_{22} = -y_{20} \triangleq -y \qquad \text{(C-8)}$$

Substituting Equation (8) into (7) and defining the functions $P_0(y)$ and $P_2(y)$ one obtains:

$$P_0(y) = P_2(y) \qquad \text{(C-9)}$$

where

$$P_0(y) = \left[1 + y - \frac{\omega_f d\ (2-h)}{1 - \omega_f \tau}\right] \exp$$

$$\left[1(1-\omega_f \tau)\ y + 2\omega_f(1-h)d\right] \qquad \text{(C-10)}$$

$$P_2(y) = (1 - y) \exp\left[(1-\omega_f \tau)\ y\right] \qquad \text{(C-11)}$$

For a limit cycle to exist, there must be an acceptable y which will satisfy Equation (9). It can be seen from Figure C-5 that the acceptable values for y are all greater than y_a, where,

$$y_a = \frac{\omega_f d\ (2-h)}{1-\omega_f \tau} \qquad \text{(C-12)}$$

Equation (9) cannot be solved; however, by plotting $P_0(y)$ and $P_2(y)$ as a function of y, a relationship necessary for the intersection can be found. Figure C-7 is a plot of both $P_0(y)$ and $P_2(y)$.

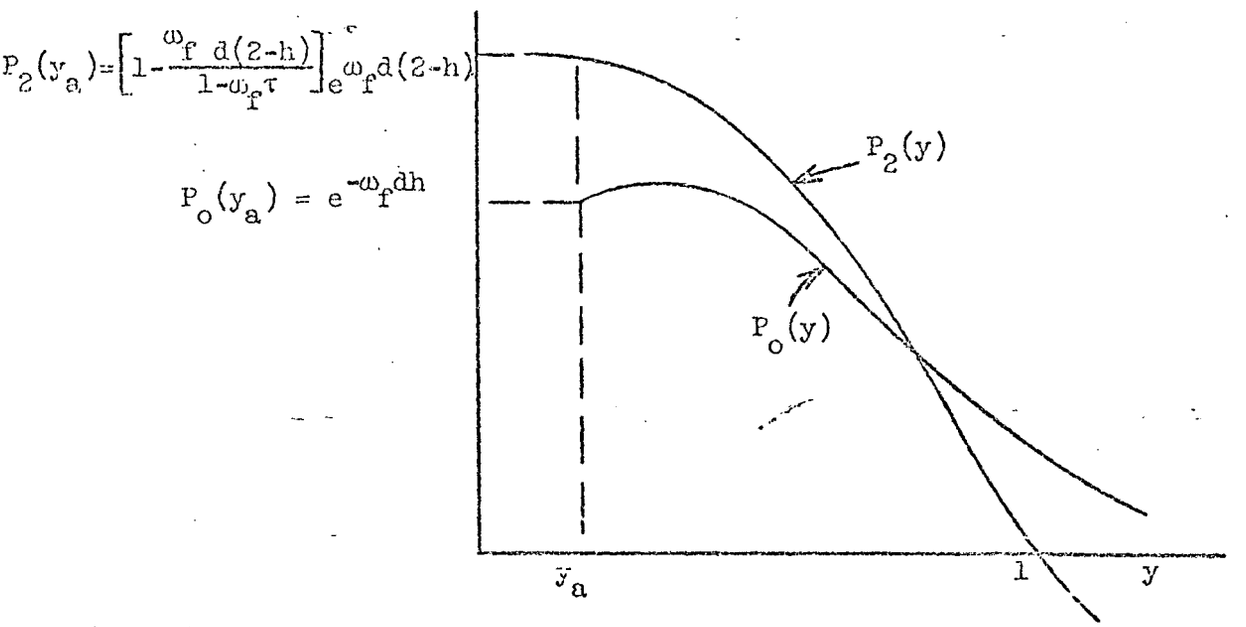

Figure C-7

Because $P_2(y) < 0$ for $y > 1$, and $P_0(y)$ is always greater than zero for all y, the curves cannot intersect in the region $y \geq 1$. It can be seen f rom the characteristics of the curves $P_0(y)$ and $P_2(y)$, a necessary condition for there intersection is

$$P_0(y_a) \leq P_2(y_a) \tag{C-13}$$

Therefore, no limit cycle will exist when

$$P_2(y_a) < P_0(y_a) \tag{C-14}$$

or

$$\left[1 - \frac{\omega_f\, d(2-h)}{1-\omega_f\tau}\right] < \exp[-2\omega_f d] \tag{C-15}$$

Substituting the system parameters for d and τ into the inequality of Equation (15) yields:

$$1 - \frac{\frac{2-h}{\tau_f K_M K_D}}{1 - \frac{K_1}{\tau_f K_M K_D}} < \exp\left[-\frac{2}{\tau_f K_M K_D}\right] \qquad \text{(C-16)}$$

From Equation (16) the value of the modulator feedback gain necessary to insure that the system will not limit cycle is:

$$\tau_f K_M K_D - \frac{2-h}{1-e^{-\frac{2}{\tau_f K_M K_D}}} < K_1 \qquad \text{(C-17)}$$

or

$$K_{1_{min.}} = \tau_f K_M K_D - \frac{2-h}{1-e^{-\frac{2}{\tau_f K_M K_D}}} \qquad \text{(C-18)}$$

Figure C-8 illustrates the minimum values for the modulator feedback as a function of K_D ($K_D \triangleq \frac{\omega_o}{D}$) for the OPEP parameters stated in Table C - 1. For the POGO orbit ($K_D = 0.226\ \text{deg}^{-1}$), the curve indicates that K_1 must be greater than 0.35 to insure that the system will not limit cycle. The value of K_1 chosen in the report was 3.68, this produces a minimum on time of two seconds.

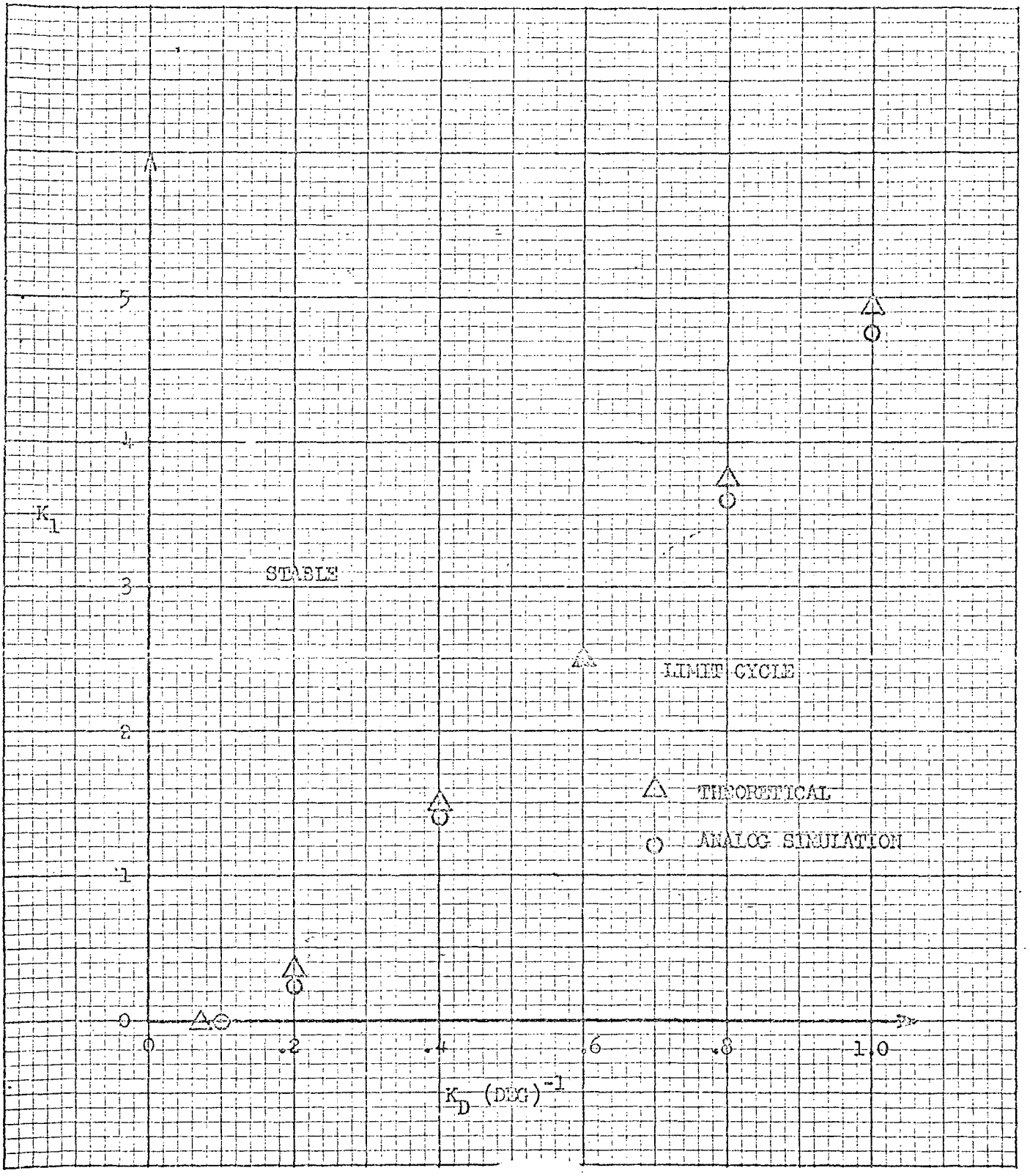

Figure C-18 Stability As A Function Of K_1

References:

C-1 9352.8-82, "OPEP Control System Design Summary," H.L. Mork 27 August 1962.

C-2 2313-00004-RV-000, "OGO Attitude Control Subsystem Description, Logic and Specifications," D. D. Otten, 4 December 1961.

APPENDIX D

SMALL ANGLE SIMULATION MODELS

The objective of this Appendix is to present the computer models used for the single axis design verification simulations. The assumptions used in model development, block diagrams for the models, and lists of nomenclature are provided herein. In addition, tables defining the range of parameter variations are provided.

D.1 Assumptions

The models and nomenclature for the system dynamics, solar array drive and OPEP are given in Appendixes A, B and C, respectively. Additional assumptions relating to the control torque sources are listed below.

Gas

a. The gas jets are assumed to respond instantaneously to the pneumatic bi-stable commands.

b. Specific-impulse of gas is constant.

Reaction Wheel

a. Reaction wheel damping due to windage is linear with wheel speed.

b. The reaction wheel "no-load" torque/speed curve of Figure D-1 applies. Momentum stored in the wheel at 1500 RPM is 1.66 ft-lb-sec for roll and pitch; the momentum stored in the yaw reaction wheel is 8.33 ft-lb-sec at 1500 RPM.

D.2 Computer Models

Block diagrams for the roll axis computer models are presented in Figures D-2 and D-3; an associated list of nomenclature is presented in Table D-1. The parameter values used for the normal mode for roll is presented in Table D-2; the roll acquisition parameter values are presented in Table D-3. Similarly block diagrams of the pitch and yaw models are provided by Figures D-4 and D-5. The pitch and yaw nomenclature are identical to roll except θ and ψ are substituted for ϕ

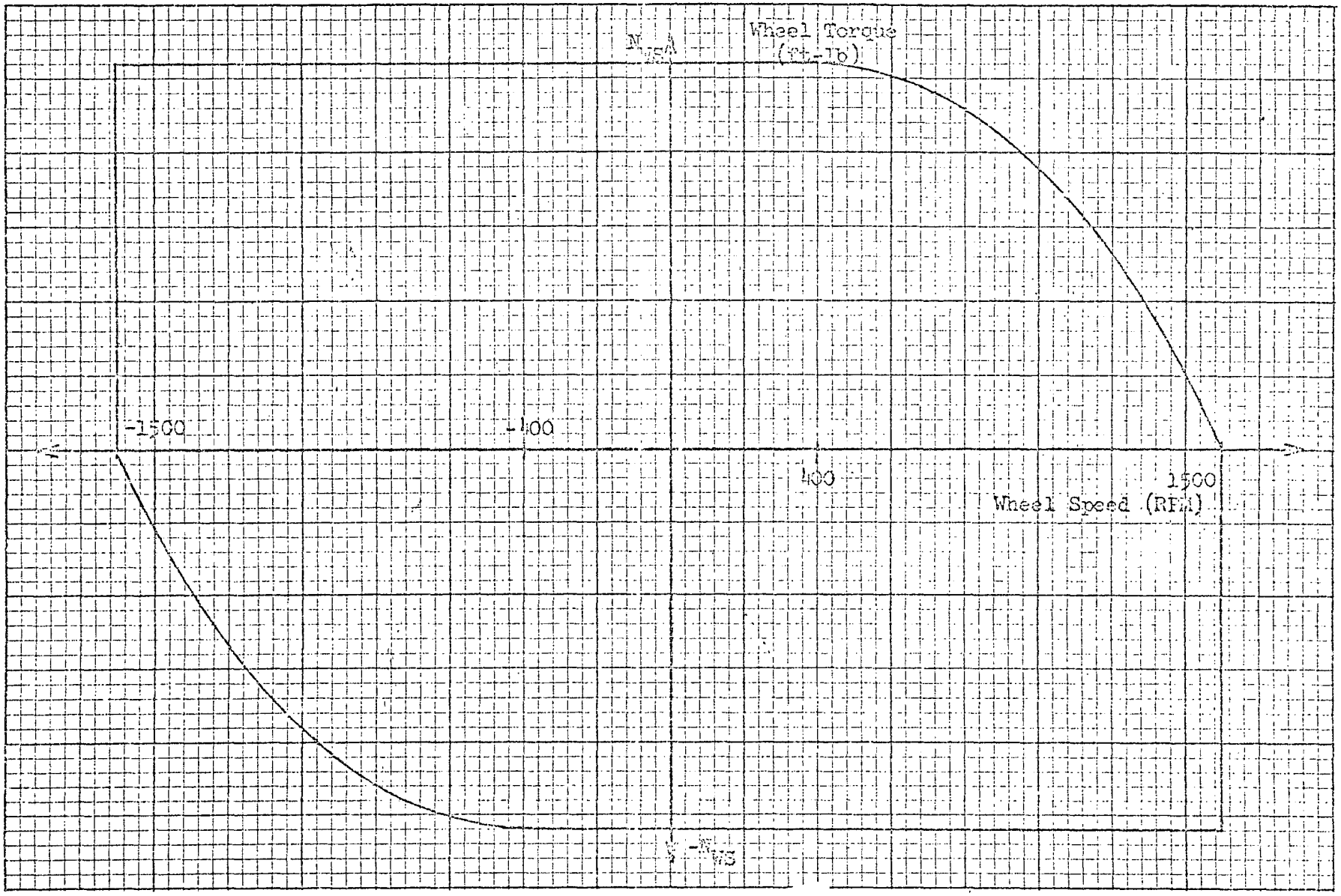

Figure D-1. Reaction Wheel Motor Torque Characteristics

where necessary. The parameter values for pitch are presented in Table D-4 and for yaw in Table D-5. The inhibit logic operation is described, a typical reaction wheel inhibit circuit is illustrated in Figure D-6.

D.3 Inhibit Logic Description

Inhibit schemes are used in the reaction wheel, gas and solar array control loops. The operation is as follows:

Reaction Wheel Inhibit

The reaction wheel inhibit prevents a torque command in opposition to the previous torque command from being applied to the reaction wheel until a fixed time "T_w" has elapsed. Operation of the reaction wheel inhibits are described by the truth tables below. The symbolism of the block diagram is utilized in the truth table.

Input to Inhibit C_w^+	Output of Inhibit C_{wi}^+
+1	+1 (If time "T_w^+" has elapsed since $C_w^- = -1$)
+1	0 (If time "T_w^+" has not elapsed since $C_w^- = -1$)

Input to Inhibit C_w^-	Output of Inhibit C_{wi}^-
-1	-1 (If time "T_w^-" has elapsed since $C_w^+ = +1$)
-1	0 (If time "T_w^-" has not elapsed since $C_w^+ = +1$)
0	0

Gas Inhibit

The gas inhibit prevents a gas correction command from being applied to the gas jets until the "same signed" reaction wheel correction command has been present for a time duration "T_g". Operation of

the gas inhibits are expressed by the truth tables below.

Gas Input C_g^+	Output of Inhibit C_{gi}^+
+1	+1 (If C_w^+ = +1 continuously during previous time duration "T_g^+")
+1	0 (If $C_w^+ \neq +1$ continuously during previous duration "T_g^+")
0	0

Gas Input C_g^-	Output of Inhibit C_{gi}^-
-1	-1 (If C_w^- = -1 continuously during previous time duration "T_g^-")
-1	0 (If $C_w^- \neq -1$ continuously during previous duration "T_g^-")
0	0

Solar Array Inhibit

The solar array inhibit prevents a solar array error command in opposition to the previous error command from being applied to the solar array motor until a time "T_p" has elapsed. The truth below define the operation of the inhibits.

Input to Inhibit (C_p^+)	Output of Inhibit (C_{pi}^+)
+1	+1 (If time "T_p^+" has elapsed since C_p^- = -1)
+1	0 (If time "T_p^+" has not elapsed since C_p^- = -1)
0	0

Input to Inhibit C_p^-	Output of Inhibit C_{pi}^-
-1	-1 (If time "T_p^-" has elapsed since $C_p^+ = +1$)
-1	0 (If time "T_p^-" has not elapsed since $C_p^+ = +1$)
0	0

Symbol	Definition
ϕ_c	- Shaping filter output
H_w	- Momentum stored in reaction wheel
N_w	- Reaction wheel torque
K_f	- Reaction wheel windage coefficient
α, τ, τ_ℓ	- Filter parameters (refer to block diagram Figure C-2)
ϕ_{dw}	- Reaction wheel bi-stable deadzone
h_w	- Reaction wheel bi-stable hysteresis
T_w	- Reaction wheel inhibit time delay
ϕ_{dg}	- Gas bi-stable deadzone
h_g	- Gas bi-stable hysteresis
N_g	- Gas torque
T_g	- Gas inhibit time delay
τ_s	- Sun sensor time constant

Table D-1 Roll Nomenclature*

* For Nomenclature of boom dynamics and solar array drive see Appendices A and B, respectively.

FOLDOUT FRAME 1

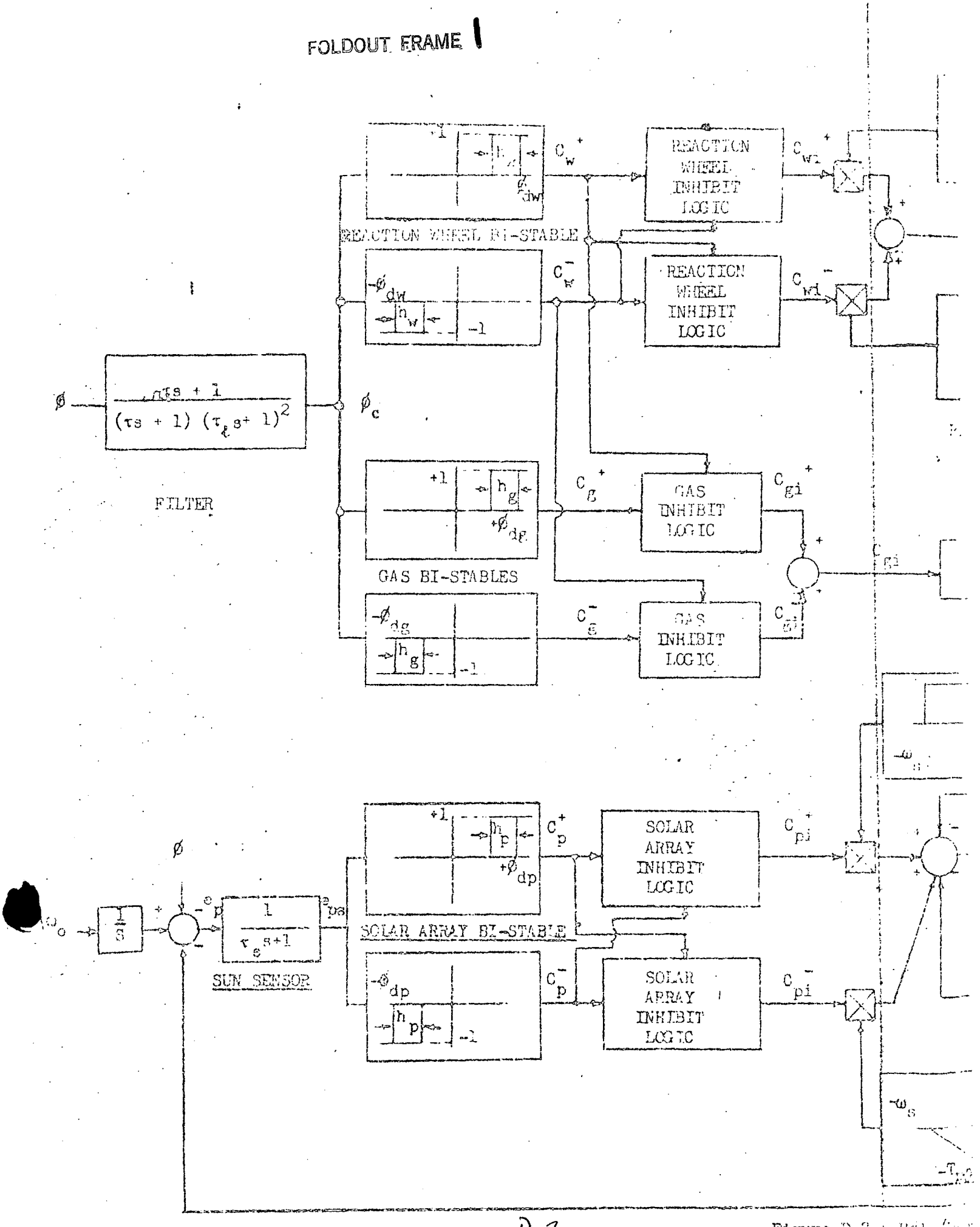

D-1-a

Figure D-2. Roll/Ye

FOLDOUT FRAME 2

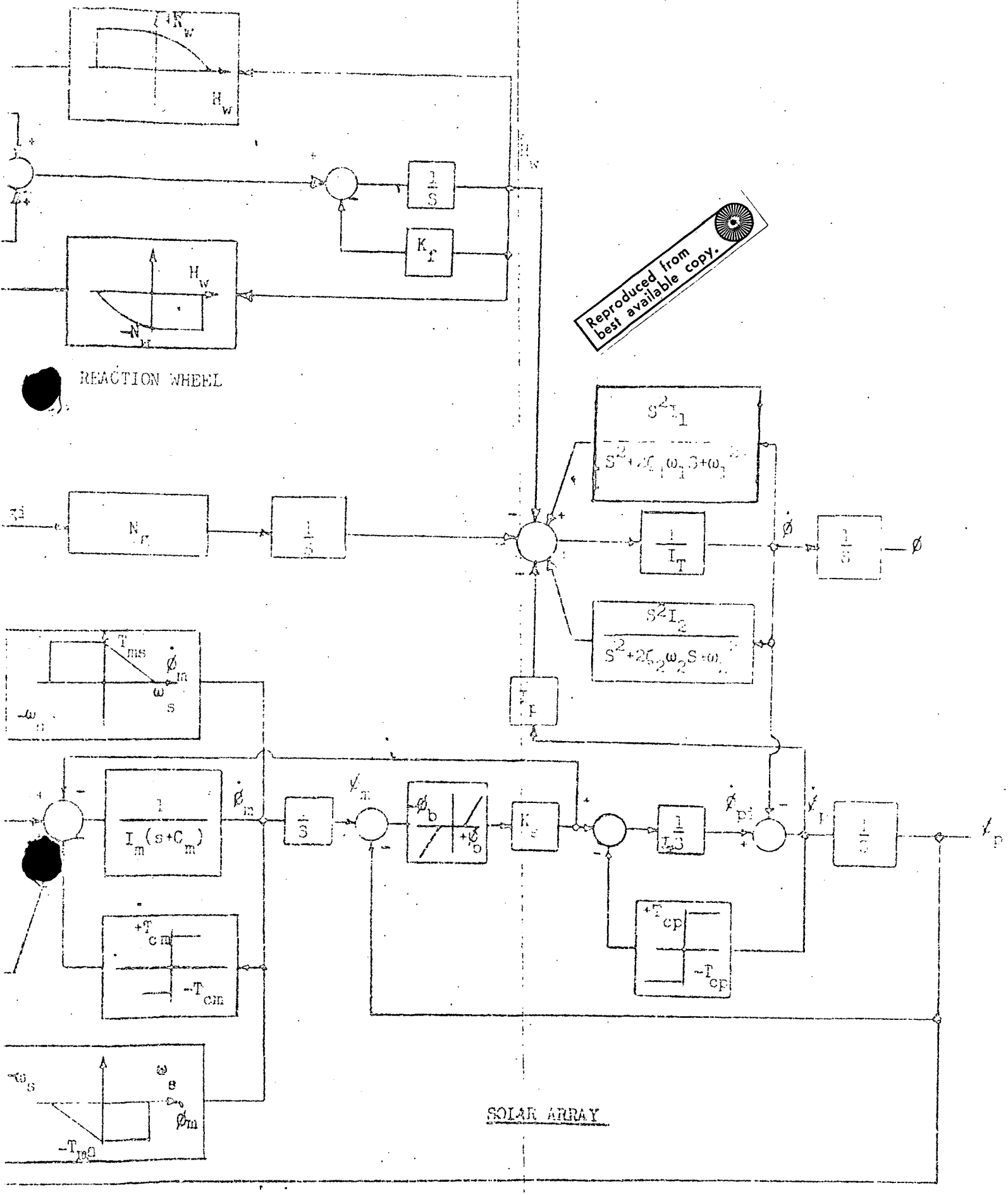

Roll/Normal Mode Block Diagram

Item	Parameter	Nominal Value	Max. Variation About Nominal
Filter	α	10.0	± 20%
	τ_ℓ	0.2 sec	± 20%
	τ	1.25 sec	± 20%
Reaction Wheel Bi-Stable	$\lvert\dot{\phi}_{dw}\rvert$	0.4°	± 20%
	h_w	.080°	± 33%
Reaction Wheel Motor	N_w	.052 ft lb	+ 20%; - 50%
	K_f	.0036 sec^{-1}	+200%; - 100%
Reaction Wheel Inhibit Logic	T_w	5.0 sec	± 50%
Gas Bi-Stable	$\lvert\dot{\phi}_{dg}\rvert$	1.0°	± 20%
	h_g	0.08°	± 33%
Gas Jets	N_g	.384 ft lb	± 20%
Gas Inhibit Logic	T_g	15.0 sec	± 20%
Boom #1	I_1	216 slug ft^2	± 20%
	ζ_1	.0025	+ 100%; - 50%
	ω_1	1.51 rad/sec	± 20%
Boom #2	I_2	209 slug ft^2	± 20%
	ζ_2	.0025	+ 100%; - 50%
	ω_2	1.66 rad/sec	± 20%
Composite Inertia	I_t	670 slug ft^2	± 15%

Table D-2 Normal Mode Roll Axis Parameter Values

FOLDOUT FRAME 1

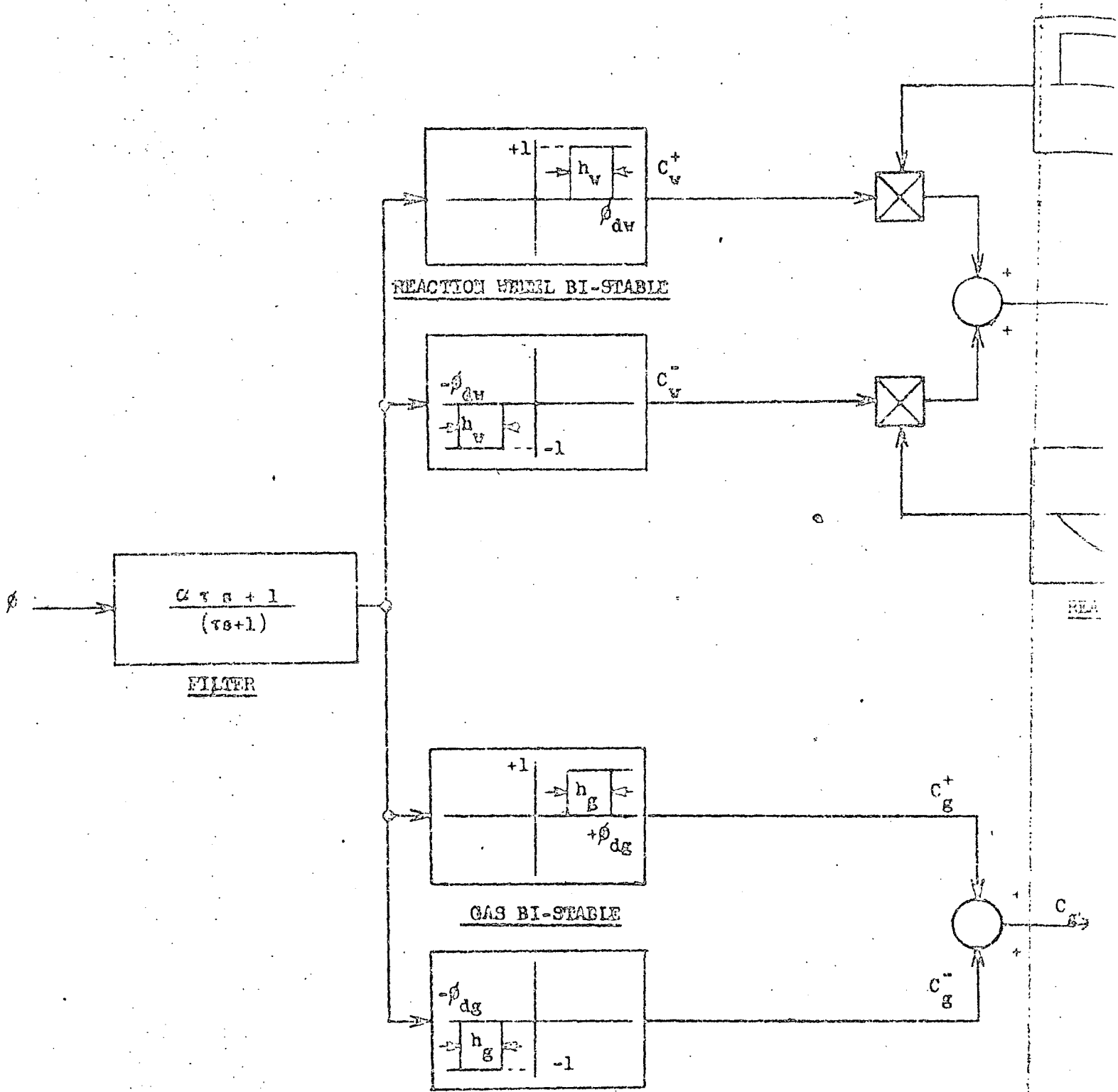

Figure D-3. Roll Sun A

FOLDOUT FRAME 2

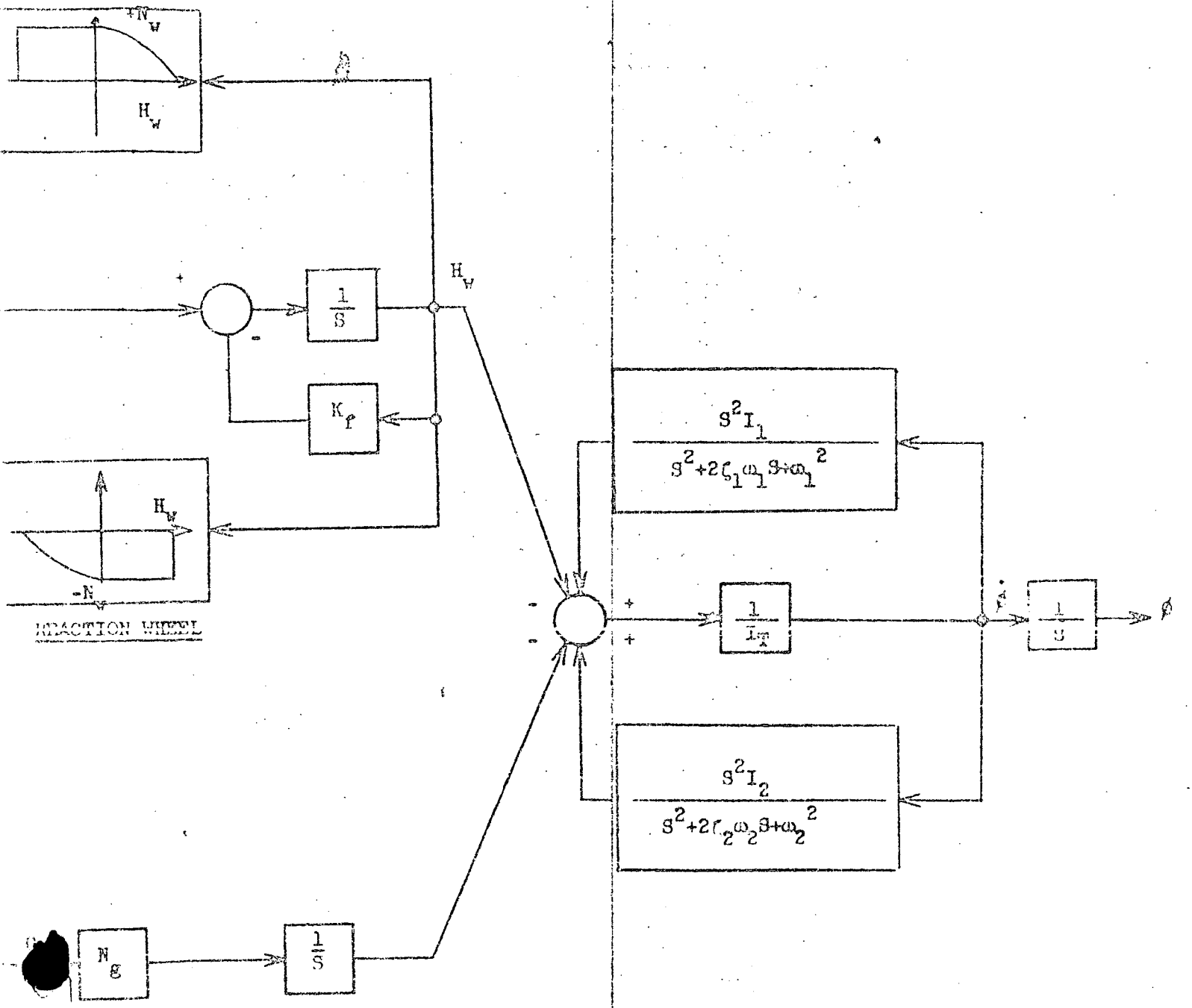

um Acquisition Mode

D-9-b

Item	Parameter	Nominal Value	Max. Variation About Nominal
Filter	α	10.0	$\pm$ 20%
	τ	1.25 sec	$\pm$ 20%
Reaction Wheel Bi-Stable	$\lvert\phi_{dw}\rvert$	1.0	$\pm$ 20%
	h_w	0.2	$\pm$ 33%
Reaction Wheel Motor	N_w	.052 ft lb	+ 20%; - 50%
	K_f	.0036 sec^{-1}	+200%; - 100%
Gas Bi-Stable	$\lvert\phi_{dg}\rvert$	2.5	$\pm$ 20%
	h_g	.2	$\pm$ 33%
Gas Jets	N_g	.384 ft lb	$\pm$ 20%

Table D-3 Roll Sun Acquisition Parameter Values

FOLDOUT FRAME 1

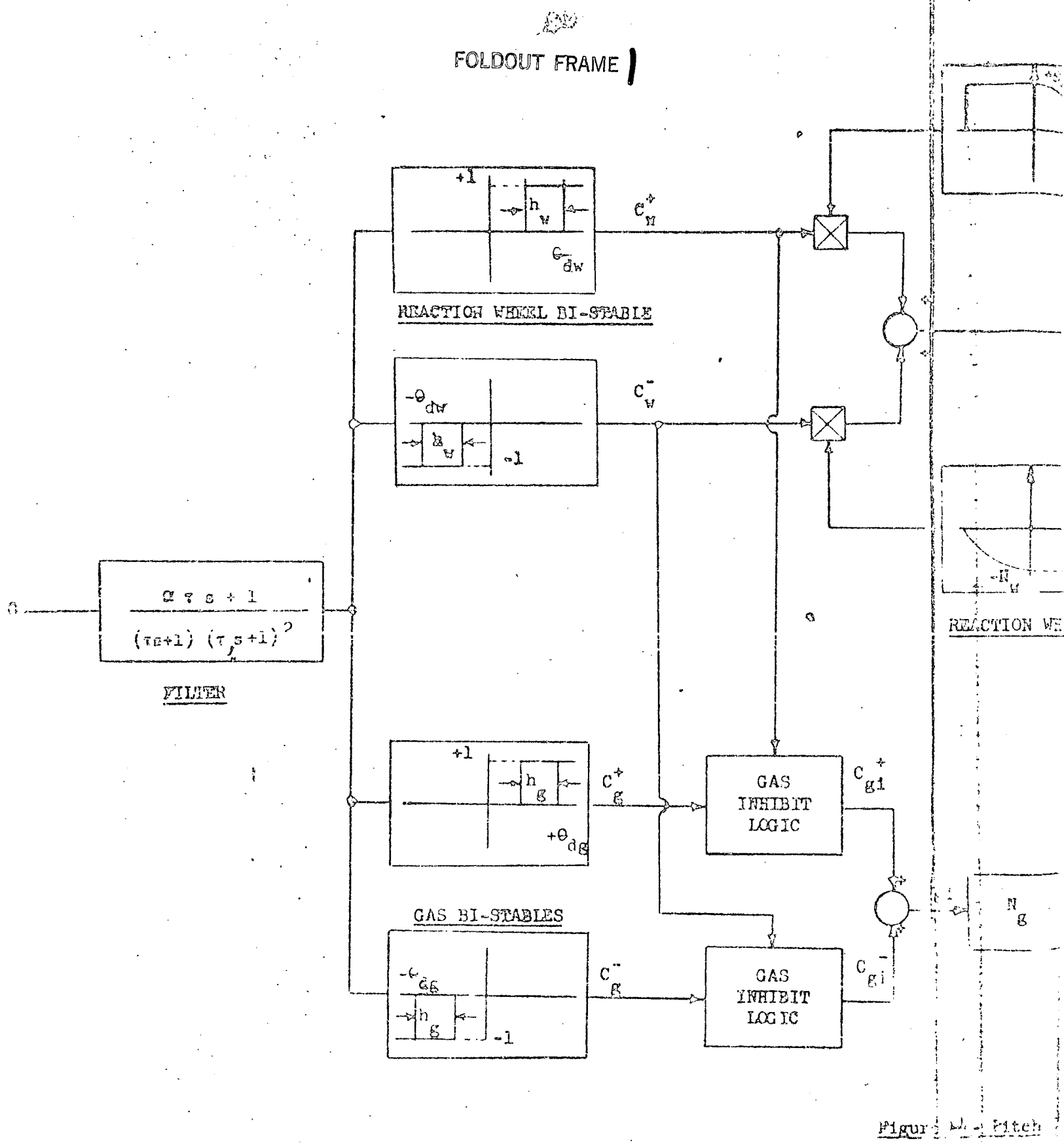

Figur[illegible] Pitch

FOLDOUT FRAME 2

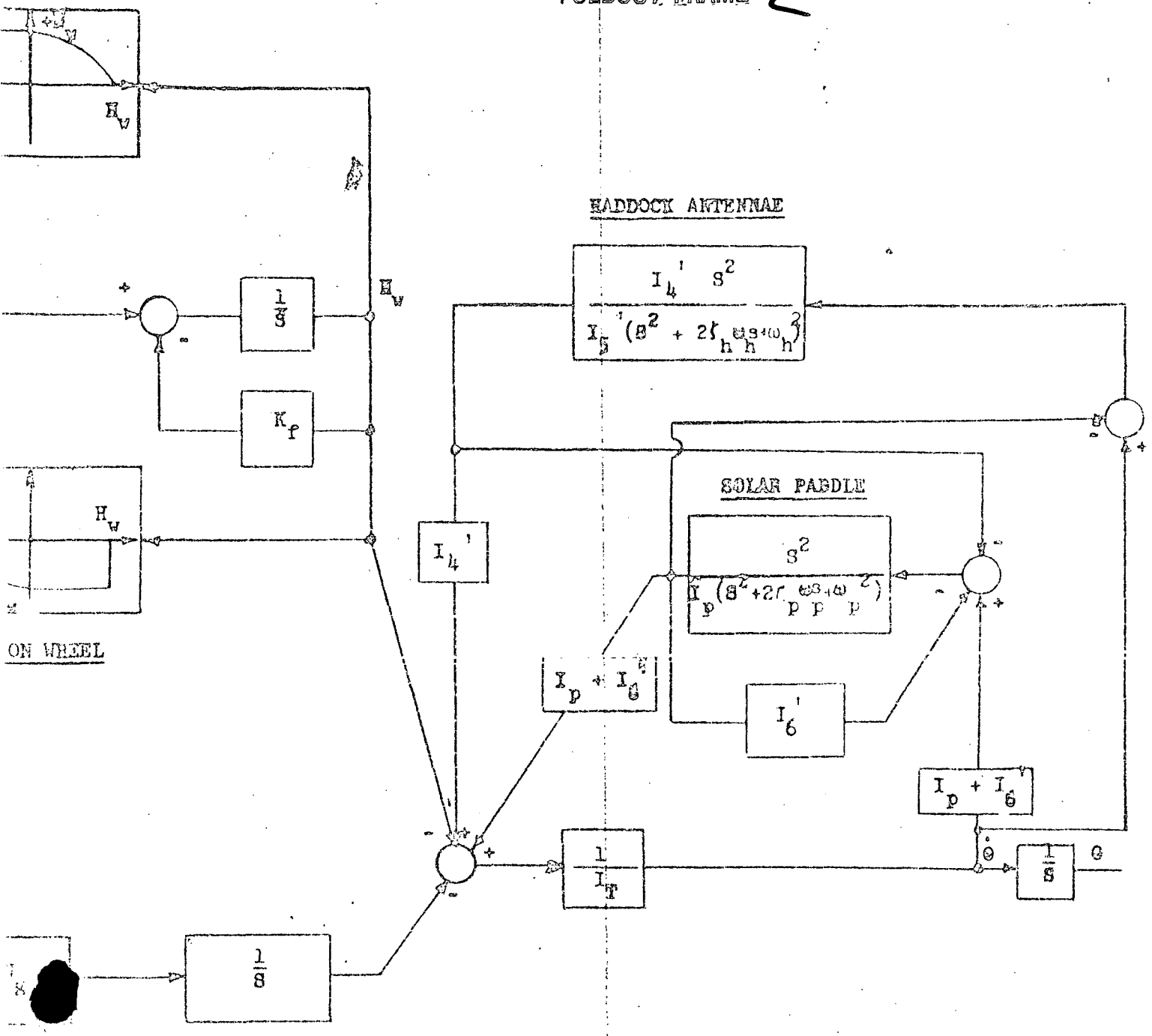

teh Control Block Diagram

Item	Parameter	Nominal Value	Max. Variation About Nominal
Filter	α	10.0	± 20%
	τ_ℓ	0.2 sec	± 20%
	τ	1.25 sec	± 20%
Reaction Wheel Bi-Stable	$\lvert\theta_{dw}\rvert$	0.4°	± 20%
	h_w	$.080^\circ$	± 33%
Reaction Wheel Motor	N_w	.052 ft lb	+ 20%; -35%
	K_f	.0036 sec	+ 200%; - 100%
Gas Bi-Stable	$\lvert\theta_{dg}\rvert$	1.0°	± 20%
	h_g	$.08^\circ$	± 33%
Gas Jets	N_g	.308 ft lb	± 20%
Gas Inhibit Logic	T_g	15 sec	± 20%
Solar Paddle	I_p	305 slug ft^2	± 20%
	ζ_p	.0233	+ 100%; - 50%
	ω_p	11.0 rad/sec	± 50%
	L_A	9.4 ft	0%
Haddock* Antennae	L_D	60 to 5 ft	----
	ζ_H	.0025	+ 0, -100%
	ω_H	.132 to 3.13 $\frac{rad}{sec}$	----
	I_4'	93.5 to 3.9 slug ft^2	----
	I_5'	81.0 to 1.36 slug ft^2	----
	I_6'	107 to 11.3 slug ft^2	----
Inertia of Main Body	I_b	57 slug ft^2	0%

Table D-4 Pitch Axis Parameter Values

* Nominal values used in simulation for Haddock antennae.

L_D = 60 ft (spool not hung up); ω_H = .157 $\frac{rad}{sec}$, I_4' = 71.8 slug ft^2, I_5' = 62.3 slug ft^2, I_6' = 83.2 slug ft^2.

FOLDOUT FRAME

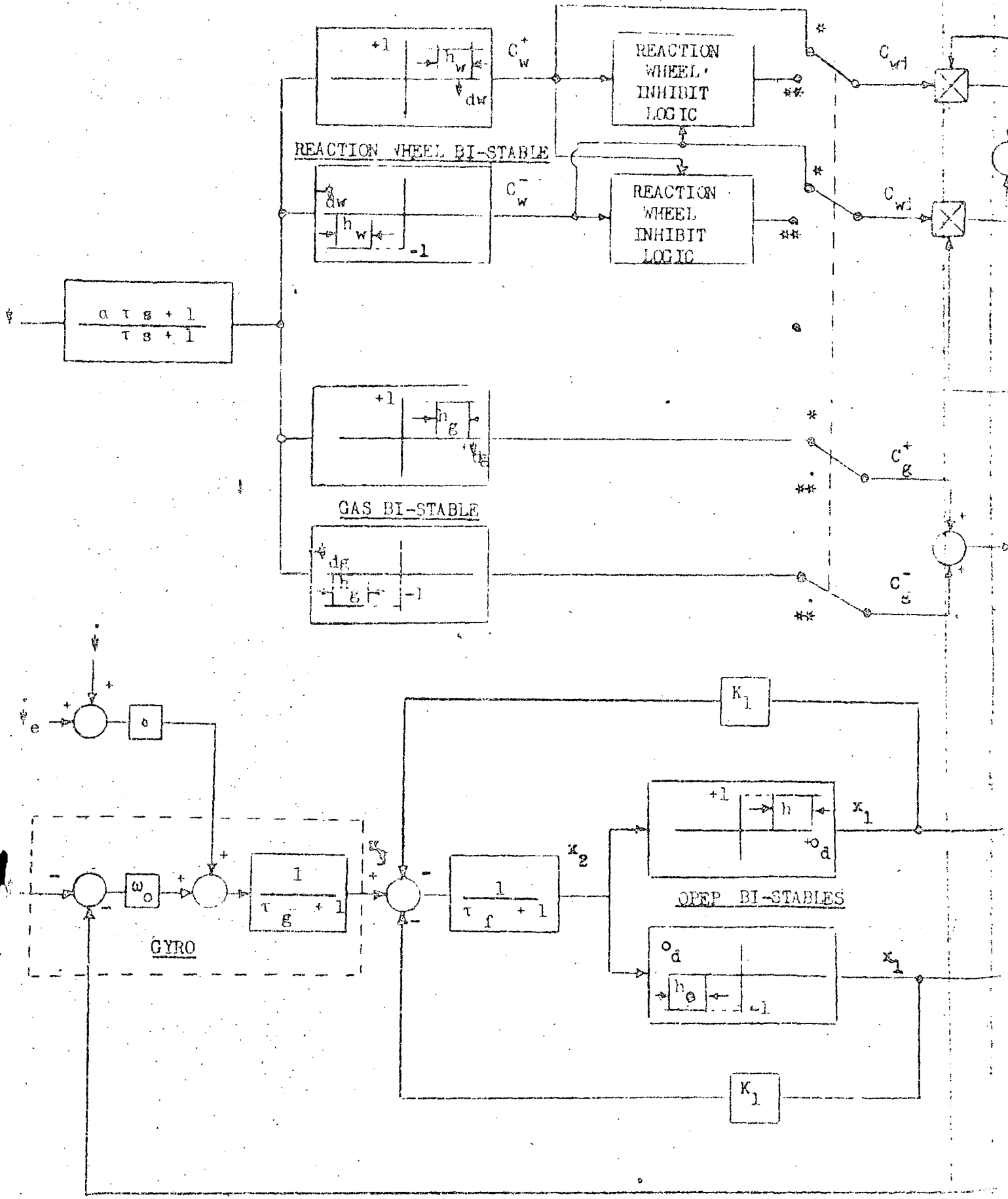

FIGURE D-5. YAW CONTROL

FOLDOUT FRAME 2

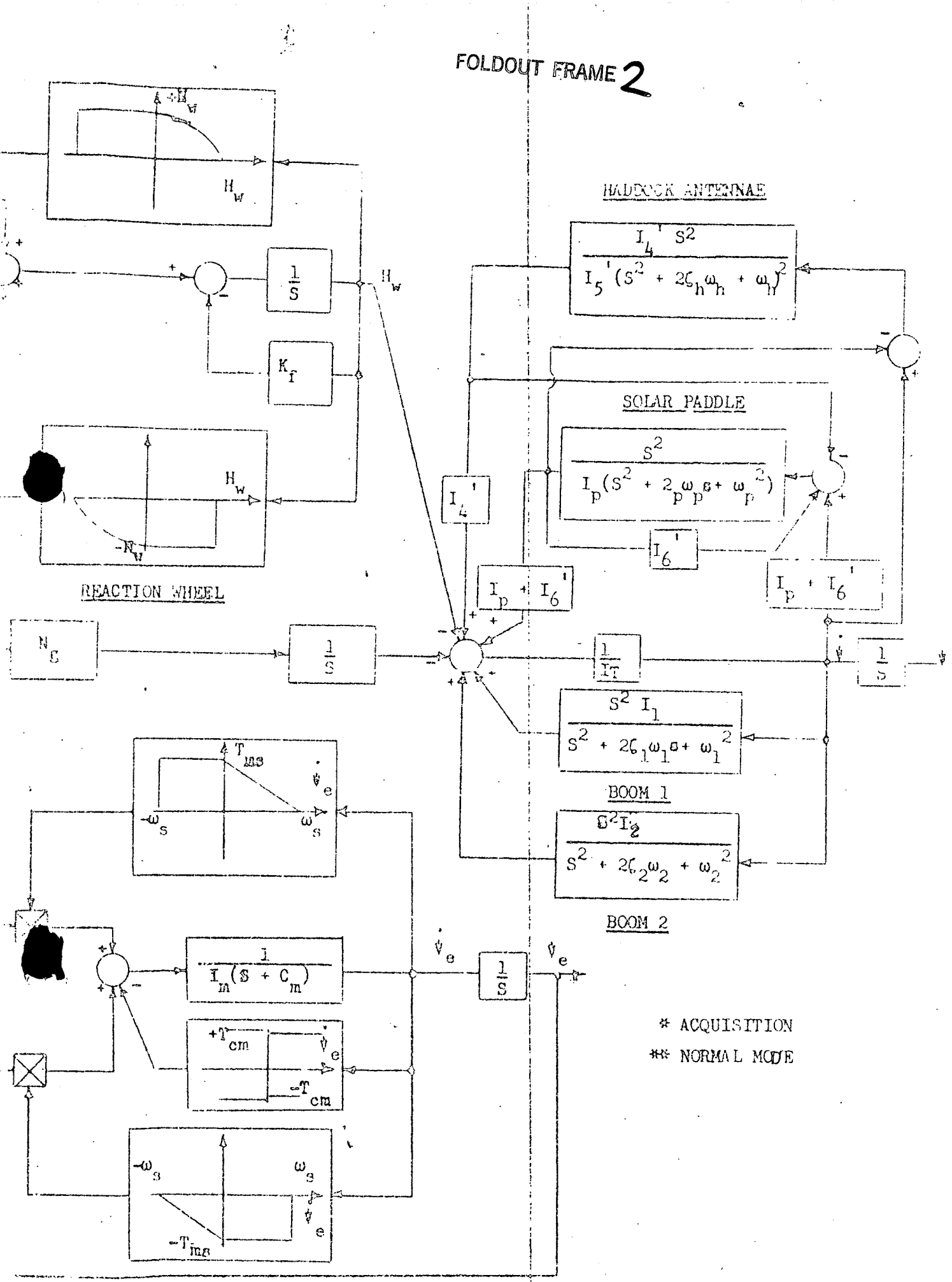

DIAGRAM D-13 - b

Item	Parameter	Nominal Value	Max. Variation About Nominal
Filter	α	10.0	$\pm$ 20%
	τ	5.0 sec	$\pm$ 20%
Reaction Wheel Bi-Stable	$\lvert\dot{\theta}_{dw}\rvert$	1.17°	$\pm$ 20%
	h_w	$.24^{\circ}$	$\pm$ 33%
Reaction Wheel Motor	N_w	.104 ft lb	+ 20%; - 50%
	K_f	.0036 sec^{-1}	+ 200%; -100%
Reaction Wheel Inhibit Logic	T_w	5 sec	$\pm$ 50%
Gas Bi-Stable	$\lvert\dot{\theta}_{dg}\rvert$	5.0°	$\pm$ 20%
	h_g	$.5^{\circ}$	$\pm$ 33%
Gas Jets	N_g	.71 ft lb	$\pm$ 20%
Solar Paddle	$I_p, \zeta_p, \omega_p, I_A$	Same as pitch axis	
Antennae	$L_D, \zeta_N, \omega_A, I_4', I_5', I_6'$	Same as pitch axis	
Boom #1	I_1	216 slug ft^2	$\pm$ 20%
	ζ_1	.0025	+ 100%; -50%
	ω_1	1.51 rad/sec	$\pm$ 20%
Boom #2	I_2	209 slug ft^2	$\pm$ 20%
	ζ_2	.0025	+ 100%; -50%
	ω_2	1.66 rad/sec	$\pm$ 20%
Main Body Inertia	I_b	213 slug ft^2	$\pm$ 15%

Table D-5 Yaw Axis Parameter Values

APPENDIX E

PREDICTION OF SOLAR ARRAY COAST ANGLE

To verify that a limit cycle could be induced in the solar array loop when the bi-stable deadzone was $0.5 \pm .1^{o}$, the following simplified model was hypothesized. The assumptions are the following:

1. Paddle is rigidly attached to the motor shaft
2. Sun sensor time constant is negligible
3. Motor attains steady-state speed ($\dot{\phi}_{m_{ss}}$) before motor is commanded "off"

From Appendix B the differential equation defining the motion is the following:

$$\ddot{\phi}_m(I_m) = T_m - \dot{\phi}_m \left(\frac{T_m}{\omega_s} + C_m\right) - T_c \left(\text{sign } \dot{\phi}_m\right)$$

where

$$T_c = T_{pc} + T_{mc}$$

For bi-stable commanding motor "on", $T_m = T_{ms}$ = motor stall torque. Let t_o = time motor is initially commanded to "on"; then

$$\dot{\phi}_m = \frac{T_{ms} - T_c \left(\text{sign } \dot{\phi}_m\right)}{C_m + \frac{T_m}{\omega_s}} \left[\left(1 - e^{-\frac{\left(C_m + \frac{T_{ms}}{\omega_s}\right)(t - t_o)}{I}}\right)\right] + \dot{\phi}(o) e^{-\frac{\left(C_m + \frac{T_m}{\omega_s}\right)(t - t_o)}{I}}$$

For the values in Table B-2

$$-\frac{\left(C_m + \frac{T_{ms}}{\omega_s}\right)}{I} \approx 17.7 \text{ sec}^{-1}$$

Therefore, the time constant is approximately 56 milliseconds, and for $t > 250$ milliseconds,

$$\dot{\phi}_m \cong \dot{\phi}_{m_{ss}}$$

where $\dot{\phi}_{m_{ss}} = \dfrac{T_{ms} - T_c (\text{sign } \dot{\phi}_m)}{C_m + \dfrac{T_m}{\omega_s}}$; thus, assumption "(3)" appears valid.

For bi-stable commanding motor "off", $T_m = 0$ since the excitation to the field winding is removed when the bi-stable command is zero. Assuming motor angular velocity is $\dot{\phi}_{m_{ss}}$ at t' (time motor is commanded to "off"),

$$\dot{\phi}_m = -\frac{T_c(\text{sign } \dot{\phi}_m)}{C_m}\left(1 - e^{-\frac{(C_m)(t - t')}{I}}\right) + \dot{\phi}_{m_{ss}} e^{-\frac{C_m (t - t')}{I}}$$

Let t_f = time when motor stops coasting. Then, using the above equations,

$$(t_f - t') = \ln\left(1 + \frac{\dot{\phi}_{mss} C_m}{T_c(\text{sign } \dot{\phi}_m)}\right)$$

For the values of Table 6-2, $(t_f - t') = .93$ sec.

Let ϕ_{mf} = motor angle at t_f

ϕ_{mo} = motor angle at t'